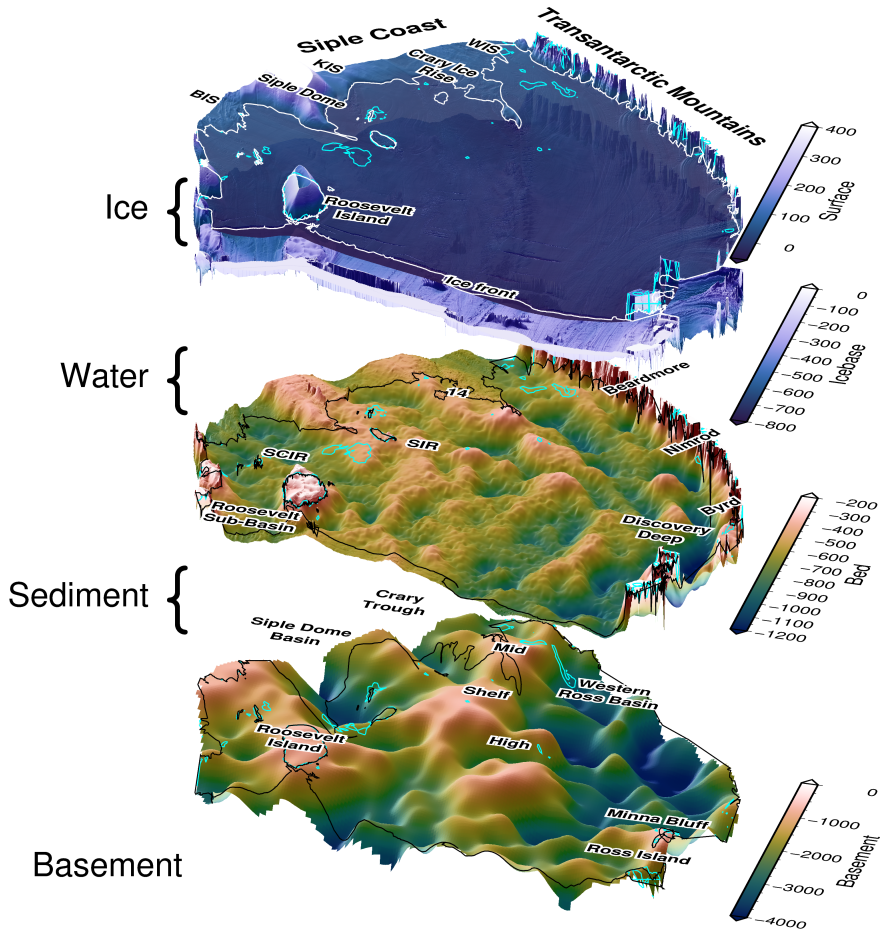


Airborne Geophysical Investigation beneath Antarctica's Ross Ice Shelf



A thesis presented for the degree of
Doctor of Philosophy in Geophysics

Matthew Tankersley



Antarctic Research Centre
Victoria University of Wellington
New Zealand
October 19, 2023

Abstract

The Ross Ice Shelf controls the flow of ice into the ocean from catchments consisting of both the East and West Antarctic Ice Sheets. These catchments hold a volume of ice equivalent to \sim 12 m of global sea level rise. To adequately understand how this ice will respond to a warming world requires knowledge of the properties and parameters which influence how the ice sheet behaves. These boundary conditions include fundamental knowledge of the Earth, such as the shape of the bed beneath the ice, the seafloor, and the geologic structures of the upper crust. Knowledge of the physiography and sub-surface geology is severely lacking beneath ice shelves due to their inaccessibility.

Here, we use airborne geophysical data from an extensive survey over the Ross Ice Shelf to better understand these boundary conditions. From the analysis of airborne magnetics data, we model the thickness of sediment, the shape of the crystalline basement, and the likely locations of faults throughout the crust under the Ross Ice Shelf. We find a continuous drape of sediment over the seafloor, including deep and narrow fault-bound sedimentary basins beneath the Siple Coast.

Using airborne gravity data, and distributed seismic constraints over the ice shelf, we develop and implement a gravity inversion to recover a higher-resolution bathymetry model beneath the ice shelf. This bathymetry model and our quantification of spatial uncertainty highlight locations likely important for sub-ice shelf ocean circulation and possible recent pinning points. In the process of these geophysical investigations, we reveal a wide range of insights relating to how bathymetry and geology play a critical role in the past, present, and future dynamics of the ice sheet, and how this region has developed over its tectonic history.

Plain language summary

The Ross Ice Shelf in Antarctica is a vast expanse of floating ice, hundreds of meters thick, which is connected to the ice on land. It plays a crucial role in slowing down the flow of ice from the Antarctic Ice Sheet into the ocean. Understanding how this ice will respond to a warming world requires knowledge of the Earth's properties that influence its behaviour. These properties include the depth of the seafloor beneath the ice shelf, the topography beneath the ice on land, and geological features like faults and rock types. However, accessing and surveying the sub-Ross Ice Shelf is challenging, leading to limited knowledge.

In this thesis, we utilized data collected during an airborne survey of the entire Ross Ice Shelf to investigate the depths of the seafloor and the underlying geology. By analyzing measurements of Earth's magnetic field across the ice shelf, we reveal the thickness of sediment beneath the seafloor. This is possible due to variations in magnetic properties between sediment and bedrock. The thickness of this layer

of sediment ranges from tens of meters to several kilometers. Additionally, we determine the shape of the underlying bedrock, which helps identify probable fault locations.

We also utilized measurements of changes in Earth's gravity field across the ice shelf to estimate the depth of the seafloor, in a process called a gravity inversion. This method is feasible since variations in the underwater topography (bathymetry) result in small, measurable changes in Earth's gravity, due to the density difference between the seafloor and the water. This bathymetry model, along with our assessment of uncertainties, identifies areas beneath the ice shelf that likely influence ocean currents as well as potential locations where the ice shelf was anchored to the bedrock in the recent past.

Through these geophysical investigations, we gained valuable insights into how features of the underlying Earth have influenced the behaviour of the overlying ice in the Ross Ice Shelf region, both historically and in the future. This information enhances our understanding of the Ross Ice Shelf region and its interaction with the underlying Earth.

Acknowledgements

I would like to express my gratitude to the following individuals and organizations for their invaluable support and guidance throughout this thesis.

First and foremost I would like to thank my advisors, Huw Horgan and Fabio Caratori-Tontini for their unwavering support, patience, and mentorship. Huw, I will always appreciate your effort to include me in the two field seasons to Antarctica. Those trips included some of my most valued experiences, which I have you to thank for. You have had an immeasurable impact on my development as a scientist yet gave me space to pursue my own interests and styles. Fabio, through your continuous encouragement and belief in my abilities you gave me the confidence to explore many challenging aspects of this thesis I would have otherwise omitted.

To two of my supporting academics, Christine Siddoway and Kirsty Tinto. Without witnessing your dedication and enthusiasm for Antarctic science I would not have pursued this PhD. I hope for years of collaboration to come! To the various members of K863; Andrew, Jenny, Hamish, Will, Bob, and Caitlin, there couldn't have been a better group to spend so much time with in the deep field. Thank you for making those two trips such an incredible part of my PhD. To the open-source coding communities, including Fatiando, PyGMT and Software Underground, especially Wei Ji Leong, Santi Soler and Leo Uieda, thank you for the wonderful tools, tutorials, and individual support you have offered me throughout my journey of learning to code.

To the various academics and staff on the 5th floor of the Cotton Building, thank you for years of great conversations over lunch, beers, or bike rides. Thank you to the friends who made living in and exploring NZ so great; Fran, Chris, Alanna, Marjo, Knut, Callum, Dina, Flo. Charlotte, thank you for the unconditional support throughout this journey, it would not have been possible or as enjoyable without you. To my family, thanks for the continuous encouragement and love from afar. Knowing I always had you all to count on back home gave me the stability I needed.

To the reviewers of this thesis; Andrew Gorman, Simon Lamb, and Paul Wimberry, thank you for your time spent thoroughly reading and contemplating on this work; your suggestions and discussions with me were much appreciated.

Lastly, to the various funders of this research including several grants I have received, thank you for the support; GNS Science, the Antarctic Research Centre and Antarctica New Zealand.

Contents

1	Introduction	15
1.1	Motivation	15
1.2	Influences on ice dynamics	15
1.2.1	Bedrock topography	15
1.2.2	Geologic structures	18
1.2.3	Basal roughness	19
1.3	Ross Ice Shelf	20
1.3.1	Past investigations	20
1.4	Research questions	21
1.5	Outline	22
1.6	Data and Code	23
2	Airborne magnetic analysis: Basement depths and sediment thickness	25
2.1	Introduction	26
2.2	Data and Methods	28
2.3	Results	29
2.4	Discussion	31
2.4.1	West Antarctic Rift System extensional basins	31
2.4.2	Consequences for ice sheet dynamics	33
2.4.3	Mid-Shelf High - Central High	33
2.4.4	Thermal subsidence and sedimentation	34
2.5	Conclusions	35
2.6	Open Research	35
2.7	Acknowledgements	35
3	Gravity inversion: a tool for bathymetry modelling	37
3.1	Introduction	38
3.2	Methods	40
3.2.1	Geophysical inversion	40
3.2.1.1	Non-Linear inversions	42
3.2.1.2	Geometric inversions	42
3.2.2	Forward modelling	42
3.2.2.1	Discretization	43
3.2.2.2	Gravity edge effects	43
3.2.3	Isolating anomalies	44
3.2.4	Regional vs. Residual gravity	45
3.2.5	Running the inversion	46
3.2.5.1	Jacobian matrix	46

3.2.5.2	Least-squares solver	48
3.2.5.3	Regularization	48
3.2.6	Stopping Criteria	50
3.2.7	Software implementation	51
3.3	Synthetic models	51
3.3.1	Simple model	52
3.3.1.1	Model setup	52
3.3.1.2	Cross validation	53
3.3.1.3	Comparing vertical derivative methods	54
3.3.1.4	Added noise	55
3.3.1.5	Down-sampled data	56
3.3.2	Ensemble of Noise and Sampling values	58
3.4	Adding a regional component	60
3.4.1	Regional separation methods	60
3.4.2	Constraint point minimization	62
3.4.2.1	Tensioned minimum curvature	63
3.4.2.2	Bi-harmonic splines	63
3.4.2.3	Gridding comparison	63
3.4.3	Inversion results	65
3.4.4	Ensemble of Noise and Sampling values	66
3.4.5	Simple model comparison	66
3.5	Ross Sea model	67
3.5.1	Observed gravity	67
3.5.2	Starting bathymetry	69
3.5.3	Gravity misfit	70
3.5.4	Inversion	71
3.5.5	Uncertainty analysis	71
3.5.6	Effects of constraint spacing	73
3.5.7	Effects of gravity data	75
3.6	Discussion	76
3.6.1	Simple synthetic model	76
3.6.1.1	Inversion results	77
3.6.1.2	Ensemble results	77
3.6.2	Regional component	79
3.6.2.1	Regional separation methods	79
3.6.2.2	Constraint point minimization	79
3.6.2.3	Inversion results	80
3.6.2.4	Ensemble results	80
3.6.3	Ross Sea model	81
3.6.3.1	Effects of the gravity data	82
3.6.3.2	Effects of the constraints	83
3.6.3.3	Uncertainties	84
3.7	Future work	85
3.8	Conclusion	85
4	Ross Ice Shelf bathymetry inversion	89
4.1	Introduction	90
4.2	Methods	92
4.2.1	Gravity reduction	92

4.2.1.1	Attraction of normal Earth	93
4.2.1.2	Topographic mass effects	94
4.2.1.3	Regional separation	98
4.2.2	Bathymetry inversion	99
4.2.3	Starting bathymetry	100
4.2.4	Uncertainty quantification	100
4.3	Past inversions	103
4.3.1	Gravity reduction comparison	103
4.3.1.1	Regional separation	105
4.3.2	Inversion comparison	106
4.3.3	Uncertainty comparison	107
4.4	Results	107
4.4.1	Starting bathymetry	108
4.4.2	Gravity processing results	111
4.4.3	Gravity reduction results	112
4.4.4	Inversion results	114
4.4.5	Uncertainty	114
4.4.5.1	Partitioning uncertainty	119
4.5	Discussion	119
4.5.1	Uncertainties and parameter importance	119
4.5.1.1	Gravity component	119
4.5.1.2	Constraints component	121
4.5.1.3	Density component	121
4.5.1.4	Interpolation component	122
4.5.1.5	Reducing uncertainties	123
4.5.1.6	Past estimations of uncertainty	123
4.5.2	Past bathymetry models	124
4.5.2.1	Starting model comparison	124
4.5.2.2	Inversion result comparisons	125
4.5.2.3	Ocean cavity comparison	129
4.5.3	Implications	131
4.5.3.1	New potential pinning points	131
4.5.3.2	Basal melting	131
4.5.3.3	Geologic and tectonic significance	133
4.6	Conclusion	134
5	Synthesis	137
5.1	Geologic structures	138
5.2	Inversion	138
5.3	Ross Ice Shelf bathymetry	140
5.4	Geologic controls	141
5.4.1	Present controls	141
5.4.1.1	Basal melt	141
5.4.1.2	Modern pinning points	142
5.4.1.3	Sediment distribution	144
5.4.1.4	Geothermal heat flux at Siple Coast	144
5.4.2	Past and future implications	145
5.4.2.1	Retreat dynamics	146
5.4.2.2	Glacial initialization	147

5.5 Future work	148
5.6 Concluding remark	150
Appendix A	151
A.1 Introduction	151
A.2 Depth to basement assumptions	151
A.3 Magnetic data collection, processing, and Werner deconvolution . . .	152
A.4 Tying magnetic basement to seismic basement	153
A.5 Tying Ross Sea magnetic basement to Ross Ice Shelf magnetic basement	154
A.6 Gridding, merging, and filtering	154
A.7 Sediment thickness and β -factor calculations	155
A.8 Uncertainties	156
Appendix B	163
B.1 Synthetic inversion with a regional field	163
B.2 Ross Sea synthetic model	164
Appendix C	169
C.1 Gravity disturbance vs anomaly	169
Appendix D Antarctic-Plots	171
D.1 Fetch	171
D.2 Map	172
D.3 Profile	172
D.4 Regions	172

List of Figures

1.1	Past observations and future predictions of sea level rise	16
1.2	Summary of existing geologic and geophysical data for Antarctica . .	17
2.1	Bathymetry, magnetics, and acoustic basement	27
2.2	Ross Sea magnetic and seismic basement comparison	29
2.3	Basement elevation and sediment thickness	30
2.4	Tectonic interpretation of the sub-Ross Ice Shelf	32
3.1	Ice shelves of Antarctica	39
3.2	Equivalent methods of discretizing a density contrast	44
3.3	Annulus approximation of a vertical prism	47
3.4	Training and testing set configuration	49
3.5	Weighting grid for the simple synthetic inversion	50
3.6	Simple synthetic model bathymetry	52
3.7	Simple synthetic gravity anomalies	53
3.8	Annulus approximation inversion results	54
3.9	Annulus approximation inversion cross-validation and profile	54
3.10	Finite differences inversion results	55
3.11	Finite differences and annulus approximation convergence curves . .	55
3.12	Synthetic inversion with noise	56
3.13	Synthetic inversion with noise, CV and profile	56
3.14	Creating a low-resolution observed gravity survey	57
3.15	Synthetic inversion with sampled gravity	58
3.16	Synthetic inversion with sampled gravity, CV and profile	59
3.17	Gravity data ensemble for synthetic model	59
3.18	Gravity anomalies with a regional field	61
3.19	Regional separation methods	62
3.20	Constraint point minimization gridding techniques	64
3.21	Synthetic inversion with regional component, CV and profile	65
3.22	Synthetic inversion with regional component results	65
3.23	Gravity data ensemble with regional component	66
3.24	Ross Sea semi-synthetic model	68
3.25	Ross Sea synthetic airborne survey	69
3.26	Ross Sea starting bathymetry	70
3.27	Ross Sea synthetic gravity anomalies	71
3.28	Ross Sea inversion, CV and convergence	72
3.29	Ross Sea inversion results	72
3.30	Ross Sea Monte Carlo simulation	74
3.31	Constraint spacing effects	75
3.32	Ross Sea ensemble of noise levels and gravity spacing	76

3.33	Grouped synthetic inversion ensemble	78
3.34	Synthetic inversion error and regional error	80
3.35	Grouped synthetic inversion with regional ensemble	81
3.36	Ross Sea inversion error and regional error	82
3.37	Grouped Ross Sea inversion with regional ensemble	83
4.1	Ross Ice Shelf inversion inputs	91
4.2	Schematic inversion workflow diagram	93
4.3	Observed gravity data reduction for Antarctica	95
4.4	Components of the topographic mass effect	96
4.5	Discretizing the topographic mass effect	97
4.6	Topographic mass effect for Antarctica	98
4.7	Schematic Monte Carlo workflow diagram	102
4.8	Random vs Latin hypercube sampling	103
4.9	Ross Ice Shelf starting bathymetry	109
4.10	Ross Ice Shelf weighting grid	110
4.11	Re-levelling of the ROSETTA-Ice gravity data	111
4.12	Gravity reduction results for the Ross Ice Shelf	113
4.13	Ross Ice Shelf singular bathymetry inversion results	115
4.14	Latin hypercube sampling distributions and correlations	116
4.15	Ross Ice Shelf inverted bathymetry and uncertainty	117
4.16	Monte Carlo results	118
4.17	Inverted bathymetry comparisons	125
4.18	Ross Ice Shelf assorted cross-sections	128
4.19	Water column thickness comparisons	130
4.20	Basal melt	132
5.1	Ross Embayment geophysical and geologic information	139
5.2	Uncertainty bounds for Ross Ice Shelf bathymetry and ocean cavity .	142
5.3	3D perspective view of Ross Ice Shelf	146
A.1	Various Ross Ice Shelf grids	157
A.2	OIB 403.3 magnetic and seismic basement comparison	158
A.3	Werner deconvolution solutions for ROSETTA-Ice lines	159
A.4	Unfiltered magnetic basement and point solutions	160
A.5	Uncertainty limits of basement and sediment thickness	161
A.6	Misfit distributions between magnetic and seismic basement	162
B.1	Comparison of four methods of regional separation	163
B.2	Constraint point minimization gridding comparison profiles	164
B.3	Synthetic inversion with regional and noise, CV and profile	165
B.4	Synthetic inversion with regional and noise, results	165
B.5	Inversion and regional error for model with regional and noise	165
B.6	Synthetic inversion with regional and re-sampling, CV and profile	166
B.7	Synthetic inversion with regional and re-sampling, results	166
B.8	Inversion and regional error for model with regional and low-res gravity	166
B.9	Inversion and regional error for Ross Sea constraint ensemble	167
C.1	Gravity disturbance vs. anomaly	169

List of Tables

3.1	Simple synthetic model summary	67
4.1	Bathymetry uncertainties comparison	120
A.1	Previous Ross Ice Shelf seismic sediment thickness measurements . .	156

Chapter 1

Introduction

1.1 Motivation

Improving projections of the rate of global sea level rise in response to a warming world is vital for effectively mitigating future environment and socio-economic impacts (Durand et al., 2022). A large portion of the uncertainties in modern and projected sea level rise is related to the contribution from the Antarctic Ice Sheet (Figure 1.1b, Bamber et al., 2022; Edwards et al., 2021; Otosaka et al., 2023; Slater & Shepherd, 2018). The Antarctic Ice Sheet contains a total volume of ice equivalent to 57.2 m of sea level rise (Fretwell et al., 2013). Satellite observations show that Antarctica contributed ~ 7.4 mm to mean sea level since 1992 (Otosaka et al., 2023), and of the various components of sea level rise, the contribution from Antarctica is accelerating the fastest (Figure 1.1a, Nerem et al., 2018). Since the early 1990s, the sea level contribution from Antarctica has increased by 25% (Otosaka et al., 2023). By the end of the century, Antarctica is projected to contribute between 0.03 and 0.28 m to mean sea level (RCP 8.5, Intergovernmental Panel on Climate Change (IPCC), 2022). Optimal strategies for preparing coastal communities to best mitigate the impacts of rising sea level depends on where in this range of uncertainties the true sea level rise will be. Some of the uncertainty in how the Antarctic Ice Sheet will respond to a warming world stems from a lack of understanding of the complex interactions between the ice and the underlying earth (e.g. Schlegel et al., 2018; Zhao et al., 2018).

1.2 Influence of bathymetry, topography, and geology on ice dynamics

The underlying Earth influences ice sheets through several mechanisms, which I group as those resulting from bedrock topography, geologic structures, and bedrock physical properties. Here I describe each of these categories of influences on the Antarctic Ice Sheet, followed by introducing the specific study area, the Ross Ice Shelf.

1.2.1 Bedrock topography

Offshore bathymetry and onshore bed topography exert several fundamental controls on how the Antarctic Ice Sheet behaves. Offshore, where the ice is floating, the

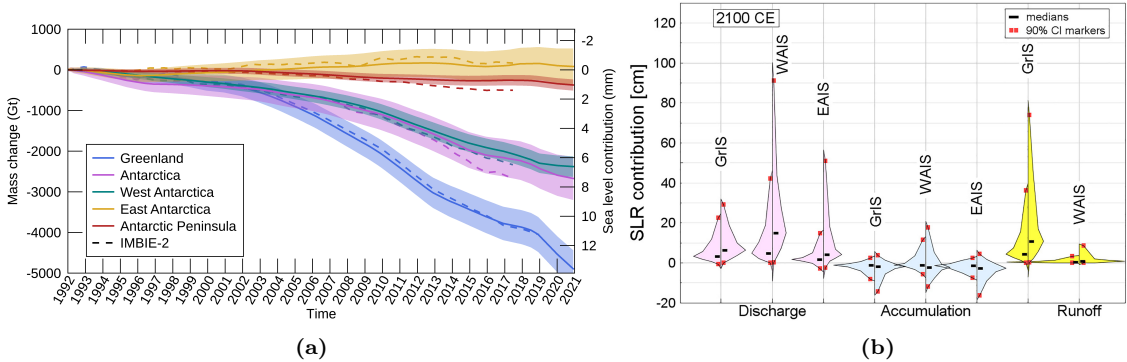


Figure 1.1: Past observations and future predictions of sea level rise. **a)** Observed cumulative mass change and sea level contributions from the various ice sheets. Data comes from satellite-altimetry estimates of volume changes, gravimetric estimates of mass changes, and quantification of input-output fluxes. Figure from Otosaka et al. (2023). **b)** Probability distributions for projected global sea level rise contributions for the year 2100 from the Greenland Ice Sheet (GrIS), West Antarctic Ice Sheet (WAIS), and East Antarctic Ice Sheet (EAIS), separated into three processes; discharge, accumulation, and runoff. Left and right sides of each distribution show the +2°C and +5°C global temperature trajectories, respectively. Figure from Bamber et al. (2022).

influence of the bathymetry is limited to the guiding of ocean circulations. Bathymetric ridges have been shown to block, or re-direct, the inflow of melt-inducing waters to the ocean cavity beneath floating ice shelves (De Rydt et al., 2014; Goldberg et al., 2020; Zhao et al., 2019). Approximately 75% of Antarctica's coastline is composed of these floating ice shelves, and 83% of total ice discharged into the Southern Ocean from Antarctica is through these shelves, highlighting their significance to Antarctica's ice budget (Rignot et al., 2013). Of the 83% of total ice loss from Antarctica through ice shelves, basal melt is responsible for approximately half (Greene et al., 2022; Rignot et al., 2013). Some of this melt occurs from surface waters, where bathymetry has little effect, but for many of the largest ice shelves, the majority of basal melt occurs along the deep grounding zone (Adusumilli et al., 2020). Here, the melt-inducing water bodies are dense and flow into the ice shelf cavities along the seafloor (Holland, 2008; Tinto et al., 2015). Therefore, bathymetric features act to guide or block these circulations from reaching the grounding zone where they can melt the ice base. In addition to steering ocean currents, bed topography, in regions of grounded ice, acts to steer the ice flow.

As revealed by extensive seismic and swath bathymetry data in Antarctica's Ross Sea (Figure 1.2a), the dynamics of an advancing or retreating ice sheet are predominantly controlled by the physiography of the bed (Anderson et al., 2019; Halberstadt et al., 2016). If large troughs and banks exist, advancing ice is initially confined by these features, while the banks remain ice-free (Anderson et al., 2014). Eventually, after the ice has covered the entire region, the retreat is initially confined to these narrow troughs, while the banks retain grounded ice for much longer (Anderson et al., 2019; Halberstadt et al., 2016). As the ice thins or retreats into regions of deeper bed topography, these banks remain grounded, while the rest of the ice sheet decouples from the bed, begins floating and forms an ice shelf (Shipp et al., 1999). This remaining grounded ice on bathymetric highs forms pinning points.

Pinning points are regions of locally grounded ice within a floating ice shelf (Matsuoka et al., 2015). The friction between the bed and ice base at these points

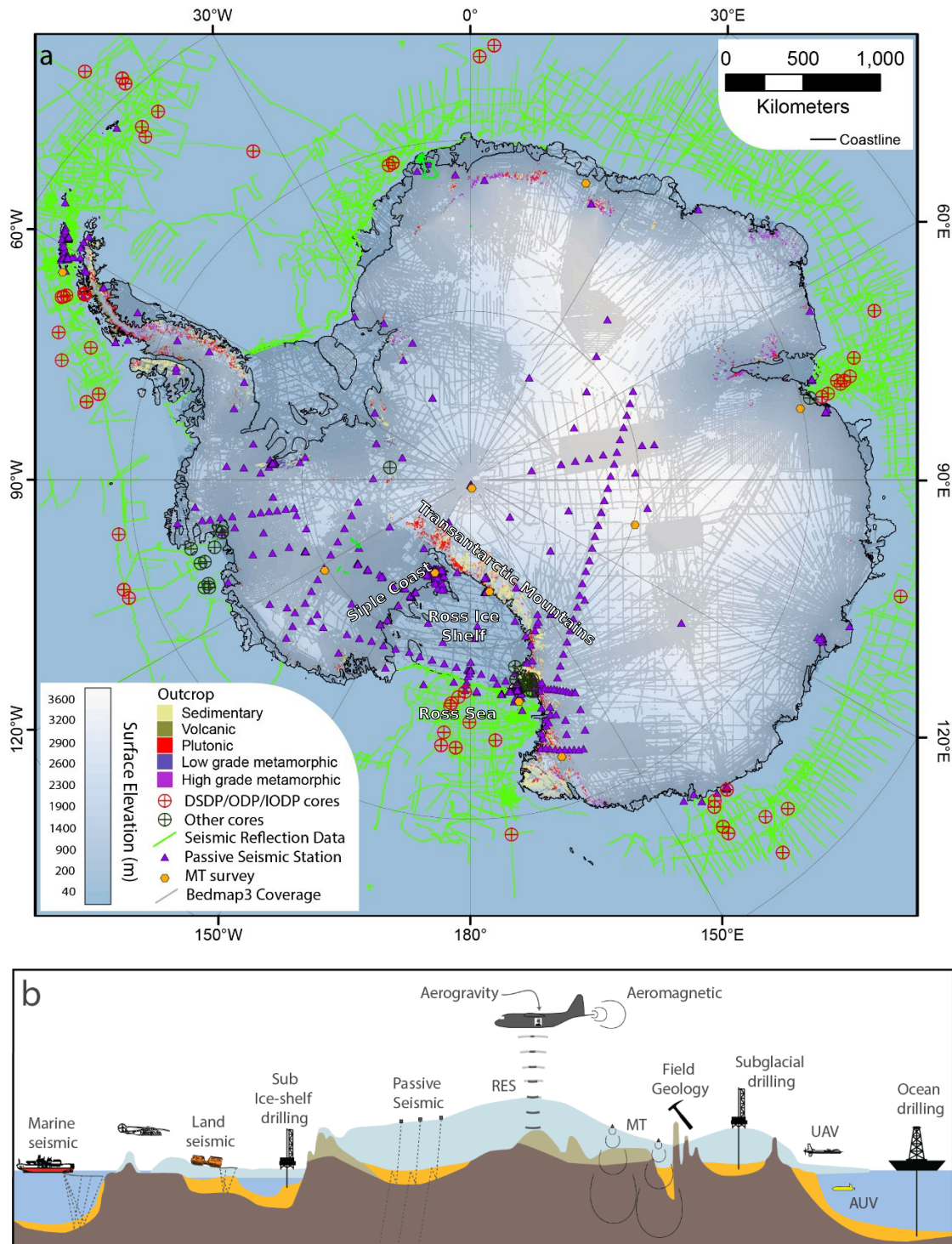


Figure 1.2: Summary of existing geologic and geophysical data for Antarctica. **a)** Map of data coverage in Antarctica indicating outcropping regions, drill core sites, seismic and magnetotelluric surveys, and bed elevation data points of Bedmap3, mostly from airborne radio-echo sounding (Frémand et al., 2022). **b)** Various methods of acquiring information sub-surface geology. Figure adapted from Aitken et al. (2023b).

impart a critical resisting force to the discharge of upstream ice; an effect known as buttressing (Dupont & Alley, 2005; Thomas, 1979). Since the base of ice shelves is flat relative to the underlying bathymetry, the morphology of the seafloor is the dominant control of the location and geometry of these pinning points. The bedrock topography has been thought to be relatively constant over a millennial timescale,

meaning that pinning points' geometries vary mostly by temporal changes in the ice thickness. However, recent studies of glacial isostatic adjustment, the vertical rebound of the Earth following deglaciation, throughout West Antarctica have demonstrated high spatial variability and short (multi-centennial-to-millennial) timescales for these vertical land movements (Barletta et al., 2018; Coulon et al., 2021; Kachuck et al., 2020). As the bedrock beneath portions of West Antarctica continues to rebound, the number and extent of these pinning points will likely increase, possibly providing a stabilizing effect to the ice sheet.

All of these above controls on ice dynamics imparted by the physiography of the bed rely on accurate knowledge of bed topography and bathymetry. Due to the inherently challenging nature of Antarctic fieldwork, and the logistical challenge of measuring bed elevations beneath thick ice, 50% of the Antarctic Ice Sheet is more than 5 km from the nearest measurement of bed elevation (Figure 1.2a, Morlighem et al., 2020). This value increases greatly if the floating ice shelves are included. For grounded ice, the dominant techniques for direct measurements of bed elevation data are airborne radio-echo sounding, over-snow radar, and seismic surveying (Figure 1.2b, Fretwell et al., 2013). In the open ocean, bathymetry data are typically collected with ship-borne multibeam echo sounding, seismic surveying (Figure 1.2b), or from satellite-altimetry. Acquiring bathymetry data beneath floating ice shelves presents a particular challenge. The efficient shipborne methods are unavailable since the ice shelves are persistent year-round, unlike the sea ice in the open ocean. Radio-echo sounding, either ground-based or airborne, cannot image through the water column. Direct observations through drilling are possible and exist, but typically require drilling through 100's to 1000's of meters of ice (Figure 1.2, Clough & Hansen, 1979; Patterson et al., 2022). Autonomous underwater vehicles (Figure 1.2b) present another option, but are expensive and have limited range (Dowdeswell et al., 2008; Nicholls et al., 2006). The only feasible method of direct observations of sub-ice shelf bathymetry is over-snow seismic surveying (Figure 1.2b). However, for the vast area of many ice shelves, even sparse coverage (~ 50 km spacing) of seismic points across the ice shelf takes several field seasons of data acquisition (Bentley, 1984).

1.2.2 Geologic structures

Additional influences on the overriding ice include the delivery of geothermal heat and subglacial water to the ice base and the vertical deformation of the bedrock in response to changing ice loads. Geothermal heat influences ice dynamics through several mechanisms; 1) increasing the temperature of the ice which lowers its viscosity, leading to enhanced flow via internal deformation (Llubes et al., 2006), 2) meltwater lubrication of the bed reduces friction, enhancing flow (Pollard et al., 2005), and 3) increasing the ability of the bed to deform via increased pore-fluid pressure, which increases ice flow (Tulaczyk et al., 2000). The latter two effects, while enhanced by geothermal heat through the melting of ice, also occur with simply the presence of liquid water at the ice-bed interface. As briefly mentioned in the above section, glacial isostatic adjustments of the bedrock following changes in ice load can influence the ice by altering the geometry and locations of grounded ice.

Each of these effects; geothermal heat flow, subglacial water availability, and

glacial isostatic adjustment, are in turn influenced by geologic structures within the upper crust. A portion of subglacial water comes from either transport along the ice-bed interface, or from the melting of the ice base. However, an often overlooked component of the subglacial hydrologic system is groundwater stored in deep sedimentary aquifers. For example, hydrologic modelling of the ice streams of the Siple Coast (Figure 1.2a) estimated the components of the hydrologic budget to be 8% from local basal melting, 47% from inflow from the ice sheet interior, and 45% from groundwater reservoirs (Christoffersen et al., 2014). These modelling observations of extensive groundwater have been recently verified beneath the Whillans Ice Stream by a magnetotelluric survey. This survey imaged an extensive groundwater aquifer within a sedimentary basin, containing at least an order of magnitude more water than the shallow hydrologic system (Gustafson et al., 2022). The vertical flow of this basinal groundwater is controlled by the pressure of the overriding ice sheet. As this overburden pressure decreases with thinning ice, groundwater is discharged to the ice base (Gooch et al., 2016; Li et al., 2022). This discharge is likely concentrated along pre-existing weaknesses or impermeable surfaces, such as fault damage zones, or the margins of crystalline basement (Jolie et al., 2021). During this ice-induced hydraulic unloading, regional geothermal heat is advected along the fluid pathways, leading to potentially highly elevated heat flow delivered to the ice base (Li et al., 2022; Ravier & Buoncristiani, 2018). In addition to concentrating both subglacial water and geothermal heat, these faults, or more generically, regions of the crust which have experienced recent faulting, will respond differently to stresses induced by glacial isostatic adjustment. To a first order, the isostatic response of the solid-earth to changing ice load is controlled by the rheology of the mantle (Whitehouse et al., 2019). However, on a more local scale, pre-existing faults are shown to accommodate glacial isostatic rebound-induced stresses (Peltier et al., 2022; Steffen et al., 2021).

To be able to understand the above influences on the ice, we must have some fundamental knowledge of the geologic structures beneath the ice. This includes knowing where sedimentary basins, and possible aquifers within, are located, where faults likely intersect the ice base, and the geometry of the crystalline basement. Each of these components is difficult to image directly. Drilling, seismic surveys, or geologic analysis of rock outcrops all provide valuable information but are not feasible to cover wide regions (Figure 1.2). Indirect methods are therefore needed. These include techniques such as gravity, magnetic, or electromagnetic methods. Each of these techniques records measurements of the spatial variation of a potential field, such as the Earth's gravity, magnetic, or electromagnetic fields. These fields are all partially dependant on a physical Earth property, such as rock density, magnetic susceptibility, or resistivity. From these relationships, sub-surface geologic information can be modelled.

1.2.3 Basal roughness

The last major influence on the ice from the underlying Earth I present is the roughness of the bed which the ice sheet flows over. This bed roughness is important on both a micro and macro scale. At a micro-scale, roughness is determined by the material of which the bed is composed. A bed of erosion-resistance crystalline basement, for example, can greatly hinder the flow of ice. This material results in high

friction with the ice base, slowing the sliding of ice (Bell et al., 1998). Conversely, beds composed of fine-grained tills allow fast ice flow. This fast flow is predominantly due to deformation within the till as the ice flows (Alley et al., 1986). In between the end members of crystalline basement and fine grain till are lithified sedimentary rocks, for example. This type of bed may initially lead to high friction with the ice, but due to their high erodability, sedimentary rock will quickly generate till (Anandakrishnan et al., 1998). A macro-scale view of basal roughness is also important for ice dynamics. As observed at the Siple Coast (Figure 1.2a) ice streams, there is a strong inverse relation between bed roughness, from scales of 5 to >40 km, and ice stream velocities (Siegert et al., 2004). The composition of the bed also plays an important role in the total effective resistance imparted on ice flow from pinning points (Still et al., 2019).

To best quantify the effect of basal roughness on ice dynamics, information on the material properties of the bed is needed. While sediment samples beneath the ice yield valuable information, they may only represent the bed at the specific location where they were sampled. The most fundamental information needed is the generic rock type of the bed, namely, is the bed loose, unconsolidated sediment, lithified sedimentary rock, or crystalline rock? Aitken et al. (2023b) provide a detailed review of Antarctica's sedimentary basins, and the methods employed to determine both the presence of sediment and the sediment thickness. These methods, as well as the methods described in the above sections, are shown in Figure 1.2, as reproduced from Aitken et al. (2023b).

With the dominant influences from the underlying Earth on ice dynamics laid out, I will now introduce the study area of this thesis, Antarctica's Ross Ice Shelf.

1.3 Ross Ice Shelf

The Ross Ice Shelf is Antarctica's largest ice shelf ($\sim 480,000$ km 2), Figure 1.2). It is situated between the Transantarctic Mountains and Marie Byrd Land. It buttresses a catchment of ice that flows from both the East and West Antarctic Ice Sheets. This catchment contains 11.6 m of global sea level equivalent (Fretwell et al., 2013; Rignot et al., 2011; Tinto et al., 2019). Compared to many other ice shelves, the Ross Ice Shelf is currently relatively stable (Moholdt et al., 2014; Rignot et al., 2013). However, geologic evidence from throughout the Ross Sea and the Siple Coast shows that in the past $\sim 7,000$ years the shelf has experienced rapid destabilization, disintegration, and large-scale grounding line retreat (e.g., Naish et al., 2009; Venturelli et al., 2020). This major Holocene retreat is thought to have been primarily caused by ocean forcings (Lowry et al., 2019), as bathymetric troughs guided in the inflow of melt-inducing ocean circulations (Tinto et al., 2019). Once destabilized, the grounding line retreat from the outer continental shelf to the present-day location was controlled primarily by the physiography and geology of the bed (Anderson et al., 2019; Halberstadt et al., 2016). This shows the importance of the underlying Earth's influence on the dynamics of the Ross Ice Shelf.

1.3.1 Past investigations

By examining various influences on ice dynamics, I identified some key data needed to understand these influences. These data included onshore bed topography, off-

shore bathymetry, the distribution of sediment, and upper crustal structures such as faults and the topography of the basement. Here, I summarize the history of data collection in the Ross Ice Shelf region specific to these geologic and physiographic features. Geological and geophysical exploration has occurred in the Ross Embayment for over a century. The earliest of these include the 1901-1904 *Discovery* expedition, the 1907-1909 *Nimrod* expedition, and the 1910-1913 *Terra Nova* expedition. These expeditions laid the groundwork of interest in the Ross Embayment from a scientific perspective. The first major survey of the Ross Ice Shelf was part of the 1957-1959 International Geophysical Year traverses. The three over-snow traverses all included a portion of the ice shelf and collected radar, gravity, and seismic data to determine ice thickness, surface elevation, and bed elevation (Crary, 1959). These surveys produced early evidence of the extensive below-sea-level bed, thin crust, and distinct geologic provinces throughout West Antarctica (Bentley et al., 1960). In the 1970s the Ross Ice Shelf Geophysical and Glaciological Survey (RIGGS, Bentley, 1984) consisted of a systematic grid of seismic surveys over the entire ice shelf with an average spacing between survey points of 55 km. After the RIGGS survey, there were a total of ~ 223 point-source seismic surveys across the ice shelf, all yielding single-point sub-ice shelf bathymetry depths. Of these, eight reported sediment thicknesses beneath. Several faults were hypothesized, based on 2D gravity profiles conducted at many of the stations (Greischar et al., 1992). Since the 1970s, there have been many additional local surveys on the ice shelf, but these have been focused along the grounding zones (e.g., Horgan et al., 2017; Muto et al., 2013b; Patterson et al., 2022; Stern et al., 1994; ten Brink et al., 1993; Wannamaker et al., 2017). The next, and most recent major data-collection campaign on the Ross Ice Shelf was the ROSETTA-ice project.

The Ross Ocean and ice Shelf Environment, and Tectonic setting Through Aerogeophysical surveys and modelling project (ROSETTA-ice, Tinto et al., 2019), was a 3-season (2015-2017) airborne geophysical survey of the Ross Ice Shelf. It flew a regular grid of flight lines, with nominal N-S and E-W line spacings of 10 and 55 km, respectively. During each flight, various geophysical data were collected, including ice-penetrating radar, gravity, magnetics and laser altimetry. So far, these ROSETTA-ice data have been used to begin characterizing the geologic nature of the crust (Tinto et al., 2019), to model the depths to the sea floor (Tinto et al., 2019), and to quantify basal melt (Das et al., 2020).

Following 60 years of surveying and exploration of the Ross Ice Shelf, our fundamental understanding of the subglacial geology and physiography is still lacking. For an area almost twice the size of New Zealand, we have approximately 8 locations of reported sediment thickness, several hypothesized locations of faults, gaps of over 100 km without bathymetric depths, and limited understanding of our uncertainty in the bathymetry where it has been modelled/interpolated. I propose several research questions which I aim to answer in this thesis.

1.4 Research questions

The aim of this thesis is to improve our knowledge of boundary conditions beneath the Ross Ice Shelf in order to better understand the past, present, and future interactions between the ice, ocean, and underlying earth. I aim to accomplish this by

answering the following questions:

1. What is the geologic structure of the upper crust beneath the Ross Ice Shelf? If there are sediments, what is their thickness and distribution? Where are the major faults likely located?
2. How can bathymetry beneath an ice shelf best be modelled? Are there further improvements that can be made to the currently employed gravity-inversion process? What are the predominant sources of uncertainty, and how can these be limited?
3. How deep is the bathymetry beneath the Ross Ice Shelf and where are we most and least certain about it?
4. What are the geologic controls on the Ross Ice Shelf's stability?

1.5 Outline

This thesis is comprised of five chapters.

This chapter, Chapter 1, establishes the context behind the research, introduces the study region, proposes a series of research questions, and contains an outline of this thesis.

Chapter 2 is adapted from a journal article published in Geophysical Research Letters (Tankersley et al., 2022), reformatted to be included in this thesis. It presents a model of the basement topography, and overlying sediment distribution, beneath the Ross Ice Shelf. I use airborne magnetic data from the ROSETTA-ice project, and a depth-to-magnetic source technique to model the sediment-basement contact. This reveals large-scale, fault-controlled extensional basins throughout the sub-Ross Ice Shelf crust. From this, I am able to draw a wide range of inferences on the likely influence of this basement topography on the past, present, and future ice sheet, as well as some tectonic implications. These results provide the first holistic view of the upper crust beneath the Ross Ice Shelf.

Chapter 3 details my development of a method to model the depth to the sea floor beneath a floating ice shelf. This method is a gravity inversion, where observations of Earth's gravitational field are used to model bathymetry beneath an ice shelf. I develop open-source Python code with the aim for other researchers to utilize the inversion. I test the inversion against a suite of synthetic and semi-realistic data. This confirms the feasibility of using gravity data to attain bathymetry depths in an Antarctic setting. Additionally, these synthetic tests reveal the relative importance of various aspects of a gravity inversion. These include the importance of *a priori* constraints on the bathymetry, the large errors which can be introduced during the removal of the regional component of gravity, and several suggestions for optimal survey design to minimize error in the resulting bathymetry model. The use of Monte Carlo simulation provides both a spatially variable estimation of uncertainty in the resulting bathymetry and an estimate of the various sources of this uncertainty.

Chapter 4 uses the inversion algorithm developed in Chapter 3 to create a new bathymetry model and associated uncertainties beneath the Ross Ice Shelf. The model shows some major differences with past bathymetry models, highlighting areas of the ice shelf that should be carefully considered in future surveys. These include a deeper bathymetric trench along the Transantarctic Mountains, a thicker ocean cavity along a portion of the ice front which may allow the incursion of warm ocean waters and a thicker ocean cavity proximal to the Siple Coast grounding line. My uncertainty analysis shows the region of highest uncertainties is along the Transantarctic Mountain Front. Within this chapter, we perform a comprehensive review of past bathymetry-gravity inversions, for all Antarctic studies, and several Greenland studies. This highlighted some key differences, which I believe I have improved on.

Chapter 5 presents a synthesis of the 3 research chapters, and provides a discussion of the research questions. Various future works are suggested and the main conclusions of this thesis are presented. The research chapters in this thesis were written with the intent to publish, including Chapter 2 which is already published. Therefore, I have chosen to keep the style of writing consistent throughout the thesis, with the use of plural possessive pronouns ("we") instead of singular ("I").

1.6 Data and Code Availability Statement

In an effort to adhere to the principles of FAIR scientific investigations, Findability, Accessibility, Interoperability, and Reusability (Wilkinson et al., 2016), we have used only open-access data and published all code¹ used in this thesis. Here we describe where this code and data can be found. All data used from other studies has been cited within each chapter and can be accessed through their respective DOIs. However, most of these datasets were downloaded using the Python package Antarctic-Plots (Tankersley, 2023). I developed this package during this PhD to help with several aspects of conducting research related to Antarctica. See Appendix D for an overview of the capabilities of Antarctic-Plots. Analysis in this study was executed on a computer with an x86_64 processor with a maximum clock frequency of 2600 MHz with 56 physical cores, 112 logical cores, and 1TB of RAM, using the Operating System Linux-Ubuntu.

Chapter 2

All of the Python code used to perform the analysis and create the figures of Chapter 2 is available from the following GitHub repository; https://github.com/mdtanker/RIS_basement_sediment, and the version of the repository used in the published paper is archived at <https://doi.org/10.5281/zenodo.6499863> (Tankersley, 2022).

Chapters 3 & 4

The gravity inversion Python code, the workflow conducted within Jupyter Notebooks, and the creation of all the figures is available from the following GitHub repository; https://github.com/mdtanker/RIS_gravity_inversion and the version of the repository used in this thesis is archived at <https://doi.org/10.5281/zenodo.8084469> (Tankersley et al., 2023).

¹This excludes one component of Chapter 2 which was performed with proprietary software.

The code for creating the figures in the remainder of this thesis, and the latex files of the thesis itself are available at the following GitHub repository; <https://github.com/mdtanker/phdthesis> and is citable with the following DOI; <https://doi.org/10.5281/zenodo.8084606>.

Chapter 2

Airborne magnetic analysis: Basement depths and sediment thickness

Abstract

New geophysical data from Antarctica's Ross Embayment reveal the structure and subglacial geology of extended continental crust beneath the Ross Ice Shelf. We use airborne magnetic data from the ROSETTA-Ice Project to locate the contact between magnetic basement and overlying sediments. We delineate a broad, segmented basement high with thin (0-500 m) non-magnetic sedimentary cover which trends northward into the Ross Sea's Central High. Before subsiding in the Oligocene, this feature likely facilitated early glaciation in the region and subsequently acted as a pinning point and ice flow divide. Flanking the high are wide sedimentary basins, up to 3700 m deep, which parallel the Ross Sea basins and likely formed during Cretaceous-Neogene intracontinental extension. NW-SE basins beneath the Siple Coast grounding zone, by contrast, are narrow, deep, and elongate. They suggest tectonic divergence upon active faults that may localize geothermal heat and/or groundwater flow, both important components of the subglacial system.

Plain Language Summary

The bedrock geology of Antarctica's southern Ross Embayment is concealed by 100s-1000s of meters of sedimentary deposits, seawater, and the floating Ross Ice Shelf (RIS). Our research strips away those layers to discover the shape of the consolidated bedrock below, which we refer to as the basement. To do this, we use the contrast between non-magnetic sediments and magnetic basement rocks to map out the depth of the basement surface under the RIS. Our primary data source is airborne measurements of the variation in Earth's magnetic field across the ice shelf, from flight lines spaced 10 km apart. We use the resulting basement topography to highlight sites of possible influence upon the Antarctic Ice Sheet and to further understand the tectonic history of the region. We discover contrasting basement characteristics on either side of the ice shelf, separated by an N-S trending basement high. The West Antarctic side displays evidence of active faults, which may localize geothermal heat, accommodate movements of the solid earth caused by changes in

the size of the Antarctic Ice Sheet, and control the flow of groundwater between the ice base and aquifers. This work addresses critical interactions between ice and the solid earth.

Key Points:

1. Aeromagnetic analysis reveals basement surface and evidence of fault-controlled extensional basins beneath Antarctica's Ross Ice Shelf (RIS).
2. Active faults at Siple Coast likely influence ice streams through control of geothermal heat, groundwater, and glacioisostatic adjustments.
3. A basement high beneath RIS spatially coincides with a lithospheric boundary, with contrasting sedimentary basins on either side.

2.1 Introduction

The southern sector of Antarctica's Ross Embayment beneath the Ross Ice Shelf (RIS; area \sim 480,000 km 2) is poorly resolved because the region is not accessible to conventional seismic or geophysical surveying. Rock exposures on land suggest that Ross Ice Shelf (RIS) crust consists of early Paleozoic post-orogenic sediments, intruded in places by mid-Paleozoic and Cretaceous granitoids (Goodge, 2020; Luyendyk et al., 2003). Following the onset of extension in the mid-Cretaceous, grabens formed and filled with terrestrial and marine deposits, continuing into the Cenozoic (e.g. Coenen et al., 2019; Sorlien et al., 2007), as the Ross Embayment underwent thermal subsidence (Karner et al., 2005; Wilson & Luyendyk, 2009). The physiography of this region then responded to the onset of glaciation in the Oligocene (Paxman et al., 2019), coinciding with localized extension in the western Ross Sea until 11 Ma (Granot & Dyment, 2018). The Oligocene-early-Miocene paleo-landscape of the Ross Sea sector was revealed by marine seismic data (e.g. Brancolini et al., 1995; Pérez et al., 2021) and offshore drilling that penetrated crystalline basement (DSDP Site 270; Ford & Barrett, 1975) (Figure 2.1). Recognition of the role of elevated topography in Oligocene formation of the Antarctic Ice Sheet (DeConto & Pollard, 2003; Wilson et al., 2013) and the likely influence of subglacial topography upon ice sheet processes during some climate states (Austermann et al., 2015; Colleoni et al., 2018) motivated our effort to determine basement topography beneath the Ross Ice Shelf.

Ice sheet dynamics are of high interest in the RIS region because its grounding zone (GZ) and pinning points (Still et al., 2019) buttress Antarctica's second-largest drainage basin (Tinto et al., 2019). Our work in this sensitive region seeks to delimit the extent and geometry of competent basement because the margins of basement highs are sites of strong contrasts in permeability that influence the circulation of subglacial waters. A spectacular example of the confinement of subglacial water between the ice sheet and basement exists in ice radar profiles for the continental interior (Bell et al., 2011), but little is known about the subglacial hydrology of deep groundwater reservoirs within sediment-filled marine basins that receive terrestrial freshwater influx (Gustafson et al., 2022; Siegert et al., 2018). These basins may contain up to 50% of total subglacial freshwater (Christoffersen et al., 2014), where the discharge and recharge along fault-damage zones (Jolie et al., 2021) is

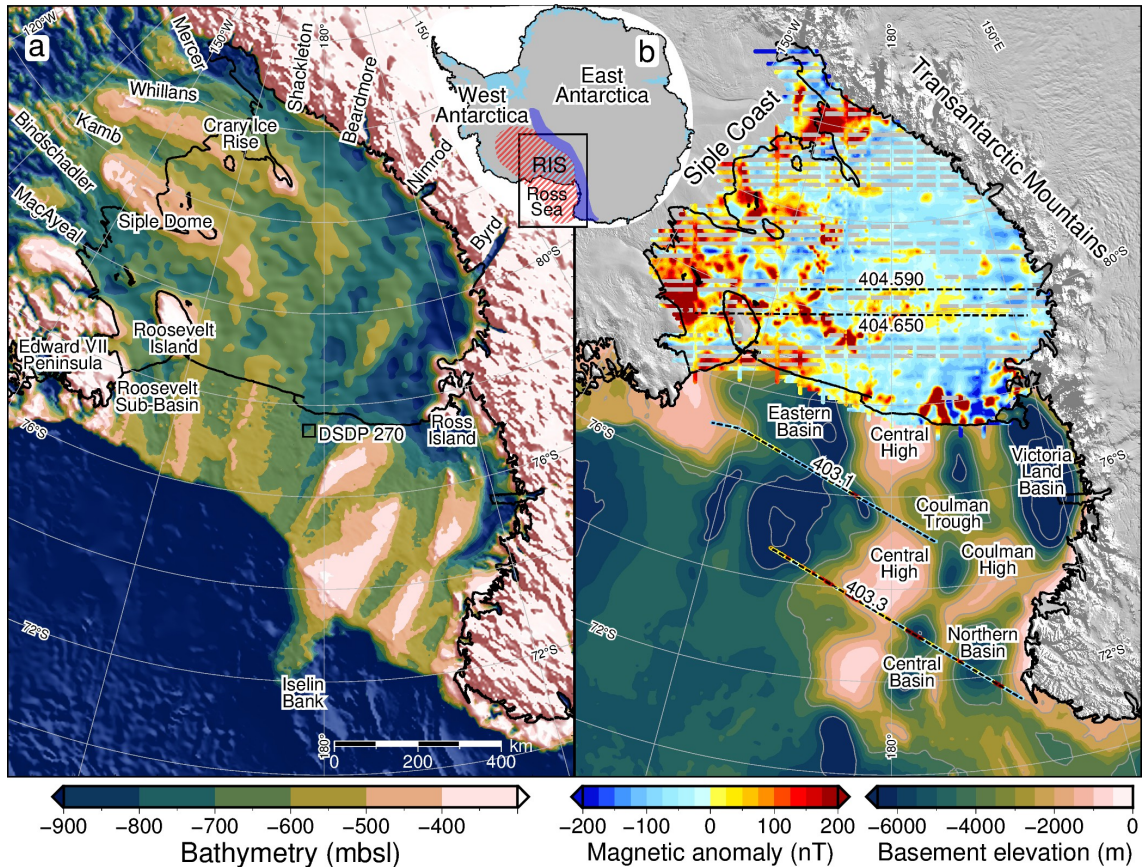


Figure 2.1: (a) Bathymetry and sub-ice bed elevations (Morlighem et al., 2020) including ROSETTA-Ice gravity-derived bathymetry (Tinto et al., 2019) beneath the Ross Ice Shelf (RIS). Labels include ice streams and outlet glaciers. (b) Basement elevation from Antarctic Offshore Stratigraphy project marine seismic compilation in the Ross Sea Brancolini et al. (1995) and air-borne magnetic data from ROSETTA-Ice (over RIS) and Operation IceBridge (black dashed lines). Inset map shows figure location, West Antarctic Rift System (hatched red), Transantarctic Mountains (dark blue), and ice shelves (light blue). Shelf edge, grounding line, and coastlines in black (Rignot et al., 2013). MODIS imagery from Scambos et al. (2007).

controlled by pressure from the overriding ice sheet (Gooch et al., 2016). Possible evidence that RIS basement margins localize basinal waters, causing the advection of geothermal heat, comes from elevated values and significant spatial variability of measured geothermal heat flux (GHF) at points around the Ross Embayment (Begeaman et al., 2017). Here we present the first map of magnetic basement topography and thickness of overlying non-magnetic sediments for the southern Ross Embayment, developed using ROSETTA-Ice (2015-2019) airborne magnetic data (Figure 2.1b, Tinto et al., 2019). Our work reveals three major sedimentary basins and a broad basement ridge that separates crust of contrasting basement characteristics.

2.2 Data and Methods

We use ROSETTA-Ice aeromagnetic data to image the shallowest magnetic signals in the crust. Assuming that the overlying sediments and sedimentary rocks produce smaller magnetic anomalies than the crystalline basement, we treat the resulting solutions as the depth to the magnetic basement (Section A.2). To do this, we implemented Werner deconvolution (Werner, 1953) on 2D moving and expanding windows of line data, isolating anomalies and solving for their source parameters (Section A.3, location, depth, susceptibility, body type). The resulting solutions are non-unique; each observed magnetic anomaly can be solved by bodies at multiple locations and depths by varying the source's magnetic susceptibility and width. The result is a depth scatter of solutions (Figures 2.2 & A.2), which tend to vertically cluster beneath the true source. This magnetic basement approach has been used to map sedimentary basins throughout Antarctica (i.e. Bell et al., 2006; Frederick et al., 2016; Karner et al., 2005; Studinger et al., 2004a) where typically, the tops of solution clusters are manually selected to represent the basement depth. Our approach expands on this method by utilizing a reliable, automated method of draping a surface over these depth-scattered solutions to produce a continuous basement surface (Section A.4 & A.5).

We implemented a 2-step tuning process that ties our RIS magnetic basement to well-constrained seismic basement in the Ross Sea, from the Antarctic Offshore Stratigraphy project (ANTOSTRAT) (Figure 2.1b, Brancolini et al., 1995). This involved using Operation IceBridge (OIB) airborne magnetic data (Cochran et al., 2014a) collected over the RIS and Ross Sea. Minimizing misfits between OIB magnetic basement and ANTOSTRAT basement, as well as between OIB and ROSETTA-Ice magnetic basements, enabled tuning of our method to optimal basement depths (Figures 2.2, A.2, A.3e&f, Section A.4 & A.5).

Our RIS results (Figure A.4) were merged with offshore ANTOSTRAT data (Brancolini et al., 1995) and smoothed with an 80 km Gaussian filter to match the characteristic wavelengths of the Ross Sea basement (Section A.6). The combined grid (Figure 2.3a) was then subtracted from BedMachine bathymetry (Figure 2.1a, Section A.7, Morlighem et al., 2020), to obtain the sediment thickness distribution for the Ross Embayment (Figure 2.3b).

These sub-RIS results together with free-air gravity data allowed us to infer the locations of regional scale faults beneath the RIS. Criteria used to locate faults include 1) high relief on the magnetic basement surface, 2) linear trends that cross

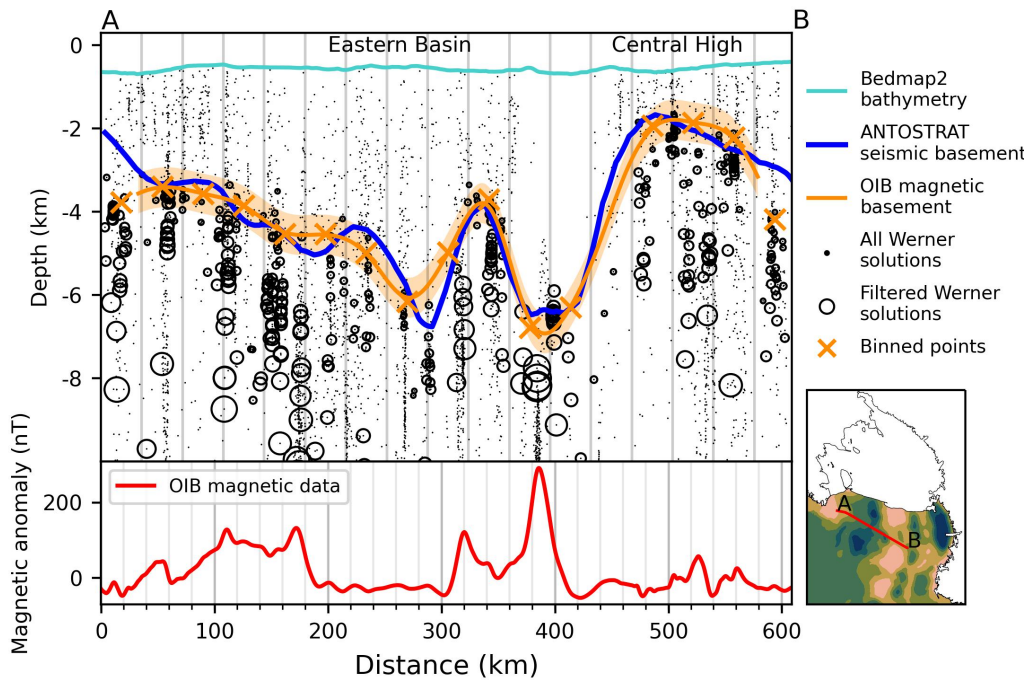


Figure 2.2: Ross Sea magnetic and seismic basement comparison. Operation IceBridge airborne magnetic data (lower panel) from segment 403.1 used in Werner deconvolution to produce magnetic anomaly source solutions (black dots). Filtering removed shallow solutions, and remaining solutions (circles scaled to magnetic susceptibility) were binned and interpolated to produce the magnetic basement (orange line with uncertainty band).

zones of shallow basement, 3) high gradient gravity anomalies (Figure A.1a, ROSETTA-Ice) and 4) large contrasts in sediment thickness. Narrow, deep, linear basins are likely to be controlled by active faults (e.g. Drenth et al., 2019; Finn, 2002). We display the inferred faults upon a base map of crustal stretching factors (β -factor; the ratio of crustal thickness before and after extension, Figure 2.4a), using an initial crustal thickness of 38 km (Müller et al., 2007), a continent-wide Moho model (An et al., 2015), and our basement surface as the top of the crust (Section A.7).

2.3 Results

We find that an almost continuous drape of sediment covers the RIS region (Figure 2.3b), with only $\sim 3\%$ of the area having <200 m of sedimentary cover. Prominent beneath the midline of the RIS is a broad NNW-SSE trending basement ridge (Figure 2.3a, Mid-Shelf High; MSH), which comprises most of the shallowest (<700 meters below sea level (mbsl)) sub-RIS basement, with several regions with as little as 100 m of sedimentary cover. Basement is deeper on the East Antarctic side of the MSH, where it averages ~ 2400 mbsl, compared to an average depth of ~ 1900 mbsl on the West Antarctic side (Figure 2.3a histogram). Sedimentary fill is ~ 400 m greater and more uniformly distributed on the East Antarctic side than the West Antarctic side (Figure 2.3b histogram).

To estimate our uncertainty (Section A.8), we examined the misfit between OIB and ANTOSTRAT basement (Figures 2.2 & A.2) and between our basement and

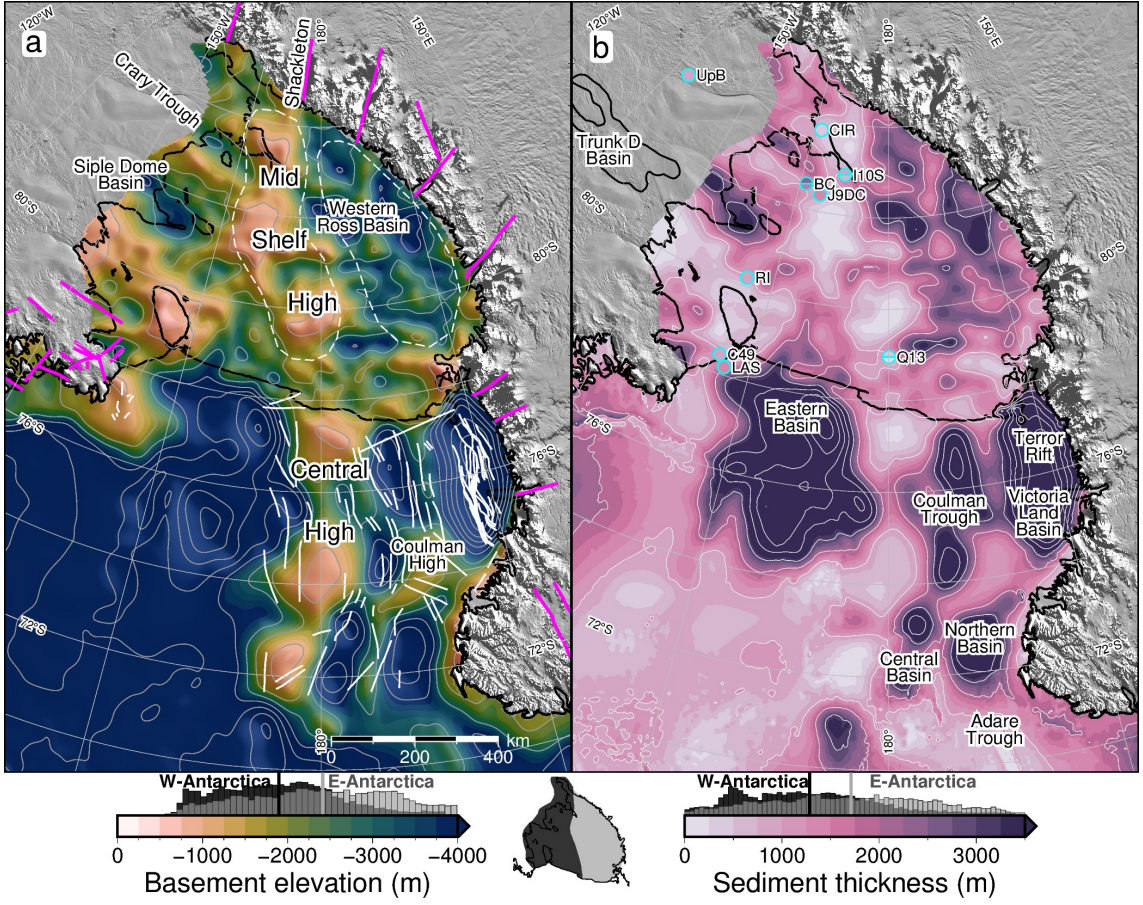


Figure 2.3: (a) Basement elevation (magnetic for Ross Ice Shelf (RIS), seismic elsewhere) contoured at 1 km intervals. Pink lines are onshore mapped and inferred faults (Ferraccioli et al., 2002; Goodge, 2020; Siddoway, 2008). White lines are offshore faults (Chiappini et al., 2002; Luyendyk et al., 2001; Salvini et al., 1997; Sauli et al., 2021). Dashed white lines show Mid Shelf High and Western Ross Basin extents. (b) Sediment thickness contoured at 1 km intervals. Previous basement-imaging RIS seismic surveys (cyan circles, Table A.1) are plotted on same color scale, with upper and lower uncertainty ranges as circle halves, where reported. Trunk D Basin outlined in West Antarctica (Bell et al., 2006). Color scales for both a) and b) are set to sub-RIS data range. Colorbar histograms show data distribution for East vs West Antarctic sides of the sub-RIS, separated by the Mid-Shelf High. Inset map shows East vs West divide. Vertical lines on histograms denote average values of each side.

OIB basement (Figures A.3e&f). There is a median misfit of 480 m (22% of average RIS depth) for basement (Figures A.5 & A.6). A similar 470 m median basement misfit is estimated by comparing our results to eight active source seismic surveys (Figure 2.3b, Table A.1). Incorporating the ~70 m uncertainty in the bathymetry model (Tinto et al., 2019), our representative sediment thickness uncertainty is 550 m (37% of average RIS thickness, Figure A.5).

A single broad and deep basin (300 x 600 km) separates the MSH and the Transantarctic Mountains (TAM) (Figure 2.3a, Western Ross Basin). The Western Ross Basin parallels the TAM and has the deepest-observed sub-RIS basement depths of 4500 mbsl, accommodating sediments up to 3800 m thick (Figure 2.3b). It contains a long, narrow NW-SE trending ridge with ~1500 m structural relief above the basement sub-basins on either side. Bordering the MSH on the east, an elongate NW-SE trending basin runs from the RIS calving front to the Siple Coast GZ (Figure 2.3a), where beneath Siple Dome we discover a 100 x 200 km depocenter reaching basement depths up to 4000 mbsl, with sediments up to 3700 m thick. We

refer to this depocenter as Siple Dome Basin, a feature bounded on the east by a basement high that trends southward from Roosevelt Island. This high rises to its shallowest point at the GZ, where its sedimentary cover is less than 100 m. A second deep, narrow basin (50 x 200 km in dimension) is found along the north margin of Crary Ice Rise, separated from the Siple Dome Basin by an NW-SE ridge underlying Kamb Ice Stream. The basin, labelled Crary Trough in Figure 2.3a, reaches basement depths of 3200 mbsl, with sediments 1800-2700 m thick. The southernmost RIS has an additional depocenter with up to 2000 m of fill beneath Whillans Ice Stream (location in Figure 2.1a).

Inferred active sub-RIS faults (Figures 2.4a & A.1) correspond to narrow, linear basement basins with high-gradient gravity anomalies, prevalent on the West Antarctic side (Figure A.1a). Inactive normal and strike-slip faults are inferred along lineaments that segment the shallow MSH into blocks and are oriented parallel to TAM outlet glacier faults. β -factors are indicative of thinned crust and are different on either side of the MSH. The TAM side shows higher β -factors (average 1.99) with low variability. The West Antarctic side has lower β -factors overall (average 1.82), but with some higher values up to 2.1 (Figure 2.4a).

2.4 Discussion

Sub-RIS sedimentary basins align with and show lateral continuity with the Ross Sea's Roosevelt Sub-Basin, Eastern Basin, Coulman Trough, and Victoria Land Basin (Figure 2.3, e.g. Cooper et al., 1995). The MSH passes northward into the Ross Sea's prominent Central High (CH). At the southern RIS margin, the narrow Siple Dome Basin has continuity with the previously identified Trunk D Basin (Figure 2.3a, Bell et al., 2006). The throughgoing trends imply regional continuity of crustal structure and a common tectonic development of the Ross Sea and RIS regions. Our sediment thicknesses are compatible with those determined by a) eight active-source seismic surveys (Figure 2.3b), for which the median misfit is 470 m (Table A.1), and b) surface wave dispersion indicating 2-4 km of sediment under the RIS, similar to our range, with the maximum beneath Crary Ice Rise (Zhou et al., 2022). Three additional western RIS seismic profiles report up to several kilometers of sediment, in general accordance with our results (Beaudoin et al., 1992; Stern et al., 1991; ten Brink et al., 1993). Additionally, machine learning applied to geophysical datasets predicts a high likelihood of sedimentary basins at the locations of Siple Dome Basin and Crary Trough (Li et al., 2022).

2.4.1 West Antarctic Rift System extensional basins

The Western Ross Basin has a configuration similar to the western Ross Sea rift basins (e.g. Salvini et al., 1997) with a broad and deep basin, separated into distinct depocenters by a linear, low relief ridge. The deeper of the depocenters, on the TAM side of the ridge, coincides with alternating high and low free-air gravity anomalies (Figure A.1a). These similarities suggest the sub-RIS continuations of Coulman Trough and Victoria Land Basin (Figure 2.3b) likely share a common tectonic origin as fault-controlled basins (Figures 2.3a & 2.4a) formed through Cretaceous distributed continental extension across the WARS (Jordan et al., 2020a). These sub-RIS basins terminate against the southern segment of the MSH (Figure

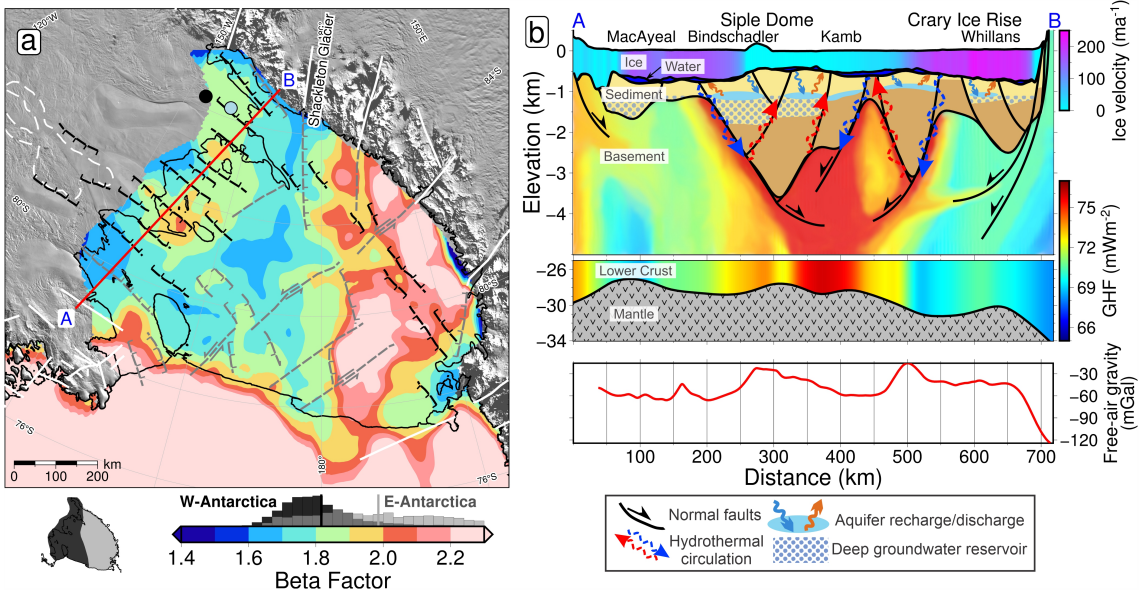


Figure 2.4: Tectonic interpretation of the sub-Ross Ice Shelf (RIS). (a) β stretching factors (Section A.7). Colorbar histogram shows data distribution of West vs. East Antarctic sides, same as Figure 2.3. Black and grey lines indicate inferred active and inactive faults, respectively, with kinematics shown with half-arrows (strike or oblique-slip) and hachures (normal-sense). White lines show previously reported faults, same as Figure 2.3a. Dashed-white outline is Trunk D Basin (Bell et al., 2006). Black and blue dots show Subglacial Lake Whillans and sedimentary basin from Gustafson et al. (2022), respectively. Cross-section A-B in red. (b) Siple Coast cross-section from A-B, showing basin sediments bounded by faults, with geothermal heat flux (GHF) through the crust (lower panel from Burton-Johnson et al. (2020), upper panel interpreted). Ice surface, ice base, and bathymetry from Morlighem et al. (2020). Ice streams coloured by velocity (Mouginot et al., 2019; Venturelli et al., 2020). Moho is from Shen et al. (2018a). Lower panel shows ROSETTA-Ice gravity. Named features are labelled on top.

2.3a).

The linear ridge within the Western Ross Basin (Figure 2.3a) may be an expression of normal or oblique faults linked to the southward-narrowing Terror Rift (Sauli et al., 2021), formed due to Cenozoic oceanic spreading in the Adare Trough (Figure 2.3b, Granot & Dyment, 2018). The Western Ross Basin, with up to 3800 m of fill, terminates along the prominent edge of the MSH that lines up with the fault-controlled trough and crustal boundary that passes southward beneath Shackleton Glacier (Borg et al., 1990). We interpret the basement lineament (Figure 2.4a) as a transfer fault separating sectors of crust extended to different degrees.

The southeastern RIS margin is distinguished by linear ridges and narrow, deep basins. The prominent NW-SE basement trends coincide with high-gradient gravity anomalies (Figure A.1a, Tinto et al., 2019) and thick sediments, suggesting normal fault control and active divergent tectonics beneath the GZ. Our Siple Coast cross-section (Figure 2.4b) displays dramatic basement relief, exceeding 2 km, in the Siple Dome Basin and Crary Trough, which we attribute to displacement upon high angle faults. Portions of basin-bounding faults were previously detected by ground-based gravity surveys upon the Whillans Ice Stream flank (Figure 2.4a, Muto et al., 2013b) and site J9DC (Figure 2.3b), where large variations in sediment thickness indicate up to 600 m of fault throw (Grieschar et al., 1992). The continuity between the narrow Siple Dome Basin (this study) and the Trunk D Basin (Figure 2.3a, Bell et

al., 2006) suggests that the active tectonic domain continues southward past the GZ. The fault-controlled tectonic basins may reflect a crustal response to the lithospheric foundering hypothesized beneath the South Pole region (Shen et al., 2018b) or be a broader regional expression of Neogene extension that formed the Bentley Subglacial Trench (Lloyd et al., 2015).

2.4.2 Consequences for ice sheet dynamics

Our basement topography and suggested crustal faults likely exert a strong influence on the overriding ice, especially along the Siple Coast. Here, we show deep and thick sedimentary basins which likely contain voluminous basinal aquifers (Figure 2.4b; cf. Gustafson et al., 2022). Where these aquifers discharge along fault-damage zones, they can enhance GHF and promote basal melting (Gooch et al., 2016), as depicted in Figure 2.4a. The elevated GHF seen at Subglacial Lake Whillans (285 mW/m^2 , Fisher et al., 2015) may arise from fault localization (Figure 2.4a). Confinement of the aquifers between the ice bed and low-permeability basement may promote fluid overpressure, enabling ice streaming (e.g. Ravier & Buoncristiani, 2018). Additionally, the Siple Coast faults likely accommodate the solid Earth's response to fluctuating ice volume. A matter receiving considerable debate (Lowry et al., 2019; Neuhaus et al., 2021; Venturelli et al., 2020), is Kingslake et al.'s 2018 finding of rapid re-advance of the Siple Coast GZ following Holocene deglaciation. The re-advance was in part due to swift glacioisostatic rebound (cf. Coulon et al., 2021; Lowry et al., 2020), a process aided by the region's low-viscosity mantle (Whitehouse et al., 2019) and likely to be accommodated upon pre-existing crustal faults, as observed in the Lambert Graben (Phillips & Läufer, 2009). Our proposed graben-bounding faults would provide a tectonic control on the glacioisostatic adjustment of the Siple Coast region.

2.4.3 Mid-Shelf High - Central High

The 650-km-long Mid-Shelf High features three shallow, blocky segments $>150 \text{ km}$ in breadth, which have only thin sediment cover ($<200 \text{ m}$). At their shallowest points, the top of basement lies within $\sim 300 \text{ m}$ of the ice shelf base, at a depth comparable to the basement high at Roosevelt Island. Roosevelt Island is a modern pinning point (Still et al., 2019) owing to the thicker sediment, there (Figure 2.3b). We introduce the MSH as a prominent pinning point at times of advance and greater extent of the Antarctic Ice Sheet, in keeping with evidence from subglacial sediment records that indicate a major ice flow divide between East and West Antarctic ice during and since Last Glacial Maximum (Coenen et al., 2019; Li et al., 2020; Licht et al., 2014).

The prominence of the MSH is due in part to the contrasting geologic properties of the East versus West Antarctic type crust and their respective responses to WARS extension. We distinguished β -factors on the TAM-side that are high and uniform, indicating distributed crustal extension. The West Antarctic side displays lower β -factors overall, but with localized extreme thinning beneath Siple Coast (Figure 2.4a). The greater amount of extension on the East Antarctic side coincides with the deeper bathymetry (Figure 2.1a), deeper basement, and thicker sediments (Figure 2.3). The contrasting properties are also evident in ROSETTA-Ice magnetic

and gravity anomalies, used by Tinto et al. (2019) to identify a north-south trending tectonic boundary along the midline of Ross Embayment. The MSH in the magnetic basement coincides with and spans this boundary, which has been further substantiated by passive-seismic studies that show a lithospheric-scale boundary (Cheng et al., 2021; White-Gaynor et al., 2019). To the north, the features continue into the Ross Sea’s Central High. Southward, the MSH basement feature trends into the TAM, where its western edge aligns with Shackleton Glacier, occupying a major fault separating the distinct geologic domains of the central and southern TAM (Borg et al., 1990; Paulsen et al., 2004), which also parallels a prominent magnetic lineament at the South Pole (Studinger et al., 2006). The structure may be an expression of the East Antarctic craton margin or a major intracontinental transform (Figure 2.4a, Studinger et al., 2006).

At the time of Oligocene initiation of the Antarctic Ice sheet, paleotopographic reconstructions of the proto-Ross Embayment depict a long, broad range, emergent above sea level (Paxman et al., 2019; Wilson et al., 2012), that we equate to the MSH-CH that divides the Embayment. The CH hosted small ice caps with alpine glaciers formed during the initial glacial stage in the region (De Santis et al., 1995), and continental ice expanded to the outer Ross Sea continental shelf from those centres (Bart & De Santis, 2012). Between the late Oligocene and mid-Miocene, the CH subsided by up to 500 m (Kulhanek et al., 2019; Leckie, 1983), receiving 100’s of meters of sediment cover (\sim 400 m at DSDP 270; De Santis et al., 1995). The geophysical similarities and continuity between the Ross Sea’s CH and the RIS’s MSH imply a similar glaciation and subsidence history for the MSH. A terrestrial/alpine stage for the MSH helps to explain the region’s potential to hold the late Oligocene’s larger-than-modern ice volumes (Pekar et al., 2006; Wilson et al., 2013), with the MSH-CH having a central role in Oligocene ice sheet development and the subsequent evolution of the ice sheet and ice shelf, as is documented in the Ross Sea (Halberstadt et al., 2016).

2.4.4 Thermal subsidence and sedimentation

Incorporating the updated basement basin extents and geometries into post-rift thermal subsidence modelling will enable better-constrained paleotopographic reconstructions. For the sub-RIS, these reconstructions (Paxman et al., 2019; Wilson et al., 2012) use a post-Eocene subsidence model based on gravity-derived basin geometries and uniform β -factors (Wilson & Luyendyk, 2009). This model predicts uniform stretching of the eastern sub-RIS from the ice front to the Siple Coast, while our β -factors show increasing stretching from the ice front to the Siple Coast. This observed additional thinning likely has resulted in more subsidence for Siple Dome and the north flank of Crary Ice Rise, which can now be accounted for in reconstructions. Our sediment thickness comparison with past models (Section A.7, Wilson & Luyendyk, 2009) shows the majority of the sub-RIS, especially the Siple Coast, contains more total sediment than previously estimated (Figure A.1f). Depending on the age of this sediment, reconstructions may need to account for the additional sediment deposition and loading.

2.5 Conclusions

Here we present a depth to magnetic basement map for the Ross Ice Shelf (RIS) from Werner deconvolution of airborne magnetic data. The RIS magnetic basement is tied to Ross Sea seismic basement, providing the first synthetic view of Ross Embayment crustal structure. Using a bathymetry model, we obtain the sediment thickness distribution and calculate crustal extension factors for the sub-RIS. The extensional features we image, resulting from West Antarctic Rift System extension, have continuity with Ross Sea basement structures to the north, and the prominent Mid-Shelf High trends northward into the Ross Sea’s Central High. This combined high separates East and West Antarctic type crust, affected by different degrees of continental extension. The Mid-Shelf High was likely subaerial in the Oligocene, able to support alpine ice caps in early Antarctic glaciation. Subsequently, it formed a prominent pinning point and ice flow divide between the East and West Antarctic Ice Sheets.

Newly identified narrow, linear, deep sedimentary basins provide evidence of active faults beneath the Siple Coast grounding zone, where thinned crust overlying anomalous mantle (Shen et al., 2018a) likely experiences elevated geothermal heat flow promoting the formation of subglacial water. Faults that control basement margins may accommodate motion caused by the glacioisostatic response to ice sheet volume changes. Subglacial sedimentary basins in this setting likely contain confined aquifers within permeable basin fill. Here, ice overburden pressure would control flow both between and within the subglacial and groundwater systems, possibly localizing geothermal heat. Updated sediment thickness and basin extents should be incorporated into new paleotopographic reconstructions of time intervals of interest for paleo-ice sheet modelling. Our work contributes critical information about Ross Embayment basement topography and subglacial boundary conditions that arise from an interplay of geology, tectonics, and glaciation.

2.6 Open Research

ROSETTA-Ice and Operation IceBridge magnetics data are available through <https://www.usap-dc.org/view/project/p0010035> and <https://nsidc.org/data/IMCS31b>, respectively. Results from this study are available to download from <https://doi.pangaea.de/10.1594/PANGAEA.941238> and a Jupyter notebook documenting our workflow and figure creation is available at <https://zenodo.org/badge/latestdoi/470814953>.

2.7 Acknowledgements

Funding support from the New Zealand Ministry of Business and Innovation and Employment through the Antarctic Science Platform contract (ANTA1801) Antarctic Ice Dynamics Project (ASP-021-01) and the National Science Foundation (1443497 and 1443534), and Antarctica New Zealand. We are grateful to Robin Bell, Isabel Cordero, Alec Lockett, Joel Wilner, Zoe Krauss, and the entire ROSETTA-Ice team for undertaking the ambitious data acquisition and processing effort. We thank

Katharina Hochmuth and Guy Paxman for thoughtful reviews which greatly improved the manuscript, as well as Chris Sorlien, Tim Stern, Simon Lamb, Lara Pérez, Ryan Venturelli, Wei Ji Leong, and Dan Lowry for valuable input. Figures used GMT6/PyGMT (Uieda et al., 2021; Wessel et al., 2019), with a script adapted from Venturelli et al. (2020). Geosoft Oasis Montaj™ was used for magnetics processing and Werner deconvolution. Open access publishing facilitated by Victoria University of Wellington, as part of the Wiley - Victoria University of Wellington agreement via the Council of Australian University Librarians.

Chapter 2, in full, is a reprint of material as it appears in Geophysical Research Letters: Tankersley, M. D., Horgan, H. J., Siddoway, C. S., Caratori Tontini, F., & Tinto, K. J. (2022). Basement topography and sediment thickness beneath Antarctica's Ross Ice Shelf. *Geophysical Research Letters*, 49, e2021GL097371. <https://doi.org/10.1029/2021GL097371>. The only changes made from the published version include formatting and replacing preprint citations with accepted paper citations. I conceived the study with my co-authors, undertook the study and analysis, and wrote the manuscript myself.

Chapter 3

Gravity inversion: a tool for bathymetry modelling

Abstract

Sub-ice-shelf bathymetry exerts a primary control on the stability of many Antarctic ice shelves through the geometry of pinning points and the guiding of melt-inducing water masses. Collecting sub-ice-shelf bathymetry data using typical polar surveying methods (e.g. seismic surveying or direct observations) can be inefficient, expensive or unfeasible. Gravity inversions provide a more practical alternative, in which observed variations in Earth's gravitational field are used to predict the bathymetry. This chapter describes a gravity inversion algorithm developed specifically for modelling bathymetry. The inversion is tested on a suite of models, created with a combination of synthetic and real bathymetric data. These tests provide the ability to 1) determine the best practices for conducting bathymetric inversions, 2) recognize the limitations of the inversions, and 3) identify where community efforts should be focused for the future of modelling Antarctica's sub-ice-shelf bathymetry. We find that estimating and removing the regional component of gravity prior to the inversion is the largest source of error in the resulting bathymetry model. To address this, we propose procedures to limit this error and provide recommendations on the minimum spatial density of bathymetry constraint points. Additionally, for common airborne gravity survey designs, we find minimizing noise in the data is more important than collecting closer-spaced data.

Plain Language Summary

The shape of the seafloor beneath the floating extensions of the Antarctic Ice Sheet exerts important controls on the ice. Controls include how the seafloor topography (bathymetry) directs the flow of warm water masses which causes melting at the base of the ice, and determines where ice is anchored to the bedrock. Conventional methods of collecting data on bathymetry are ineffective, impractical, or expensive when applied to ice shelves. One alternative method of acquiring sea floor depths is a method called gravity inversion. Variations in bathymetry can be detected by measurements of Earth's gravity over an ice shelf as a result of the difference in density between seawater and the seafloor. Here, we develop a refined technique for performing a gravity inversion and test the method on artificial data to examine its

effectiveness and learn which parts of the inversion are most prone to errors. We find that removing the portion of the gravity data that results from deep geologic structures is the largest source of error. To limit the impact of this and other sources of error in the inversion, we suggest researchers focus on collecting as many point measurements of bathymetry depth (from seismic surveys) and attempt to limit the noise in the gravity data as much as possible.

Key Points:

1. We present a new constrained geometric gravity inversion algorithm for recovering density contrasts.
2. Synthetic models show the regional-residual separation of the gravity data prior to inversion is the dominant source of error.
3. Quality over quantity for gravity data; efforts should be focused on reducing noise not increasing coverage.

3.1 Introduction

In the last two decades, the Antarctic Ice Sheet has experienced significant ice mass loss, averaging 118 billion tons per year, contributing 5.2 mm to sea-level rise (Smith et al., 2020a). This mass loss has been concentrated along the coast, where ocean currents are able to bring warm waters in contact with the ice (Rignot et al., 2019). Much of Antarctica is fringed with floating extensions of the ice sheet, known as ice shelves (Figure 3.1). These ice shelves provide a critical buttressing effect on the upstream ice, slowing the flow of ice from the continent into the oceans (Dupont & Alley, 2005). This buttressing results from lateral drag along the margins of the ice shelf and friction between the ice and the bed at pinning points. Thinning of the ice shelves lowers these resistive forces. Due to the cold climate and lack of surface melt, the majority of Antarctic ice shelves' thinning occurs as basal melt. This basal melt (Figure 3.1b) occurs from contact with relatively warm ocean waters, such as circumpolar deep water and high-salinity shelf water (CDW and HSSW) (Jenkins et al., 2010; Rignot et al., 2019).

These deep-lying warm masses of water originate offshore from the ice shelves and thus can only induce basal melting if they circulate under the shelves. A large enough ocean draft, the distance between the ice base and the bathymetry (Figure 3.1a), is required for this circulation to be possible. This connection between ocean draft and basal melting is shown by generally low ice shelf basal melt rates for shelves, or sections of shelves, with shallow ocean drafts (e.g. Pritchard et al., 2012; Tinto et al., 2019). Additionally, deep bathymetric troughs in regions of otherwise thin drafts, or conversely, bathymetry ridges in regions of thick drafts, can control the incursion of these water masses (St-Laurent et al., 2013; Yang et al., 2021).

While the elevation of the ice base for many of Antarctica's ice shelves is relatively well-constrained, the water depth is poorly known. The relatively good understanding of the ice base comes from a combination of airborne radar surveys (e.g. Das et al., 2020) and satellite altimetry measurements (e.g. Griggs & Bamber, 2011), in conjunction with the hydrostatic equilibrium assumption (Bamber & Bentley, 1994). Conversely, there is no equivalent fast and cheap technique to directly survey the bathymetry beneath floating ice shelves. Radar (ground or airborne)

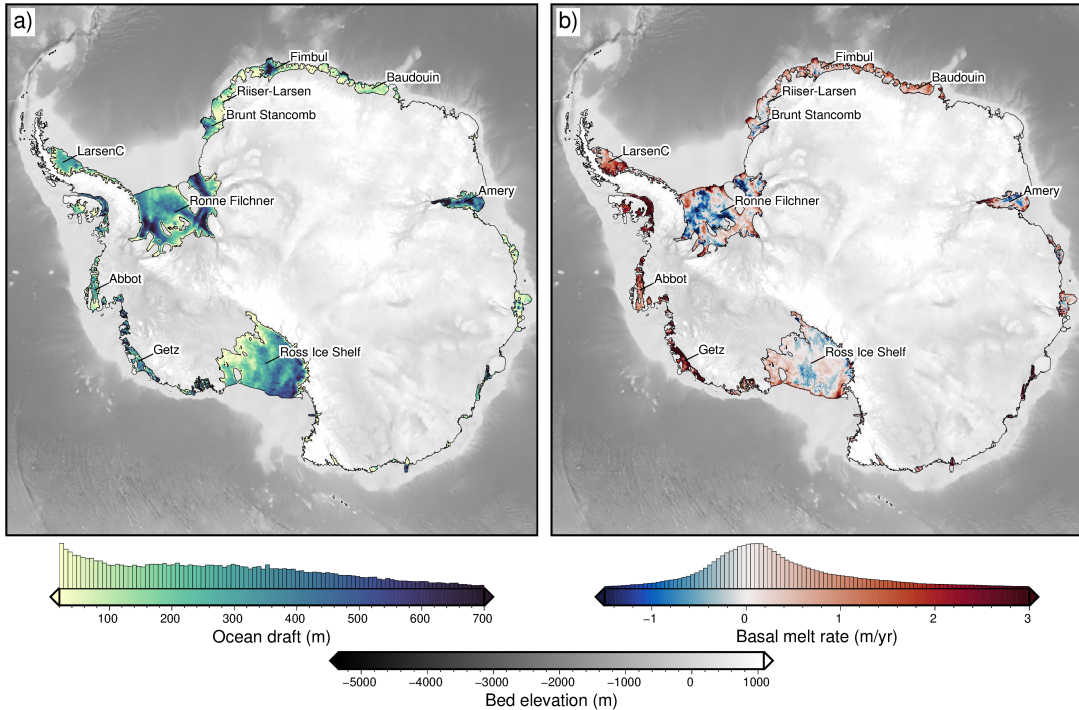


Figure 3.1: Ice shelves of Antarctica. **a)** Water column thickness beneath the ice shelves from Bedmachine data (Morlighem, 2022; Morlighem et al., 2020). **b)** Basal melt rate for the ice shelves from Adusumilli et al. (2020). Both plots show bed elevations in the gray colormap. The 10 largest ice shelves are labelled.

cannot image through the thick water, over-ice seismic surveys are slow and expensive, and numerous direct observations through drill holes are impractical. Due to the density contrast between the water and the sediment, the bathymetry surface produces a measurable gravity signal. This signal can be observed from airborne or ground-based gravity surveys, which provides a method, if used correctly, to model sub-shelf bathymetry. This method is a gravity inversion; a geophysical technique to take measurements of an energy source and estimate the physical properties responsible for these measurements (e.g., Menke, 2012; Oldenburg & Li, 2005; Tarantola, 2005). In this case, the energy source is Earth's gravitational field and the physical Earth property is the depth of the density contrast between the ocean and seafloor. This chapter will first introduce the gravity inversion technique in general, followed by the specific style of gravity inversion, a geometric inversion, which is used here. Next, a suite of synthetic models will be used to assess the performance and limitations of the inversion. The suite of models includes:

1. a simple synthetic topography.
2. a synthetic topography with a regional component of the gravity signal.
3. a semi-realistic model, using real Antarctic bathymetry and basement topographies to create the synthetic observed gravity.

With this suite of models, we will test the effects of various levels of noise, the data spacing of the observed gravity, the number of prior constraints, and various inversion methods and parameters. Finally, we will discuss the general limitations of using gravity inversions to recover bathymetry and will provide guidance for conducting gravity inversion for sub-ice-shelf bathymetry.

3.2 Methods

There are two fundamental types of geophysical modelling, forward modelling, and inverse modelling. Forward modelling is the process of simulating observed data from a model of physical properties. For a gravity application, this may be calculating the gravitational field resulting from a sedimentary basin of a given geometry and/or density model. In general, forward problems are well-posed, meaning there is a unique answer (Oldenburg & Li, 2005). In contrast, inverse modelling, or inversion, is the process of determining physical properties from observed data. For the previous example, this would entail using observed gravity data to predict the sediment thickness of a basin. Inverse problems are generally ill-posed. For a given set of gravity observations, there is a multitude of sedimentary basin configurations which reproduce the observed data with the same degree of accuracy. This is referred to as non-uniqueness and makes geophysical inversions a difficult procedure compared to forward modelling.

3.2.1 Geophysical inversion

In general, inversions consist of three components;

1. Forward operator (f): This is a mathematical means of linking a physical Earth property to the expected geophysical response. It accomplishes the task of forward modelling, as described above.
2. Physical property model (p): This is a representation of the physical Earth property of interest. While real-world properties are continuous (i.e. a smoothly varying topography), computation often necessitates discretization (i.e. a DEM (digital elevation model), see section 3.2.2.1). The starting model (p_0) typically will include the prior geologic knowledge of the region. To discretize the topography we use a layer of adjacent, vertical right-rectangular prisms.
3. Fit function (ϕ): This function describes the similarity between the observed data and the predicted data (resulting from the forward calculation of the property model ($f(p)$)). The goal of the inversion is to minimize this function so that $f(p)$ is as close to the observed data as possible.

Here, a mathematical derivation of a generalized discrete inversion problem is shown, following closely to the derivation of Oliveira and Uieda (2014). The inversion problem can be framed as finding the set of physical parameters (\vec{p}) which when modelled with the forward operator (f) produce predicted data (\vec{d}^{pred}) as close to the observed data (\vec{d}^{obs}), as possible. This inversion is discrete because the topography is represented with a series of grid cells, instead of a continuous function. The difference between the observed and predicted data gives the misfit \vec{m} , where

$$\vec{m} = \vec{d}^{obs} - \vec{d}^{pred} = \vec{d}^{obs} - \vec{f}(\vec{p}). \quad (3.1)$$

Here, the ℓ^2 -norm (mean squared error) of the misfit is the metric used to define the *closeness* between the predicted and observed data, where

$$\|\vec{m}\|_2 = \sqrt{\sum_{i=1}^N [d_i^{obs} - \vec{f}_i(\vec{p})]^2}, \quad (3.2)$$

where N is the number of observed data points.

This is defined as the *fit function*, $\phi(\vec{p})$. The fit function can also be expressed as

$$\phi(\vec{p}) = \vec{m} \cdot \vec{m} = [\vec{d}^{obs} - \vec{f}(\vec{p})] \cdot [\vec{d}^{obs} - \vec{f}(\vec{p})]. \quad (3.3)$$

In this context, the inversion problem is to determine a vector of parameters $\tilde{\vec{p}}$ of length M which minimizes $\phi(\vec{p})$. This minimum occurs where the gradient of $\phi(\vec{p})$ at the vector $\tilde{\vec{p}}$ has zero length. The gradient of $\phi(\vec{p})$ evaluated at any \vec{p} is an M -dimensional vector is defined as

$$\nabla \phi(\vec{p}) = \begin{bmatrix} \frac{\partial \phi(\vec{p})}{\partial p_1} \\ \frac{\partial \phi(\vec{p})}{\partial p_2} \\ \vdots \\ \frac{\partial \phi(\vec{p})}{\partial p_M} \end{bmatrix}. \quad (3.4)$$

Evaluating the gradient at the i^{th} element, using Equation 3.3 gives

$$\begin{aligned} \frac{\partial \phi(\vec{p})}{\partial p_i} &= \frac{\partial}{\partial p_i} \sum_j [d_j^{obs} - f_j(\vec{p})] \cdot [d_j^{obs} - f_j(\vec{p})] \\ &= \sum_j \frac{\partial}{\partial p_i} [d_j^{obs} - f_j(\vec{p})] \cdot [d_j^{obs} - f_j(\vec{p})] \\ &= -2 \sum_j \frac{\partial f_j(\vec{p})}{\partial p_i} \cdot [d_j^{obs} - f_j(\vec{p})] \end{aligned} \quad (3.5)$$

Substituting Equation 3.5 into the elements of Equation 3.4 gives

$$\nabla \phi(\vec{p}) = -2 \mathbb{J}(\vec{p}) [\vec{d}^{obs} - \vec{f}(\vec{p})], \quad (3.6)$$

where \vec{p} is the parameter vector of dimension M , \vec{d}^{obs} is the observed data vector of dimension N and \mathbb{J} is the Jacobian matrix of dimension $M \times N$, and is given by

$$\mathbb{J}(\vec{p}) = \begin{bmatrix} \frac{\partial f_1(\vec{p})}{\partial p_1} & \cdots & \frac{\partial f_N(\vec{p})}{\partial p_1} \\ \vdots & \ddots & \vdots \\ \frac{\partial f_1(\vec{p})}{\partial p_M} & \cdots & \frac{\partial f_N(\vec{p})}{\partial p_M} \end{bmatrix} \quad (3.7)$$

Each element of the Jacobian matrix is given by

$$\mathbb{J}_{ij} = \frac{\partial f_j(\vec{p})}{\partial p_i}, \quad (3.8)$$

which is the partial derivative of the j^{th} predicted data with respect to the i^{th} physical parameter. The *Jacobian* (\mathbb{J}) is a sensitivity matrix that describes how much the predicted data changes for an infinitesimal change in the physical parameter. For example, let's consider the case of a gravity inversion attempting to recover the density of subsurface cubes. The model consists of 100 cubes, and there are 10 observation points. The Jacobian would be a 100×10 matrix where $\mathbb{J}_{1,1}$ (the first

entry) would be the 1st cube's gravitational derivative with respect to density at the first observation point. The Jacobian, therefore, describes how sensitive each pair of cubes and observations are to a change in density.

Once the Jacobian is created, a matrix equation of the form $Ax = b$ is set up, where A is the Jacobian, x is the unknown variable, and b is the data misfit.

$$\mathbb{J}\vec{x} = \vec{m} \quad (3.9)$$

A solution to this linear equation can be found directly, by finding the inverse or pseudo-inverse matrix of the Jacobian, or iteratively via a least-squares solver (Jacoby & Smilde, 2009). The solution gives the correction which when applied to the physical parameters of interest minimizes the misfit between the observed data and the starting model.

3.2.1.1 Non-Linear inversions

The derivative of the forward operator with respect to the parameter of interest determines the linearity of an inversion. For a gravity inversion attempting to recover rock density, the derivative of gravity with respect to density is constant, and thus the inversion is considered linear (Aster et al., 2018). Conversely, a gravity inversion attempting to recover the depth to a surface, or the thickness of a layer, is non-linear since the vertical derivative of gravity (derivative with respect to depth) is dependent on the depth. Non-linear inversion cannot be solved directly, with matrix inversion (Jacoby & Smilde, 2009). They must be linearized; which is the purpose of the Jacobian matrix. The Jacobian enables a minimum-norm solution to be found with an iterative solver, where at each iteration, the calculated corrections (\vec{x}) are applied to the starting model, the residuals (\vec{m}) are recalculated, the Jacobian is updated, and Equation 3.9 is solved again, giving a new set of corrections. This is repeated until $\phi(\vec{p})$ is suitably low.

3.2.1.2 Geometric inversions

Most gravity inversions aim to recover the distributions of densities in the subsurface. For this technique, the model domain is discretized into a series of polygons (for 2D) or polyhedrons (for 3D), and the inversion aims to predict the density of each polygon. This is widely used due to its relevance in mineral exploration (Oldenburg & Pratt, 2007). Less commonly used are gravity inversions which aim to recover the depth, shape, or volume of features. This style of gravity inversions are referred to as geometric inversions. They are typically used to estimate relief of the Moho (e.g Borghi, 2022; Uieda & Barbosa, 2017) or the sediment-basement contact (e.g. Barbosa et al., 2007; Santos et al., 2015). In this chapter, geometric inversions are used to recover the bathymetry. This use case of gravity inversion is unique to studying the cryosphere. In locations without ice cover, bathymetry data is typically collected with shipborne multi-beam echo sounding, airborne LiDAR, or satellite altimetry.

3.2.2 Forward modelling

To perform a geometric gravity inversion, first, the gravitational field produced by a topographic surface must be able to be calculated. This topography is approxi-

mated as a constant density contrast between the overlying and underlying materials. The topography is often modelled as a series of adjacent vertical right-rectangular prisms. For a certain observation point, the gravitational field produced by this layer of prisms is the sum of the forward gravity of each prism. This forward gravity calculation of a prism is accomplished with the analytical solutions given by Nagy et al. (2000), as implemented in the Python package Harmonica (Fatiando a Terra Project et al., 2023).

3.2.2.1 Discretization

There are several options for discretizing a density contrast as a series of prisms (Figure 3.2). The most conceptually simple method is for the prisms to represent the true density and geometry of the material on either side of the surface (Figure 3.2b). In this method, the topography is represented by the base of the upper prisms, and by the tops of the lower prisms. Alternatively, the contrast can be represented by a layer of prisms either above or below the surface, ending at an arbitrary reference, typically the minimum or maximum value of the surface (Figure 3.2c-d). For this, the prism's density values are relative to the medium on the other side of the surface (i.e. if prisms are below the surface, their densities are $\rho_{below} - \rho_{above}$). The last option is to choose a flat reference surface (typically the mean value of the surface or sea level) and create prisms between this and the surface (Figure 3.2e). Prisms above the reference are assigned a positive density contrast ($\Delta\rho = \rho_{below} - \rho_{above}$), and prisms below the surface a negative density contrast ($\Delta\rho = \rho_{above} - \rho_{below}$). All of these methods result in similar forward gravity calculations. Note that the absolute density option (Figure 3.2b) has twice as many prisms as the other options, significantly increasing its computational expense, regardless of whether or not a buffer zone is used.

3.2.2.2 Gravity edge effects

Any forward gravity calculation of a surface will include gravitational edge effects. These effects are typically a decay in the gravitational field towards the edges of the prism model due to the void space (density of 0) beyond the edge of the model. The magnitude of decay is dependent on the average thickness and density of prisms near the edge. Larger or denser prisms create a large contrast with the void space, resulting in a greater amount of decay. Therefore, the absolute density method of discretization (Figure 3.2b) produces the largest edge effects due to the high-density values and large total thickness of the prisms. The relative density methods (Figure 3.2c-d) produce a smaller edge effect, since the prisms are only above or below the surface, reducing their total thickness. The density values are also less than in the absolute density method. The reference surface method (Figure 3.2e) produces the smallest edge effects due to both a) the mean prism thickness being smaller, and b) positive and negative density prisms having opposite edge effects, partially cancelling each other out. This is only applicable if the reference level is located within the range of the values of the surface. Note that with a reference level completely above or below the surface, the reference method becomes identical to methods c) and d) of Figure 3.2.

A buffer zone can be used to reduce the impact of these edge effects by calculating forward gravity confined to an inner region, while the prism model extends beyond.

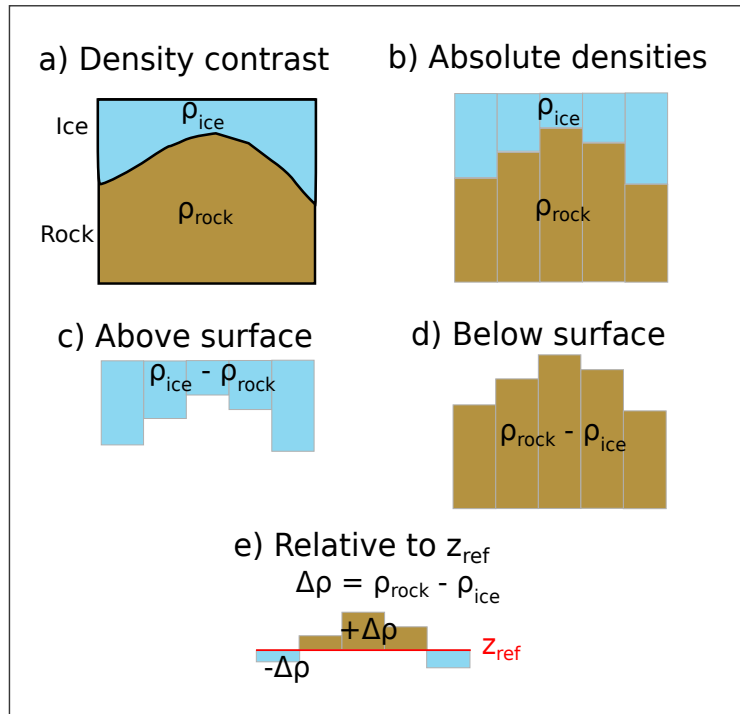


Figure 3.2: Equivalent methods of discretizing a density contrast (a) across a surface. b) Use absolute densities of the mediums above and below the reference, with prisms on either side. c-d) Use the density contrast across the surface, with prisms either above or below, and the sign of the density contrast reflecting whether they are above or below. e) Use a reference surface, with prisms above having a positive density contrast and prisms below a negative contrast.

This limits the majority of the edge effects to outside the region of calculation. Too large of a buffer zone will add an unnecessary amount of computation (more prisms), while too small of a zone will introduce unacceptably large edge effects to the calculations.

3.2.3 Isolating anomalies

For a successful geometric gravity inversion, the component of the observed gravity field resulting from the density contrast of interest must be isolated from all other gravity signals. This section describes the process of isolating the required anomaly. Since this chapter consists of synthetic gravity, the discussion of correcting raw gravity measurements and deriving the various gravity anomalies is omitted. See Chapter 4 for further discussion of gravity data processing. Here, *synthetic observed gravity* is taken to mean the gravity effect resulting solely from deviations between the true synthetic model, and a simple reference model, defined by a flat surface with a constant density above and a constant density below. This is considered a partial topo-corrected gravity disturbance, since the gravity effect of other layers, such as ice and water, if present, is assumed to have been corrected for. The misfit, \vec{m} , in Equation 3.1, is defined as this synthetic observed gravity minus the forward gravity effect of the starting bathymetry.

3.2.4 Regional vs. Residual gravity

The topography-free gravity disturbance is often simplified as consisting of two components, the regional and residual fields. The regional field typically dominates the signal and is often the result of deeper and broader structures, such as Moho variations. Superimposed on this signal is the residual field, which is typically the result of shallower structures. The terms residual and regional are relative; here, they are taken to mean the gravity effect of the bathymetry versus that of all deeper structures, respectively. In this inversion, the residual, regional, and misfit are related by

$$\vec{m} = \vec{m}_{res} + \vec{m}_{reg}, \quad (3.10)$$

where \vec{m} is the overall data misfit, from Equation 3.1. The residual misfit, \vec{m}_{res} , is the desired input into the inversion, and thus the regional component, \vec{m}_{reg} , must be removed prior to the inversion. This step proves to be one of the most challenging steps of a bathymetric inversion, especially in areas of limited constraints (Brisbourne et al., 2014). Removing an incorrect regional field, whether it is too much or too little, will directly impact the resulting bathymetry results. Regional-residual separation is also highly non-unique and benefits greatly from *a priori* constraints. Many methods of regional separation rely on the simplifying assumption that the regional field consists of longer-wavelength anomalies, while the residual field dominates the short-wavelength components. Here, four methods of estimating the regional component of gravity are described.

1. Low-pass filter: With the assumption outlined above, a low-pass filter can be used to isolate the regional gravity. For this, a Gaussian wavelength filter is used and the filter width can be varied based on the expected regional anomaly wavelengths. This method requires the data to be gridded over the entire domain, which may be a problem for sparse surveys, or irregularly shaped domains. The choice of wavelength is subjective and needs to be carefully considered. See Eisermann et al. (2020) for a bathymetry inversion utilizing this method of regional separation.
2. Trend removal: Similar to the low-pass filter method, a trend can be fit to the misfit data, representing the regional field. The order of the polynomial trend is subjective and can be varied to suit the data. Again, this parameter choice requires care.
3. Equivalent source prediction: The equivalent sources technique is a method commonly used to grid, smooth, or upward-continue gravity data. It creates a set of point sources with densities, which when forward-modelled, reproduce the measured gravity data. These sources are then used to predict the gravity anomaly at any desired point. The source depths can be varied to achieve the desired regional component. This technique is beneficial over low-pass filter and trend removal in that it does not require the data to be gridded and can thus accommodate sparse surveys, or compilations of surveys at varying altitudes. It is computationally expensive compared to the above methods. Additionally, source depths are a subjective parameter, which needs to be carefully chosen. Past bathymetry inversions have used upward continuation as a means to define the regional field (e.g., Tinto et al., 2015).

4. Constraint point minimization: The last method makes use of constraint points where the bathymetry depths are known. This inversion defines the residual component of the misfit as the gravity effect from deviations of the true bathymetry with respect to the starting bathymetry. At constrained points, there is no deviation between the starting and true bathymetries, and thus the residual component of the misfit should be zero at the constraints. This means the total misfit value at the constrained points is equal to the regional component (Equation 3.10). By sampling the misfit at each constrained point, and fitting a surface to these values, a regional component is estimated. This technique has a few advantages. It imposes a form of smallness regularization, where the inversion won't significantly alter the depth of the constraint points since the input residual at the points is ~ 0 mGal. Additionally, except for the gridding technique, this method doesn't require a subjective parameter, unlike the other methods. Similar to the low-pass filter and trend removal, this method requires gridded data. If this data is sparse, or the constrained points are not located near gravity observation points, some inaccuracies will be introduced. This technique has been used in several bathymetry inversions (An et al., 2019a; Millan et al., 2020; Yang et al., 2021).

Other methods used to approximate the regional component include using high-altitude (satellite) gravity data (Muto et al., 2016; Tinto et al., 2015), the forward modelling of a geologic model, either inferred from 1) other geophysical data (Hodgson et al., 2019), 2) *a priori* geologic knowledge (Tinto & Bell, 2011), or 3) from an approximated crustal density distribution (Cochran et al., 2020; Tinto et al., 2019). Once estimated, the regional component is then removed from the total misfit, giving the residual misfit. This residual misfit ideally results solely from discrepancies between the starting and true bathymetries.

3.2.5 Running the inversion

Here, the necessary steps for running an inversion are explained. First, the Jacobian matrix is calculated (Equation 3.7). Next, the matrix equation (Equation 3.9) is solved, giving the necessary corrections to apply to the bathymetry. Additionally, this solution needs to be constrained to account for the inherent non-uniqueness of the inversion. This is accomplished with various forms of regularization; i.e., a unique solution is determined subject to minimize an additional objective function.

3.2.5.1 Jacobian matrix

The first step of the inversion is to calculate the sensitivity matrix, the Jacobian (Equation 3.7). Each entry of the Jacobian (Equation 3.8) is the vertical derivative of gravity of a prism relative to a single observation point. While a solution exists to the analytical vertical gravity derivative of a prism, we use an approximation to limit the computational expense (Nagy et al., 2000). Here two methods are derived for approximating the vertical gravity derivative resulting from a prism; 1) an annular approximation and 2) a finite differences approach.

Annulus approximation

A vertical prism can be approximated as a sector of an annulus (a cylindrical shell), as in Figure 3.3. This approximation greatly simplifies the calculation of the vertical

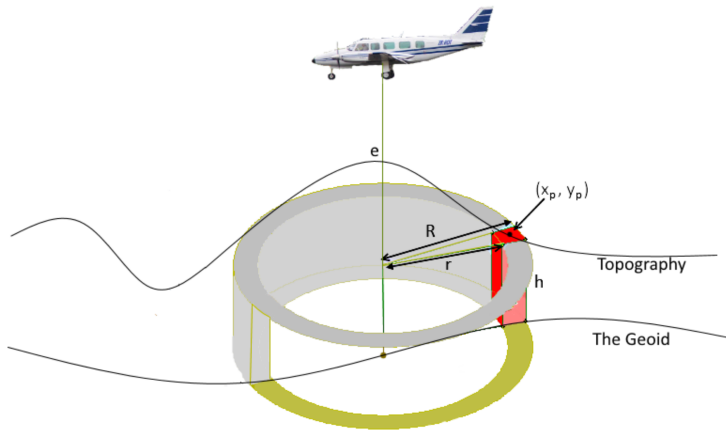


Figure 3.3: An illustration of an annulus of topography as an approximation for a vertical prism. From McCubbine (2016).

derivative of the prisms' gravity. The vertical component of gravity of an entire annulus (grey hollow cylinder in Figure 3.3) is defined by

$$\delta g = 2\pi G\rho(R - r + \sqrt{r^2 + h^2} - \sqrt{R^2 + h^2}) \quad (3.11)$$

where ρ is the density, G is the gravitational constant, r and R are the inner and outer radii, respectively, and h is the average height of the cylinder (Hammer, 1939). r , R , and h are relative to the observation point, located in the centre bottom of the annulus. McCubbine (2016) provides an adaption of Equation 3.11 which isolates the gravity of just a portion of this annulus (red section in Figure 3.3). This is accomplished by adding an additional factor f , relating the area of the annulus to the area of a sector of it:

$$f = \frac{\alpha^2}{\pi(R^2 - r^2)} \quad (3.12)$$

where

$$r = \sqrt{x^2 + y^2} - \sqrt{\frac{\alpha^2}{2}} \quad (3.13)$$

$$R = \sqrt{x^2 + y^2} + \sqrt{\frac{\alpha^2}{2}} \quad (3.14)$$

where α is the prism width, x , y , and z are coordinates of the prism centre, relative to the observation point. This factor f is then multiplied by Equation 3.11 to give the vertical component of gravity for a section of an annulus, $\delta g_{annulus} = f\delta g$.

Taking the derivative of this with respect to h gives

$$\frac{\partial g}{\partial h} = 2f\pi G\rho h \left(\frac{1}{\sqrt{r^2 + h^2}} - \frac{1}{\sqrt{R^2 + h^2}} \right). \quad (3.15)$$

While the approximation of a prism as a section of an annulus introduces some errors, the calculation is efficient and simple to implement.

Finite differences approximation

Another option to calculate the vertical derivative for the Jacobian matrix is with numerical differentiation. For this, a small prism is added above each existing prism, its forward gravity is calculated and the result is divided by the small prism's height. This approximates the vertical derivative of gravity at the surface of the prism, relative to the observation point.

Both methods adequately determine the Jacobian. The annulus method is a more simple calculation and is thus faster, but is likely less accurate and introduces singularities. These singularities occur if the prism is directly beneath the observation point, so that either the inner or outer radii are negative (Figure 3.3). These singularities are resolved by shifting the observation point to a prism edge. Conversely, the finite differences method, while it is a numerical approximation, uses analytical solutions for calculating the forward gravity (Fatiando a Terra Project et al., 2023; Nagy et al., 2000), and thus is valid in the entire domain, with no singularities. This increased robustness makes the computation slower. Section 3.3.1.3 compares the effectiveness and computation time of both of these methods.

3.2.5.2 Least-squares solver

With the Jacobian matrix and the vector of gravity residuals, Equation 3.9 can be solved to find the set of surface correction values that minimize the fit function. Here, the matrix equation $\mathbb{J}\vec{x} = \vec{r}$ is solved with an iterative damped least squares algorithm (LSQR Paige & Saunders, 1982). The algorithm gives the minimum-norm solution, where for a set of solutions that each fit the data with the same accuracy, the solution with the minimum $\|p\|^2$ is chosen. LSQR accepts a damping parameter, which helps regularize the problem, preventing the solution from becoming too large. The choice of the damping value is important as it directly affects the inverted results. The optimal value can be chosen with a cross-validation routine following that of Uieda and Barbosa (2017), as described below.

3.2.5.3 Regularization

Regularization is a series of techniques used to help constrain ill-posed inversion problems (Aster et al., 2018). Most potential field inversions, due to their inherent non-uniqueness, are ill-posed, containing many solutions which equally satisfy the data. Here regularization is split into *smallness* and *smoothness*. *Smallness* deals with adhering to *a priori* constraints, i.e. having the inverted surface elevation match the previous bathymetry measurements (constraint points). *Smoothness* helps to achieve realistic topographic results, without major jumps or excessively steep slopes.

Smoothness

To achieve a form of smoothness regularization, damping is applied at each iteration to the solver of the matrix equation. One method to choose an optimal damping value is cross-validation of the input gravity data (Uieda & Barbosa, 2017). An effective inversion should produce a topography that, when forward-modelled, accurately recreates observed gravity data that weren't included in the inversion. This idea is the basis of the cross-validation routine. The observed gravity data is split

into two sets, a *training* and a *testing* set. For an individual damping value, the inversion is run using only the training set. The final inverted bathymetry is then forward-modelled onto the observation points of the testing set. The difference between the observed and forward gravity at these testing points is calculated. The root mean square (RMS) of the differences provides a metric for the effectiveness of the damping; this is referred to as the *score*. This process is then repeated for a suite of damping values, and the value which produces the lowest score is used as the optimal damping value. In this inversion, the gravity data, whether they are airborne flight lines or scattered ground stations, are interpolated onto a regular grid (see Section 3.3.1.5). To create the testing set of observed gravity data, the original data are interpolated onto a grid at half the desired grid spacing. This leaves the training set with the desired number of points. This grid spacing configuration is shown in Figure 3.4.

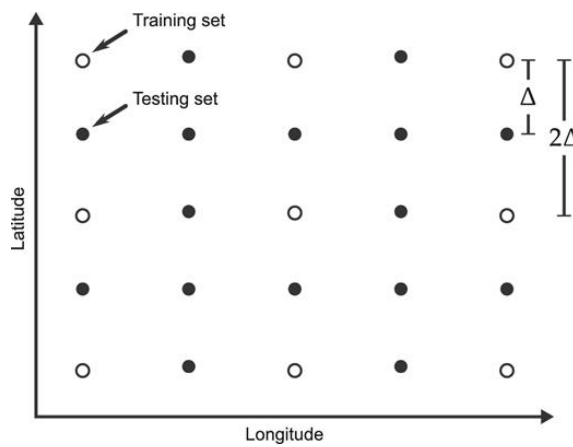


Figure 3.4: Configuration of observed gravity data observation points, split into training and testing sets. Reprinted from Uieda and Barbosa (2017).

Smallness

A form of smallness regularization is applied here to ensure the inversion results adhere to any *a priori* bathymetry constraints. A portion of this smallness regularization is already accounted for when using the constraint point minimization method of regional-residual separation. This method minimizes the residual component of the gravity misfit at the constraint points by assigning the majority of the misfit to the regional component. However, non-zero residual values near the constraints will result in a non-zero correction of the prisms immediately surrounding the constraint. For further smallness regularization, a weighting grid (Figure 3.5) is used to ensure the surface correction values at each iteration are 0 at constraint points. If only the prism immediately at the constraint point is fixed, a *pedestal* effect commonly develops. This is where the nearby prisms' surfaces freely move during the inversion, yet the constrained prism is fixed, resulting in either a pedestal or a hole. To avoid this, the weighting grid smoothly decays from a value of 0 at the constraints, to a value of 1 at a distance. To create this grid, the minimum distance between each grid cell (prism) and the nearest constraint point is calculated. These values are then normalized from 0 to 1 (Figure 3.5). At each iteration, the least squares solver yields a grid of surface correction values. Before being added to the prism layer, the grid is multiplied by this weighting grid. This results in surface corrections of 0 for prisms located at constraint points, unmodified surface correction values far from

constraint points, and a smooth taper between these two endmembers.

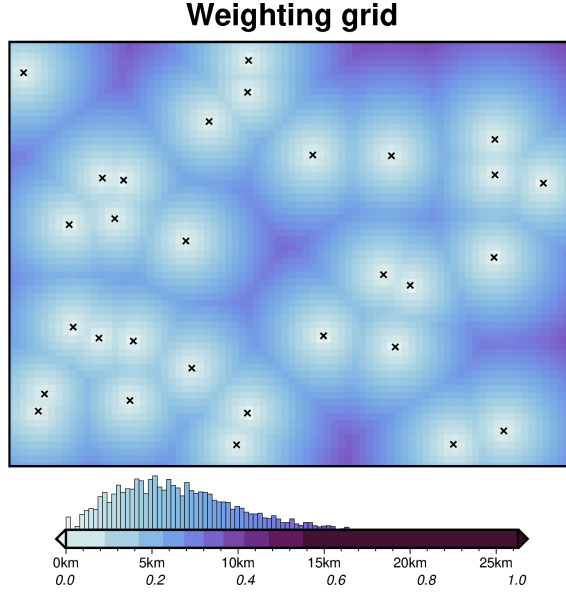


Figure 3.5: Weighting grid for the simple synthetic inversion, created from the minimum distance between each grid cell and the nearest constraint (black crosses). Grid values are normalized from 0 to 1 to produce the weighting grid (lower colourmap annotations).

The above sections outline a single iteration of the inversion. Once the surface correction is calculated and the weights are applied, these values are added to the starting bathymetry (or the last iterations inverted bathymetry). This is then re-discretized into prisms. The updated prisms are then forward modelled to create a new predicted gravity, \vec{d}^{pred} . This is subtracted from the observed gravity, \vec{d}^{obs} , to get a new misfit, \vec{m} . Using the same original regional component, the updated residual gravity misfit, \vec{m}_{res} , is calculated. This is now the input into the second iteration of the inversion. This process is repeated until a user-determined termination. Next, we outline the four criteria for ending the inversion.

3.2.6 Stopping Criteria

The inversion is terminated on one of four stopping criteria:

1. when the inversion reaches a maximum number of iterations (N)
2. when the ℓ^2 -norm of the residual ($\|\vec{m}\|_2$, Equation 3.1) is less than a set ℓ^2 -norm tolerance
3. if there is no significant variation in the ℓ^2 -norm between iterations (i.e. the $\Delta\|\vec{m}\|_2$ is less than a set tolerance)
4. if the ℓ^2 -norm increases above a certain threshold of the starting ℓ^2 -norm.

The maximum number of iterations is set as a safety margin to avoid excessively long-running inversions. The ℓ^2 -norm tolerance is used to end the inversion before excessive over-fitting of noise in the data. This should be set to the square root of the assumed noise level of the gravity data. The $\Delta\ell^2$ -norm tolerance is used to

end inversions that have reached their limit of reducing the ℓ^2 -norm. Finally, the upper limit of ℓ^2 -norm terminates run-away inversions, which occurred during the development of the inversion due to coding errors but is retained here as a fail-safe.

3.2.7 Software implementation

The inversion algorithm described here is implemented within the Python programming language. The algorithm uses many open-source scientific libraries. These include Harmonica for the forward gravity modelling of prisms and equivalent sources calculations (Fatiando a Terra Project et al., 2023; Soler & Uieda, 2021), Verde for various spatial operations (Uieda, 2018), PyGMT and Antarctic-Plots for figure creation (Tankersley, 2023; Uieda et al., 2021), Scipy for least squares regression (Virtanen et al., 2020), and Optuna for hyperparameter optimization (Akiba et al., 2019). The majority of the experiments were run in Jupyter notebooks (Pérez & Granger, 2007), which are documented to explain the details of using the software. All source code, results, and figures involved in this chapter are made available in an online GitHub repository (https://github.com/mdtanker/RIS_gravity_inversion). See Section 1.6 for the hardware used in this study.

3.3 Synthetic models

To assess the performance of the inversion and showcase its use, it is applied to a suite of synthetic test models. Each model has three components; 1) the ‘true’ bathymetry surface, which the inversion is expected to model, 2) the ‘observed’ gravity data, and 3) the ‘starting’ bathymetry model, which is a low-resolution version of the true surface. The only inputs into the inversions are the observed gravity data and the starting bathymetry. The true bathymetry is only used to evaluate the performance of each inversion. The observed gravity data contains the forward gravity calculated from the true bathymetry, plus, in some cases, additional noise and other gravity signals such as a regional field. The starting bathymetry is created by sampling the true bathymetry at a set of points. These values are then used to re-grid the data for the entire region using a bi-harmonic spline interpolator (Uieda, 2018). This simulates the bathymetric knowledge of many ice shelves, where few direct measurements of bathymetry exist, such as drill holes, or single-point seismic surveys. These points are referred to as the constraints. The models tested here include:

1. A simple model (Section 3.3.1): This model sets a baseline performance expectation of the inversion, with no noise, dense gravity observation points, and no additional components included in the observed gravity. The synthetic bathymetry is created with Gaussian functions of various amplitudes and wavelengths. With this same simple model, the observed gravity data is re-gridded at a lower resolution, and random noise is added, to better simulate a gravity survey.
2. A simple model with a regional field (Section 3.4): Using the same model as above, a ‘regional’ component of the gravity field is added to the observed data.

3. A semi-realistic model (Section 3.5): This last model is created from real bathymetry data from Antarctica’s Ross Sea. This model tests the inversion’s capabilities with more realistic bathymetric features expected for sub-ice-shelf environments.

3.3.1 Simple model

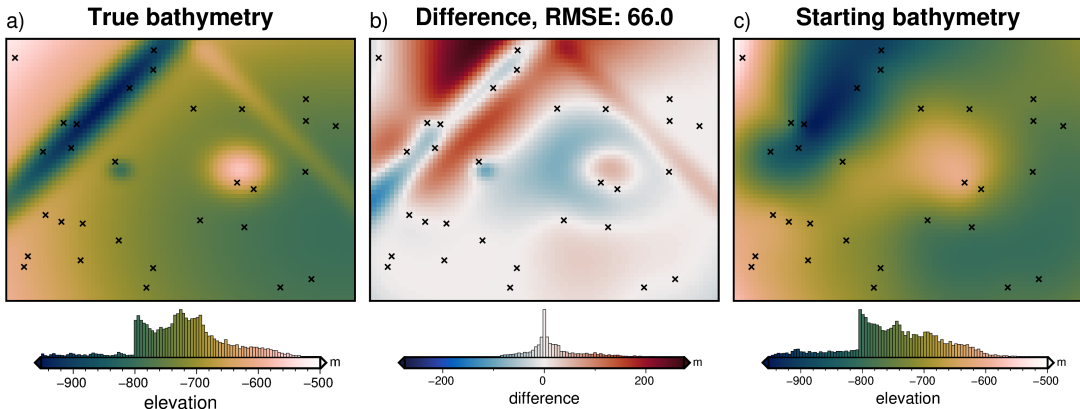


Figure 3.6: Simple synthetic model bathymetry. **a)** True bathymetry created from Gaussian functions, **b)** difference between a and c, and **c)** starting bathymetry, created from the sampling and re-gridding of the true bathymetry at 30 points (black crosses).

3.3.1.1 Model setup

Simulating typical sub-ice-shelf bathymetry, this model (Figure 3.6a) has an average elevation of ~ -700 m and ranges between ~ -400 m and ~ -1000 m. It contains features of various wavelengths, amplitudes, and shapes; namely two circular features and two linear features. Overall, the grid is eastward deepening and contains a shallow and wide E-W trough through the centre. The model domain is 80 x 60 km, with 1 km grid cells (4800 cells). A 6 km buffer zone in all directions was included to limit gravitational edge effects. 30 randomly located constraint points were used to create the starting bathymetry (Figure 3.6c). The starting bathymetry has an RMS difference with the true bathymetry of 66 m.

To forward model the gravity of the true bathymetry, a layer of adjacent vertical right-rectangular prisms was created using the reference discretization method (Figure 3.2e) with the mean elevation as the reference level. A density contrast of $\Delta\rho = 1276 \text{ kg m}^{-3}$ (contrast between seawater (1024 kg m^{-3}) and sediment (2300 kg m^{-3})), was used, with $+\Delta\rho$ for prisms above the reference, and $-\Delta\rho$ for prisms below the reference. The forward gravity of this prism layer was calculated at a constant height of 1000 m (roughly 1700 m above the bathymetry) on a regular grid at half the grid spacing (500 m) of the bathymetry. This represents the observed gravity data (Figure 3.7a) and consists of both the training and testing data sets used for the cross-validation (Section 3.2.5.3, Figure 3.4).

The low-resolution starting layer was discretized in the same method, and the same density contrast was used. The forward gravity of these starting layer prisms results in the predicted gravity (Figure 3.7c). To account for any offset between

the observed and predicted data, the observed data is DC-shifted to minimize the differences at the constraint points. The difference between the shifted observed and the predicted data gives the gravity misfit (Figure 3.7b). Since there is no regional component in this synthetic model, the input into the inversion, the residual misfit, is equal to this total misfit (Equation 3.10). This residual misfit describes the ability of the starting model to predict the observed data.

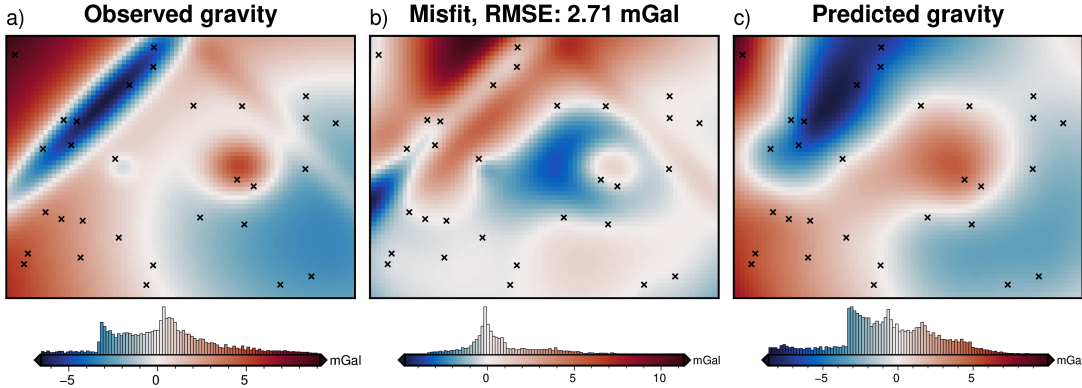


Figure 3.7: a) Synthetic gravity data generated from the true bathymetry, b) the residual anomaly, defined as the difference between a and c, and c) the predicted gravity from the starting bathymetry (Figure 3.6c).

3.3.1.2 Cross validation

To find the optimal value for the regularization damping parameter, the cross-validation method of Uieda and Barbosa (2017) is used (Section 3.2.5.3). The full set of observed data with a 500 m spacing ($N = 19481$), was separated into the training ($N = 4941$) and testing set ($N = 14540$). With the grid configuration from Figure 3.4, the resulting training data was on a regular 1 km grid, which matches the grid of the bathymetry. This training data set was used as the input to 10 inversions. Each inversion used a different damping value between 10^{-4} and 10^{-1} . The resulting inverted bathymetry of each inversion was then forward-modelled on the observation points of the testing data set (not used in the inversion). The RMS difference between the forward-modelled gravity value and the initial residual misfit values was calculated, giving the cross-validation score (Figure 3.9a). Of the 10 inverted bathymetry models, the model with the lowest score is retained.

This model is shown in Figure 3.8c, and resulted from a damping value of 10^{-2} . This inverted bathymetry has an RMS difference with the true bathymetry of 8 m and an RMS difference at the constraint points of 1 m. Figure 3.9b shows a profile across the model. The overlap of the true (red) and inverted (blue) bathymetry in the first panel shows the effectiveness of the inversion at recovering the true bathymetry. The lower panel shows the inversion's ability to minimize the misfit between the observed gravity (red) and the forward response of the inverted bathymetry (blue). The inversion was able to recover all the features of the true bathymetry, with only minor errors along the edges of the domain, and adjacent to constraint points. For this simple model, the inversion converged in 37 iterations, with a total computation time of 30 seconds and a final RMS residual misfit of 0.022 mGal. It terminated due to the ℓ^2 -norm decreasing between the set threshold of 0.15 (0.0225 mGal).

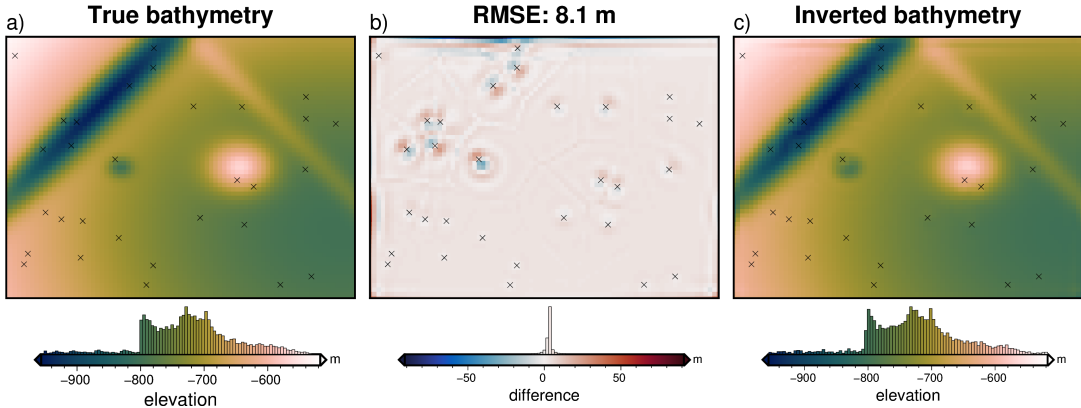


Figure 3.8: Inverted results with optimized parameters, using the annulus approximation method of calculating the Jacobian matrix. **a)** True bathymetry, **b)** difference between a and c, and **c)** final inverted bathymetry. Black crosses are constraint points. The RMS difference with the true bathymetry at these constraints is 1 m

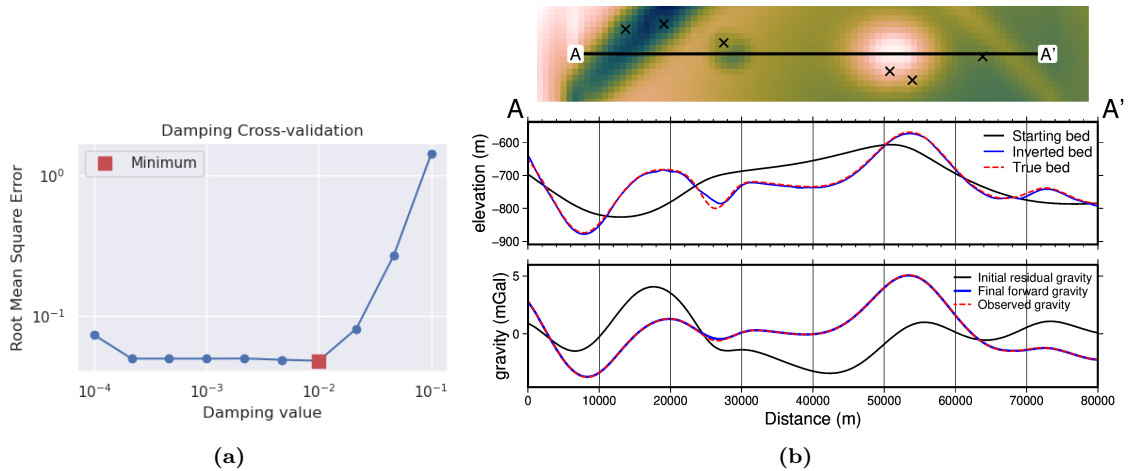


Figure 3.9: Cross-validation and profiles for the simple synthetic inversion. **a)** Cross-validation curve showing the optimal damping parameter (red square). Both axes are on a logarithmic scale. **b)** 2D profile of the inversion results. The top panel shows profile location and constraint points (black crosses). The middle panel contains topographic profiles of the starting, inverted, and true bathymetries. The bottom panel contains gravity anomaly profiles.

3.3.1.3 Comparing vertical derivative methods

Section 3.2.5.1 presented two methods for calculating the vertical derivative of gravity of a prism. This vertical derivative is used to create the Jacobian matrix (Equation 3.9) and needs to be calculated at each iteration of the inversion. The above cross-validation and inversion were performed using the *annulus approximation* of the vertical derivative. Here, this process is repeated with the *finite differences* method of the vertical derivative. Figure 3.10 shows the results of this inversion. The optimal damping parameter was 10^{-2} , and the inversion resulted in an RMS difference with the true bathymetry of 9 m, compared to 8 m for the annulus approximation. Figure 3.11 shows the inversion convergence curves for the inversion of the annulus approximation and the finite differences methods. The inversion with the annulus approximation was $\sim 500\%$ faster to converge than the finite differences method (30 sec vs 169 sec). Because these vertical derivatives need to be recalculated at each iteration, a large portion of the inversion time is spent performing these calculations. This comparison shows the annulus approximation is not only

significantly faster, but results in comparable, or slightly more accurate, inversion results. For the remainder of this chapter, only the annulus approximation will be used.

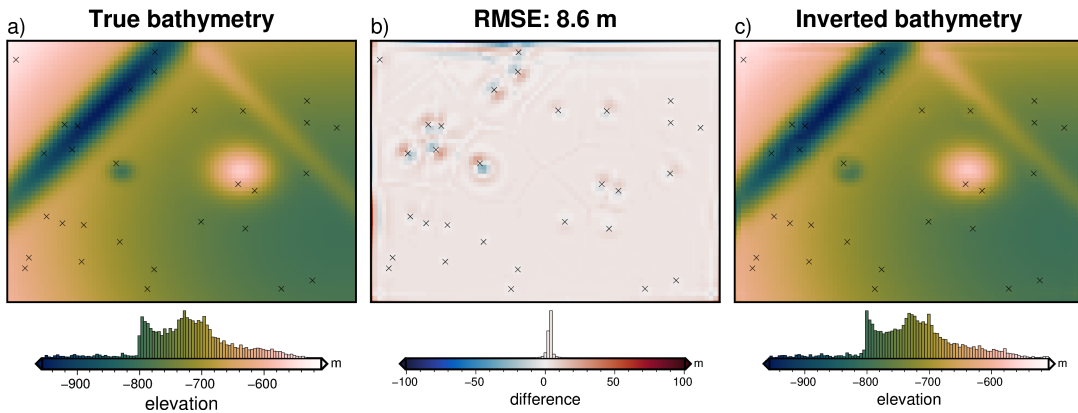


Figure 3.10: Inversion results with optimized parameters using the finite differences method. **a)** True bathymetry, **b)** difference between a and c, and **c)** final inverted bathymetry. Black crosses are constraint points. The RMS difference with the true bathymetry at these constraints is 1 m

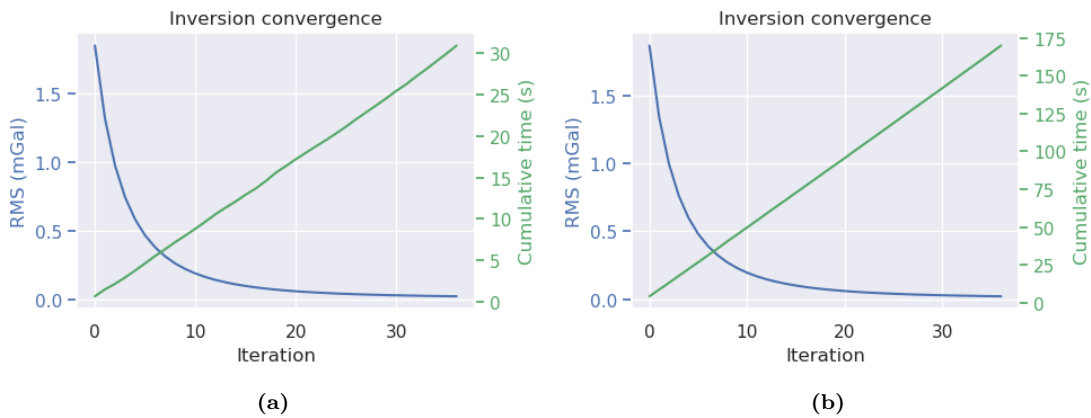


Figure 3.11: Inversion convergence curves for the two methods of creating the Jacobian matrix. Blue line (left y-axis) shows the RMS of the residual misfit at each iteration of the inversion. Green line (right y-axis) shows the cumulative time to complete the inversion. **a)** Results for the annulus approximation method of finding the vertical derivative. **b)** Results for the finite differences method.

3.3.1.4 Added noise

To test the effect of noise in the gravity data, which is inevitable in data collection, especially so in airborne surveying, the observed gravity was contaminated with noise. The noise has a Gaussian distribution with a mean of 0 mGal and a standard deviation of 2% of the max absolute value of the data ($\sim .16$ mGal). Similarly, Rashidifard et al. (2021) used 5% noise in their synthetic gravity inversion while Uieda and Barbosa (2017) use 5 mGal of noise, which for their synthetic application equated to $\sim 1\%$ of the max absolute value. Using this noise-corrupted gravity data, the same damping parameter cross-validation was run as previously (Figure 3.13a), and the lowest score was achieved with a damping value of 10^{-2} . Figure 3.12 shows the inversion results of this noise-contaminated model. The inversion converged in 18 iterations, with a total computation time of 13 seconds and a final RMS residual

misfit of 0.16 mGal. It terminated after the ℓ^2 -norm became lower than the set tolerance of 0.4 (0.16 mGal). This tolerance was set to match the known level of noise. The inverted bathymetry had an RMS difference of 12 m with the true bathymetry and an RMS difference of < 1 m at the constraint points. Figure 3.13b shows the inversion is still able to reproduce the observed gravity (lower panel), but a component of the noise was introduced into the final bathymetry (upper panel). All major features of the true bathymetry are recovered, albeit not as accurately as the no-noise model (Figure 3.8).

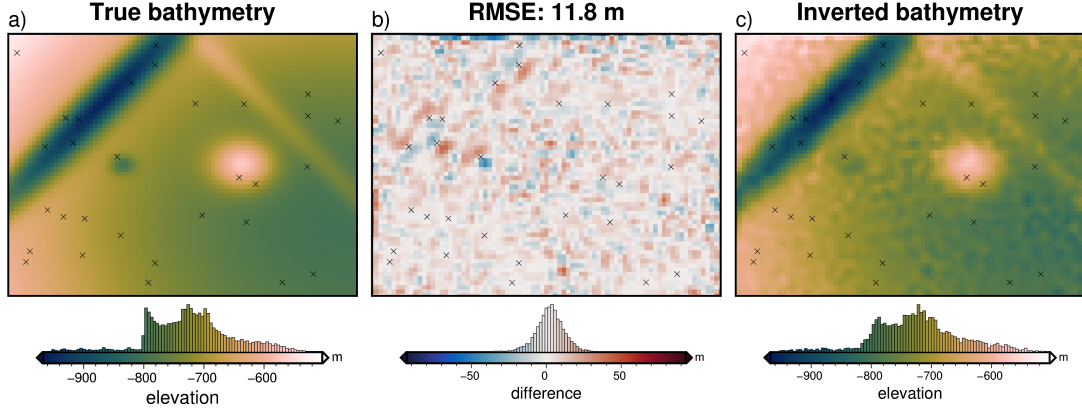


Figure 3.12: Simple synthetic model inversion results with 2% added noise (0.16 mGal). **a)** True bathymetry, **b)** difference between a and c, **c)** final inverted bathymetry. Black crosses are constraint points. The RMS difference with the true bathymetry at these constraints is < 1 m.

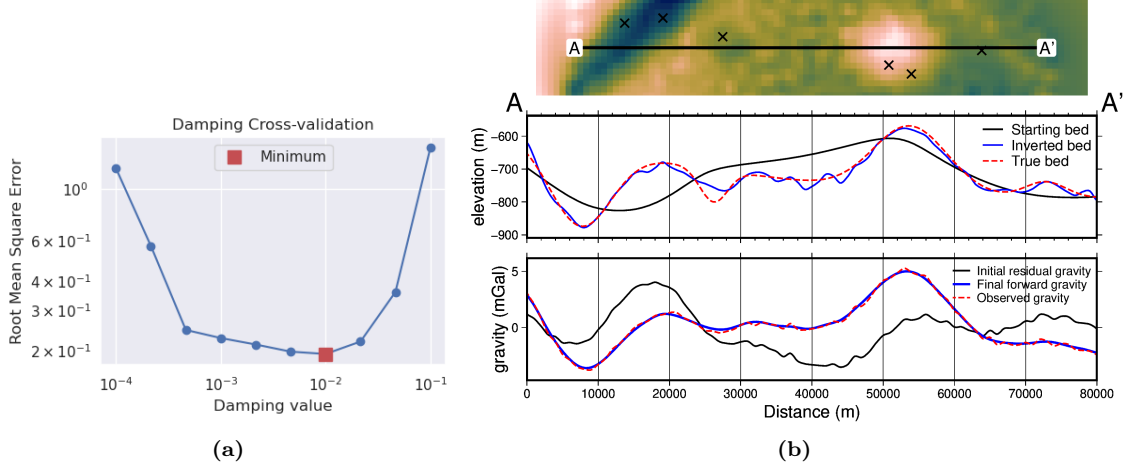


Figure 3.13: Cross-validation and profiles for the inversion with noise. **a)** Cross-validation curve showing the optimal damping parameter (red square). **b)** 2D profile of the inversion results. The top panel shows profile location and constraint points (black crosses). The middle panel contains topographic profiles of the starting, inverted, and true bathymetries. The bottom panel contains gravity anomaly profiles.

3.3.1.5 Down-sampled data

The previous two models used observed gravity data collected on a grid of observation points at the same grid spacing as the prism layer (1 km). This represents a very dense gravity survey. Gravity surveys are often relatively sparse compared to the resolution of the surface they are attempting to recover in an inversion. This section tests the effect of changing the resolution of the gravity data, to simulate

a coarser gravity survey. Simply sampling the gravity data at a coarser resolution leads to a checker-boarding effect, where the inversion alters prisms nearby the gravity observations, but not prisms further away. For this reason, it is recommended here to re-grid the observed gravity data at a similar grid spacing to the prism layer. This can be accomplished with standard gridding techniques, such as minimum curvature or bi-harmonic splines (see section 3.4.2). However, these techniques aren't well suited for potential field data since they don't account for the variation in observation heights (Soler & Uieda, 2021). An alternative method of interpolating the gravity data onto a finer resolution grid is the equivalent sources technique (Dampney, 1969)¹.

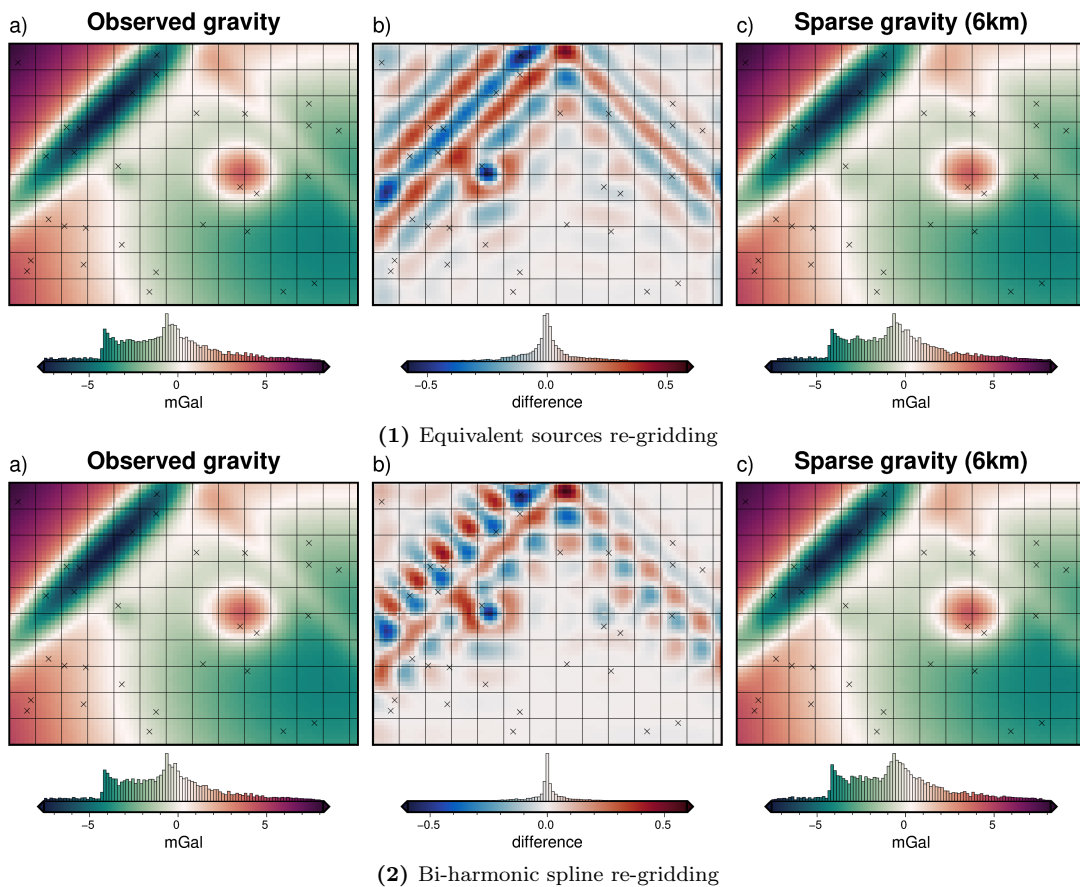


Figure 3.14: Creating a low-resolution observed gravity survey. **Top panel** shows results using the equivalent source technique of gridding gravity data. **Bottom panel** shows simple gridding using a bi-harmonic spline. **a)** Original observed data on a 1 km grid, **b)** gravity signal lost due to sampling and re-gridding, **c)** the low-resolution observed gravity (6 km spacing) re-gridded at 1 km with either equivalent sources (top) or a regular gridding algorithm (bottom). Black crosses show constraint points and black lines show 6 km grid.

Here, the original gravity data, on a 1 km grid, is sampled at a 6 km spaced grid to represent a low-resolution survey with observations every 6 km. A series of point sources are created at depth, and their densities are altered to best reproduce the observed gravity data. Once this process of fitting the source parameters to the data is accomplished, the gravity field can be predicted anywhere. For this application, the equivalent sources are predicted onto an even 1 km grid, to match the spacing

¹The equivalent sources technique is also used in this study as a means of regional separation (see section 3.2.4, this is a similar application but for different purposes).

of the bathymetry. Figure 3.14 shows the results of this process (top panel) and the results using simple gridding without equivalent sources (bottom panel). *Subplot a* shows the original observed gravity data (just training points) on a 1 km grid. This grid is sampled onto a 6 km grid (black grid lines) and re-gridded at 1 km (*subplot c*). *Subplot b* shows the difference, which represents the lost data resulting from the sparse survey. Typically the equivalent sources gridding technique is most beneficial to account for variations in observation heights. Here, even with constant elevations, there are noticeable differences between equivalent source gridding and simple gridding with bi-harmonic splines.

The equivalent-source resampled grid is used, with no added noise, in the same inversion procedure as the previous sections. The cross-validation (Figure 3.16a) resulted in an optimal damping value of 10^{-2} . The inverted bathymetry with this damping value is shown in Figure 3.15. The inversion was completed in 29 seconds and 38 iterations with a final RMS residual misfit of 0.019 mGal. The inversion was terminated due to the ℓ^2 -norm decreasing below the set threshold of 0.15 mGal $^{1/2}$. The inverted bathymetry had an RMS difference of 11 m with the true bathymetry and an RMS difference of 1 m at the constraint points. While the overall difference from the true bathymetry is low, this inversion failed to fully recover the small circular depression. Figure 3.14 shows that the nearest observation point (intersection of gridlines) was on either side of this anomaly, and thus the sparse gravity survey used here failed to image the true magnitude of the feature. Figure 3.15b shows the absence of this feature in the inverted bathymetry.

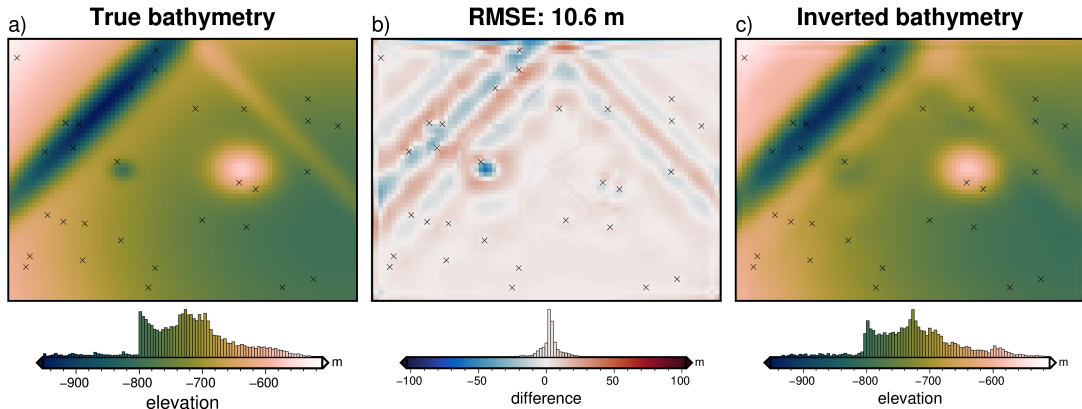


Figure 3.15: Simple synthetic model inversion results with input data resampled at 6x the bathymetry grid spacing (6 km). **a)** True bathymetry, **b)** difference between a and c, and **c)** final inverted bathymetry. Black crosses show constraint points. The RMS difference with the true bathymetry at these constraints is 1 m.

3.3.2 Ensemble of Noise and Sampling values

To test the relative importance of the level of noise and the resolution of the gravity data (i.e. station/flight line spacing), an ensemble of 100 inversions was run, with 10 noise levels between 0 and 9%, and 10 gravity resolutions between 1 and 10 km. The noise level percentages are of the maximum absolute value of the data, equating to 10 levels between 0 and 0.85 mGal. The differing gravity resolutions were created with the sampling and re-gridding of equivalent sources outlined in the above section. For each set of noise and spacing values, the cross-validation routine was used to

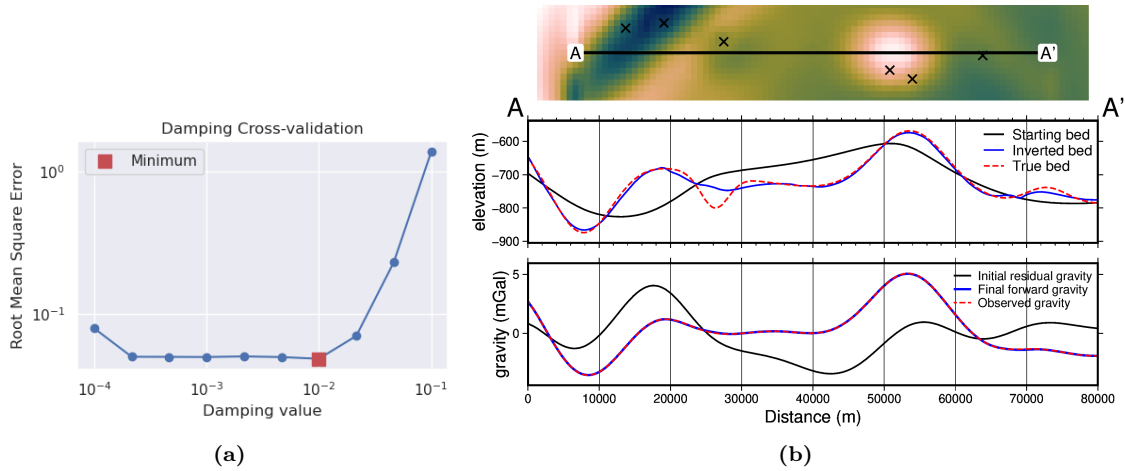


Figure 3.16: Cross-validation and profiles for the 6 km resampled inversion. **a)** Cross-validation curve showing the optimal damping parameter. **b)** 2D profile of the inversion results. The top panel shows profile location and constraint points (black crosses). The middle panel contains topographic profiles of the starting, inverted, and true bathymetries. The bottom panel contains gravity anomaly profiles.

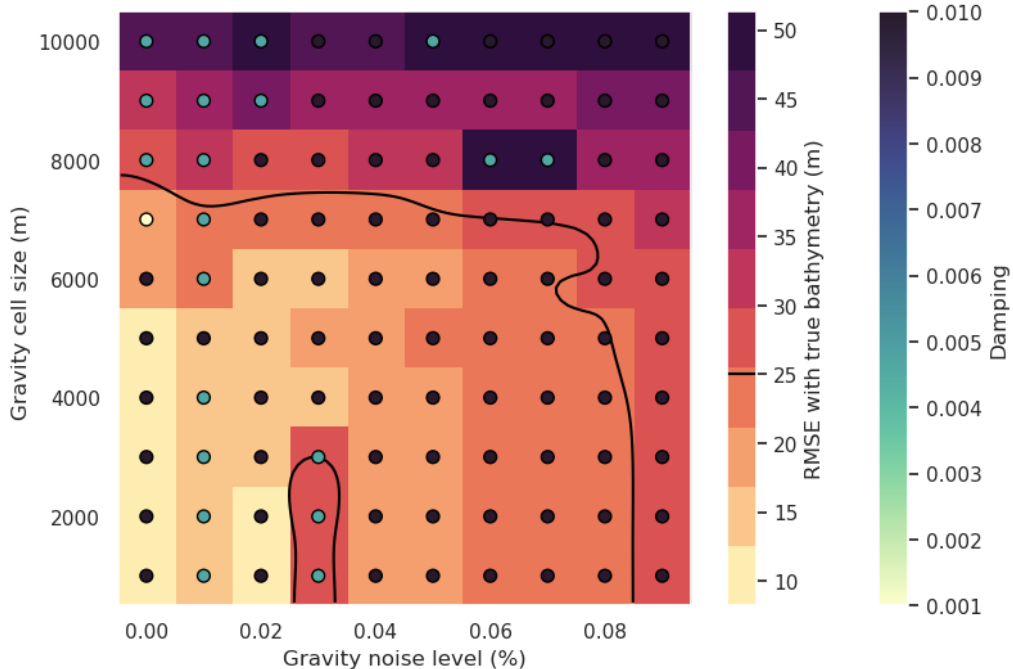


Figure 3.17: Ensemble of noise levels and gravity spacing for the simple synthetic model. Grid cell colour indicates each inversion's RMS difference with the true bathymetry. The circles' colour indicates the optimal damping value found for each inversion's cross-validation. Black line shows the 25 m RMSE contour, indicative of the amplitude of the smallest amplitude features.

find the optimal damping parameters and associated inverted bathymetries. Each of these 100 inversions were then compared to the true bathymetry yielding an RMS difference for each.

Figure 3.17 shows the results of this ensemble of inversion. Each grid cell represents a single inversion, with the level of noise and gravity resolution for the inversion indicated by the x and y axis, respectively. The background colour (warm colours) indicates each inversion's resulting RMS difference with the true bathymetry. Coloured circles show the optimal damping value for each inversion

found through cross-validation. This shows a general decrease in the inversion's accuracy with either more noise or lower-resolution gravity data. The smallest bathymetric features which this inversion ideally should recover have amplitudes of tens of meters (small circular depression and narrow ridge). The RMSE here indicates a base-level of error in the inversions, while the error in the vicinity of the short wavelength bathymetry features is likely higher (Figure 3.15b). Inversions with RMSEs of 10's of meters will likely fail to resolve these small features. For this inversion, an RMSE of 25 m (black contour in Figure 3.17) approximately equates to a gravity observation spacing greater than 8 times the prism layer spacing, and a noise level higher than 8% of the survey's max absolute value.

3.4 Adding a regional component

Now that the inversion has been demonstrated to adequately recover bathymetry with various levels of noise and resolutions of the input gravity data, an additional complexity is added. This complexity is a regional component of the observed gravity field. To account for this, the inversion remains the same, but the regional component of the gravity misfit must be removed beforehand (Equation 3.10). In this section, first, the four methods of regional separation laid out in 3.2.4 are compared. Next, one of these methods, constraint point minimization, is further investigated. Lastly, the effects of noise and gravity survey spacing are explored.

This model uses the same starting bathymetry (Figure 3.6) as the previous section, but the observed gravity includes a regional field, which represents the portion of observed gravity signal resulting from unknown crustal sources, such as anomalous bodies or crustal thickness variations. This component (Figure 3.18b) is calculated from a synthetic topography with a median elevation of -4300 m and a density contrast of 700 kg m^{-3} . Its range of gravity values is set to be the dominant signal in the observed gravity, but not large enough to fully mask the signal of the bathymetry signal. Figure 3.18 shows the various components of the gravity and resulting misfit for this model.

3.4.1 Regional separation methods

The four methods of regional separation discussed in section 3.2.4 each have at least one hyper-parameter which affects their calculation of the regional field. For each method these include

1. Low-pass filter: the distance width of the Gaussian filter.
2. Trend removal: the degree of the polynomial trend fit to the misfit.
3. Equivalent source prediction: the depth and damping parameters of fitting sources to the data (Soler & Uieda, 2021).
4. Constraint point minimization: parameters for the associated gridding method, such as the tension factor for minimum curvature gridding (Smith & Wessel, 1990) or the minimum distance and damping parameter for bi-harmonic spline gridding (Uieda, 2018).

Since for this synthetic model, the true regional field is known (Figure 3.18b), the effect of the parameters associated with each of the four methods can be explored.

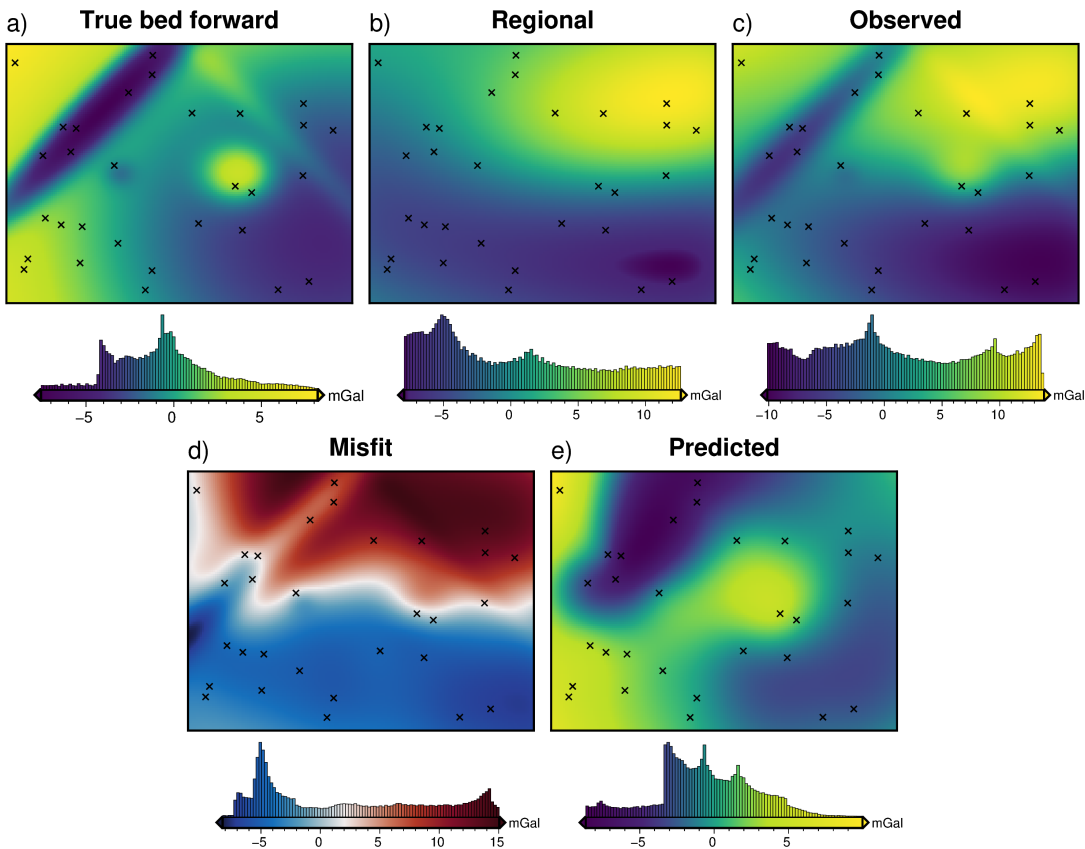


Figure 3.18: Gravity components and anomalies for the simple synthetic model with the addition of a regional field. **a)** the forward gravity of the true bathymetry, **b)** the regional component of gravity, **c)** the observed gravity from the combination of a and b, **d)** the gravity misfit from the difference between c and e, and **e)** the predicted gravity from the forward calculation of the starting bathymetry.

Excluding the constraint point minimization method, an optimization is run for each method, with the goal of finding the parameter values which minimize the RMS difference between the true and calculated regional gravity. Each optimization has 20 trials. The constraint point minimization doesn't require optimization because the various gridding parameters won't significantly affect the RMS difference between the resulting regional field and the true field. However, the gridding parameters will affect the inversion itself; this is explored in the next section. For this comparison of the regional removal method, the constraint point minimization method uses bi-harmonic spline gridding, and the gridding damping parameter is chosen with a cross-validation (Uieda, 2018). The best regional field (lowest RMS with the true regional field) of each method was found with the following parameters:

1. a 30 km filter width for the low pass filter method
2. a 3rd order trend for the trend removal method
3. source depth of 89 km and a damping value of 1.72 for the equivalent source technique
4. an interpolator damping of 1.27×10^{-8} for the bi-harmonic spline interpolator of the constraint point minimization method.

Each of these regional fields was then removed from the gravity misfit, producing the residual anomalies (Figure 3.19a-d). These resulting residuals were then input

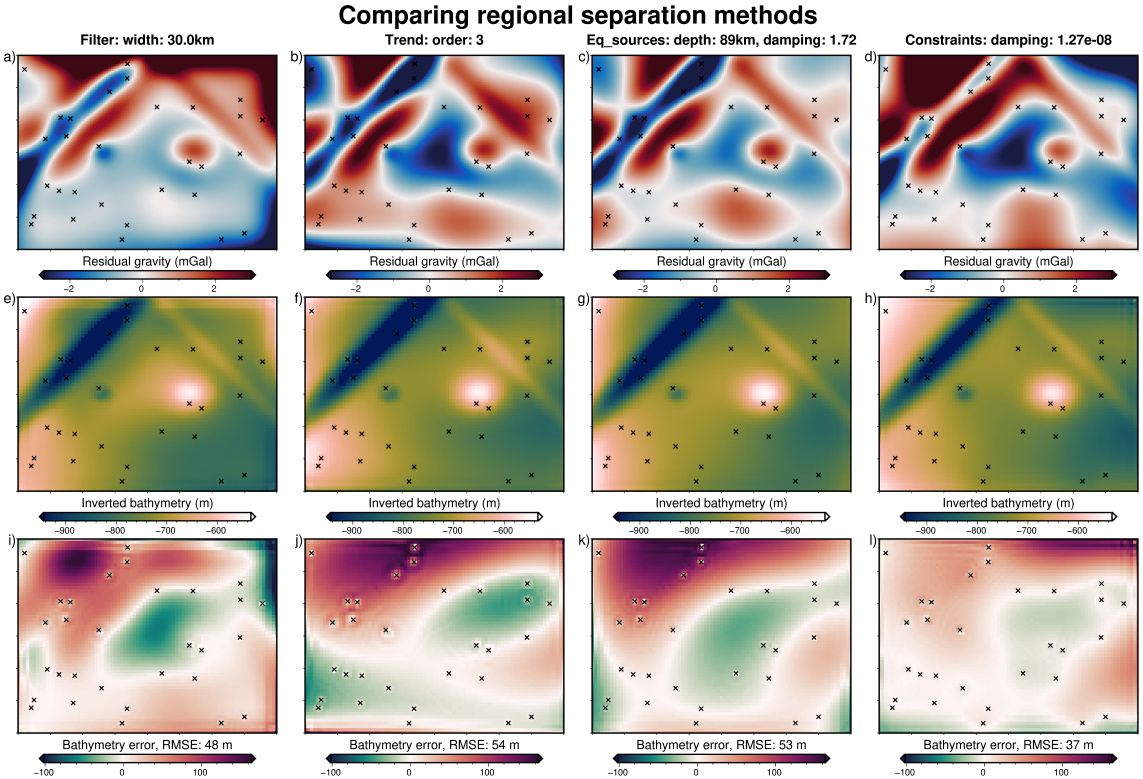


Figure 3.19: Comparison of inversions with 4 regional separation methods. First row (**a-d**) shows residual gravity misfit after regional separation. Second row (**e-h**) shows the inverted bathymetry for each method. Third row (**i-l**) shows the error of the inverted bathymetries with the true bathymetry. Constraint points are shown as black crosses. Colourmaps are identical for each row. Profiles of these data are shown in Figure B.1 of Appendix B.

into an inversion, resulting in the inverted bathymetries of d-h of Figure 3.19, and the bathymetry error relative to the true bathymetry was found (Figure 3.19i-l). For these inversions, the same damping parameter cross-validation was conducted, as described in Section 3.3.1.2. This comparison of regional separation methods shows that the constraint point minimization method (Figure 3.19l) produces the best inverted bathymetry, both visually (Figure 3.19h), and based on the RMS difference with the true bathymetry (37 m). Figure B.1 in Appendix B shows a profile of the resulting regional fields and inverted bathymetries of these various methods of regional separation. The remainder of this section further examines the constraint point minimization method of regional separation.

3.4.2 Constraint point minimization

The constraint point minimization method assumes that at locations of known bathymetry, there is no residual component of gravity misfit, and the regional component entirely equals the misfit. To implement this, misfit values at the constraints are sampled and used to create a region-wide grid of regional values. This grid is then removed from the misfit to get the residual misfit (Equation 3.10). This gridding can be accomplished by many techniques, which at an initial inspection appear to produce similar results. Here, two methods of gridding and their gridding parameters are compared, and the impact on the inverted bathymetry are shown. These gridding methods are tensioned minimum curvature (Smith & Wessel, 1990) and bi-harmonic splines (Sandwell, 1987).

3.4.2.1 Tensioned minimum curvature

Tensioned minimum curvature gridding is a commonly used technique for gridding sparse data which fits the smoothest possible surface while still matching the data (Wessel & Bercovici, 1998). It allows variation in the location of maximum curvature through the tension factor parameter. A tension factor of 0 results in the minimum curvature solution (maxima and minima allowed anywhere), while a value of 1 localizes the curvature at the data points (maxima or minima only allowed at the data points) (Smith & Wessel, 1990). A tension of 0.25 is suggested for potential field data (Wessel et al., 2019). Tensioned minimum curvature has been used in several bathymetric inversions for constraint point minimization (An et al., 2019a; Millan et al., 2020; Yang et al., 2021).

3.4.2.2 Bi-harmonic splines

The second method of gridding the sampled gravity misfit values uses bi-harmonic splines. This method uses Green's functions and the least squares fit to the data (Sandwell, 1987). Computation time for this technique is approximately proportional to the cube of the number of data, making it computationally expensive for large datasets (Deng & Tang, 2011). There is a damping parameter value that can be adjusted, to smooth the resulting interpolation. As implemented in the *SplineCV* class of the Python package Verde (Uieda, 2018), automated cross-validation of the data can be used to identify the damping value which best predicts the data. Once the parameter is determined, and the data is interpolated, the interpolation can be predicted at any location, such as on the nodes of a uniform grid.

Despite its slow run time with large datasets, bi-harmonic spline gridding has several advantages over tensioned minimum curvature gridding. It allows the incorporation of data uncertainties into the fitting via a weighting parameter. With the use of cross-validation, there are no subjective parameters that can significantly alter the results. Lastly, the predicted data don't need to be on a regular grid, which is useful for irregularly shaped domains that don't adhere to a rectangular region. In their bathymetry inversion, Millan et al. (2020) point out features in their inverted bathymetry which likely result from the minimum curvature gridding technique. Apart from this, there appears to be little work related to the how the gridding procedure affects this aspect of a bathymetry inversion.

3.4.2.3 Gridding comparison

In this section, the effect which the gridding process has on the inverted bathymetry is analyzed. Four sets of regional separations were conducted, three using the tensioned minimum curvature technique, and one using the bi-harmonic spline technique. For the three minimum curvature separations, the tension factors used were the end members, 0 and 1, and the suggested value for geopotential data, 0.25. For the bi-harmonic spline, a cross-validation with 20 varying damping values was conducted, and the best resulting damping value was used. For each of the four calculated regional fields, the resulting residual fields (Figure 3.20a-d) were used as inputs to an inversion. All four residual anomaly data were included in an inversion damping parameter cross-validation, as described in Section 3.3.1.2. The difference between the resulting inverted bathymetry and the true bathymetry of each model

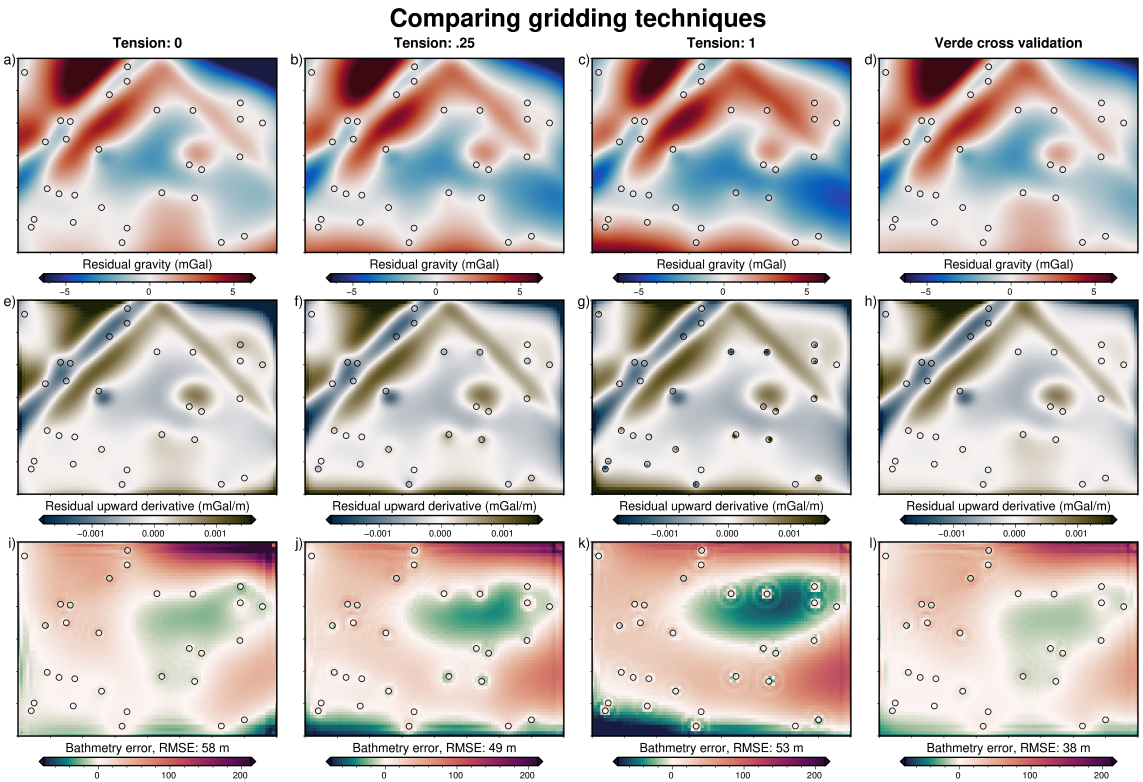


Figure 3.20: Comparison of gridding techniques for the constraint point minimization method of regional-residual separation. By sampling the misfit at constraints, and re-gridding over the entire domain, the regional component of the misfit is estimated. Gridding methods include minimum curvature gridding with tension factors of 0 (**column 1**), 0.25 (**column 2**), 1 (**column 3**), and cross-validated bi-harmonic spline gridding (**column 4**). Resulting gridded regional components were removed from the misfit grids to produce the residual grids (**a-d**). Second row (**e-h**) shows the vertical derivative of the residual, to highlight the gridding variations. Third row (**i-l**) shows the error of the inverted bathymetries with the true bathymetry. Constraint points are shown as open circles. Colourmaps are identical across all columns. Profiles of these data are shown in Figure B.2 of Appendix B.

is shown in Figure 3.20i-l. To help visualize the difference in the resulting residual grids, 3.20e-h shows the vertical derivative of the residual fields. This highlights that while the residual values at the constraints are all similar, the slope of the residual in the vicinity of the grids is strongly dependent on the gridding method ². Additionally, the minimum curvature gridding is shown, in subplots a-c, to create large artificial anomalies away from constraint points (low values in upper right corners). These gridding artifacts result in large errors in the resulting bathymetry 3.20i-k. The bi-harmonic spline interpolator (last column in 3.20) is shown to produce a residual field that adheres to the constraints, has smooth curvature near constraints, and doesn't create large artificial anomalies. The effectiveness of this interpolator is confirmed by the low RMS difference between the inverted and true bathymetry (38 m). Figure B.2 in Appendix B shows a profile of the resulting regional fields and inverted bathymetries of these various gridding methods. With the bi-harmonic spline gridding techniques shown to be the most effective, the remainder of this chapter uses this gridding technique for the constraint point minimization method of regional separation.

²Note that the gridding process creates the regional field (not shown in Figure 3.20), which when subtracted from the total misfit gives the residual field. The residual grid is affected by these gridding effects through the removal of the regional field.

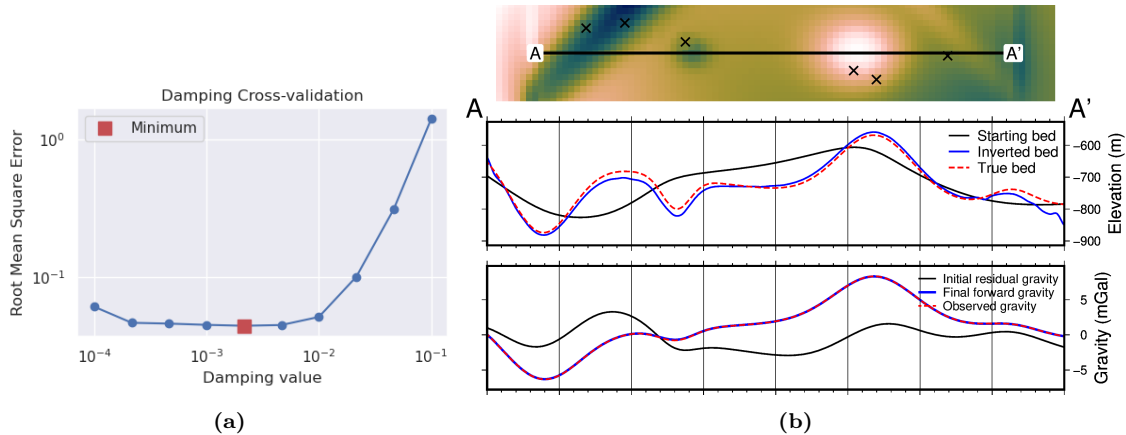


Figure 3.21: Cross-validation and profiles for the simple synthetic inversion with a regional component removed. **a)** Cross-validation curve showing the optimal damping parameter (red square). **b)** 2D profile of the inversion results. The top panel shows profile location and constraint points (black crosses). The middle panel contains topographic profiles of the starting, inverted, and true bathymetries. The bottom panel contains gravity anomaly profiles.

3.4.3 Inversion results

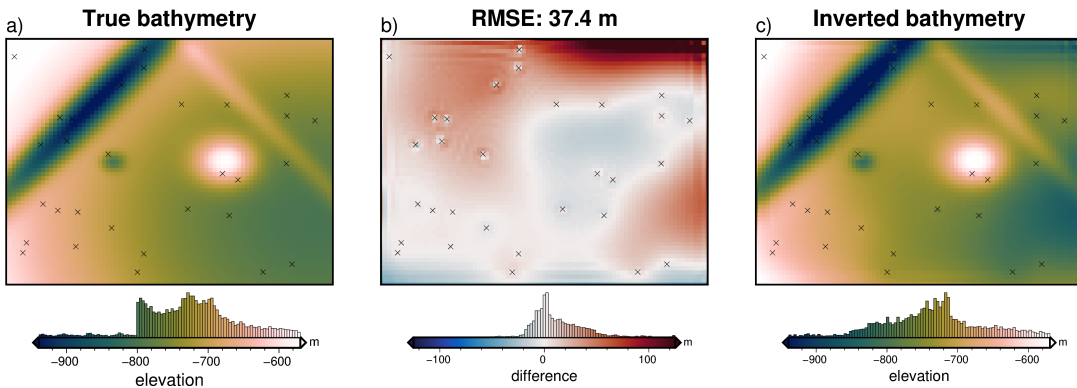


Figure 3.22: Simple synthetic model inversion with a removed regional component. **a)** True bathymetry, **b)** difference between a and c, **c)** final inverted bathymetry. Black crosses are constraint points. The RMS difference with the true bathymetry at these constraints is 2 m.

Using the cross-validated bi-harmonic gridding method to separate the regional component of the gravity misfit, the resulting residual misfit was used in an inversion. The same gravity data cross-validation method of determining the optimal damping parameter is used (Figure 3.21). The optimal damping parameter was found to be $\sim 10^{-2.6}$. The resulting inversion is shown in Figure 3.22. The inverted bathymetry had an RMS difference with the true bathymetry of 37 m and an RMS difference at the constraints of 2 m. The inversion was completed in 66 seconds, with 39 iterations and a final RMS residual of 0.022 mGal. The inversion was terminated due to the ℓ^2 -norm decreasing below the set threshold of $0.15 \text{ mGal}^{1/2}$. All four bathymetric features were recovered, but a lack of constraints in a few regions (the upper-right corner) lead to a miscalculation of the regional field and a subsequent over-deepening of the bathymetry.

The regional separation, parameter cross-validation, and inversion were repeated with additive noise and re-sampling of the gravity data to a coarser resolution (Appendix B.1). As in section 3.3.2, this above workflow was also repeated for an ensemble of noise levels and gravity data grid spacings, as discussed next.

3.4.4 Ensemble of Noise and Sampling values

Following the method outlined in Section 3.3.2, an ensemble of 100 inversions with varying levels of noise and gravity observation spacings was conducted. The noise and gravity spacing changes were applied to the original observed data, and the forward calculation of the starting model, initial misfit calculation, and regional field removal were all repeated. Each model was then inverted with a cross-validation, and the resulting RMS differences with the true bathymetry are shown in Figure 3.23.

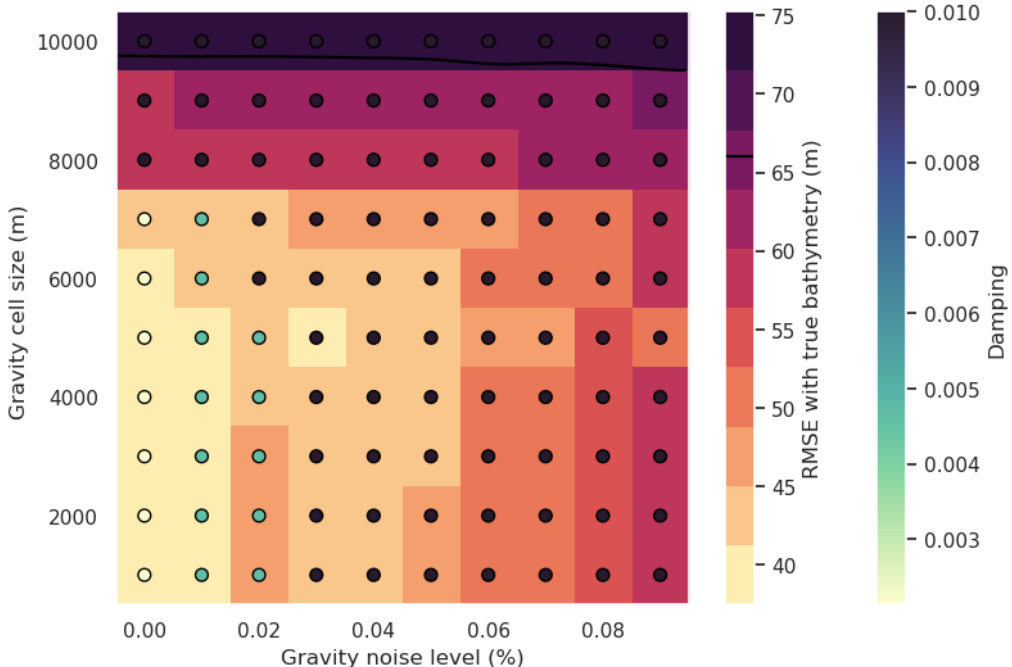


Figure 3.23: Ensemble of noise levels and gravity spacing for the simple synthetic model with a regional field. Grid cell colour indicates each inversion’s RMSE with the true bathymetry. The circles’ colour indicates the optimal damping value found for each inversion’s cross-validation. Black line shows the 66 m contour, representing the RMS difference between the true and starting bathymetry.

3.4.5 Simple model comparison

Table 3.1 compares the performance of each of the above inversions. The four inversions without a regional component of the gravity data (annulus approximation, prism approximation, with noise, and resampled), all recovered the bathymetry with an RMSE of ~ 10 m. With the regional component, the lowest RMS was raised to 37 m. The constraint point minimization method of regional separation produced significantly more accurate bathymetry models than the other methods. With these optimal methods and baseline performance standards, a new synthetic model is introduced which was created to emulate the expected bathymetry features and gravity anomalies associated with a sub-ice-shelf environment.

	RMS (m)	RMS at constraints (m)	Total time (hr:min:sec)	# iterations	Final residual RMS (mGal)
No regional component					
Starting bathymetry annulus	66 8	0.04 1	— 00:00:30	— 37	2.7 0.022
finite differences	9	1	00:02:49	37	0.022
2% noise	12	< 1	00:00:13	18	0.16
6 km re-grid	11	1	00:00:29	38	0.019
With regional component					
Starting bathymetry filter trend equivalent sources constraint point minimization	66 48 54 53 37	0.04 — — — 2	— — — — 00:01:06	— — — — 39	7.4 — — — 0.022
2% noise 4 km re-grid	45 38	2 2	00:00:12 00:00:51	13 38	0.23 0.022

Table 3.1: Summary of the simple synthetic model inversion results.

3.5 Ross Sea model

Here a semi-realistic model is introduced. In the past section, two synthetic topographies (bathymetry and a crustal layer) were used in forward modelling to create synthetic gravity data. Here, real topographic data are used to create the synthetic gravity. This model is termed semi-realistic since the gravity is synthetically calculated, but it results from geologically real surfaces. This model uses data from Antarctica’s Ross Sea (Figure 3.1, north of Ross Ice Shelf). The bathymetry data are from the IBCSO v2 data compilation (Dorschel et al., 2022), resampled at a 5 km resolution (Figure 3.24a). This data are mostly from shipborne multi-beam echo sounding. To create the regional component of gravity, basement depths from the ANTOSTRAT compilation of shipborne seismic data have been used (Brancolini et al., 1995), at a 5 km resolution (Figure 3.24b). The inversion domain is 320×420 km and a buffer zone of 40 km was included in all directions, resulting in 8000 grid cells per surface.

3.5.1 Observed gravity

The bathymetric and crustal surfaces were discretized with the reference discretization method (Figure 3.2e) with the mean elevation of each surface as its reference level. A density contrast of $\Delta\rho = 1276 \text{ kg m}^{-3}$ (contrast between seawater (1024 kg m^{-3}) and sediment (2300 kg m^{-3})), was used, with $+\Delta\rho$ for prisms above the reference, and $-\Delta\rho$ for prisms below the reference. For the basement, a density contrast of $\Delta\rho = 200 \text{ kg m}^{-3}$ was used, representing the contrast between sediment (2300 kg m^{-3}) and low-density basement rock (2500 kg m^{-3}). This contrast was set so that the resulting forward gravity of the basement was slightly greater in magnitude than that of the bathymetry. The forward gravity of each layer was calculated at a regular grid of observation points with a 5 km spacing, at a constant elevation of 1 km (Figure 3.24c-d). This created the full-resolution synthetic observed gravity dataset. To represent an airborne gravity survey, this grid is sampled along synthetic flight lines.

This synthetic survey (Figure 3.25b) consisted of five N-S and 24 E-W flight lines.

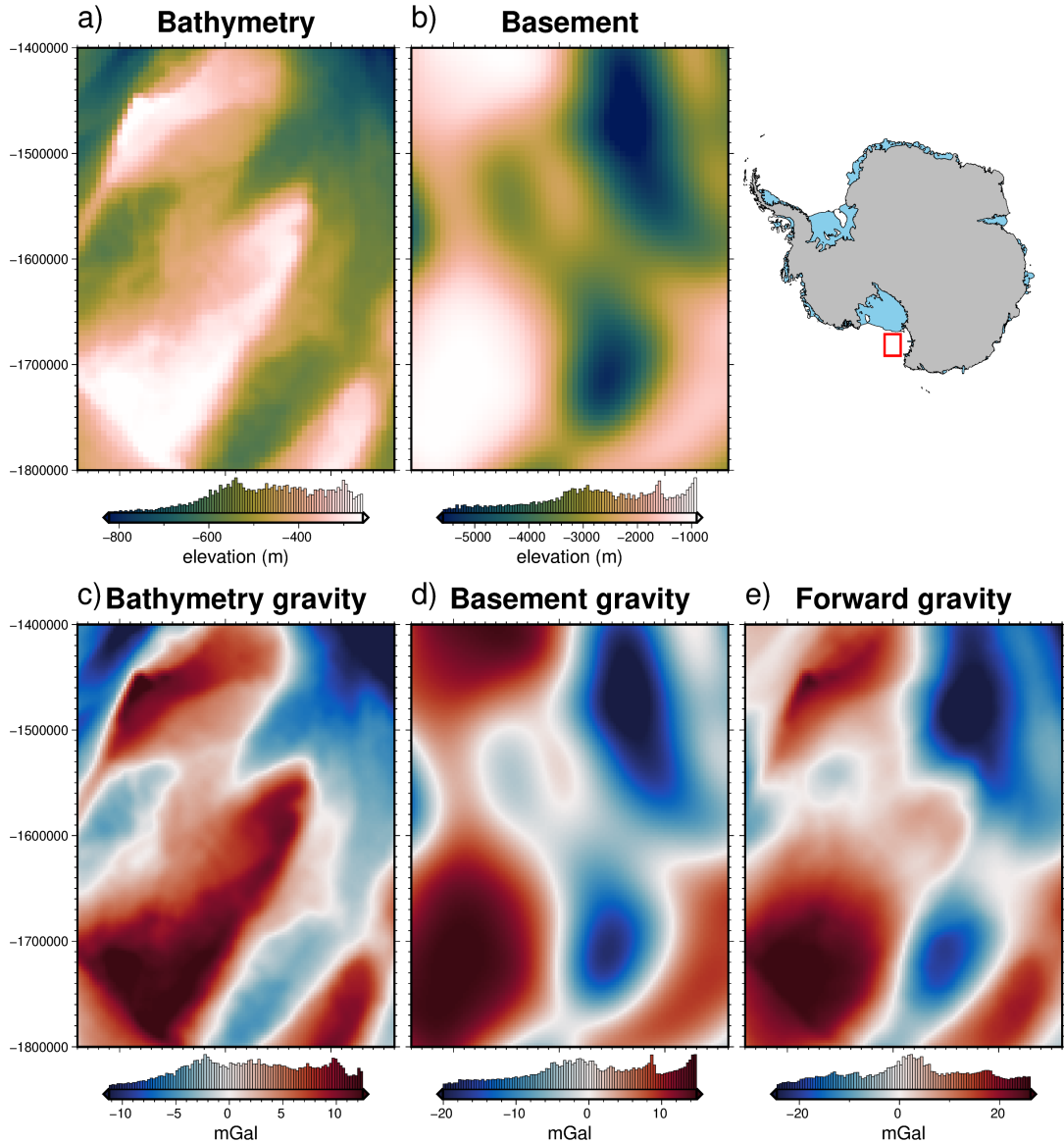


Figure 3.24: Ross Sea semi-synthetic model. **a)** Bathymetry data at 5 km resolution from IBCSO v2 (Dorschel et al., 2022), **b)** basement topography from the ANTOSTRAT project at 5 km resolution (Brancolini et al., 1995), **c)** forward gravity calculated at a regular 5 km grid at 1 km altitude for the bathymetry and **d)** for the basement. **e)** Total forward gravity from the combinations of c and d. Location of Ross Sea inversion domain shown as red box.

Spacing between lines was 50 km for the N-S lines and 15 km for the E-W lines. One N-S line and 3 E-W were omitted to represent missed flights. Along line spacing of data was 5 km. This survey configuration is similar to other Antarctic airborne surveys (Tinto et al., 2019). The full resolution gravity (Figure 3.25a) was sampled at these flight line locations, and the resulting values were fitted with equivalent sources. Gravity observations were then predicted from these sources on an even 5 km grid³ over the whole domain (Figure 3.25c). Lastly, the survey data were contaminated with noise from a Gaussian distribution, with a mean of 0 and a standard deviation of 0.6 mGal (2% of the max absolute value of the full-resolution data). The difference between the true gravity and this noise-contaminated synthetic survey (Figure 3.25b) represents the typical loss of data resulting from a sparse airborne

³The gravity observations were actually interpolated onto a 2.5 km grid to account for the testing data.

survey. The RMS difference is 0.75 mGal. The largest differences are located within the flight line data gaps.

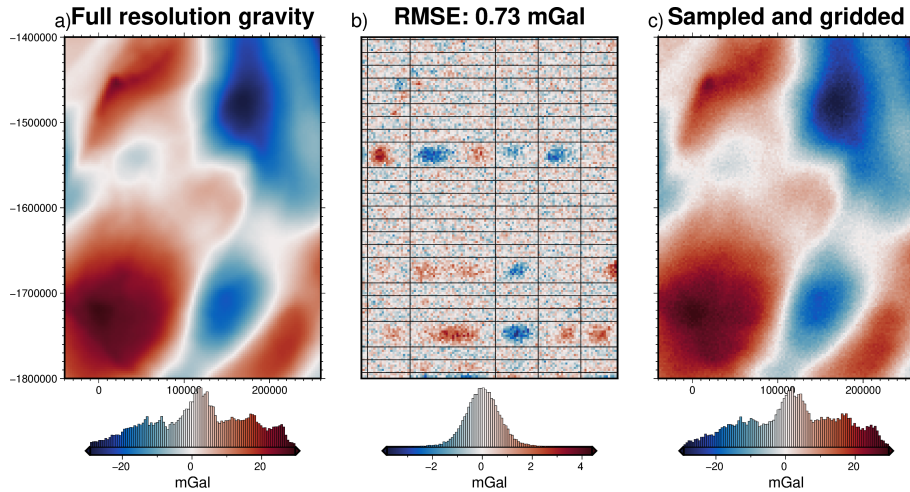


Figure 3.25: Ross Sea synthetic airborne survey. **a)** Full-resolution gravity data from the forward calculation of the bathymetry and basement. **b)** Difference between a and b, with black lines showing the synthetic airborne survey points. **c)** Gravity data from sampling along flight lines and re-gridded with equivalent sources.

3.5.2 Starting bathymetry

The bed elevations around the borders of ice shelves are generally well-constrained. Bathymetry depths from the open ocean portion of the ice shelf border can be found through satellite altimetry or multi-beam sonar surveys. The remainder of the ice shelf border consists of grounded ice. Bed elevations beneath grounded ice can be efficiently imaged or modelled with methods such as airborne radar or mass-conservation modelling (Morlighem et al., 2020). Many Antarctic ice shelves also contain sparse direct measurements of bathymetry from seismic surveying. This resulting configuration for many ice shelves is generalized by a very well-constrained border with sparse constraints located within. Here, this configuration is mimicked for a hypothetical ice shelf in the Ross Sea.

Within the model domain, a polygon is created to represent the ice shelf border (Figure 3.26). Outside this border, constraint points are placed in each grid cell of the model ($N = 3503$, small black dots in Figure 3.26). Within the border, constraints are placed on a semi-regular grid. To represent a spatial constraint density similar to other Antarctic ice shelves⁴, 1 constraint per 2500 km^2 is used. This equates to 39 constraints. In the previous models, the true bathymetry was sampled at the constraints and the resulting values were gridded for the entire domain. Here, to represent measurement uncertainties for attaining the constraint point depths, after each point is sampled, Gaussian noise is added to the values before gridding.

Points outside of the ice shelf are contaminated with noise from a Gaussian distribution with a standard deviation of 5 m. This represents the well-constrained methods associated with bed observations on either grounded ice or in the open

⁴The Ross Ice Shelf has ~ 1 constraint per 2200 km^2

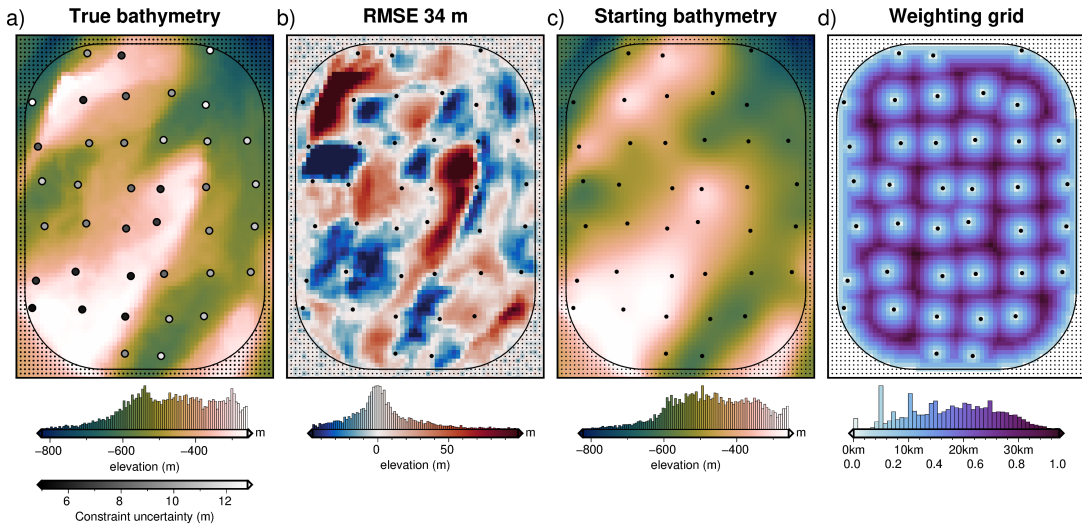


Figure 3.26: Gridding of the Ross Sea starting bathymetry. **a)** True bathymetry at 5 km resolution from the IBCSO v2 compilation (Dorschel et al., 2022). Constraint points (coloured dots), show the uncertainty values of each point. These uncertainties were used as the standard deviations of the Gaussian function for contaminating the sampled data with noise before regridding. **b)** Difference between a and b, **c)** starting bathymetry from the sampling and gridding of the constraint points with added noise. **d)** Weighting grid used in the inversion. Grid colours show both the distance between each grid cell and the nearest constraint point and the weight values (0 - 1) from the normalization of these distances. Small black dots and large black dots indicate constraints outside and inside of the ice shelf border, respectively. Semi-rounded black line shows the outline of the synthetic ice shelf.

ocean. Points within the shelf are contaminated with noise based on their depth. The Gaussian distribution used has a standard deviation of 2% of each point's depth. This simulates increasing measurement uncertainty with depth. Brisbourne et al. (2020) provide depth uncertainties for seismically imaged bathymetry beneath the Larsen C ice shelf, which have an average uncertainty as the percentage of depth from the surface of $\sim 2\%$. For our points, this equates to an RMS noise value of ~ 10 m for the ice shelf constraints. The uncertainty (the standard deviation of the Gaussian function used, not the actual value of the noise) of each point is shown in Figure 3.26a. This noise-contaminated sparse data is then gridded with a cross-validated bi-harmonic spline yielding the starting bathymetry. This interpolator takes the uncertainties of each point into account so that highly uncertain points don't introduce a bias into the interpolation (Uieda, 2018). The difference between the true and starting bathymetries had an RMS of 34 m over the whole grid, and an RMS at the constraint points of 10 m.

3.5.3 Gravity misfit

The starting bathymetry was discretized and forward modelled at the observation points with a density contrast of 1276 kg m^{-3} . This forward gravity was then subtracted from the observed gravity to get the gravity misfit (Figure 3.27a). Using the constraint point minimization method, the regional field was estimated with a bi-harmonic spline interpolator (Figure 3.27b), which was subsequently removed, leaving the residual misfit (Figure 3.27c). As in the above section, the interpolator takes the uncertainty of each constraint point into account to avoid overfitting the regional field to highly-uncertain constraint points.

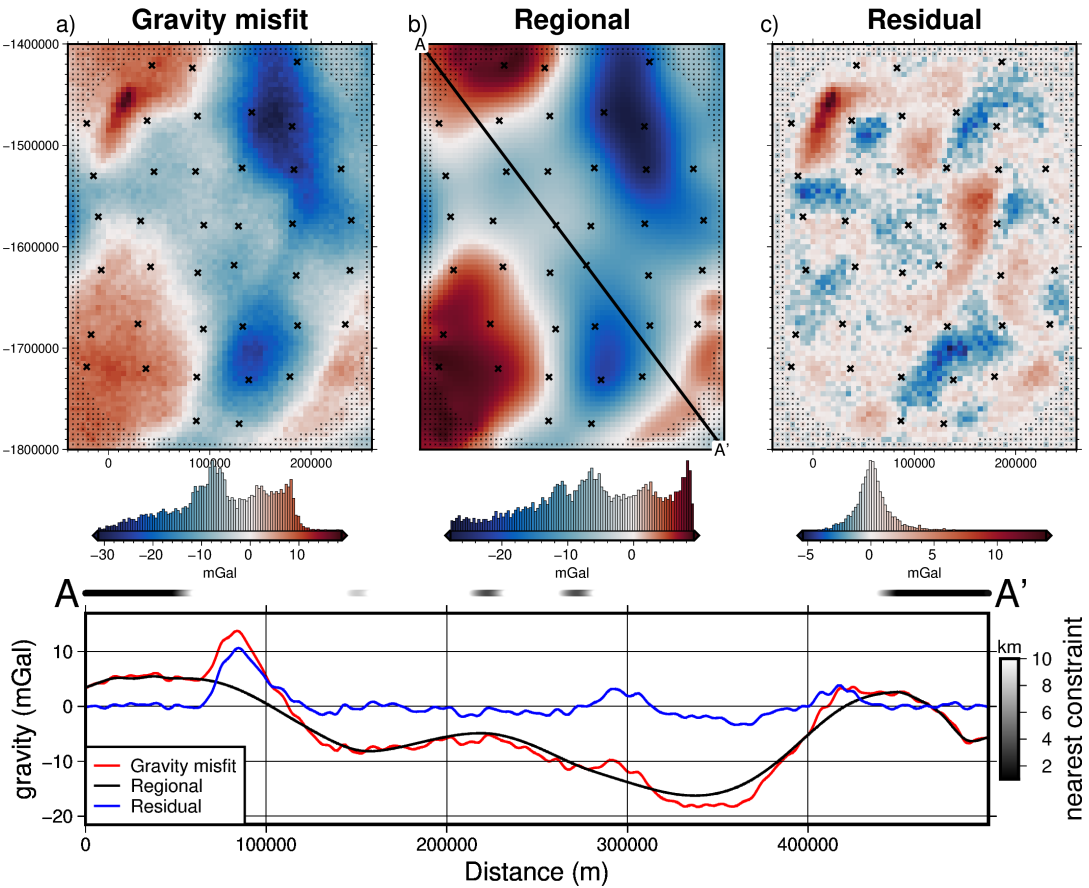


Figure 3.27: Ross Sea synthetic gravity anomalies. **a)** total gravity misfit, **b)** the estimated regional component using the constraint point minimization method, and **c)**, the residual misfit, as the difference between the total misfit and the regional component. Black crosses, large and small, show constraints inside and outside the ice shelf, respectively. **Lower panel** shows profile A to A' of gravity misfit and the regional and residual components. Distance to the nearest constraint at each point along the profile shown in black to white colours at top of profile.

3.5.4 Inversion

This residual misfit was then used in a cross-validation of 16 damping parameter values (Figure 3.28a). The inversion with the lowest cross-validation score was then chosen as the best model. During the inversions, a weighting grid was used to constrain the bathymetry at the points of known depths (Section 3.2.5.3). This grid (Figure 3.26d) is a normalized (0-1) grid of the minimum distance between each grid cell and the nearest constraint point. The inversion result and the difference from the true bathymetry are shown in Figure 3.29. The inversion had an RMS difference with the true Ross Sea bathymetry of 21 m and an RMS at the constraints of < 1 m. The inversion converged in 12 seconds at 15 iterations and had a final residual misfit of 0.43 mGal (Figure 3.28b).

3.5.5 Uncertainty analysis

Since the true Ross Sea bathymetry for this inversion is known, a direct measurement of the spatial uncertainty of the resulting bathymetry is simple to calculate (Figure 3.29b). This spatial uncertainty is useful to provide alongside the bathymetry results. It informs ocean modellers where results can be confidently interpreted and

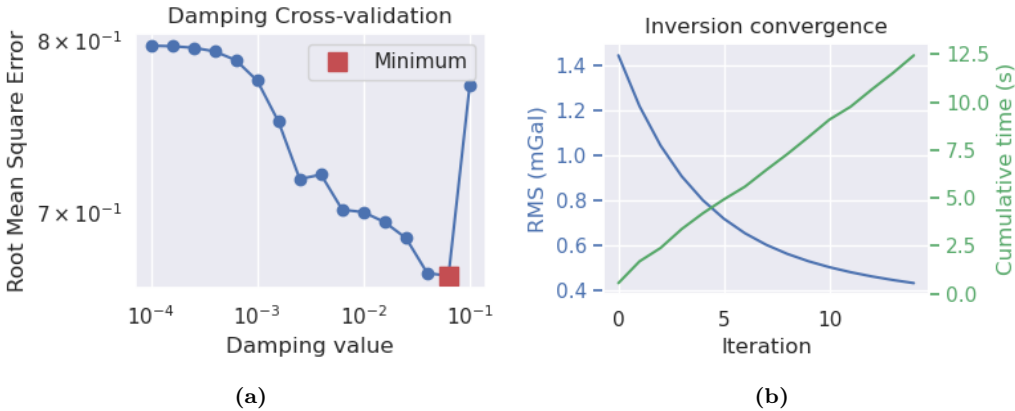


Figure 3.28: a) Cross-validation curve showing the optimal damping parameter (red square). b) Convergence of the inversion misfit. Blue line (left y-axis) shows the RMS of the residual misfit at each iteration of the inversion. Green line (right y-axis) shows the cumulative time to complete the inversion.

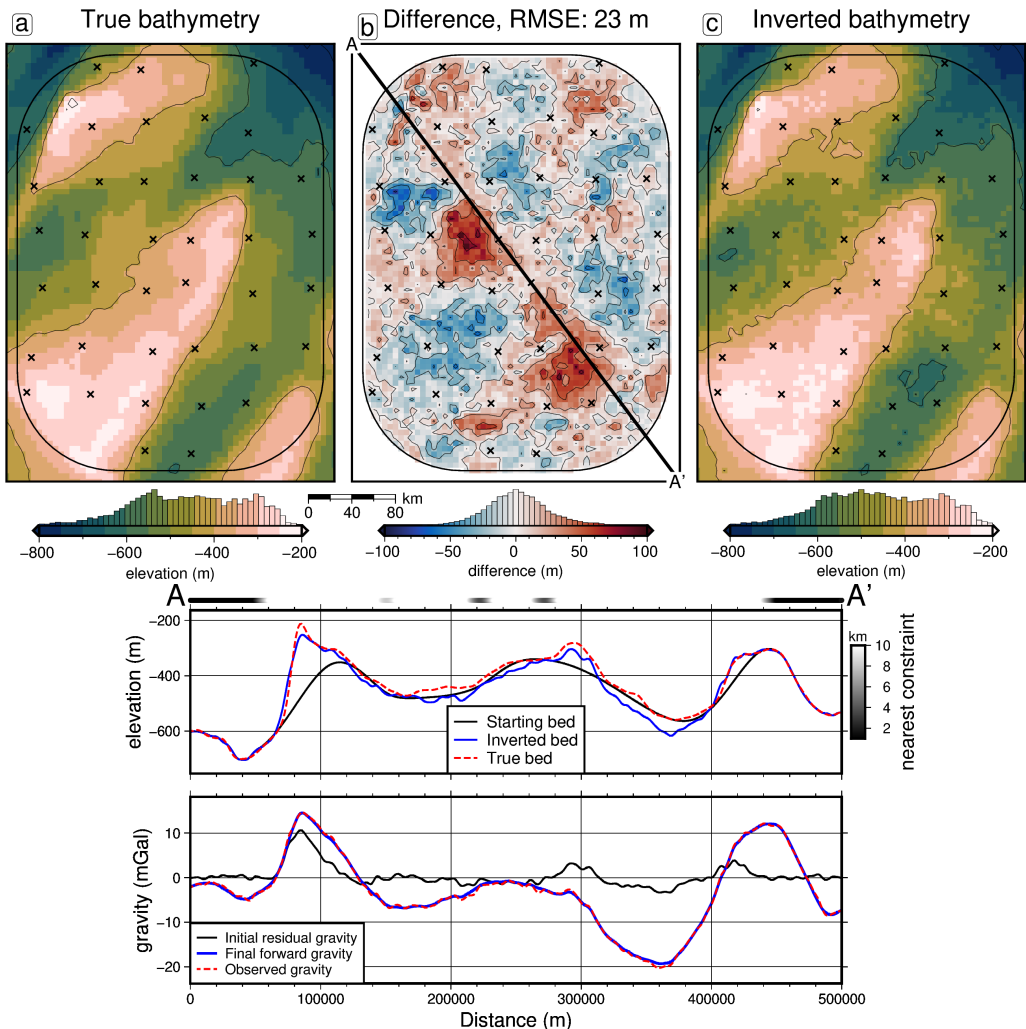


Figure 3.29: Ross Sea synthetic model inversion results. a) True bathymetry, b) difference between a and c, and c) final inverted bathymetry. Black crosses are constraint points. The RMS difference with the true bathymetry at these constraints is < 1 m. Lower panel) Profile from A to A'. The top panel contains topographic profiles of the starting, inverted, and true bathymetries. The bottom panel contains gravity anomaly profiles. Distance to the nearest constraint at each point along the profile shown in black to white colours at top of profile.

highlights regions to focus future data collection. Here, a method of uncertainty analysis for this inversion is proposed, and the resulting uncertainty is compared to the inversion error to get a sense of the accuracy of our calculation of uncertainty. This uncertainty analysis is accomplished with Monte Carlo simulations (Helton et al., 2006; Jansen et al., 1994).

Here, 20 inversions are run with the same damping parameter cross-validation as conducted previously. For each inversion, the input parameters are sampled from distributions of their possible values. These prior distributions represent all plausible parameter values and thus the resulting inverted bathymetries should cover the range of plausible inversion outcomes. For each grid cell, the weighted standard deviation of the 20 inverted bathymetry values of that grid cell was calculated. The weighting came from the inverse square of each inversion's RMS difference between the inverted grid values and the constraint point depths. This reduces the bias from inversions with large misfits to the actual constraint points (Schnaadt & Heinson, 2015). Chapter 4 Section 4.2.4 contains a detailed description of this uncertainty analysis methodology.

The parameters included in the Monte Carlo sampling are:

1. the observed gravity data, sampled from a normal distribution with a mean equal to the observed values and a standard deviation of 0.6 mGal (2% of the maximum absolute value).
2. the constraint point depths, sampled from a uniform distribution with a centre as the measured point depth and bounds of ± 5 m for the points outside the ice shelf, and $\pm 2\%$ depth for points within the shelf.
3. the bathymetry density contrast. This is defined as the difference between the densities of water and sediment. The mean value was taken to be 1276 kg m^{-3} ($2300 - 1024 \text{ kg m}^{-3}$). A standard deviation of 400 kg m^{-3} was used.

Four suites of Monte Carlo simulations were run and are shown in 3.30. Each of the above parameters: gravity, constraints, and densities, were included in their own Monte Carlo simulations, and the fourth simulation included all parameters together. Simulations that included the sampling of the constraint depths required the re-calculation of the starting bathymetry, the starting forward gravity, gravity misfit, regional separation, and finally running the inversion. Simulations that included sampling the density values required recalculating the forward gravity, misfit, regional separation, and running the inversion. Simulations that included the sampling of gravity values only required recalculating the regional field and running the inversion. These values were sampled from their respective distributions using Latin hypercube sampling (Jansen et al., 1994). This allows an adequate coverage of the parameter space with only 20 inversions. See Chapter 4 Section 4.2.4 for further details.

3.5.6 Effects of constraint spacing

Here we test the effects of the number and spacing of constraint points on the accuracy of the inversion. The constraints outside the ice shelf are kept as they have been in the previous section, at the same grid spacing as the bathymetry (5 km).

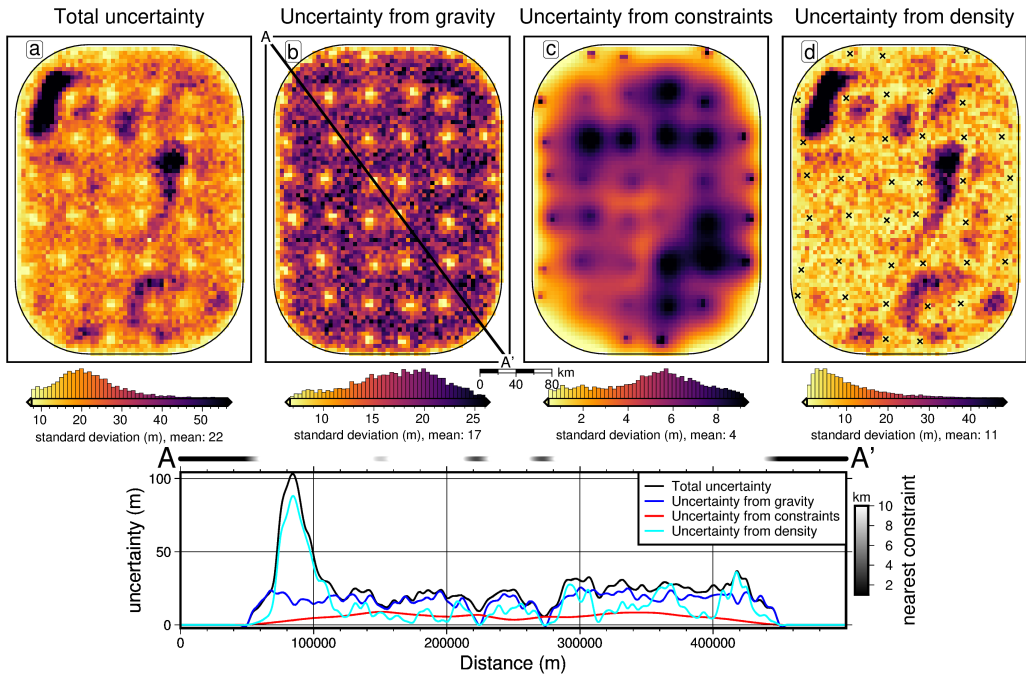


Figure 3.30: Monte Carlo simulation results for the Ross Sea synthetic inversion. Cell-wise weighted standard deviations of all inversions in each simulation. **a)** Total uncertainty from the sampling of gravity data, constraint depths, and density contrast value. **b)** Sampling of only the gravity data values. **c)** Sampling of only the constraint point depths. **d)** Sampling of only the density contrast. To aid in interpretation, locations outside of the ice shelf have been masked. Constraints within the ice shelf are shown as black crosses in **d**. **Lower panel**) Profile from A to A' of the total uncertainty and individual components. Distance to the nearest constraint at each point along the profile shown in black to white colours at top of profile.

Constraints within the ice shelf are re-created on a regular grid, where the spacing of the grid, and thus the number of constraints, is varied from 10 km (959 constraints) to 100 km (9 constraints). The depth of the true bathymetry is sampled at each constraint. As in the previous section, points outside the shelf are contaminated with Gaussian noise with a standard deviation of 5 m. Noise for constraints within the ice shelf is relative to each point's depth (to simulate seismic survey uncertainties). These noise-contaminated constraint point depths are used in a bi-harmonic spline gridding to create the starting bed for each of the 10 constraint sets. The RMS difference between each of the starting beds and the true bed is shown as green dots in Figure 3.31a. From these starting beds the inversion workflow was conducted, as below:

1. The forward gravity of the starting beds were calculated.
2. The misfits with the observed gravity (Figure 3.25a) were calculated⁵.
3. The regional component of the misfit was estimated and removed with the constraint point minimization method.
4. The residual misfit was inverted with the cross-validation routine.
5. The difference between each inverted bed and the true bed was found.

⁵To isolate the effects of changing the constraint density, the full resolution observed gravity with no added noise was used here, instead of the synthetic survey gravity.

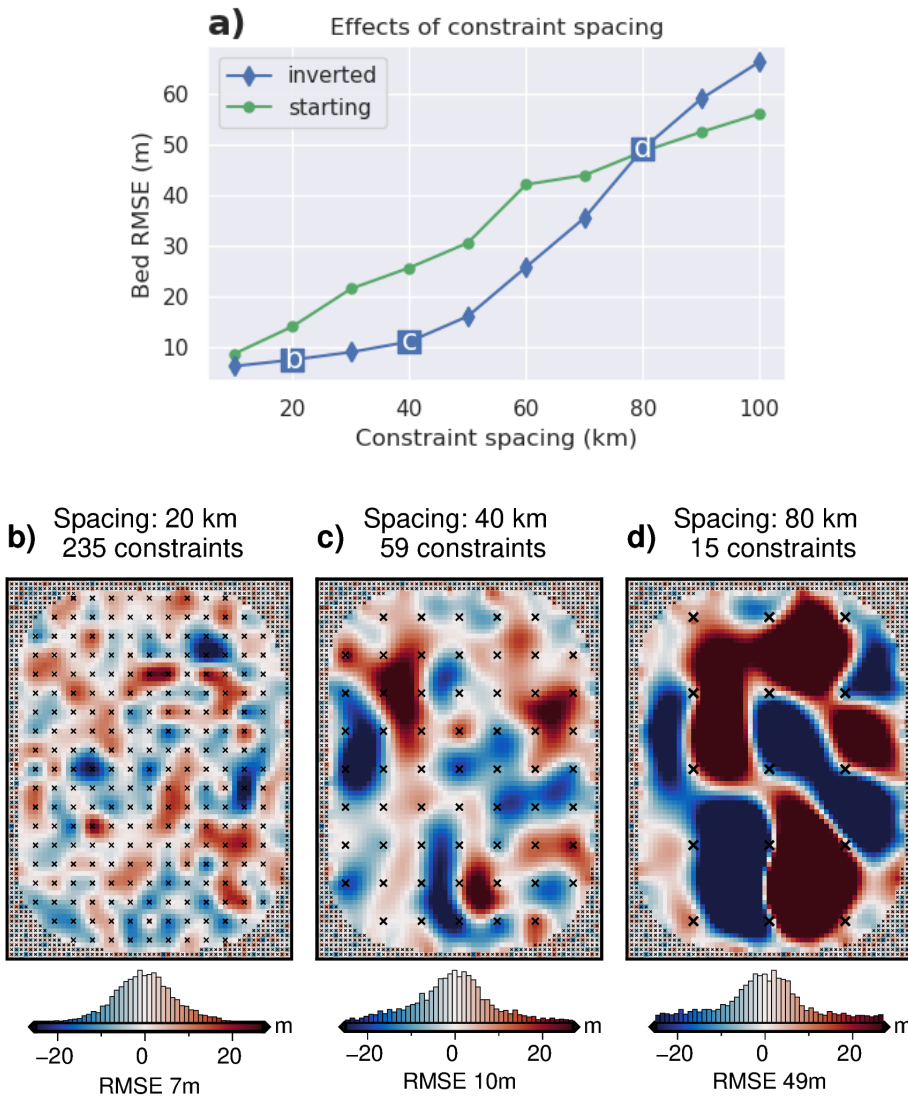


Figure 3.31: Effects of constraint spacing on inversion accuracy. **a)** Bathymetry error (RMSE) relative to the true bathymetry for 10 different constraint spacing. Green (circles) shows the starting error and blue (diamonds) shows the error after inversion. Labels b, c, and d refer to the three inversion error results shown as subplots. **b-d)** Inversion error grids for three of the ten configurations of constraints (labelled on a)). Note b-d use the same colour map. Small black crosses show constraints outside the ice shelf, and larger black crosses show inside constraints with the corresponding constraint spacing.

Figure 3.31 shows the results of this analysis. Subplot a) shows the relationship between constraints spacing and the RMSE with the true bed of the starting bed (green circles) and the final inverted bed (blue diamonds). Three of the inverted bed errors are shown in subplots b-d. See Appendix B.2 for plots of the regional separation errors for these three inversions.

3.5.7 Effects of gravity data

As the above section analyzed the impact of the number of constraint points on the inversion’s accuracy, here we investigate the impact of the quality and quantity of input gravity data. Following the methods of the two ensembles presented in the simple synthetic inversion (Figure 3.3.2 & 3.23), an ensemble of 100 inversions

with varying levels of noise and gravity observation spacing's are conducted with this Ross Sea model. The observed gravity data were contaminated with noise as described in the past sections, with 10 levels between 0 and 9% of the maximum absolute value. To simulate a more sparse gravity survey, the previous two ensembles sampled the full-resolution gravity data onto a coarser evenly spaced grid and then re-gridded the sparse data with equivalent sources back to the full resolution of the bathymetry. Here instead of evenly spaced grids, we use airborne flight lines.

We use a constant along-line observation spacing of 5 km but vary the spacing between flight lines. The N-S and E-W lines both use the same between-line spacing. The full-resolution gravity is then sampled at these points, and the sparse data is re-gridded to the full resolution (5 km) with equivalent sources. The noise and line spacing changes were applied to the original observed data, and the forward calculation of the starting model, initial misfit calculation, and regional field removal were all repeated. Each model was then inverted with a cross-validation, and the resulting RMS differences with the true bathymetry are shown in Figure 3.32.

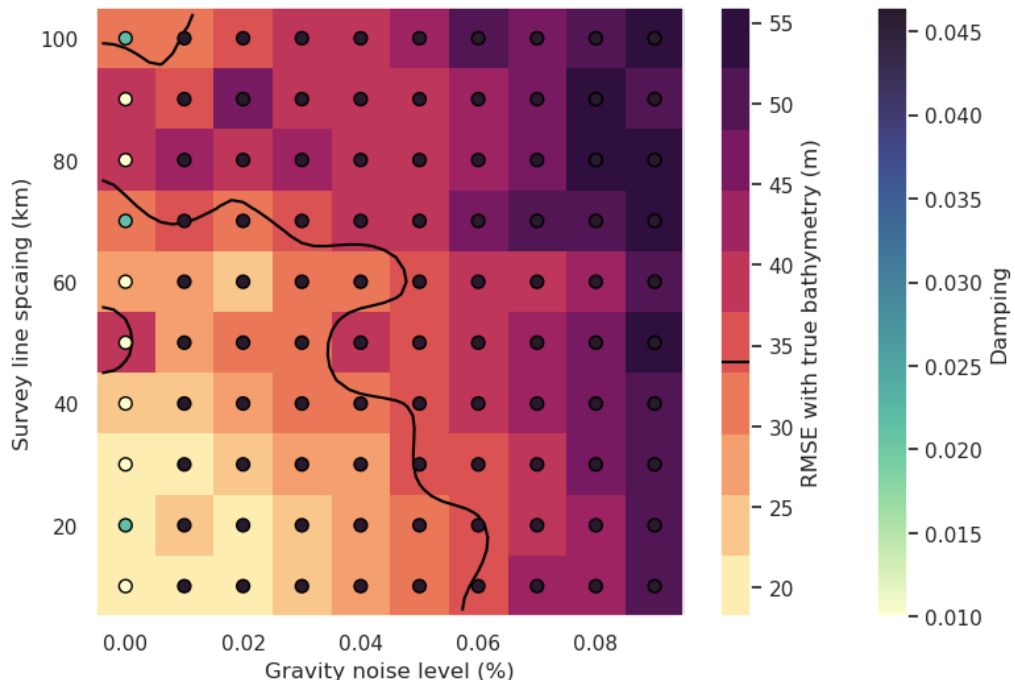


Figure 3.32: Ensemble of noise levels and airborne gravity line spacing for the Ross Sea synthetic model. Grid cell colour indicates each inversion's RMSE with the true bathymetry. Circles' colour indicates the optimal damping value found for each inversion's cross-validation. Black line shows the 34 m contour which represents the RMS difference between the true and starting bathymetry (Figure 3.26b).

3.6 Discussion

3.6.1 Simple synthetic model

The simple synthetic model of Section 3.3.1 was introduced to 1) present the basic workflow of the inversion, 2) determine the best options for various components of the inversion and 3) demonstrate the capabilities and limitations of the inversion.

The starting bathymetry had an RMS difference with the true bathymetry of 66 m (Figure 3.6). This error demonstrates the limitations of gridding sparse data. Even with a very high spatial constraint density (1 constraint per 160 km²) compared to most ice shelves (Fretwell et al., 2013), simply gridding the constraints greatly misinterpreted the true bathymetry. To reduce this bathymetric error, we presented three inversions, a noise-free full-resolution inversion, a noise-contaminated full-resolution inversion, and a noise-free lower-resolution inversion.

3.6.1.1 Inversion results

All of these inversions (without a regional component) were able to reduce this RMS difference with the true bathymetry to ~ 10 m and recover all bathymetric features of interest. We demonstrated that the two methods of calculating the vertical derivative of gravity produced similar results, but the annulus approximation was significantly faster ($\sim 5\times$). Additionally, for each of these inversions, the weighting grid, based on the distance to the nearest constraints (Figure 3.5), successfully constrained the resulting inverted bathymetry at the points of prior bathymetry observations. Each inversion's constraint point RMS difference with the true bathymetry was $<\sim 2$ m, and the technique avoided any pedestal effect around the constraints in the resulting bathymetries. Interestingly, the inversion with low-resolution (6 km) gravity data yielded a very similar RMSE compared to the inversion with the full-resolution (1 km) data. This demonstrates that for recovering bathymetric features of wavelengths similar to those found in our synthetic model, high-resolution gravity surveys may not be necessary to achieve adequate results from an inversion.

3.6.1.2 Ensemble results

To test this theory further, we conducted an ensemble of 100 inversions with 10 levels of noise contamination and 10 gravity survey resolutions. The resulting RMS difference of each inversion with the true bathymetry is shown in Figure 3.17. All inversions in this ensemble, including the worst-case scenario of 9% noise and a gravity observation grid of $10\times$ the bathymetry spacing, still resulted in an RMS difference lower than that of the starting bathymetry (66 m). It is worth noting that this metric for the accuracy of the inversion, the root mean squared (RMS) difference with the true bathymetry, is used to give extra weighting to the outlier errors, as opposed to using a mean average error (MAE). These outliers typically include the features of interest in a bathymetry inversion. Figure 3.33a shows these ensemble results grouped by cell size. For each cell size value (colour of lines), the inverted bed RMSE for the range of noise levels is shown. This shows a roughly linear relationship between noise and RMSE, regardless of cell size. This means there is a continuous improvement in the inversion's accuracy with lower levels of noise. Conversely, figure 3.33b shows these ensemble results grouped by the noise level. For each noise level (colour of lines), the inverted bed RMSE for the range of cell sizes is shown. This shows an exponential relationship between gravity survey resolution and RMSE. This exponential relationship is strongest for low noise levels. This means inversion accuracy greatly benefits from increasing the survey resolution (decreasing the cell size), but this benefit diminishes once the survey resolution is at a certain point. Here, surveys at or below ~ 6 km resolutions result in a diminishing improvement in RMSE. The linear relationship between noise and RMSE, and the exponential relationship between resolution and RMSE can also be seen by the

spacing of lines in either figure. The close spacing of the low-cell-size lines (purples) in Figure 3.33a show the diminishing improvements at small cell size surveys, while the continuous spacing of lines in Figure 3.33b shows the linear relationship.

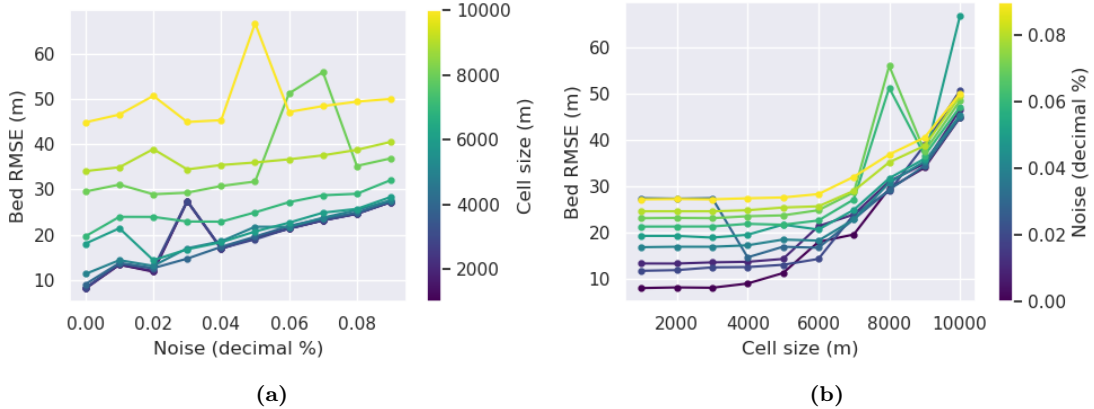


Figure 3.33: Ensemble results for the simple synthetic inversion, grouped by **a)** gravity survey cell size, and by **b)** noise level. Each line in a) corresponds to a row of Figure 3.17 and each line in b) corresponds to a column.

In a typical gravity survey, there is often a trade-off between the number of observations made and the quality (noise) of the data. This is due to the time restrictions of both the total data collection period (i.e. the length of a field season in Antarctica), and the necessity to repeat base-station measurements to account for instrument drift. Collecting more data in the same time period inevitably results in increased noise. At a certain point, this increased noise will have a greater negative effect on the inversion results, than will be counteracted by the increased amount of data. These are important considerations for survey design. Figure 3.33b shows that for a given noise level, there is little benefit in increasing the gravity survey resolution from ~ 6 km to 1 km. For this survey domain (60×80 km), a 6 km resolution results in ~ 130 gravity station, while with a 1 km resolution, this increases to 4800 observation points. Simplistically speaking, if keeping total survey time constant, this means at 6 km spacing as opposed to 1 km spacing, either $\sim 36\times$ more area could be surveyed, or higher quality data could be collected, with shorter base station loops, more repeated ties, and more careful measurements.

The results from the noise-contaminated inversion (Figure 3.12 & 3.9b) show that this gravity noise is directly reflected in the inversion results. For this reason, data, either the observed data or the residual misfit, is typically low-pass filtered prior to inversion (i.e. Boghosian et al., 2015; Yang et al., 2020a). This is typically done with either a time-based filter for airborne surveys, or a spatial filter (Jordan et al., 2010). With this filtering, there is a trade-off between removing the noise and removing the true signal. Due to this, we have chosen to omit the filtering in these synthetic examples.

3.6.2 Simple model with a regional component

3.6.2.1 Regional separation methods

The addition of a regional component to the observed gravity data adds a major complexity to the inversion workflow. The actual inversion remains the same, but this regional component must be estimated and removed beforehand. We tested four methods of regional estimation; 1) a low-pass filter, 2) fitting a polynomial trend to the data, 3) predicting the data with a set of deep point sources, and 4) attributing the entire misfit value to the regional field at constraint points and interpolating between these values. Figure 3.19 compares the inversion results of each of these methods. While each method recovered the short wavelength bathymetry features, the misestimation of the true regional field for each method introduced long-wavelength errors in the inversion results. We show that the constrain point minimization method most accurately estimated the region, and thus produced the best inversion results. For the simple regional field used here, the filter and trend methods achieved reasonable results, but the effectiveness of these methods is expected to be reduced with more complex regional fields associated with real data.

While the constraint point minimization worked best for this model, each of these methods may work better in specific scenarios. All the methods except the equivalent source method require the gravity data to be gridded over the entire region of interest. For sparse gravity surveys the interpolation required may introduce large errors. For this scenario, the equivalent source technique is likely the most appropriate. In scenarios with few bathymetry constraints and where the regional field is expected to be simple, the trend and low-pass filter methods are efficient and can be effective. However, if there are distributed bathymetry constraints, such as in this synthetic scenario, constraint point minimization is likely the best choice. This technique will only effectively remove regional anomalies with a wavelength equal to or greater than the average constraint spacing. If the constraints are sparse relative to the expected regional anomaly wavelengths, this method will underestimate the regional component. Lastly, if the bathymetry contains long-wavelength features which would result in long-wavelength anomalies, the trend, filter, and equivalent source techniques may include these in the regional removal. Therefore, the inverted bathymetry, while recovering the super-imposed short-wavelength bathymetry features, will underestimate the long-wavelength features. It is for these reasons that regional separation is perhaps the most important aspect of a bathymetry inversion.

3.6.2.2 Constraint point minimization

This constraint point minimization technique requires the gridding of sparse measurements of the regional field. We explored the impact of this gridding process on the resulting inversion. Figure 3.20 shows the results of four different gridding processes. Minimum curvature gridding without tension (tension of 0, Figure 3.20a) produces a smoothly varying surface at the constraints but introduces artificial minima and maximum at points far from any constraints. This erroneous effect is minimized with a higher tension factor. Using a tension factor of 1, figure 3.20c shows the limited erroneous minima and maxima, but this added tension results in high gradients in the surface immediately near the constraint points (Figure 3.20g). These high gradients in the resulting residual anomalies create a *ringing* effect in

the inverted bathymetry (Figure 3.20k). For these reasons, an intermediate tension factor of 0.25 is suggested for potential field data. While this limits the negative effects of both low and high tension, there are still false minima and maxima (Figure 3.20b), and high gradients at the constraints (Figure 3.20f). The last gridding technique uses bi-harmonic splines. The optimal damping parameter associated with this technique is chosen from a cross-validation of the constraint points. This technique, while being more computationally expensive, solves both issues of tensioned minimum curvature.

3.6.2.3 Inversion results

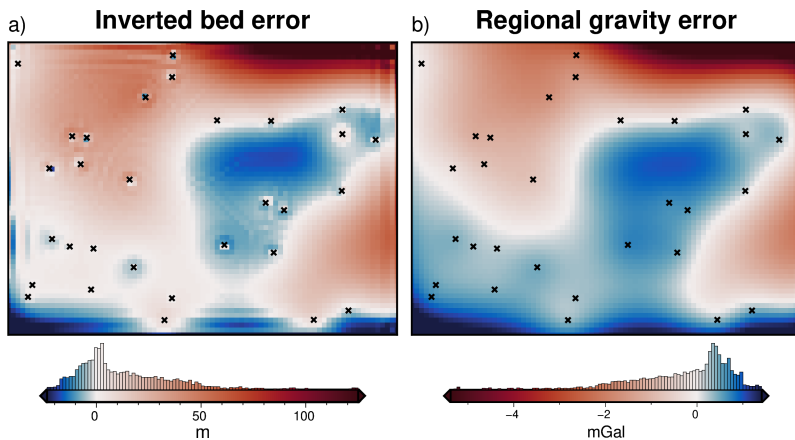


Figure 3.34: Source of inverted bathymetry error for the simple synthetic model with a regional field. **a)** Inverted bathymetry error from Figure 3.22b. **b)** Error in the estimation of the regional component of gravity from comparison with the true regional component (Figure 3.18b). Black crosses show constraint points. Colourmaps are inverted to highlight the similarities and the median has been removed from the regional error.

With both the optimal regional separation method and the optimal gridding method determined, we performed a cross-validated inversion with the remaining residual misfit. This inversion was able to recover all the short-wavelength bathymetry features but introduced some long-wavelength errors. Figure 3.34 shows the inverted bathymetry error alongside the error in estimating the regional component of gravity. Comparing these shows that almost all of the inverted bathymetry error is tied to the inaccuracies of determining the regional component. the remaining error is all minor short-wavelength features, mostly around constraint points. They appear to result from the weighting grid implementation of regularization. Since the errors in the regional estimation are the dominant source of error in most inversions, as shown above, and by other Antarctic bathymetry inversions (Brisbourne et al., 2014), we have shown these details of the gridding process are a vital and often overlooked step in many studies.

3.6.2.4 Ensemble results

As with the simple model, an ensemble of noise and gravity survey spacing experiments were performed with this model containing a regional component. The lowest resulting RMS difference with the true bathymetry was raised from values of ~ 10 m for the inversion without the regional component, to the lowest value of ~ 40 m with the additional regional component. The black line in Figure 3.23 shows the

66 m contour, which represents the RMS difference between the true and starting bathymetries. Inversions that fall outside (above) this line resulted in a worse bathymetry than the starting model. This shows that for this model, inversion is only worth conducting if the gravity survey has a spacing less than ~ 9 km ($\sim 9 \times$ the spacing of the desired bathymetry resolution). Figure 3.35 show these ensemble results grouped by cell size and noise level. There is a linear relationship between gravity noise and the resulting bathymetry RMSE, for all gravity survey spacings. There is an approximately exponential relationship between gravity survey resolution (cell size) and resulting bathymetry RMSE. The degree of this exponential relation decreases with increased noise.

For this model, the *elbow* of the exponential curves in Figure 3.35b is at $\sim 6 - 8$ km survey resolutions ($6-8 \times$ bathymetry resolution). This suggests that for a survey resolution finer than ~ 8 km, there is little benefit in collecting more data. This is supported by the close spacing of low-cell-size lines (purples) in Figure 3.35a. The effort would be better spent collecting data over a wider region, reducing noise in the data, or if possible collecting more bathymetric constraints.

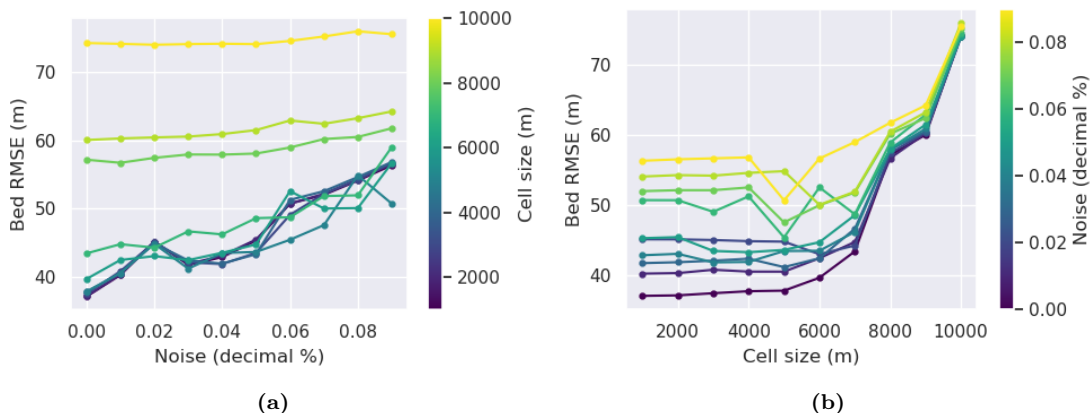


Figure 3.35: Ensemble results for the synthetic inversion with a regional component, grouped by **a)** gravity survey cell size, and by **b)** noise level. Each line in a) corresponds to a row of Figure 3.23 and each line in b) corresponds to a column.

3.6.3 Ross Sea model

The Ross Sea semi-realistic model was created to better emulate the gravity and bathymetries expected for ice shelves. A few extra complexities were added to this model compared to the purely synthetic models. An ice shelf border was included, with a high density of constraints outside of the border, and sparse constraints within. All the constraints had an associated uncertainty, instead of directly sampling the true bathymetry depths. The observed gravity was calculated along the flight paths of a typical airborne survey, instead of along a uniform grid. The main inversion in this section had 2% noise added and had flight lines with 50 km N-S spacing and 15 km E-W spacing. The inversion successfully reduced the starting bathymetry error from an RMSE of 34 m to 23 m. The resulting bathymetry shows a recovery of most of the lost bathymetry features, but some noise from the gravity data has been introduced into the bathymetry. Sharp bathymetry features (upper left corner) and smooth features were both recovered. The constraint points were

relatively evenly distributed (Figure 3.26d), resulting in a relatively even distribution of bathymetry misfits.

Of these errors, the largest were located at the gaps in the synthetic survey where there were missing flight lines (Figure 3.25b). To understand the cause of the remaining errors, we compare the inverted bathymetry error with the regional separation error (Figure 3.36). The strong correlation between these two grids shows that the majority of errors in the inversion are tied to the miscalculation of the regional field, as was seen in the simple synthetic inversion with a regional field. The remaining errors appear to be from the flight line gaps and noise in the gravity data.

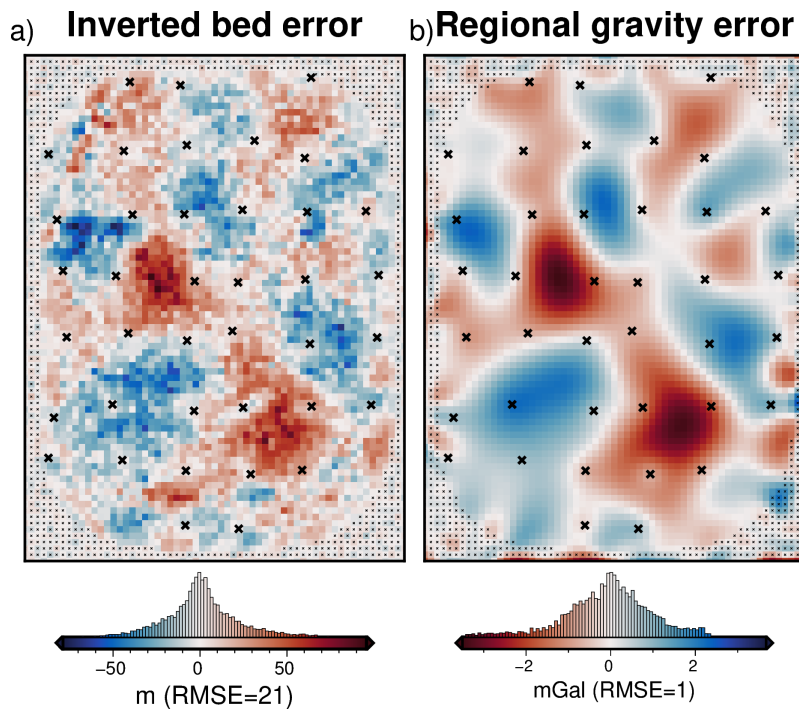


Figure 3.36: Comparison of the inverted bathymetry error and the error in the regional field estimation. **a)** Inverted bathymetry error from Figure 3.29b. **b)** Error in the estimation of the regional component of gravity from comparison with the true regional component (Figure 3.24d). Black crosses show constraint points. Colourmaps are opposed to highlight the similarities and the median has been removed from the regional error.

3.6.3.1 Effects of the gravity data

The ensemble of gravity data noise levels and flight line spacings from Section 3.5.7 shows the relative importance of these two aspects of a gravity survey. As for the previous ensembles, Figure 3.37 shows these results grouped by line spacing and by the noise level. For the Ross Sea model, both factors have a roughly linear relationship with inverted bathymetry error. The slopes for the lines of best fit for Figure 3.37a and b means the inversion RMSE increases by ~ 10 m for either a 4% increase in the noise level or a 60 km increase in the average flight line spacing. The inversions with a small line-spacing (purple lines) of Figure 3.5.7a are closely grouped, relative to the higher line spacings. This shows that at already low line spacings (40 km) there may be little benefit to reducing the line spacing further. Conversely, there is a larger spread for the low noise inversions (purple lines) in Figure 3.5.7b. This

shows that even at low noise levels, further decreases may still provide important improvements to the inversion outcome. As in the previous ensemble results, for a field application, this demonstrates the important tradeoff between quantity and quality of gravity data.

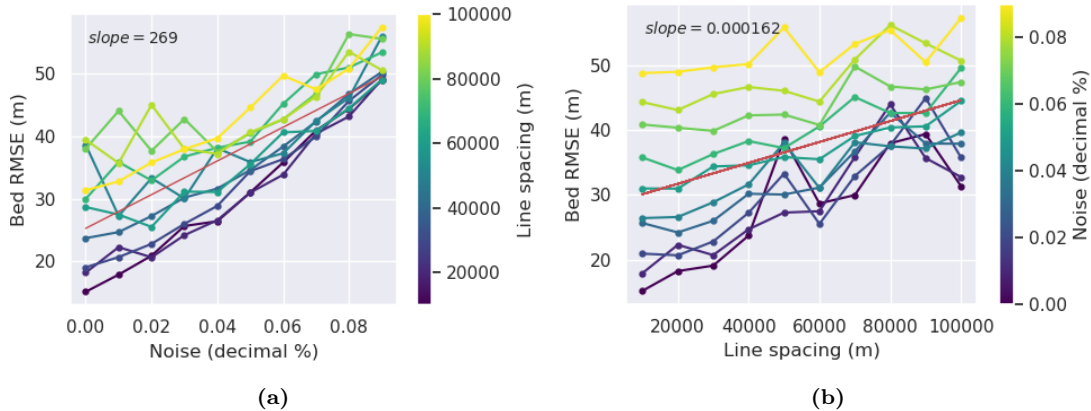


Figure 3.37: Ensemble results for the Ross Sea inversion, grouped by **a)** gravity survey line spacing, and by **b)** noise level. Each line in a corresponds to a row of Figure 3.32 and each line in b corresponds to a column. Red lines show the line of best fit, with their slopes shown in the upper left corners.

These specific relationships between noise, line spacing, and inversion error, while not applicable to all survey configurations, show the importance of choosing an appropriate survey design. This analysis with synthetic data could be included in a pre-survey plan, to explore the effects of differing survey configurations.

3.6.3.2 Effects of the constraints

These synthetic inversions have shown that the removal of the regional field presents the biggest challenge for gravity inversions for bathymetry. The most robust technique for removing the regional field requires a distribution of points of known bathymetry across the inversion region. Since the largest errors in the inverted bathymetries occur at the largest distance to constraints, an even distribution of constraints will best be able to estimate the regional field. Section 3.5.6 explored the effects of varying the numbers of constraints, while keeping the remaining components of the inversion constant. Figure 3.31a shows the bathymetry RMSE with the true bathymetry both before (green) and after (blue) the inversion is conducted.

Figure 3.31a shows for this synthetic model that for average constraint spacing's less than ~ 20 km there is little improvement made by running an inversion. This is due to the starting bathymetry model already being relatively accurate, with the inversion only producing minor adjustments between constraint points. At the other end of the spectrum, with constraint densities greater than ~ 70 km, the inverted bathymetry has an error similar to or higher to the un-inverted bathymetry. This is due to the inaccuracies in calculating the regional field with only very sparse constraints. For these scenarios, the errors introduced by the inversion are greater than the errors of simply interpolating the constraint points. The inverted bathymetry error curve (Figure 3.31a) shows that for this survey, once below a certain constraint spacing (~ 30 km) there is little benefit to having additional constraints.

3.6.3.3 Uncertainties

We have demonstrated that the majority of the inverted bathymetry error is related to the estimation of the regional component of gravity. Without knowing the true regional component, as we do in these synthetic examples, estimating the uncertainty in the interpolation between constraint points of the regional field is difficult. The uncertainty of each grid cell is likely strongly dependant on the distance to the nearest constraint, as well as the depth uncertainties of these nearby constraints. While we show this to be true with our synthetic models, a quantitative method of predicting this uncertainty has yet to be implemented here. The field of conventional bathymetry surveying has developed uncertainty analysis tools that may be applicable to this (Bourgeois et al., 2016).

These tools are able to account for both the depth uncertainty of each measurement, and the distance of each grid cell to the nearest measurement. Future work will benefit from a quantitative assessment of the uncertainty of gridding the regional field from the constraint point values. While the uncertainty of the regional removal accounts for the majority of the uncertainty of the inverted bathymetry, it is technically completed before the inversion and is thus not a component of the inversion uncertainty. To address the uncertainty resulting from the inversion process, we introduced a suite of Monte-Carlo simulations in Section 3.5.5. The results in figure 3.30 show a mean uncertainty for the entire region of 22 m. The majority of this uncertainty is attributed to the uncertainty in the gravity data, as shown by histograms of Figure 3.30. Here we discuss the significance of each component of the uncertainty analysis:

1. **Gravity uncertainty:** The uncertainties in the gravity data result in a relatively uniform bathymetry uncertainty across the region of 17 m. A simple calculation with the Bouguer slab formula with a density contrast of 1276 kg m^{-3} and our assumed gravity uncertainty of 0.612 mGal (%2 max absolute value) gives a value of 11.5 m ($\Delta g_{boug} = 4.18e-5\rho h$). This may show the conventionally used Bouguer slab approximation is underestimating the true uncertainty in inversions resulting from gravity data uncertainty. This uncertainty is lowest at the constraints, due to the use of the weighting grid in the inversion.
2. **Constraint depth uncertainty:** The contribution to the bathymetry uncertainty from the depth uncertainty of the constraint points is small, with a mean of ~ 4 m. This uncertainty resulting from the constraints is also concentrated around the constraint points. This shows improving the constraint point uncertainties will not greatly improve the inversion, and will only improve it in the immediate vicinity of constraints.
3. **Density uncertainty:** The bathymetry uncertainty component resulting from the prism densities is heterogeneous, with some spatially limited, but large values. The mean value is ~ 11 m, but some areas are up to 50 m. These high uncertainties are strongly correlated with the error in the starting bathymetry (Figure 3.26b). This is due to the change in density contrast resulting in a change in the total bathymetry correction calculated in the inversion. In other words, the residual misfit can be minimized by a large surface correction with a low-density contrast or a small surface correction with a large-density contrast.

The combined Monte-Carlo simulation (Figure 3.30a) shows the expected features of an uncertainty map. It has a base level uncertainty similar to the Bouguer slab thickness from the assumed gravity uncertainty, it is generally lowest at the constraints and highest in the large constraint gaps, and it is high where the inversion has produced a large change from the starting model.

3.7 Future work

Running this inversion with the various synthetic models gave us the ability to assess the inversion performance. From this assessment, we have determined several components which would benefit from additional investigation.

1. Implement an additional cross-validation routine to estimate the optimal density contrast, as in Uieda and Barbosa (2017). Here, we have used the same density contrasts for the creation of the observed gravity data and for the inversion itself. In a non-synthetic scenario, this contrast would need to be estimated.
2. Test the effects of flight line orientation relative to the dominant trend of geologic structures.
3. Implement a more robust method of enforcing the constraint points. This may likely be in the form of a bounded least squares solver or some form of manipulation of the Jacobian matrix.
4. Quantify the uncertainty of the regional separation process. This will likely include techniques used in conventional bathymetry surveying (Bourgeois et al., 2016; Calder & Elmore, 2017), or a sequential Gaussian simulation (Perozzi et al., 2021).
5. Testing the effects of pre-filtering the gravity data, either spatially or temporally, to remove the effects of noise (Jordan et al., 2010).

3.8 Conclusion

With the goal of modelling the bathymetry beneath a floating ice shelf, we present a geometric gravity inversion method that 1) adheres to prior bathymetry point measurements, within their uncertainties, 2) produces a smooth and realistic bathymetry, 3) accounts for the regional gravity field and 4) is computationally efficient and fully-open source. To demonstrate the effectiveness, as well as the limitations, we conducted a series of inversions using synthetic and semi-realistic data. These inversions showed the importance of accurately estimating and removing the regional component of gravity prior to the inversion. We showed that for the constraint arrangement for many Antarctic ice shelves, the optimal method for estimating this regional field is with a constraint-point minimization. In addition, we further explored this method by testing various gridding (interpolation) techniques and found a clear increase in performance when using a cross-validated bi-harmonic spline instead of the typically used tensioned minimum curvature.

Here we reiterate a few of the key findings from this chapter:

1. Estimating and removing the regional component of gravity for typical inversion scenarios is the most important aspect of the inversion procedure. For typical bathymetry inversions, the optimal method for estimating the regional field is constraint point minimization.
2. When collecting data for an inversion, it is best to aim for quality over quantities for the gravity data, and conversely, quantity over quality for bathymetry constraint measurements.
3. We provide general guidelines on the optimal ranges of constraint density, gravity survey line spacing, and gravity noise, for which conducting an inversion is suitable.

Testing the various models with differing levels of gravity noise and numbers of gravity observation points highlights an important factor in planning a gravity survey. We show for the Ross Sea synthetic model, which likely emulates the scenario expected from many Antarctic ice shelves, **there are diminishing returns for average flight line spacings smaller than ~ 40 km if the goal is to recover bathymetry features typical of the Ross Sea. However, the inverted bathymetry's accuracy is strongly affected by noise in the gravity data.** With this, the typically airborne survey focus on quantity over quality may need to be reassessed. If 40 km spaced flight lines produce similar results to 20 km lines, flying half the number of lines will save a significant amount of time. This time could be used to either expand the area of the survey or reduce the noise in the data. Reducing the data noise for an airborne survey may not always be feasible, but a few measures may be taken to attempt this, all of which are aided by the increased survey time allowed by reducing the number of flight lines. These include repeating lines or sections which are noisy, limiting flights to good weather windows, increasing the number of tie-lines, making shorter loops for base-station ties, or flying at lower altitudes and or ground speeds.

The previous measurements of bathymetry, referred to as the constraints, are a vital part of an inversion for bathymetry. Due to the non-uniqueness of an inversion, there are an infinite number of inverted bathymetry models which will equally match the observed data. These constraints provide the ground truth necessary to confidently chose a model out of these infinite choices. Additionally, if not more importantly, they provide the primary method of accounting for the regional component of gravity. Since this is shown to be the largest source of uncertainty, the constraints are the most important aspect of the inversion. We tested the effects of varying the spatial density of the constraint points. The results (Figure 3.31) show the range of constraint point spacings for the Ross Sea synthetic model which justifies conducting a gravity inversion if the goal is to recover bathymetry with a 5 km resolution.

The optimal constraint spacing is $\sim 20\text{-}70$ km. Smaller spacing values already have an adequate amount of information and little is gained over a simple interpolation of the data. At spacings larger than ~ 70 km, the errors in estimating the regional field are larger than the improvements made by the inversion. These values, while specific to the Ross Sea scenario, provide an important context for the feasibility of conducting bathymetry inversions. Taken together with the above assessment of the relative importance of gravity data noise and density, some general

guidelines are provided.

As long as the gravity data is on the order of magnitude of $2\text{-}4 \times$ the spacing of the desired bathymetry resolution, and the noise levels are low, **efforts should be focused on collecting more bathymetry measurements**. The uncertainty of these depth measurements is relatively unimportant (Figure 3.30c), meaning quantity over quality is acceptable here. The final spatial uncertainty of the inverted bathymetry is strongly tied to the distance to the nearest constraint. This suggests that an even distribution of the constraints is important. However, if specific regions of the survey are expected to have larger amplitude regional anomalies, an increased spatial density of constraints over this region would be beneficial. With these recommendations, future planning for Antarctic fieldwork should be able to collect data that prioritizes the accurate assessment of sub-ice-shelf bathymetry.

Chapter 4 applies the inversion presented here to model the bathymetry beneath Antarctica's Ross Ice Shelf.

Chapter 4

Ross Ice Shelf bathymetry inversion

Abstract

Antarctica's Ross Ice Shelf buttresses large catchments of ice from both the East and West Antarctic Ice Sheets. Changes to the current stability of the ice shelf, likely through basal melt of the sensitive grounding zones or pinning points, will reduce this buttressing and accelerate the Antarctic Ice Sheet's contribution to global sea level rise. The distribution of basal melt is predominantly controlled by the ocean cavity thickness and the channelling of ocean waters by bathymetric features. Bathymetry is, however, poorly known for the Ross Ice Shelf. Here we use airborne gravity data and distributed seismic constraints across the ice shelf to create an updated sub-ice shelf bathymetry model. We accomplish this with a non-linear geometric gravity inversion, available as open-source Python code. Monte Carlo sampling of the inversion inputs provides a robust means of addressing spatial uncertainty and the relative significance of each component of the inversion. The resulting bathymetry closely matches the seismic constraints and reveals significant changes compared to past bathymetry models. We find several likely locations of past pinning points, locations where enhanced basal melting is likely, and sites of possible tectonic significance.

Plain Language Summary

The floating Ross Ice Shelf slows the flow of a large amount of ice into the ocean. Melting at the base impacts the ice shelf's ability to slow down this upstream ice. The shape of the seafloor beneath the ice shelf (bathymetry), acts to guide ocean currents which cause this melting. Our knowledge of the bathymetry beneath the Ross Ice Shelf comes from a series of point measurements with an average distance between points of over 40 km. Here, we use measurements of Earth's gravity collected over the ice shelf to estimate the shape of the bathymetry beneath. This technique provides an increased resolution of the bathymetry and informs us about where we are most and least confident of the bathymetry depth. With this new model of sub-ice-shelf bathymetry, we highlight locations where melt-inducing ocean currents are likely directed, and several places with the seafloor very close to the base of the ice. These results will better inform ocean circulation models beneath the ice shelf, and therefore the likely future contributions of the Ross Ice Shelf to sea level rise.

Key Points

1. We present a new bathymetry model beneath Antarctica's Ross Ice Shelf from a gravity inversion.
2. A Monte Carlo simulation provides a detailed spatial uncertainty analysis.
3. Results highlight locations where the updated bathymetry may impact ocean circulation models or where the shelf may have been recently grounded.

4.1 Introduction

Much of Antarctica's coastline is fringed by floating extensions of the Antarctic Ice Sheet. These floating masses of ice, referred to as ice shelves, are connected to the grounded ice on the continent. Over 80% of Antarctica's grounded ice drains to the oceans through these ice shelves (Rignot et al., 2013). While they are floating, and thus already displace their mass equivalent of seawater, they are vital to the current and future contribution of the Antarctic Ice Sheet to global sea level rise (Fürst et al., 2016; Jacobs et al., 1992). The ice shelves slow the flow of upstream ice into the ocean by imparting a resistive force, known as buttressing. This buttressing occurs from lateral drag along the sides of the ice shelves and resistive stresses incurred where they flow over pinning points (localized areas of grounded ice) (Dupont & Alley, 2005; Matsuoka et al., 2015). Changes to the geometry of the ice shelves can reduce their restraining effect on the flow of grounded ice, leading to an increased mass flux of ice across the grounding zone, thus increasing the ice sheet's contribution to global sea level rise (e.g., Pritchard et al., 2012; Scambos et al., 2004).

The largest ice shelf on Earth is the Ross Ice Shelf (Figure 4.1, Fretwell et al., 2013). Situated in West Antarctica, along the boundary with East Antarctica, the Ross Ice Shelf comprises ice from both the East and West Antarctic Ice Sheets; a combined catchment totalling 11.6 meters of potential global sea level rise (Tinto et al., 2019). While the Ross Ice Shelf is in approximate steady-state, that is a near net-zero mass change (e.g., Moholdt et al., 2014; Rignot et al., 2013), geologic evidence shows rapid disintegration (Naish et al., 2009; Yokoyama et al., 2016) and extensive grounding line retreat (Spector et al., 2017; Venturelli et al., 2020) may have occurred as recently as the mid-Holocene (~ 7 kyr B.P.). Ocean forcing, specifically basal melting along the grounding zone, is thought to drive these rapid grounding line retreats (Lowry et al., 2019). The current stability of the ice shelf is in part attributed to the lack of warm Circumpolar Deep Water penetrating into the cavity (Dinniman et al., 2011; Tinto et al., 2019). Ocean waters that do penetrate the cavity, such as High Salinity Shelf Water, are dense and relatively cold. Despite their temperature, they are responsible for significant melting at the large depths of the grounding zone (Adusumilli et al., 2020) due to the pressure suppression of the freezing temperature of ice (Tinto et al., 2019).

This High Salinity Shelf Water is formed on the continental shelf from the creation of sea ice. Due to their density and the reverse slope of the continental shelf, they flow into the cavity, guided by bathymetric troughs (Jacobs et al., 1992; Tinto et al., 2019). There are many examples of bathymetric features controlling the routing of these sub-shelf waters (e.g., De Rydt et al., 2014; Dutrieux et al., 2014;

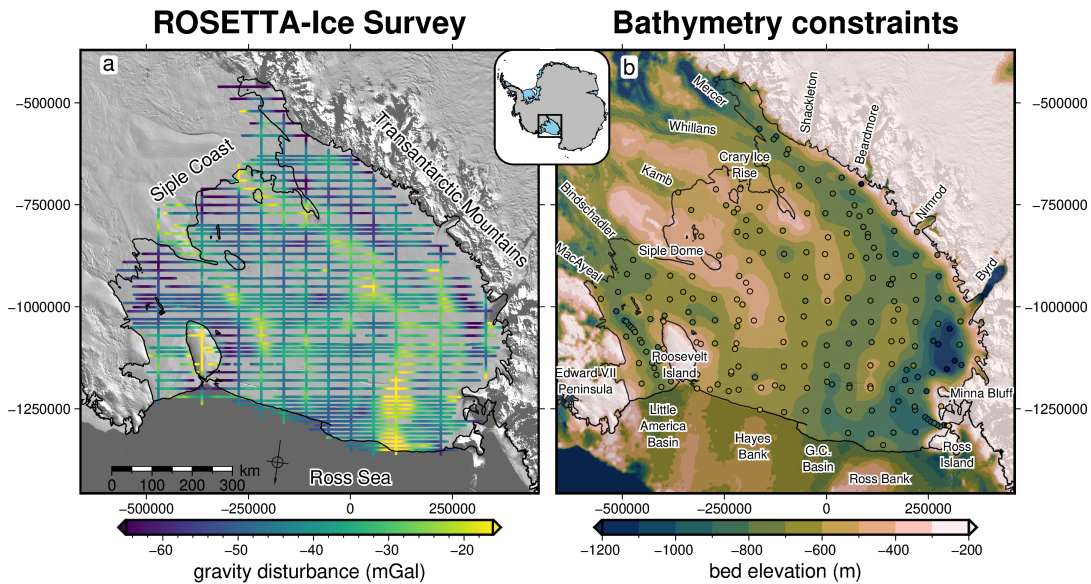


Figure 4.1: Input datasets for the Ross Ice Shelf bathymetry inversion. **a)** ROSETTA-Ice airborne gravity disturbance data (cleaned and re-levelled). **b)** Bedmap2 bed elevations in background, with individual constraint points within the ice shelf boundary (dots) on the same colour scale. Black line in both figures shows the grounding line and ice front from Mouginot et al. (2017). Background imagery is from MODIS-MOA (Scambos et al., 2007). Regional names shown in **a** and specific location names shown in **b**, which include ice streams along the Siple Coast, outlet glaciers along the Transantarctic Mountains, and bathymetry features in the Ross Sea. The RMS difference between the constraint point values and the BedMap2 gridded values is 138 m.

Gladish et al., 2015; Zhao et al., 2019). Additionally, ocean modelling sensitivity testing highlights the importance of bathymetric features to sub-shelf circulations and melt (De Rydt et al., 2014; Goldberg et al., 2020). Bathymetry, therefore, plays a key role in the stability of the Ross Ice Shelf through its likely control on the basal melt magnitude and distribution (Goldberg et al., 2019) and through the buttressing effect of bathymetric pinning points (Still et al., 2019).

Direct observations of the sea floor beneath the Ross Ice Shelf (excluding along its periphery) are limited to two drill holes. The first was the 1977 J9 drill hole north of Crary Ice Rise as part of the Ross Ice Shelf Project (Clough & Hansen, 1979). The second was the 2017 HWD2 drill hole near the centre of the ice shelf (Stevens et al., 2020). Apart from these two drill holes, all other inferences of sub-shelf bathymetry depths have been from seismic surveying, or the gravity inversion of Tinto et al. (2019). The majority of seismic surveys on the Ross Ice Shelf were accomplished during two projects, the International Geophysics Year traverses of the late 1950s and early 1960s (Crary et al., 1962; Crary, 1959; Crary & Robinson, 1962), and the Ross Ice Shelf Geophysical and Glaciological Survey (RIGGS, 1973-1974 Bentley, 1984). These extensive surveys systematically covered the entire ice shelf, collecting 223 observations of bathymetry with a mean spacing of approximately 40 km between points (Figure 4.1b).

These seismic and drill hole depths have been included in various Antarctic bed and bathymetry products (Fretwell et al., 2013; Le Brocq et al., 2010; Timmermann et al., 2010). As discussed later, Tinto et al. (2019) conducted a gravity inversion over the entirety of the ice shelf with data from the Ross Ocean and ice Shelf Environment, and Tectonic setting Through Aerogeophysical surveys and modelling

project (ROSETTA-Ice). This provided a significantly improved resolution over just the interpolation of the sparse seismic data. This gravity-inverted bathymetry was later incorporated in the BedMachine bed compilation (Morlighem, 2022; Morlighem et al., 2020). This chapter focuses on once again improving the sub-Ross Ice Shelf Bathymetry model. Following Tinto et al. (2019), we also use a gravity inversion of the ROSETTA-ice data to model the bathymetry. However, we conduct additional processing of the gravity data, and apply an entirely new gravity inversion algorithm, as described in Chapter 3. Additionally, our method provides an assessment of the spatial uncertainty of the resulting model, a useful component needed for the ocean modelling community (Goldberg et al., 2020).

4.2 Methods

Here we describe the three main methodologies of this chapter; 1) the gravity reduction process (Figure 4.2a), 2) the bathymetric inversion process (Figure 4.2b), which is explained in detail in Chapter 3 and briefly re-introduced here, and 3) the use of a Monte Carlo simulation to quantify spatial uncertainty in the resulting bathymetry.

4.2.1 Gravity reduction

A common task in geophysics is the removal of predictable noise to help amplify the signal of interest. This is the basis of gravity reduction; the process of isolating the desired gravity signal from the raw measurements of the Earth’s gravitational field. The magnitude of Earth’s gravitational acceleration, which we will refer to as *gravity* from here-on, ranges from $\sim 978,000$ to $\sim 983,000$ mGal, from the equator to the poles, respectively (Hofmann-Wellenhof & Moritz, 2006). The range in these values, approximately 5000 mGal, vastly outweighs the typical values of gravity anomalies resulting from geologic features of interest. These anomalies of interest are typically on the order of magnitude of 10’s of mGal. This exemplifies the issue of removing *noise* which has a significantly greater magnitude than the *signal* of interest.

Here, we start the gravity reduction process with observed gravity. We take observed gravity to be the signal which is produced by 1) the gravitational attraction of all massive bodies in Earth and 2) the rotation of the Earth. This means non-geological and time-dependent effects such as machine drift, tidal changes, aircraft manoeuvres and the effect of measuring gravity on a moving platform (Eötvös correction) have already been removed from the observed gravity (Hinze et al., 2005; Hinze et al., 2013). With this, observed gravity is defined as;

$$g_{obs}(p) = \gamma(p) + g_{geology}(p) \quad (4.1)$$

where, for an observation point p , $g_{obs}(p)$ is the observed gravity, $\gamma(p)$ is the attraction of the *normal* Earth and $g_{geology}(p)$ encompasses the gravity effects of all deviations between the *normal* Earth and the real Earth. This *normal* Earth is often taken as a single surface (here the reference ellipsoid) with a constant density above (ρ_{air}) and a constant density below (ρ_{crust}). Therefore, deviations between the *normal* and real Earth include 1) any masses above the ellipsoid which don’t have the uniform density of air or 2) any masses below the ellipsoid which don’t

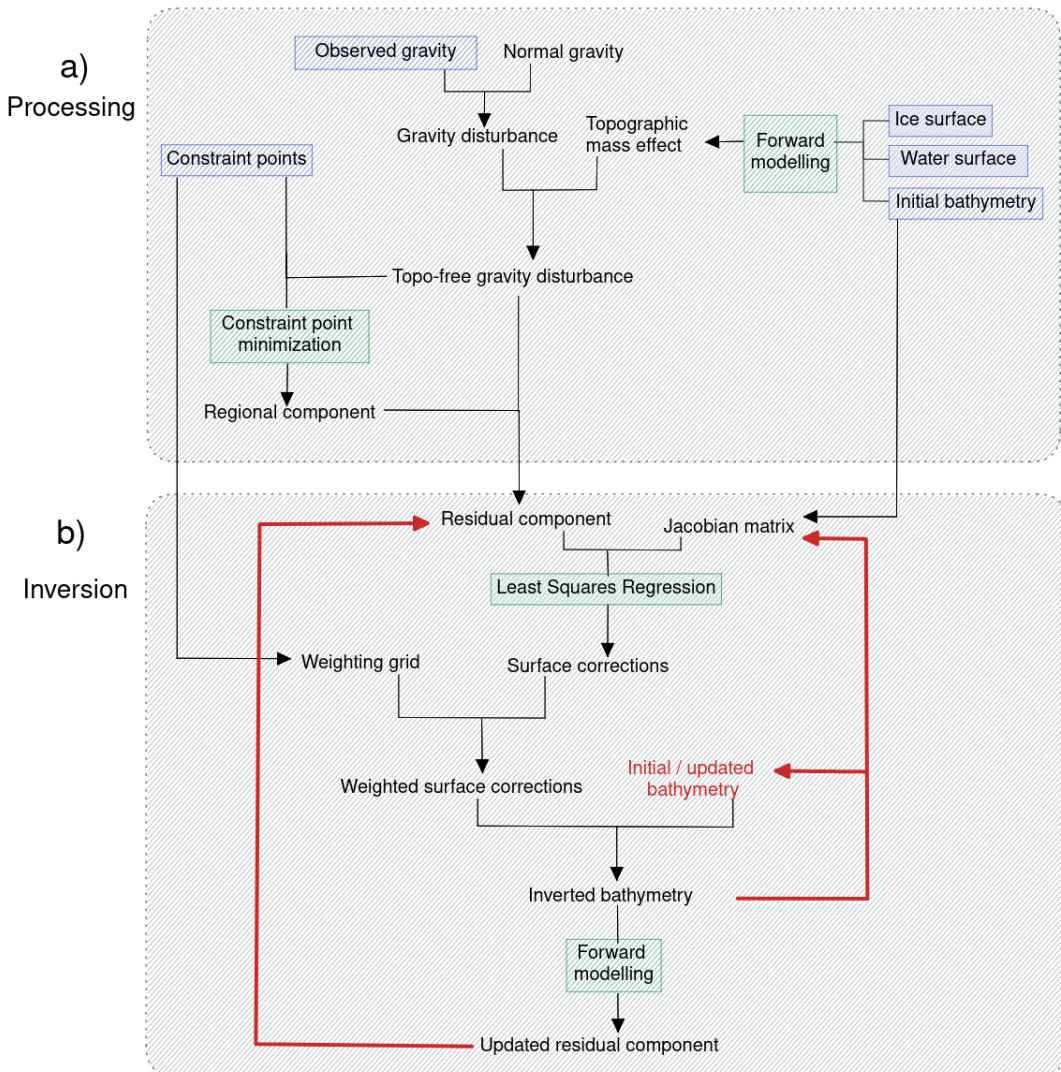


Figure 4.2: Schematic workflow diagram for **a)** gravity processing steps and **b)** running the inversion. Blue boxes show the input datasets, green boxes show the key processes and red lines signify iterative components of the inversion.

have the uniform density of crust. For a bathymetry inversion, the gravity signal of interest is a component of g_{geology} , which we must separate from γ .

4.2.1.1 Attraction of normal Earth

Observed gravity varies greatly due to the observation point's position, both based on latitude and elevation. Due to the oblate shape of the Earth, gravity is generally lower at low latitudes due to 1) increased distance from the centre of Earth's mass, and 2) more importantly, the increased tangential velocity (Jacoby & Smilde, 2009). Additionally, there is a decay of gravity with increased elevation, due to an increased distance from the centre of Earth's mass. These effects aren't related to the geologic variations of interest and thus should be removed. Historically, these effects of latitude and elevation were approximated separately, using the International Gravity Formula (*Latitude correction*) and the *Free-air correction*, respectively (Hinze et al., 2005). Alternatively, Li and Götze (2001) derived an analytical solution to the

gravity effects of an ellipsoid, at any point on or above its surface¹. With this, the Latitude and Free-air corrections are combined, and their approximations are replaced with closed-form solutions. By subtracting the normal gravity from the observed gravity at each observation point the gravity disturbance is found, where

$$\delta g(p) = g_{obs}(p) - \gamma(p), \quad (4.2)$$

where for an observation point p , $\delta g(p)$ is the gravity disturbance, $g_{obs}(p)$ is the observed gravity, and $\gamma(p)$ is the normal gravity (Paštěka et al., 2017).

The observation point, p , is defined by three coordinates; latitude, longitude, and geometric height (ellipsoidal height). It is a common mistake in geophysical studies for the normal gravity calculation to use the point p 's orthometric height (geoidal height or mean sea level), instead of its geometric height (Oliveira et al., 2018). This results in the calculation of normal gravity at a different point in 3D space relative to the observation. This calculation, while truly determining the gravity anomaly (a.k.a. free-air anomaly), is not well-suited for geological interests because the gravity anomaly contains signal from centrifugal acceleration effects due to the different locations of the points. Conversely, the gravity disturbance is defined as the difference between gravity and normal gravity at the same point, and thus only contains signal resulting from geologic sources (Hofmann-Wellenhof & Moritz, 2006). The difference between the gravity anomaly and the disturbance for Antarctica ranges from -20 to +20 mGal (See Figure C.1 in appendix C for a comparison). It is common for studies to correctly use the gravity disturbance while referring to it as the free-air anomaly to adhere to tradition. Combining Equations 4.1 and 4.2, shows that the gravity disturbance, δg , results solely from deviations between the theoretical model of the Earth (the *normal* Earth) and the true density variations and topography of the Earth (Vajda et al., 2004). Figure 4.3 compares the observed gravity, the normal gravity, the gravity disturbance, and the gravity anomaly for Antarctica.

4.2.1.2 Topographic mass effects

Typically, geophysical studies are interested in interpreting or inverting gravity signals resulting from subsurface features. To accommodate this, all other gravity effects must be computed and removed from the gravity disturbance. These other effects include the gravity resulting from masses bound by known surfaces, referred to as *topographic* or *terrain masses*. These surfaces include, but are not limited to, the rock surface (topography), the ocean surface (geoid), the seafloor (bathymetry), and the ice surface. Together, the gravity resulting from these masses is referred to as the *topographic mass effect*. Correcting the gravity disturbance for these topographic masses yields the *topo-free gravity disturbance* δg_{TC} , where

$$\delta g_{TC}(p) = \delta g(p) - g_{topo}(p). \quad (4.3)$$

¹Note that the normal gravity calculation with this analytical solution is not valid below the ellipsoid. While this is irrelevant for most locations on Earth, West Antarctic has negative geoid elevations, meaning observations near sea level are likely below the reference ellipsoid, invalidating the normal gravity calculation. For these situations, the use of a quasi-ellipsoid is recommended (Paštěka et al., 2017; Vajda et al., 2008b)

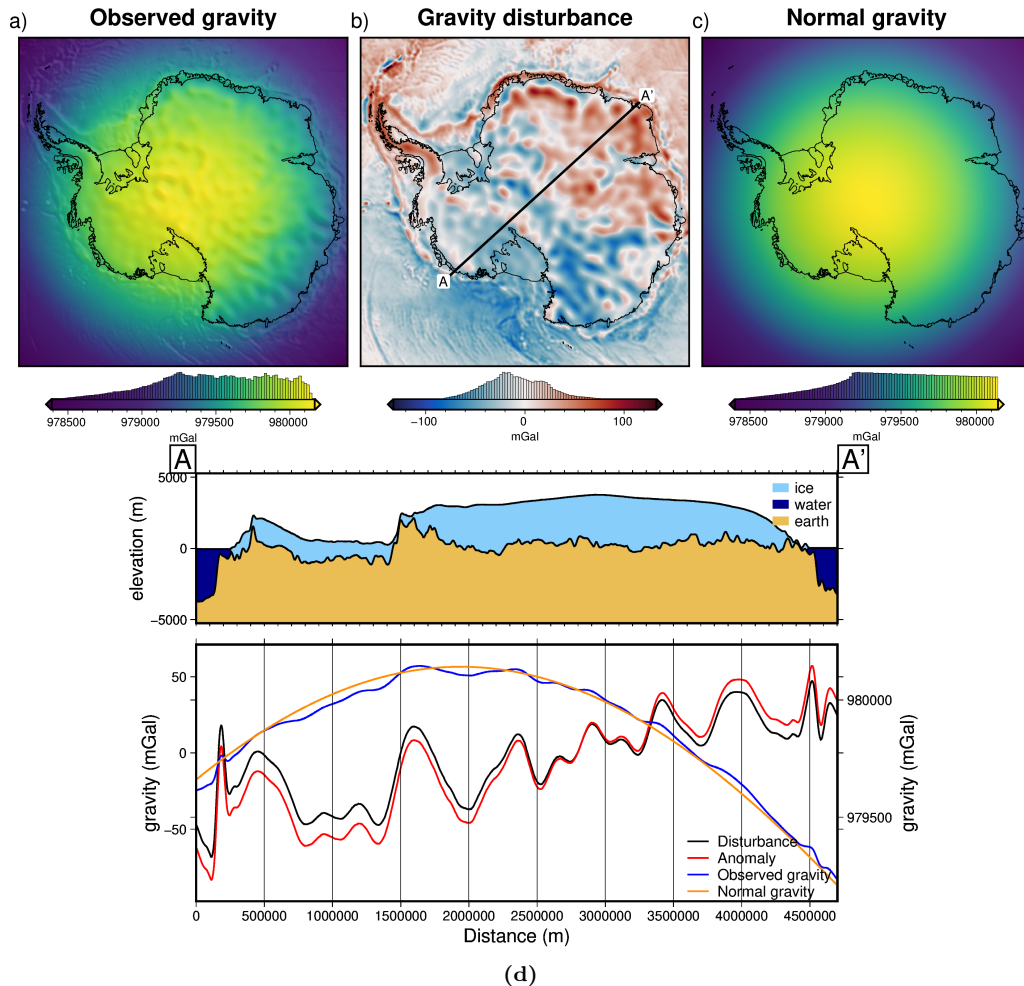


Figure 4.3: Observed gravity data reduction for Antarctica. **a)** Observed gravity data from Förste et al. (2014) at a geodetic observation height of 10 km. **b)** The gravity disturbance at 10 km height, defined as **a-c.** **c)** The normal gravity calculated at the same observation points as **a** using the closed-form equations of Li and Götze (2001). **d)** Profile A-B across Antarctica, location shown in **b.** Gravity disturbance (black) and anomaly (red) values are on the left y-axis, while observed (blue) and normal (orange) gravity values are on the right y-axis.

$g_{topo}(p)$ represents the summed topographic mass effect. δg_{TC} is sometimes referred to as the *Bouguer disturbance*, owing to the historic use of the *Bouguer anomaly*. In accordance with Vajda et al. (2007), we refer to it as the *topo-free gravity disturbance* to clarify that the ellipsoid has been used instead of the geoid in all reduction steps. In the past, the topographic mass effect has been split into the Bouguer slab correction and the terrain correction. The Bouguer slab correction approximates the topographic masses as laterally infinite flat slabs, while the terrain correction accounts for the overestimation of the Bouguer slab resulting from the assumption of the flat slab. With modern computing able to efficiently calculate the gravity resulting directly from a topographic surface (Fatiando a Terra Project et al., 2023), there is no need for the separate two-step correction.

The topographic mass effect reflects all topographic deviations (including topography of the ice, water, and seafloor) between the *normal* Earth and the real Earth. The *normal* Earth model is shown in Figure 4.4a, as defined by air above the ellipsoid and crust below. A simplified model of the true Earth is shown in Figure 4.4b, and contains air, ice, water, crust, and various geologic bodies within the crust. These

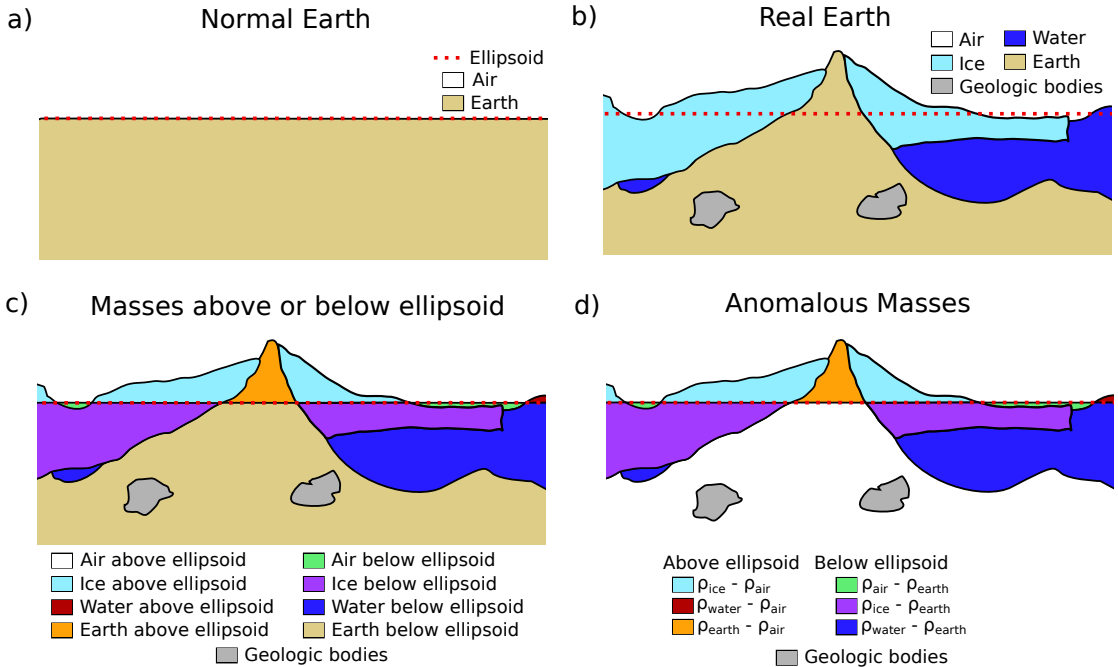


Figure 4.4: Components of the topographic mass effect and resulting topo-free gravity disturbance, or Bouguer disturbance. **a)** The normal Earth model, **b)** a simplified real Earth model. **c)** Topographic masses separated into components above and below the ellipsoid. **d)** Real Earth topographic masses which are anomalous with respect to the normal Earth. Note if the reference level (red dashed line) is switched from the ellipsoid to the geoid, this would result in a Bouguer anomaly.

masses are separated in Figure 4.4c into components above and below the ellipsoid. From this, the masses which are anomalous with respect to the *normal* Earth can be distinguished, as shown in Figure 4.4d. These anomalous masses include water, ice, and crust above the ellipsoid, and air, ice, water, and geologic bodies below the ellipsoid. The gravitational effect of these anomalous masses can be approximated by assuming each mass's density and setting it relative to the density of the component of the *normal* Earth which the mass is replacing. These relative densities are shown in the key of Figure 4.4d. Calculating and summing the gravity effect of each of the components of Figure 4.4d (excluding the geologic bodies) gives the topographic mass effect. Subtracting this from the gravity disturbance gives the topo-free gravity disturbance².

To compute the topographic mass effect, the anomalous masses from Figure 4.4d are discretized into a series of vertical right-rectangular prisms. To achieve the geometry and density configuration of Figure 4.4d, three sets of prisms are used, as shown in Figure 4.5c-e.

1. Prisms between the ice surface and the ellipsoid are assigned densities of $\rho_{ice} - \rho_{air}$ for prisms above the ellipsoid, and $\rho_{air} - \rho_{ice}$ for prisms below the ellipsoid.
2. Prisms between the water surface (ice base) and the ellipsoid are assigned densities of $\rho_{water} - \rho_{ice}$ for prisms above the ellipsoid, and $\rho_{ice} - \rho_{water}$ for prisms below the ellipsoid.

²The use of the reference ellipsoid as the bounding surface of the topographic mass effect calculations results in a topo-free gravity disturbance while using the geoid as the bounding surface would result in a Bouguer anomaly (Vajda et al., 2006).

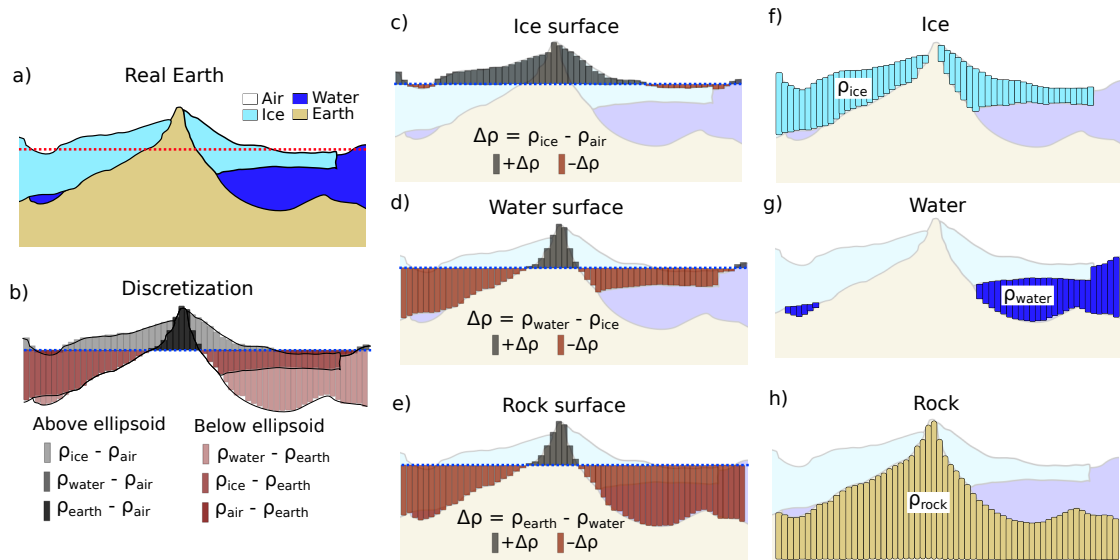


Figure 4.5: Discretizing the topographic mass effect. **a)** The simplified real Earth model, with air, ice, water, and earth. **b)** the resulting anomalous masses relative to the *normal* Earth, as shown in Figure 4.4d. **c)** Prisms between the ellipsoid and the ice surface, **d)** prisms between the ellipsoid and the water surface (ice base), and **e)** prisms between the ellipsoid and the rock surface (topography onshore and bathymetry offshore). Overlap of prisms from **c-e** creates the different shades shown in **b**. The alternative discretization approach, commonly used, is shown in **f-h** where the prism layers are bound both above and below by topographic layers, or arbitrary references (bottom of prisms in **h**), instead of by the normal Earth reference surface (ellipsoid). Additionally, density values of the prisms are related to the material they discretize and are not relative to the expected density of the normal Earth.

3. Prisms between the rock surface (topography onshore and bathymetry offshore) and the ellipsoid are assigned densities of $\rho_{\text{earth}} - \rho_{\text{water}}$ for prisms above the ellipsoid, and $\rho_{\text{water}} - \rho_{\text{earth}}$ for prisms below the ellipsoid.

This configuration of prisms correctly discretizes the topographic mass effect because the ice surface is equal to the water surface in areas of no ice thickness, and the water surface is equal to the rock surface in areas of no water thickness. Due to this, the overlap between the three sets of prisms, shown in Figure 4.5b gives the appropriate densities, as defined in Figure 4.4d. From these three sets of prisms, the topographic mass effect can be calculated at the gravity observation points using the analytical solutions of Nagy et al. (2000). As a demonstration, the topographic mass effect for Antarctica is calculated using topographic data from Bedmap2 (Fretwell et al., 2013), referenced to the WGS-84 ellipsoid. The observed satellite gravity data has a low spatial resolution, so the lower resolution of Bedmap2 over BedMachine v3 is insignificant. The calculated topographic mass effect, the gravity disturbance, the resulting topo-free gravity disturbance, and the topographic mass effect from the alternative method of discretization (Figure 4.5f-h) are shown in Figure 4.6.

The theoretical topo-free gravity disturbance is the gravity effect caused by and only by anomalous subsurface bodies, which have a density different from the assumed constant density of the crust. In reality, there are additional components of the topo-free gravity disturbance resulting from 1) noise in the observed data, 2) non-uniform densities used in the topographic mass effect calculation, and 3) inaccurate topographic data used for the topographic mass effect calculation. In most geophysical applications, the uncertainty of the topographic data is small compared

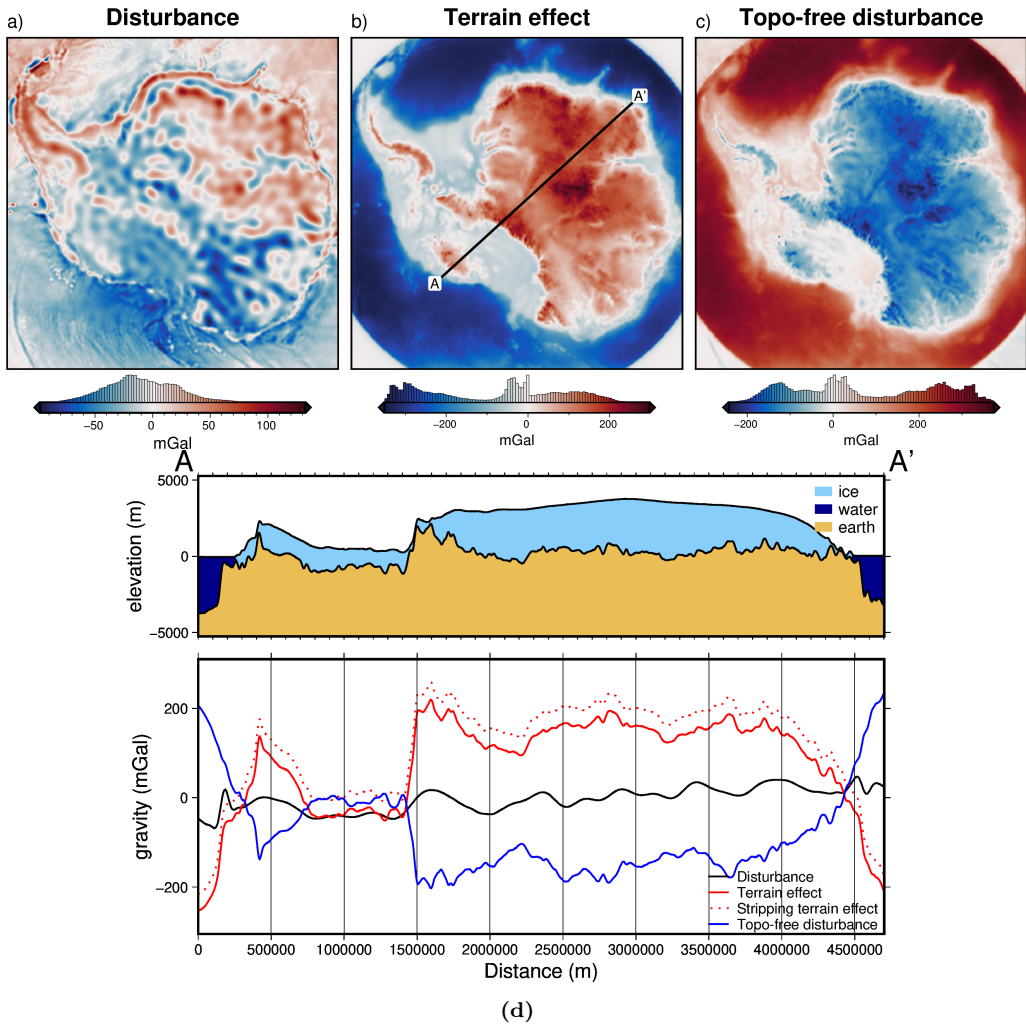


Figure 4.6: Topographic mass effect at 10 km height for Antarctica, from Bedmap2 topographic data (Fretwell et al., 2013). **a)** Gravity disturbance at a geodetic observation height of 10 km, from Figure 4.3b. **b)** The combined gravity effect of the anomalous masses defined in Figure 4.4d and discretized following 4.5b. **c)** The topo-free gravity disturbance, calculated as **a** - **b**. **d)** Profile A-A' across Antarctica, location shown in **b**. The dotted red line shows the terrain mass effect results of the alternative discretization method shown in Figure 4.5f-h. A DC shift was applied to attempt to remove the offset.

to other uncertainties in the analysis, and thus component #3 is assumed to be zero. Conversely, for the case of a bathymetry inversion, this component of the topo-free disturbance resulting from the inaccuracies of the topography (bathymetry) data is the signal of interest. Next, we will isolate this component from the remainder of the topo-free gravity disturbance.

4.2.1.3 Regional separation

Here, we separate the topo-free gravity disturbance into components resulting from 1) subsurface geologic variations and 2) inaccuracies between the true bathymetry and the low-resolution bathymetry data used for the terrain mass effect. These are referred to as the regional and residual components, respectively. Chapter 3 highlighted the importance of accurately estimating and separating this regional component from the residual. The regional estimation was found to be the largest

source of uncertainty in several synthetic bathymetry inversions, as well as other Antarctic bathymetry inversions (Brisbourne et al., 2014). While there are many techniques to estimate the regional component, we will use constraint point minimization due to its demonstrated effectiveness over the other methods (Section 3.2.4). This technique samples the topo-free gravity disturbance at points of known bathymetry depth, referred to as the constraint points. Since the depth is known here, the residual component of gravity should be near zero, and thus the regional component should entirely equal the topo-free gravity disturbance. Using these sampled values, the entire model domain is gridded with an interpolation, using either bi-harmonic splines (Uieda, 2018) or minimum curvature (Smith & Wessel, 1990). The resulting grid makes up the regional component, and when subtracted from the topo-free gravity disturbance gives the residual component. This residual component is the input into the inversion.

4.2.2 Bathymetry inversion

Here we start by briefly summarising the bathymetry inversion workflow described in Chapter 3, and shown schematically in Figure 4.2b. Then we compare our method to several other commonly used bathymetry inversion algorithms. The basis of modelling bathymetry with a gravity inversion is that the bathymetry surface, which is a contrast between lower-density material (seawater) and higher-density material (sediment) creates a measurable effect on Earth’s gravity. Our inversion begins by computing the Jacobian matrix (Equation 3.7), which is a quantitative means of describing the sensitivity of the residual gravity data to changes in the height of each grid cell of bathymetry. In other words, the Jacobian quantifies the ratio between the amplitude of bathymetric features and the gravity anomaly resulting from them. From this Jacobian matrix, the optimal change to apply to each bathymetry grid cell to minimize the residual gravity data is estimated. This is in the form of a surface correction grid, with a value for each grid cell of bathymetry. Since there are locations of already known bathymetry depths (constraint points), this surface correction grid should be zero at these points. To achieve this, a weighting grid is calculated (Section 3.2.5.3), which is based on the minimum distance between each grid cell and the nearest constraint point. These distance values are then normalized from 0 to 1, with 0 being the cells closest to the constraints, and 1 being the cells furthest. The surface correction grid is multiplied by this weighting grid, to achieve a correction value of 0 m at the constraints, smoothly tapering off to the full estimated correction values at a distance.

With this weighted surface correction grid, the original bathymetry depths are updated. To ensure the updated bathymetry doesn’t intersect the ice base, the ice base topography is set as an upper-bounding surface. The forward gravity of this updated bathymetry is then re-calculated, with the prism configuration and densities shown in Figure 4.5e. The updated forward gravity is used to recalculate the topo-free gravity disturbance. Using the same regional component as calculated before the inversion (Section 4.2.1.3), an updated residual gravity is computed. This is then input into the next iteration of the inversion (red lines in Figure 4.2b). Iterations continue until a set of user-defined stopping criteria are met; 1) a maximum number of iterations is reached, 2) a minimum value of the ℓ^2 -norm of the residual

is reached, or 3) there is no significant variation in the ℓ^2 -norm in two consecutive iterations.

This process describes a single *inversion*. The critical step in this inversion, determining the surface correction values from the sensitivity matrix, includes a damping parameter that controls the smoothness of the resulting inverted bathymetry. This damping parameter value directly affects the resulting bathymetry model and needs to be carefully chosen. For this, we follow the cross-validation routine described in Chapter 3 from Uieda and Barbosa (2017). This involves running the entire inversion for a suite of different damping parameter values. The input gravity data to these inversions is split into a *testing* set and a *training* set. The inversion only uses the *training* set. After each inversion, the forward gravity effect of the updated bathymetry model is calculated at the points of the *testing* set. The root mean squared difference between the testing gravity values and the forward gravity values gives the *score* of each cross-validation. The damping parameter which produces the lowest score is chosen as the optimal value.

4.2.3 Starting bathymetry

An initial bathymetry model for the inversion is needed to compute the topographic mass effect and to run the inversion. The weighting grid constrains the inversion from changing the starting grid values at the constraint points. For this reason, the starting model should be carefully created. As discussed in the previous chapter (Chapter 3, Section 3.4.2), there are several methods of creating the starting model from the sparse measurements at the constraint points. Here, we use and compare two techniques for interpolating these constraint point values over the entire domain; tensioned minimum curvature (Smith & Wessel, 1990) and bi-harmonic splines (Sandwell, 1987). See Chapter 3 Section 3.4.2 for the details of these gridding techniques.

4.2.4 Uncertainty quantification

A major component missing from many bathymetry inversions is assessing the spatially variable uncertainty in the resulting bathymetry depths. This uncertainty arises from a multitude of sources, including uncertainty in 1) the gravity data measurements, 2) constraint point depths, 3) user-defined variables, such as ice, water, or sediment density, and 4) uncertainties associated with the various methodologies of the inversion. Here we use a sampling-based approach to estimate the uncertainty, where the uncertainty of the *inputs* is used to assess the uncertainty of the *output*, in this case, the inverted bathymetry. This general method of uncertainty analysis is referred to as Monte Carlo sampling (Jansen et al., 1994).

For a generalized problem of inputs \mathbf{x} and a function $\mathbf{y}(\mathbf{x})$, Monte Carlo simulation provides a means to answer the two following questions; 1) what is the uncertainty in $\mathbf{y}(\mathbf{x})$ given the uncertainty in \mathbf{x} ? and 2) what are the relative importance of the various components of \mathbf{x} with respect to $\mathbf{y}(\mathbf{x})$ (Helton et al., 2006)? While there are many components that contribute to the overall inversion uncer-

tainty, here we will examine 1) uncertainty in the gravity data values, 2) depth uncertainty of the constraint points, 3) uncertainty in the chosen density values used for ice, water, and earth, and 4) uncertainties related to user-chosen parameter values in the inversion. Uncertainties that are not covered here are those which relate to processes of the inversion which don't have associated measurable input uncertainties. This includes the use of spatially non-variable density values for ice, water, or earth, or the effects of discretizing a real topographic surface as a series of prisms.

The Monte Carlo simulation consists of sampling the input parameters N times from their respective distributions (Figure 4.7b) and running the entire inversion workflow for each of the N parameter sets (Figure 4.7c). For each bathymetry grid cell, the weighted standard deviation of the N resulting inverted bathymetries is found (Figure 4.7d). This grid of cell-specific standard deviations show where the input parameters have a large effect on the bathymetry results. This grid is used as our estimate of the spatial uncertainty in the inversion. The grid of cell-specific weighted median values is then taken to be the optimal inversion result. These cell-specific statistics are weighted by the inverse square of each inverted bathymetry's RMS difference with the constraint point depths (Figure 4.7d). This reduces the bias of inversions in the ensemble which performed poorly, as defined by not adhering to the constraints (Schnaidt & Heinson, 2015). To assess the relative importance of the input parameters, in addition to the complete Monte Carlo simulation, additional simulations are run where each parameter's effect is isolated. For these, only a singular parameter is sampled from its distribution, so that the resulting spatial standard deviation is due solely to the uncertainty of that parameter.

The parameters included in the Monte Carlo sampling are: 1) the gravity disturbance data, 2) the constraints point depths, 3) the gridding parameters to create the starting bathymetry, 4) the density of ice, 5) the density of water, 6) the density of sediment, and 7) gridding parameters for the constraint point minimization technique of regional gravity estimation (Figure 4.7b). For the full Monte Carlo simulation, with all the above inputs sampled from their respective distributions, the entire inversion workflow needs to be repeated with each of the N parameter sets. This includes 1) creating the starting bathymetry model from the constraint points (Section 4.2.3), 2) calculating the terrain mass effect to get the topo-free gravity disturbance (Section 4.2.1.2), 3) estimating the regional component of the disturbance and removing it (Section 4.2.1.3), and 4) running the damping parameter value cross-validation (Section 4.2.2) to obtain the inverted bathymetry (Figure 4.7). For the individual Monte Carlo simulations, only portions of this workflow need to be repeated. For example, if only the gravity disturbance is sampled, only the regional field and inversion need to be re-run. The starting bed and topographic mass effect calculated during the baseline inversion are re-used.

Due to the computational demand of a full inversion workflow, the total number of inversions in each Monte Carlo simulation is limited. To ensure the uncertainty distributions of the inputs are adequately sampled with this limited number of possible runs, we have used Latin hypercube sampling where possible (Jansen et al., 1994). This sampling technique is well suited for computationally demanding tasks since it ensures proper coverage of the uncertainty distributions of the sampled values, despite a low number of samples Helton et al., 2006. To accomplish this, for a

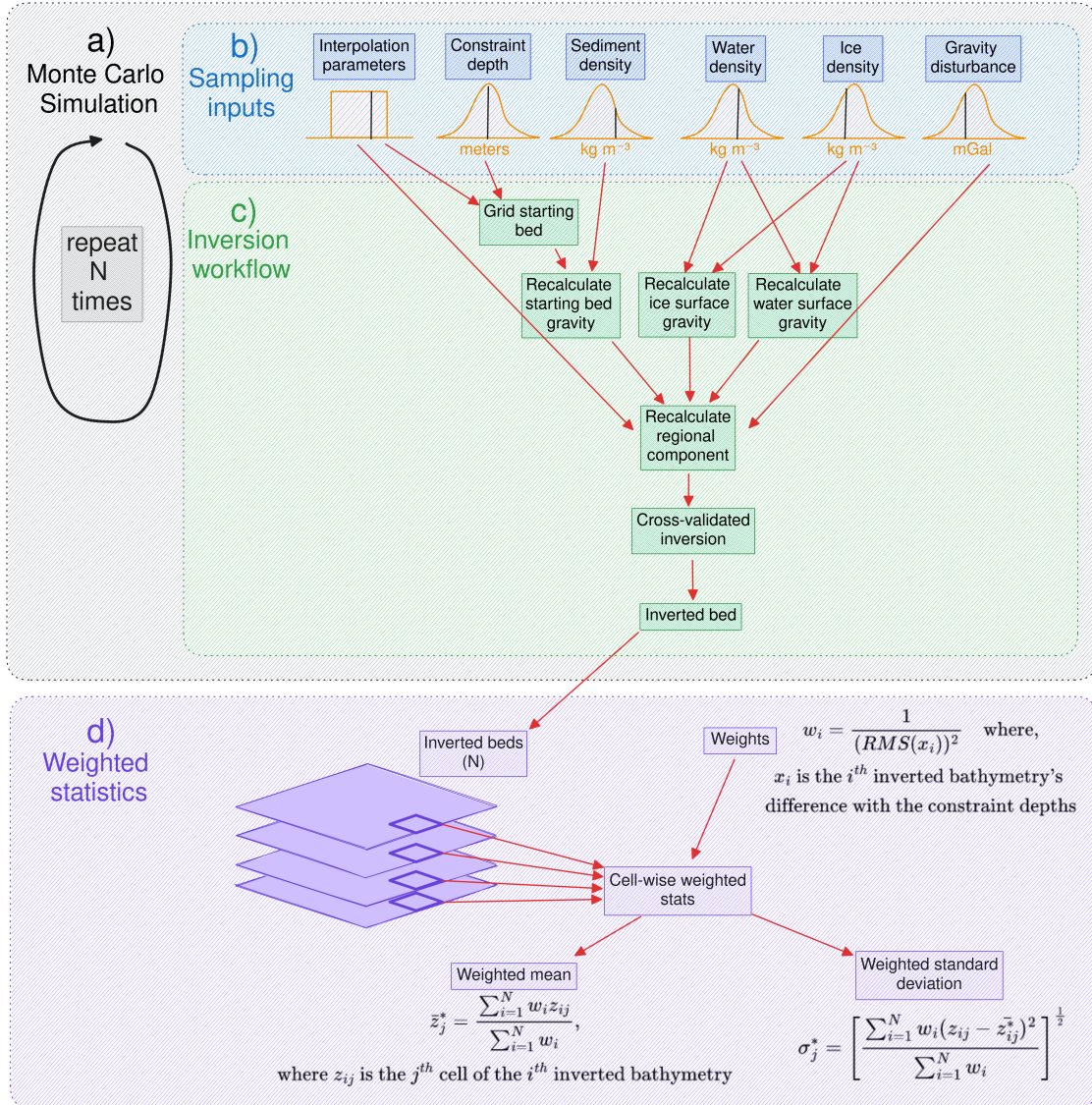


Figure 4.7: Schematic workflow diagram for the Monte Carlo uncertainty analysis. **a)** The Monte Carlo simulation, consisting of **b)** sampling the inputs from their respective distributions, and **c)** implementing the various components of the workflow, depending on which inputs have been sampled. This process is repeated N times, yielding N inverted bathymetry grids. **d)** Weighted cell-specific statistics are computed. Each inverted bathymetry grid (large purple boxes) is weighted by the respective inversion's constraint depth RMSE. These weights are used to compute the weighted mean and weighted standard deviation of each grid cell (bold purple square).

Monte Carlo simulation of N runs, the given distributions are split into N intervals of equal probability and one value is chosen from each interval. The N values for each parameter are then randomly paired to get N sets of sampled input parameter values (Helton et al., 2006). Since the gravity data and constraint points are each sampled on a point-by-point basis, Latin hypercube sampling is unnecessary and random sampling is used. Figure 4.8 shows a $N = 9$ comparison of random sampling and Latin hypercube sampling for a two-parameter simulation.

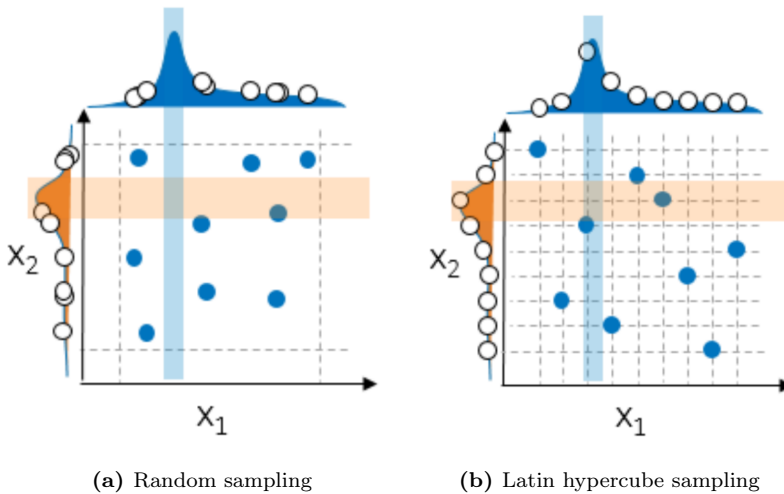


Figure 4.8: Comparison of sampling methods for a Monte Carlo simulation of two variables (X_1 and X_2) with 9 samples drawn from each. **a)** Random sampling, where values are drawn at random from each variable's distribution, and **b)** Latin hypercube sampling, where values are drawn from equal-probability intervals. Note the effective coverage of the distributions in **b** relative to **a**. The figure is adapted from Koch et al. (2017).

4.3 Relation to past bathymetry inversions

The fundamental theory in all bathymetry inversions is based on the fact that the density contrast across the bathymetry surface produces a measurable gravity effect. This phenomenon gives rise to several techniques to convert observed gravity data into bathymetric depths. This by definition is a geophysical inverse problem (Oldenburg & Li, 2005), but the methods chosen to solve it vary from 3D rigorous inversions to iterative 2D forward modelling. Our inversion method follows a classical least-squares approach to solving the inverse problem, while our uncertainty and sensitivity analysis follows a Bayesian approach (Aster et al., 2018). Here, we compare our inversion method and workflow to other bathymetry inversions. We attempt to include all past studies related to Antarctica, as well as several from Greenland. We start by comparing our technique for the gravity reduction process, followed by differences in the actual inversion, and finally by differences in our assessment of uncertainty.

4.3.1 Gravity reduction comparison

One of the largest differences between our method and past studies is the gravity reduction process. We employ a rigorous terrain mass effect calculation to obtain a topo-free gravity disturbance, often referred to as a Complete Bouguer Anomaly (Vajda et al., 2007). Theoretically, this gravity signal contains only effects due to subsurface density anomalies and inaccuracies in calculating the terrain mass effect. Our method isolates the gravity effect of this inaccuracy since it is due to the deviations between the starting model of bathymetry and the true bathymetry. This is referred to as our residual component of the topo-free gravity disturbance. While most other bathymetry inversion studies achieve a similar residual anomaly, they complete this procedure in a theoretically different way, which may be introducing unnecessary errors. The differences arise from other studies ignoring the reference

surface (the ellipsoid) for all calculations after the normal gravity correction.

The sign of a gravity disturbance value informs the interpreter as to whether the true Earth has either excess or deficient mass at that location with respect to the normal Earth. Therefore, the absolute level of gravity disturbance data should be retained, even though direct offsets (DC shifts) don't alter the amplitude of the gravity anomalies. For this reason, the reference surface used in the normal gravity calculation (here the ellipsoid) should be continued to be used in all further calculations of topographic masses, including in the forward calculation made during the inversion, as shown in Figure 4.5 b. Many studies instead have discretized the ice, water, and starting bathymetry surfaces into prism layers which either have arbitrary references or density values not relative to the normal Earth model. This alternative discretization is shown in Figure 4.5f-h. For example, the gravity effect of ice, if not just ignored (e.g., Cochran & Bell, 2012; Jordan et al., 2020b; Millan et al., 2017; Yang et al., 2020b), is typically removed via a "stripping" technique (Vajda et al., 2008a), (e.g., Greenbaum et al., 2015; Millan et al., 2020; Muto et al., 2013a; Yang et al., 2021). This stripping involves calculating the forward gravity of prisms with tops defined by the ice surface, bottoms defined by the ice base, and densities defined by the assumed density of ice (Figure 4.5f). Additionally, the prisms which comprise the starting bathymetry model for many inversions are bound above by the starting bathymetry, and below by an arbitrary constant depth (Figure 4.5h) (e.g., Muto et al., 2013a; Tinto et al., 2019). The forward gravity calculations of this style of discretization can introduce several errors.

1. The largest of these errors is an offset in the mean value of the forward gravity relative to the observed gravity. This offset needs to be estimated and removed prior to comparison with the observed data. The DC-shift used to remove the offset is typically estimated by finding a value that minimizes the difference between the observed and predicted data at locations of known bathymetry (e.g., Boghosian et al., 2015; Cochran et al., 2020; Constantino et al., 2020; Eisermann et al., 2020; Millan et al., 2017; Muto et al., 2013a). This additional step, referred to as "pinning", is unnecessary in our implementation, due to adhering to a rigorous determination of the terrain mass effect. If an incorrect DC shift is applied, the significance of the zero level of the topo-free gravity disturbance is lost. The value of 0 signifies that the simplified model of the Earth (i.e. the starting bathymetry model) is equal to the true Earth density distribution. Shifting this zero-level due to errors in estimating the DC-shift may lead to a vertical offset in the inverted bathymetry, especially if the inversion domain isn't well constrained. The DC-shifted terrain mass effect and the rigorous terrain mass effect for Antarctica are compared in Figure 4.6d.
2. The forward gravity calculation with this style of discretization results in slightly different amplitude anomalies compared to the true terrain mass effect. This difference is due to the different densities assigned to the prism layer between the two techniques (Figure 4.5). While this difference is likely below the range of uncertainties in the gravity error, it is an unnecessary addition of error to the gravity reduction process.
3. The last drawback to using this alternative discretization is an increased gravitational edge effect. As shown in Figure 4.5, the average densities and prism

heights are larger with this technique. This increases the overall decay of calculated gravity at the edges of the model space, due to the contrast with the void-space beyond the model domain. To account for this, a larger buffer zone is needed, which can significantly increase the computational requirements during forward modelling (see Chapter 3 Section 3.2.2.2).

4.3.1.1 Regional separation

The last step in the gravity reduction process for bathymetry inversion is separating the regional and residual signals, where the residual signal should theoretically be entirely a result of the bathymetry surface. Some techniques commonly used for this are described in Chapter 3 Section 3.2.4. Past bathymetry inversions have used a variety of these techniques, as summarized below.

1. Zero or uniform adjustment; For small inversion domains the regional field is sometimes assumed to be minimal. In these scenarios, past studies have either limited the inversion domain to where the regional field is assumed small (Boghosian et al., 2015; Cochran & Bell, 2012), used a uniform value for the regional component (Muto et al., 2013b), or found a constant density value for the starting model which minimize the gravity misfit (An et al., 2017; Millan et al., 2018; Millan et al., 2017).
2. Low-pass filtering; for inversion domains with an expected regional field slightly larger than the above scenario, low-pass filtering of the gravity data can approximate the regional component (Eisermann et al., 2020; Hodgson et al., 2019).
3. Geologic modelling; To account for the regional field, some studies create geologic models of varying density to estimate the regional field. These models are typically informed from other geophysical data (Greenbaum et al., 2015; Hodgson et al., 2019), *a priori* geologic knowledge (Cochran et al., 2014b; Constantino et al., 2020; Tinto & Bell, 2011), or from an approximated crustal density distribution (Cochran et al., 2020; Eisermann et al., 2021; Tinto et al., 2019; Wei et al., 2020).
4. Upwards continuation / high altitude surveys; This technique estimates the long-wavelength regional component by either upward continuing the gravity data to large altitudes, using separate gravity data collect from high-altitude surveys (Muto et al., 2016), or a combination of both (Tinto et al., 2015)
5. Constraint point minimization; the last commonly used technique utilizes the assumption that the desired residual component is near-zero at points of known bathymetry. From this assumption, the regional component at these constraint points is entirely equal to the gravity anomaly value. To estimate the regional field, the gravity values are sampled at the constraint points and interpolated over the region. This technique has been used in several recent inversions where sparse constraint points are available (An et al., 2019a; An et al., 2019b; Jordan et al., 2020b; Millan et al., 2020; Vaňková et al., 2023; Yang et al., 2021; Yang et al., 2020a). While implemented in a different method, this constraint point minimization follows the same concept as several studies which use the constrained locations to derive a spatially variable density model, accounting

for the regional field (Eisermann et al., 2021; Tinto et al., 2019; Wei et al., 2020).

Here, we use the constraint point minimization technique for estimating and removing the regional component of the topo-free gravity disturbance.

4.3.2 Inversion comparison

We have developed a conventional non-linear geometric gravity inversion algorithm, as often used in modelling density contrasts, such as sedimentary basins (e.g., Martins et al., 2010; Santos et al., 2015), or the Moho (e.g., Pappa et al., 2019; Uieda & Barbosa, 2017). This algorithm is similar in concept to inversions used in other bathymetric studies but differs in its implementation. Past inversion techniques used for bathymetry modelling can be grouped into several categories;

1. algorithmic approaches. This method termed the "topographic shift method" (Hodgson et al., 2019; Jordan et al., 2020b), while not a formal inversion, calculates the equivalent rock thickness from the residual component of gravity, adds this to the starting bathymetry model, and constrains the results by the locations of known bathymetry.
2. 2D profile inversions. Using the method of Talwani et al. (1959), and often implemented within the commercial software Geosoft Oasis Montaj, these inversions retain the 2D nature of the airborne flight lines and invert only along the path of the flight (Boghosian et al., 2015; Cochran et al., 2014b; Cochran et al., 2020; Constantino & Tinto, 2023; Tinto & Bell, 2011; Tinto et al., 2015; Wei et al., 2020).
3. 3D frequency-based inversions. This category of inversion uses a Fourier transformation to calculate the forward gravity effect of a continuous topographic surface, forgoing the need to discretize the topography into vertical prisms (Oldenburg, 1974; Parker, 1972). This Fourier transform is then iteratively modified to minimize the misfit to the observed gravity. This method, particularly its implementation within the commercial software Geosoft Oasis Montaj, is frequently used for bathymetry inversions (An et al., 2017; An et al., 2019a; An et al., 2019b; Cochran & Bell, 2012; Eisermann et al., 2020; Eisermann et al., 2021; Greenbaum et al., 2015; Millan et al., 2018; Millan et al., 2017; Millan et al., 2020; Studinger et al., 2004b).
4. Simulated Annealing. This global optimization technique (Kirkpatrick et al., 1983) performs many forward calculations of possible bathymetry surfaces and slowly converges on a model which minimizes the misfit with the observations. This method, similar to our Monte Carlo uncertainty analysis, has the benefit of providing an uncertainty estimate of the resulting bathymetry based on the uncertainty in the inversion inputs. This has been used in several bathymetric inversions (Filina et al., 2008; Muto et al., 2013a; Muto et al., 2016; Roy et al., 2005; Yang et al., 2021; Yang et al., 2018; Yang et al., 2020a)
5. Regularized least-squares inversions. This style of inversion is the conventional approach to solving non-unique inverse problems (Aster et al., 2018). While this method is commonly used for other geometric gravity inversions

(e.g., Moho and basement), to our knowledge it is only applied to bathymetry inversions here, and in Vaňková et al. (2023).

4.3.3 Uncertainty comparison

Here we compare our uncertainty analysis to those from other bathymetry-gravity inversion studies. Most of these past studies provide an estimation of uncertainty, but only a few provide spatially variable uncertainties (e.g., An et al., 2019a; Muto et al., 2016). Typically, these inversion uncertainties are assumed to result from three sources.

1. Uncertainty in the gravity data. The uncertainties resulting from the gravity data uncertainty are typically estimated using a Bouguer slab approximation, with an assumed density of the contrast between rock and water ($\sim 1600 \text{ kg m}^{-3}$), and a gravity uncertainty approximated from the RMS crossover values of the airborne gravity survey (e.g., Boghosian et al., 2015; Constantino et al., 2020; Tinto et al., 2019). Alternatively, a simple conversion factor has been proposed of 100 m of inversion uncertainty per 5 mGal of gravity uncertainty (An et al., 2019a; An et al., 2019b).
2. Assumptions of the geologic structure. The uncertainty resulting from assumptions of the geologic structure is typically simplified as uncertainties in the choice of the constant density contrast between sediment and seawater. This uncertainty is sometimes approximated as a ratio of change in density to change in inverted relief as a percentage (e.g., $\sim 3\%$ relief for 50 kg m^{-3} Tinto et al., 2019) or by altering the density and comparing the results (Boghosian et al., 2015).
3. Uncertainties in the past measurements of bathymetry (constraints). Lastly, constraint point measurement uncertainties are typically assumed to result in a 1:1 uncertainty in the inverted bathymetry (e.g., Boghosian et al., 2015; Tinto et al., 2019).

Our uncertainty analysis, through Monte Carlo simulation, provides robust spatial uncertainty estimates for each of these three sources of uncertainty. Similar to the above methods, Monte Carlo simulation only addresses uncertainties related to the uncertainty of the inputs to the inversion.

4.4 Results

Here we apply the above-described methods to recover a higher resolution bathymetry beneath Antarctica's Ross Ice Shelf. First, we show the results from an individual workflow, as depicted in Figure 4.2. This includes the starting bathymetry model, the topo-free gravity disturbance calculations, and the resulting inverted bathymetry. Next, we present the Monte Carlo simulation results, where this entire workflow is repeated many times with varying values of input data and parameters.

4.4.1 Starting bathymetry

Existing options for a starting bathymetry model for the sub-Ross Ice Shelf include Bedmap2 (Fretwell et al., 2013) or BedMachine v3 (Morlighem, 2022; Morlighem et al., 2020). BedMachine v3 for the Ross Ice Shelf contains the gravity-inverted bathymetry results from Tinto et al. (2019). To avoid over-interpretation of the gravity data (starting an inversion with the results of a separate inversion) we opted to not use BedMachine for the starting model. Bedmap2 bed elevations for the Ross Ice Shelf were created through the interpolation of the point constraints (Fretwell et al., 2013). These point constraints within the ice shelf (Figure 4.1b) were compiled from several surveys, including the early traverses of the 1950s and 60s (Crary et al., 1962; Crary, 1959; Crary & Robinson, 1962)³, and the Ross Ice Shelf Geophysical and Glaciological Survey (RIGGS, 1973-1974 Bentley, 1984) ($N = 223$). However, the gridding algorithm used (ArcGIS Topogrid), while producing smooth results for the Ross Ice Shelf, didn't strictly adhere to the constraint point depths. This can be seen through the comparison of constraint point depths and Bedmap2 grid values at the same location (Figure 4.1b). The RMS difference between the constraint depths and the grid depths within the ice shelf is 138 m. The largest differences are concentrated along the Transantarctic Mountain Front, where Bedmap2 grid values are much shallower than the constraint points. Due to this over-smoothing of the constraints, we have opted to create our own starting bathymetry model.

Our starting model was created from the combination of various seismic survey constraint points on the ice shelf, and bed data from BedMachine v3 (Morlighem, 2022; Morlighem et al., 2020) outside of the ice shelf. To create this, the BedMachine v3 bed elevations, relative to the WGS-84 ellipsoid, were masked within the Ross Ice Shelf, based on the MEASUREs v2 Ross Ice Shelf boundary (Mouginot et al., 2017; Rignot et al., 2013). These data were converted from gridded data into point data and merged with the various bathymetry data within the ice shelf. A continuous grid of bathymetry depths at a 5 km cell size was then interpolated from the combined data inside and outside the shelf. The interpolation can be accomplished with two gridding methods, bi-harmonic splines (Sandwell, 1987), and minimum curvature (Smith & Wessel, 1990). While the bi-harmonic spline method appears to have several advantages over minimum curvature (Chapter 3 Section 3.4.2), such as the ability to apply weights to the data, interpolating the above Ross Ice Shelf data resulted in significant unconstrained minima and maxima. Initial inversion results showed these erroneous features carry through to the final inverted bathymetry. Due to this, we have opted to interpolate the data to create the starting bathymetry model using tensioned minimum curvature. This method resulted in less extreme un-constrained minima and maxima.

To test the importance of the tension value used in the minimum curvature gridding, we performed 6 interpolations, with tension values of 0, 0.2, 0.4, 0.6, 0.8, and 1 (Figure 4.9a-f). From these six resulting bathymetry models, we calculated the standard deviation (Figure 4.9g) and the cell-specific mean (Figure 4.9h). These statistics were weighted, in the same method described in Figure 4.7d. The weight

³These surveys included the Ross Ice Shelf Traverse (1957-1958), the Little America Station Byrd Trail Traverse (1958), the Victoria Land Traverse (1958-1959), and the Discovery Deep Traverse (1960), see Bennett (1964) for the data and descriptions.

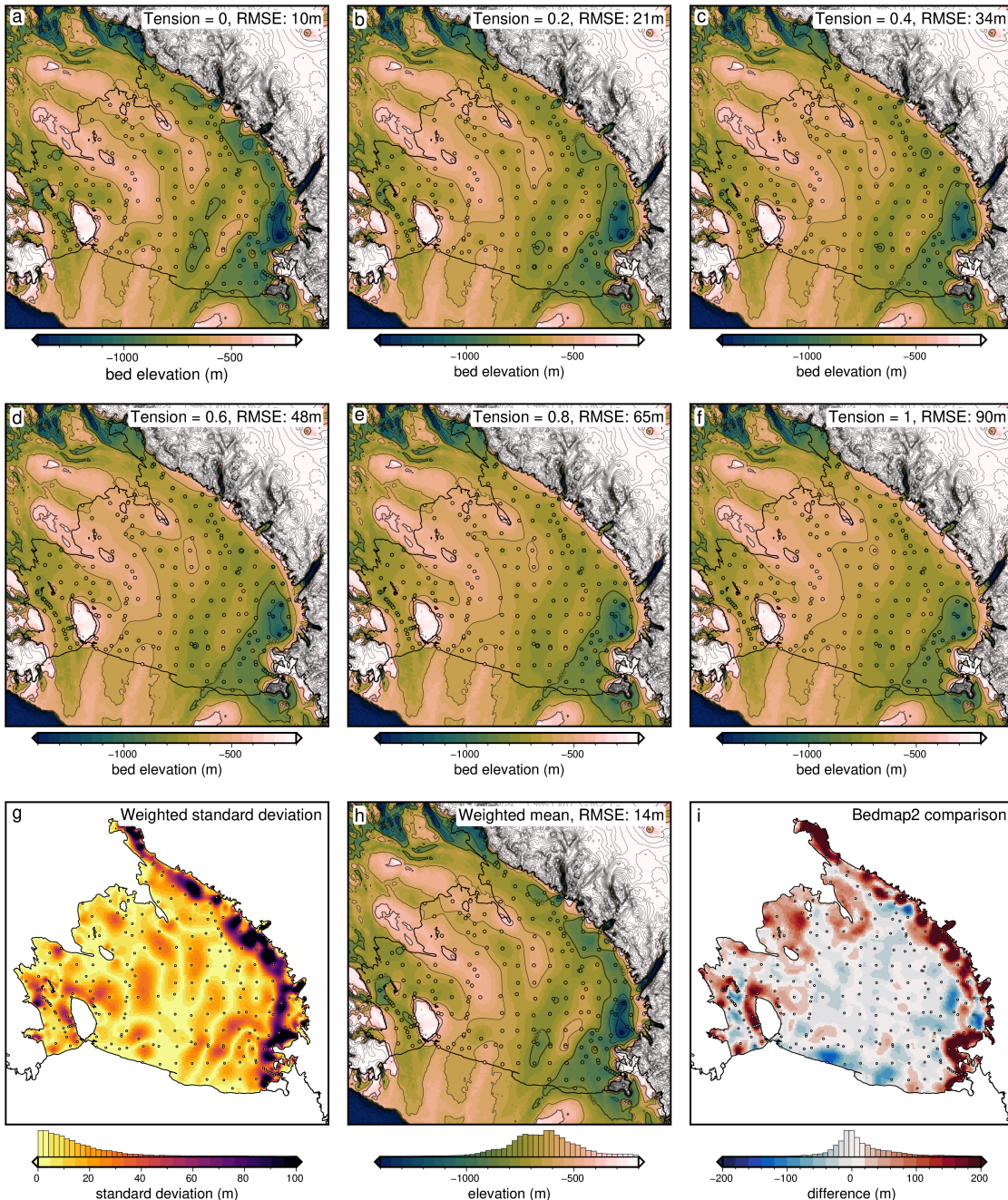


Figure 4.9: Starting bathymetry models from the interpolation of constraint points within the ice shelf and BedMachine v3 gridded data outside of the shelf (Morlighem, 2022; Morlighem et al., 2020). The ice shelf border, from Mouginot et al. (2017), is shown as the solid black line, representing the grounding line and the calving front. **a-f)** Bathymetry models resulting from 6 varying tension factor values of minimum curvature interpolation. Contours shown at 400 m intervals. **g)** The cell-specific weighted standard deviation of the six models (**a-f**). **h)** The cell-specific weighted mean bed elevation from the six models. **i)** The difference between Bedmap2 bathymetry and the mean model (**h**). The RMS difference is 95 m. Blues show where the mean model is shallower than Bedmap2, while reds show where the mean model is deeper. Root mean square error (RMSE) values in the plot titles are between the constraint point depths and the values at those points on the interpolated grids.

value used for each grid was the inverse square of the RMS difference between the constraint point depth values and the resulting grid values at the same points. These RMS values are shown in the figure titles of Figure 4.9a-f. This weighted mean starting model is compared to Bedmap2 bathymetry (Figure 4.9i). Note that

while low tension factors result in models that closely match the constraints, they also produce local maxima and minima away from the data, which is not ideal since these features can be seen to carry through the inversion to the final bathymetry, as discussed later. Alternatively, higher tension values produce models that don't match the constraints as well (higher RMS values), but they don't have as many erroneous features. For this reason, we use the cell-specific mean of the six models as our starting bathymetry (Figure 4.9h). This model has an RMS difference from BedMap2 within the ice shelf of 95 m.

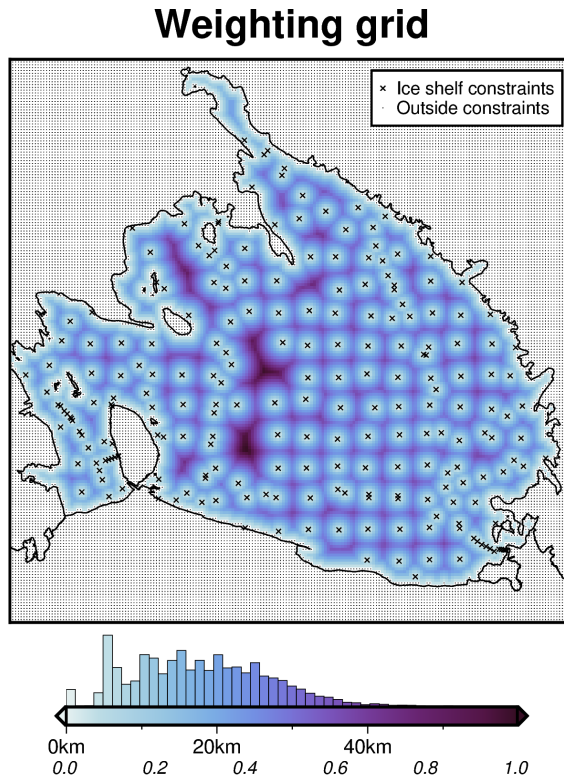


Figure 4.10: Weighting grid used in the Ross Ice Shelf bathymetry inversion. Grid colours show both the distance between each grid cell and the nearest constraint point and the weight values (0 - 1) from the normalization of these distances. Constraint points are defined as either direct measurements of bathymetry within the ice shelf (black crosses), or any grid cell outside of the ice shelf (small black dots). The ice shelf border, from Mouginot et al. (2017) is shown as the solid black line, representing the grounding line or the calving front.

From these constraint points used to create the starting bathymetry, a weighting grid was created (Figure 4.10). This grid was calculated from the distance between each grid cell and the nearest constraint point. This minimum constraint distance (top annotations of Figure 4.10 colourbar) was then normalized between 0 and 1 to create the weighting grid (bottom annotations of Figure 4.10 colourbar). As all grid cells outside of the ice shelf border are considered constraint points non-zero weights and minimum constraint distances are confined to within the ice shelf border. The colourbar histogram shows a mean minimum constraint distance within the ice shelf of approximately 20 km, and an upper limit of approximately 60 km. Within the shelf, there are 223 constraint points. Over an area of $\sim 480,000 \text{ km}^2$ (Mouginot et al., 2017), this equates to a constraint density of ~ 1 constraint per $46 \times 46 \text{ km}$ (2154 km^2).

4.4.2 Gravity processing results

We use airborne gravity data from the Ross Ocean and ice Shelf Environment, and Tectonic setting Through Aerogeophysical surveys and modelling project (ROSETTA-Ice). This project was created with the goal of investigating the interactions between ice, ocean, and earth of Antarctica's Ross Ice Shelf (Tinto et al., 2019). The survey consisted of 3 field seasons (2015-2017) of airborne geophysical surveying with a survey design consisting of E-W flight lines, at a nominal spacing of 10 km, and N-S tie lines with a nominal spacing of 55 km (Figure 4.1a). Flights were flown at an average of 750 m above the ice surface and a speed of 180 knots (93 ms^{-1}). The survey was designed to maximize the overlap between the flight lines and the past bathymetry constraints across the ice shelf from the RIGGS seismic surveys (Bentley, 1984). The data collection and initial processing were performed by Tinto et al. (2019) and are briefly summarized here. The gravity data were collected with a combination of a LaCoste and Romberg gravimeter upgraded with a ZLS UltraSys control system, an iMAR inertial measurement unit, and a DgS gravimeter. The ZLS data were tied to an absolute gravity reference station at McMurdo Station. Poor-quality data from the ZLS were replaced with the iMAR or DgS values. The accelerations of the aircraft were calculated from GPS data and removed from the gravity signal. The Eötvös correction was applied, to account for measuring gravity on a moving platform (Harlan, 1968). At each observation point, the effects of the normal earth were calculated and removed, giving the gravity disturbance values (See Section 4.2.1.1). Levelling was then performed using the cross-over values between E-W flight lines and N-S tie lines.

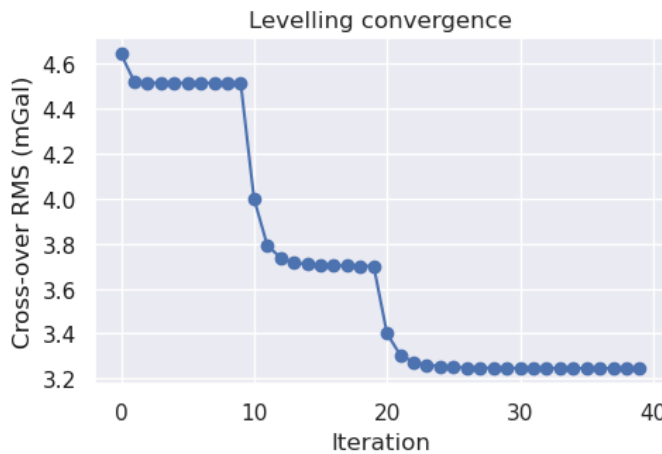


Figure 4.11: Re-leveling of the ROSETTA-Ice gravity data. First, flight lines were individually upward continued, then cross-over point mistakes were found. These were used in 0th, 1st, and 2nd order iterative levelling, alternating between levelling flight lines to tie lines and vice versa at each iteration. The RMS cross-over errors at each iteration are shown. The major steps show the 0th, 1st, and 2nd order stages of levelling.

Since this bathymetry inversion is strongly influenced by noise in the gravity data, as demonstrated in Chapter 3 Section 3.6.3.1, we have performed additional processing to the published ROSETTA-Ice dataset. Erroneous sections of flight line data were manually removed, and the dataset was re-leveled. The levelling procedure utilizes the gravity difference between E-W and N-S flight lines at cross-over points. While the flight paths intersect in 2-D space, their altitudes typically differ,

meaning there is no true cross-over point in 3-D space. To account for this, the flight lines are individually upward continued to a constant elevation of 1 km (ellipsoidal height). The mean elevation of the cleaned data was ~ 790 m, and 1 km was greater than 96% of the data. This limited the amount of downward continuation while retaining a spatial resolution close to the original data. This continuation was calculated using the equivalent source technique (see Section 3.3.1.5 Dampney, 1969; Soler & Uieda, 2021). Since the cross-over points are now true 3-D intersections, the difference between E-W and N-S lines at these points (mis-ties) can be used to re-level the dataset. Here, we alternate between levelling the E-W lines to the N-S lines, and vice versa. We start with a 0th order levelling, where only DC shifts are applied. Followed by a 1st and 2nd order levelling, where 1 and 2-degree polynomials, respectively, are fit to the mis-ties, and used to level the lines. The results of this levelling procedure are shown in Figure 4.11. For each order of levelling several iterations are performed. The step-wise convergence of the RMS mis-tie values shows the 0th, 1st, and 2nd order levelling stages. The re-leveelling procedure brought the RMS mis-tie from ~ 4.8 mGal to ~ 3.2 mGal.

Finally, this re-levelled gravity disturbance line data were gridded onto a regular grid at 2.5 km spacing, using equivalent sources. Since the inversion only affects the bathymetry within the ice shelf border, as implemented with the weighting grid (Figure 4.10), the interpolated gravity grid is masked beyond 10 km outside of the ice shelf border (Figure 4.11b). This 2.5 km gridded data ($N = 85,914$) consists of both the *testing* ($N = 64,435$) and *training* ($N = 21,479$) sets used in the cross-validation. With the grid configuration shown in Chapter 3 Figure 3.4, the *training* data used in the actual inversion are on a regular 5 km grid.

4.4.3 Gravity reduction results

The terrain mass effect was calculated at each of the gridded gravity data points. For this calculation, the three layers of prisms shown in Figure 4.5c-e were created from BedMachine v3 (Morlighem, 2022; Morlighem et al., 2020) ice surface and water surface data and the mean starting bathymetry from Figure 4.9h. All data are referenced to the WGS-84 ellipsoid. The ice surface elevations used from BedMachine v3 are in ice equivalent, meaning they have had a firn depth correction applied, making for a slightly lower surface elevation to account for spatially variable firn thickness (Morlighem et al., 2020). An ice equivalent surface is suitable for calculating the terrain mass effect since it gives the estimated thickness of the ice shelf with a density of ice, instead of the true ice shelf thickness, with a layer of low-density firn above. Comparing the forward gravity calculated from the true geometry of ice shelf thickness, the ice equivalent thickness, and a 2-layer model with firn and ice, show minimal differences, and thus we use the ice equivalent thickness in the terrain mass effect. The densities used in the terrain mass effect calculations were 1 kg m⁻³ for air, 915 kg m⁻³ for ice, 1024 kg m⁻³ for seawater (Griggs & Bamber, 2011), and 2300 kg m⁻³ for seafloor. Since we use a single value for the density of the seafloor, it should represent the expected average density of the seafloor over the entire region. Chapter 2 showed a continuous drape of sediment over the seafloor. We chose 2300 kg m⁻³ to be in the middle between unconsolidated sediment (~ 1900 kg m⁻³) and low-density crystalline rock (~ 2700 kg m⁻³) (Schön, 2015). The inversion domain

was 1 million km² (1000 km × 1000 km). To avoid gravitational edge effects in the forward calculations, the prism layers were extended in all directions by a 40 km buffer zone, resulting in 120,000 prisms. The resulting terrain mass effect was subtracted from the gravity disturbance to get the topo-free gravity disturbance. These data are shown in Figure 4.12.

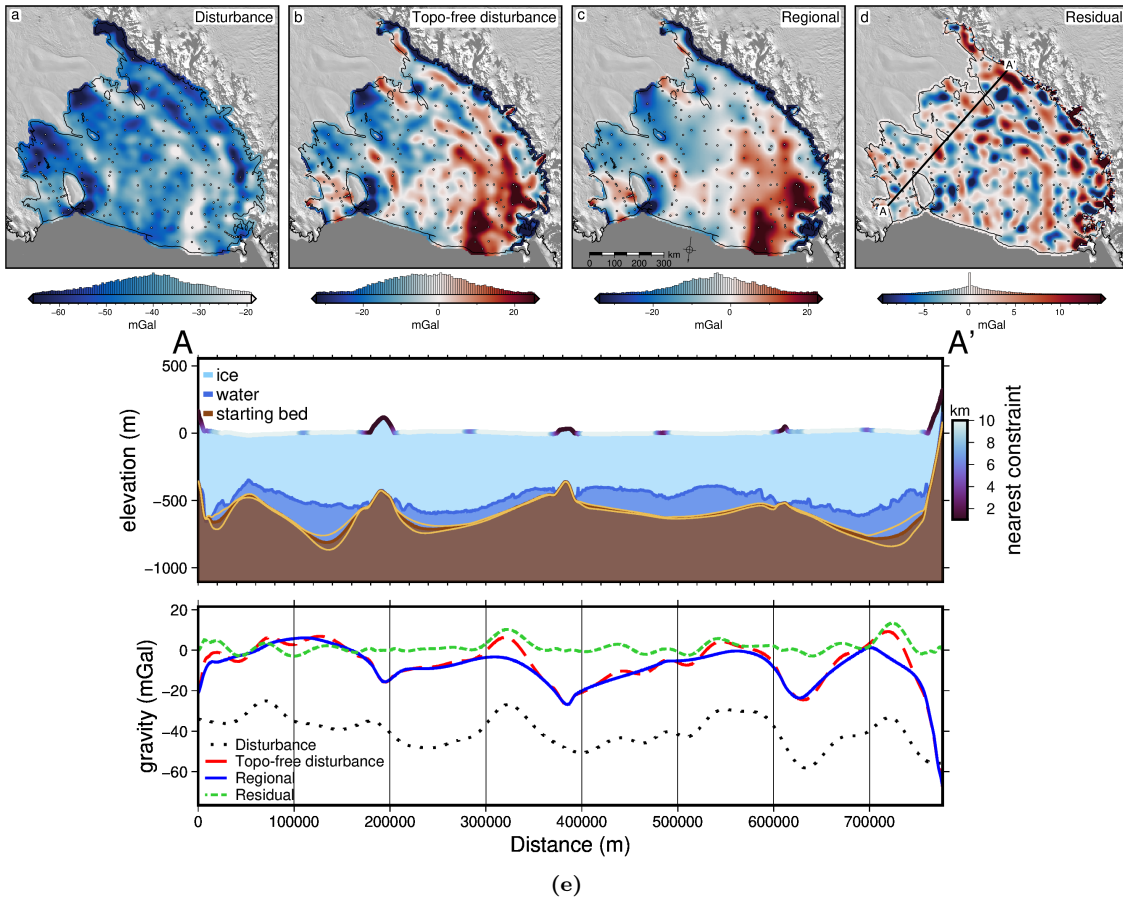


Figure 4.12: Gravity reduction results for the Ross Ice Shelf. **a)** Gravity disturbance, **b)** topo-free gravity disturbance, after the removal of the terrain mass effect, **c)** regional component of the topo-free disturbance, estimated with constraint point minimization, and **d)** residual component of the topo-free disturbance, as the difference between **b** and **c**. Background imagery is from MODIS-MOA (Scambos et al., 2007) and grounding line and coastlines are from (Morlighem, 2022). Constraint points within the ice shelf are shown as dots. **e)** Profile from A to A', location shown in **d**. **Upper panel** shows cross-section, with ice surface and ice base from BedMachine v3 (Morlighem, 2022; Morlighem et al., 2020). Brown layer shows the mean starting bed model with bounding uncertainty (light brown lines) from the standard deviation of the various starting bed models in Figure 4.9. The colour of ice surface shows the distance to the nearest constraint point. **Lower panel** shows data from **a-d** along the profile.

The topo-free gravity disturbance was subsequently separated into the regional and residual components. This was accomplished with constraint point minimization (Chapter 3 Section 3.2.4). While the synthetic data of the past chapter showed a clear benefit of using a bi-harmonic spline interpolation over a minimum curvature interpolation, we use minimum curvature here. As with the interpolation for the starting bathymetry model, bi-harmonic spline interpolation led to excessive unconstrained maximum or minima. The resulting regional and residual components are shown in Figure 4.12.

4.4.4 Inversion results

With the residual component of the topo-free gravity disturbance as the inversion input (Figure 4.12d), we ran 10 inversions with varying levels of damping. Each inversion used a density of 1024 kg m^{-3} for ocean water and 2300 kg m^{-3} for the density of the seafloor. For each value of the damping parameter, the cross-validation score was calculated by forward modelling the gravity effect of the resulting bathymetry model onto the locations of the testing gravity data. The RMS difference between the residual component of the topo-free gravity disturbance and the forward-modelled results at these testing points gave the score. These scores are shown in Figure 4.13a. The lowest score was achieved with a damping value of 10^{-2} .

This inversion took 8 iterations and 135 seconds⁴ and converged due to a lack of change in the ℓ^2 -norm between subsequent iterations (Figure 4.13b). The RMS of the residual gravity started at 6.1 mGal prior to the inversion and was reduced to 4.0 mGal (Fig 4.13b).

The inverted bathymetry model for the sub-Ross Ice Shelf, at a 5 km resolution, is shown in Figure 4.13c. Note that this is just the result of a single inversion. Our final inverted bathymetry model is achieved through the Monte Carlo simulation, as described below. The RMS difference between the inversion results and the starting model at the constraints is 16 m. The thickness of the water column, defined as the difference between BedMachine v3 ice base and the inverted bathymetry, is shown in Figure 4.13d.

4.4.5 Uncertainty

We used a series of Monte Carlo simulations (Figure 4.7) to assess both the spatial uncertainty of the resulting inverted bathymetry and the importance of the various components and parameters of the inversion. By varying the inputs of the inversion within their ranges of uncertainties, we can gather a range of the possible bathymetry results, which when compared shows where the inversion results are more or less certain. The inputs and their respective uncertainty distributions included in the sampling are:

1. Gravity disturbance data; sampled from a normal distribution with a mean of the data point, and a standard deviation of the RMS mis-tie of the line data after levelling (3.3 mGal).
2. Constraint point depths; sampled from a normal distribution with a mean of the measured depth, and a standard deviation of 10 m for points outside of the ice shelf, and 5% of depth from the ice surface for points within the ice shelf (mean of 36 m).
3. The density of ice, water, and sediment; all sampled from normal distributions with means of 915 kg m^{-3} , 1024 kg m^{-3} , and 2300 kg m^{-3} respectively, and standard deviations of 5 kg m^{-3} , 5 kg m^{-3} , and 400 kg m^{-3} . The small standard deviations of ice and water compared to sediment reflects the relative certainty

⁴See Appendix 1.6 for a description of the hardware used.

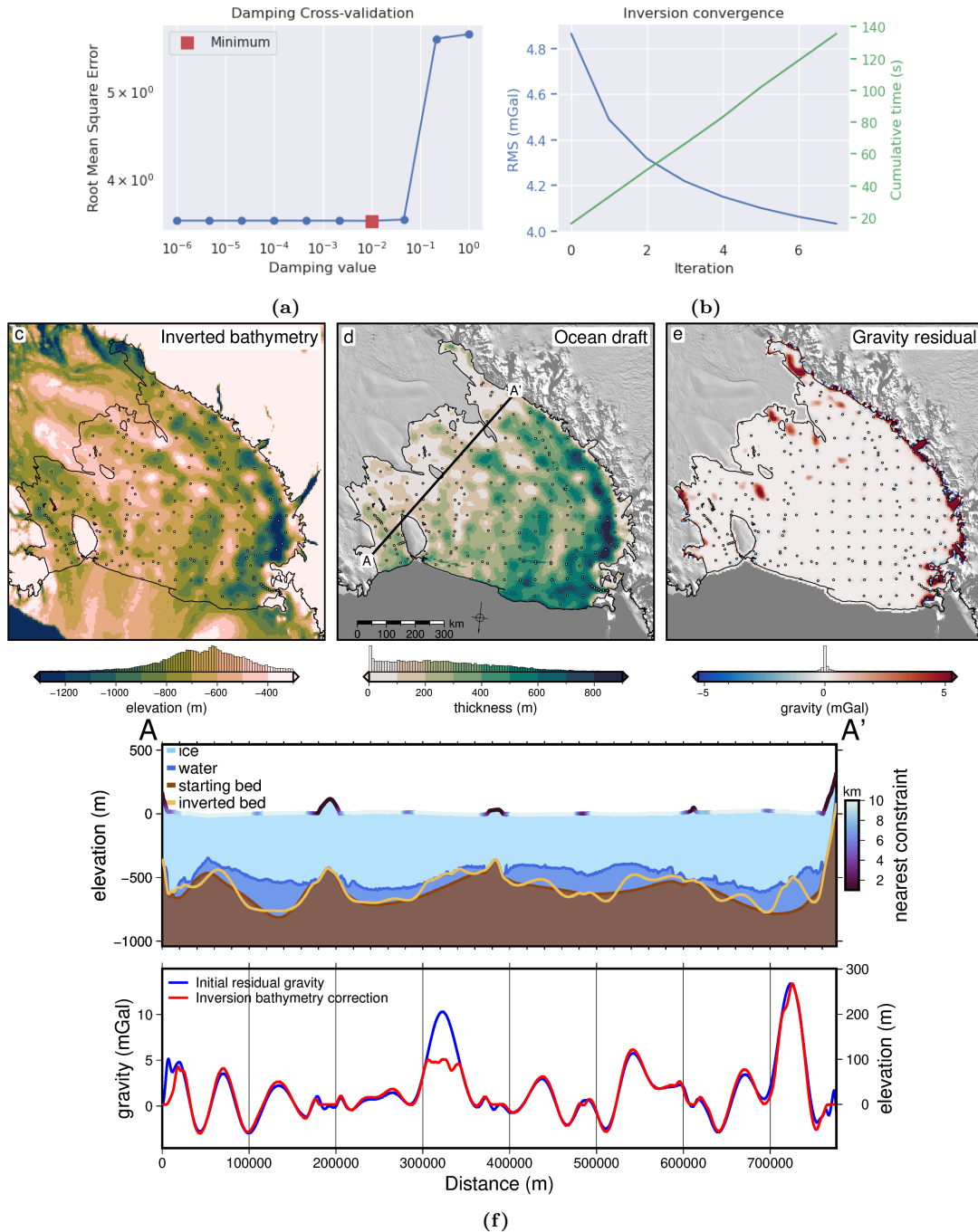


Figure 4.13: Ross Ice Shelf singular bathymetry inversion results. **a)** Damping parameter cross-validation with the lowest score shown in red. **b)** Convergence curve and cumulative inversion time for the optimal inversion. Blue line (left y-axis) shows consecutive iteration's RMS residual component of the topo-free gravity disturbance. Green line (right y-axis) shows cumulative time to run the inversion. **c)** Inverted bathymetry, **d)** water column thickness between the inverted bathymetry and Bedmachine v3 icebase (Morlighem, 2022; Morlighem et al., 2020), **e)** final residual component of the topo-free gravity disturbance. **f)** **Profile A to A'**. **Upper panel** shows ice surface and icebase from BedMachine v3, both the starting bathymetry (dark brown) and the inverted bathymetry (light brown). The colour of the ice surface shows the distance to the nearest constraint point. **Lower panel** shows the initial residual gravity used as input to the inversion (blue line, left y-axis), and the total correction (red line, right y-axis) applied to the starting bathymetry surface during the inversion to get the inverted bathymetry.

of the value and spatial heterogeneity of the density of ice and water, compared to those of the material comprising the sea floor. For the Ross Ice Shelf,

the entire region is likely to be draped is at least 10's of meters of sediment (Chapter 2, Tankersley et al., 2022). With a mean of 2300 kg m^{-3} and a standard deviation of 400 kg m^{-3} , these values span the range from unconsolidated sediment to low-density crystalline rock (Schön, 2015).

4. The tension factor used in minimum curvature gridding for interpolating both the starting bathymetry model and the regional component of gravity. The tension factor values were sampled from a uniform distribution between 0 and 1.

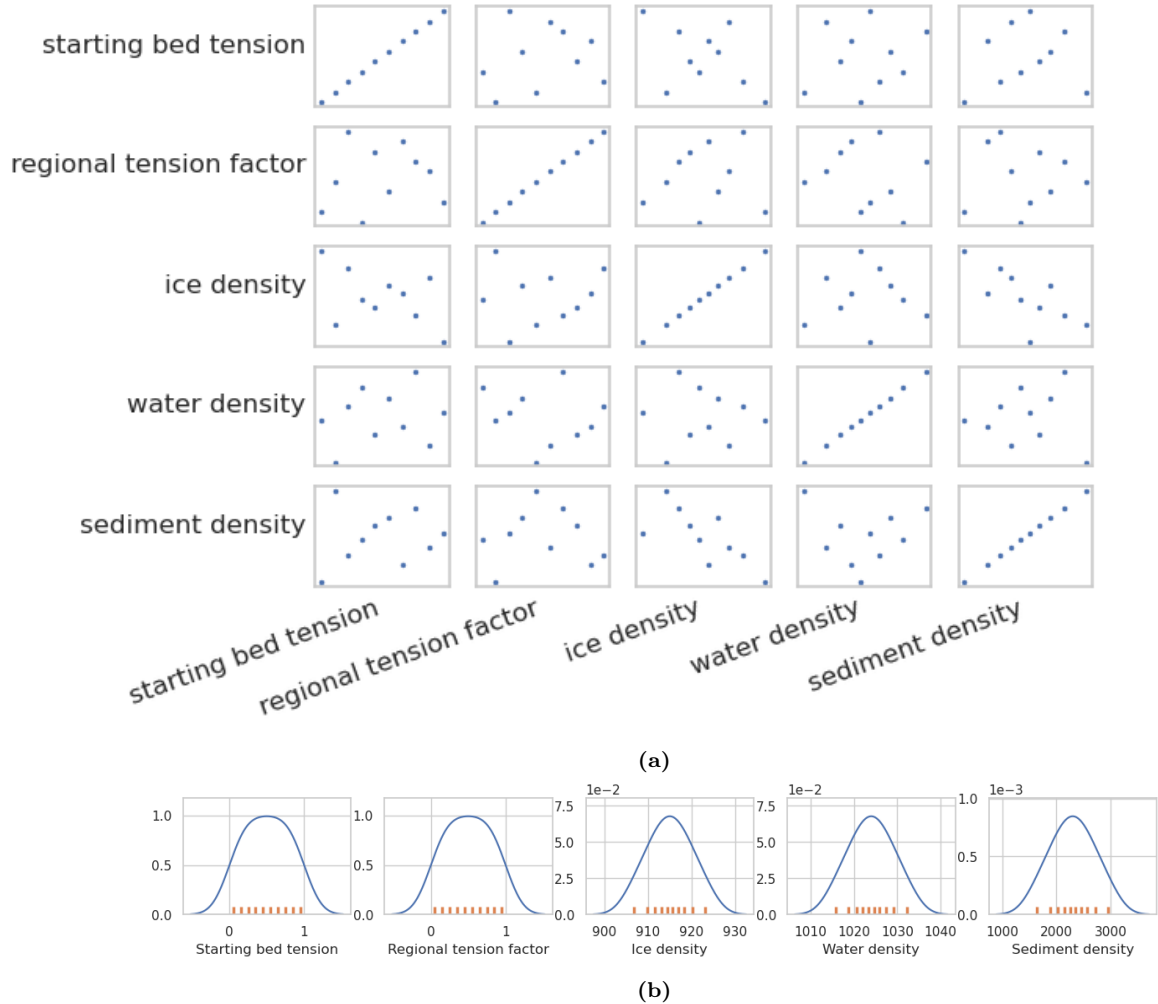


Figure 4.14: Latin hypercube sampling results for the 10 inversions of the full Monte Carlo simulation. **a)** Correlations between each pair of the 5 sampled input parameters. **b)** Resulting distributions of the 10 sampled values of each parameter. Blue line shows kernel density estimates fit to each set of sampled values, which are shown as orange ticks.

Figure 4.14 shows the results of the Latin hypercube sampling of the 5 input variables (not including the gravity and constraints data). The correlations between each set of variables show that pairwise correlation was minimal. This is ideal since these inputs are unrelated, and therefore their sampled values should be uncorrelated (Helton et al., 2006). This also shows that with only 10 samplings, the Latin hypercube sampling was able to provide adequate spatial coverage of the individual distributions (4.14b) as well as all the pairwise distributions combinations (4.14a).

Each simulation consisted of 10 runs. We performed a *full* simulation, where each of the above inputs were sampled (Figure 4.15). We performed five additional

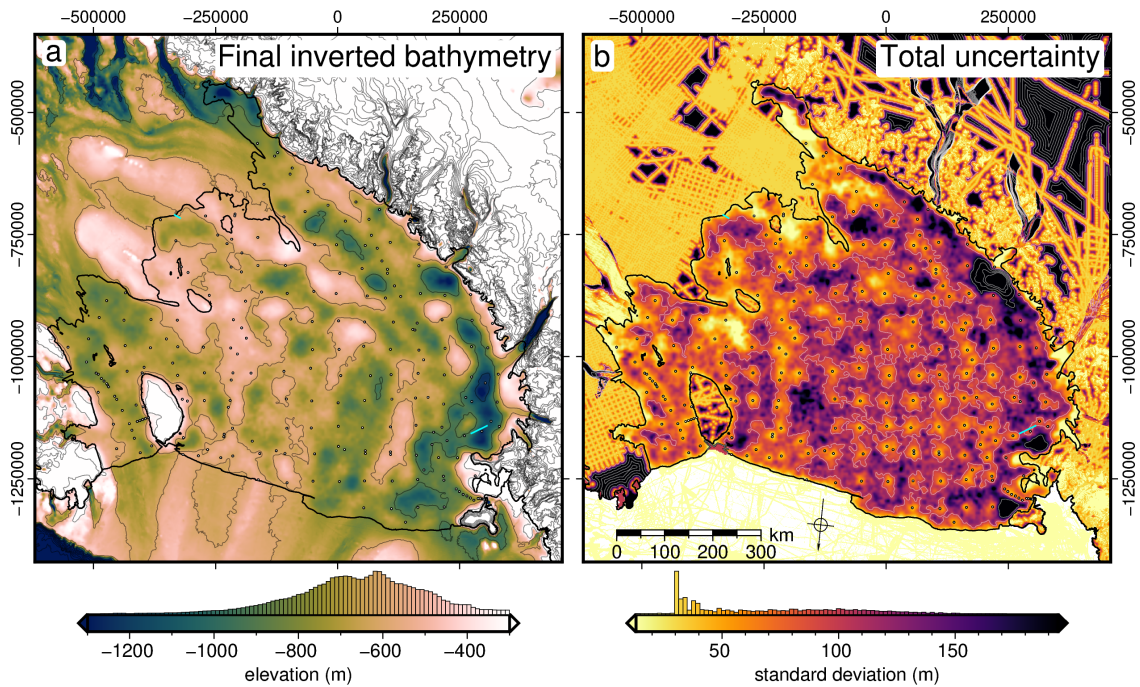


Figure 4.15: Final bathymetry depths and uncertainties from the full Monte Carlo simulation, merged with 500m resolution elevation and uncertainty data outside of the shelf from BedMachine v3 (Morlighem, 2022; Morlighem et al., 2020). **a)** Final inverted bathymetry model, calculated as the weighted mean of the full Monte Carlo simulation. Shown with 300 m contours. **b)** Uncertainty estimation of the inverted bathymetry from the cell-specific weighted standard deviation of the inverted bathymetry results from the full Monte Carlo simulation. Shown with 100 m contours. Constraints within the ice shelf are shown as dots in **a**. Grounding line and coastline are shown in black (Morlighem, 2022). Background imagery is from Scambos et al. (2007). Cyan lines show Discovery Deep and Kamb Ice Stream seismic surveys.

simulations (Figure 4.16) where 1) only the gravity data were sampled, 2) only the constraint point depths were sampled, 3) only the density values of ice, water, and sediment were sampled, 4) only the tension factor for interpolating the starting bathymetry model was sampled, and finally 5) only the tension factor for interpolating the regional component of gravity was sampled. Each simulation results in a series of inverted bathymetries. Finding the cell-specific weighted standard deviation of the bathymetry depths for each of these simulations gives an estimation of the uncertainty resulting from the associated parameter. The cell-specific statistics of these simulations were low-pass filtered to remove high-frequency noise induced by the random sampling. For the full simulation (Figure 4.15b) the weighted mean of the resulting bathymetries gives the final inverted bathymetry results of this study (Figure 4.15a). Note that this final bathymetry model resulting from the Monte Carlo simulation is similar, but distinct from the inverted bathymetry resulting from a single inversion without the Monte Carlo simulation, shown in Figure 4.13c.

The final bathymetry and uncertainty grids were resampled to a resolution of 500 m, from their original 5 km resolutions, masked outside of the ice shelf, and merged to the 500 m resolution bed and uncertainty data of BedMachine v3. This final bathymetry has a mean elevation of ~ 700 m within the ice shelf. The deepest point is $\sim -1370 \pm 187$ m, located near the Byrd Glacier outlet (Figure 4.1b). Bathymetric features appear to have continuity with features from BedMachine v3 data outside of the ice shelf. The RMS difference between the bathymetry and the

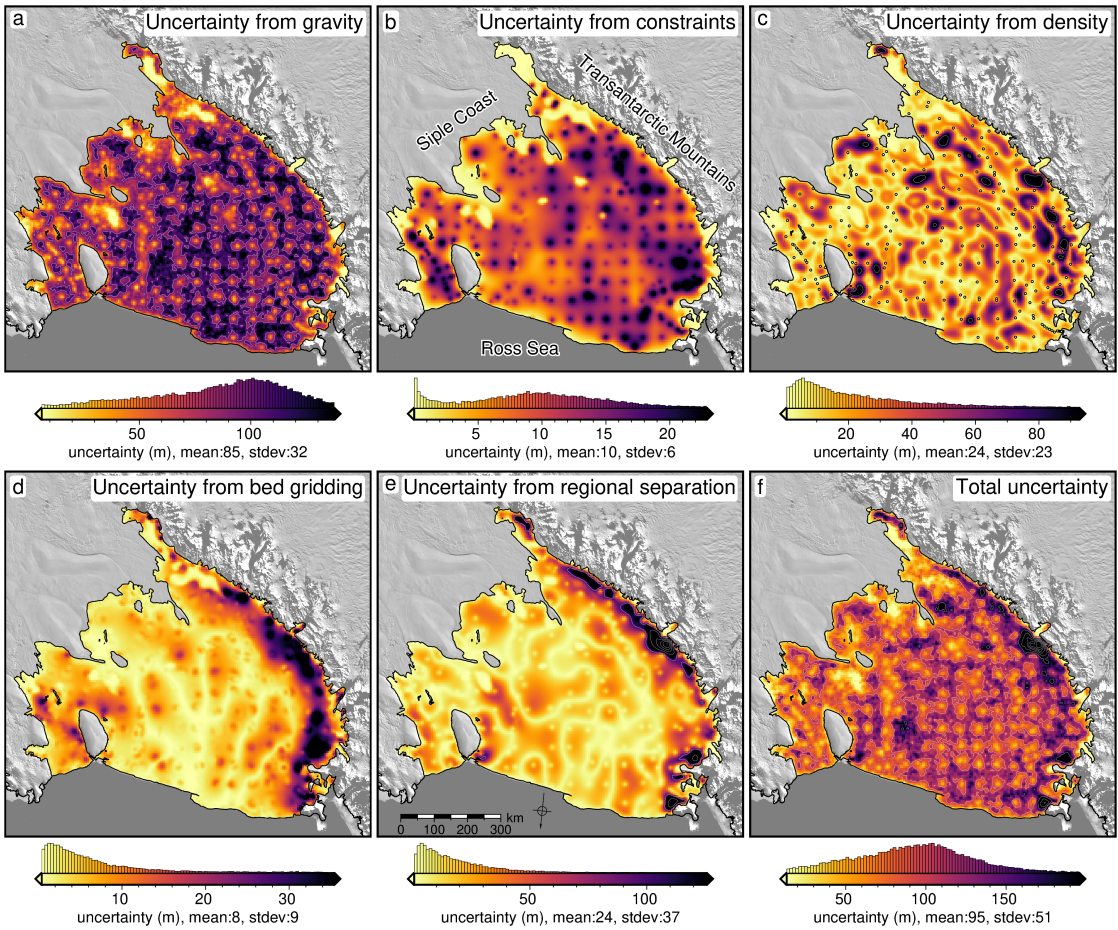


Figure 4.16: Sensitivity analysis for the inversion input data and parameters. Cell-specific weighted standard deviations of the inverted bathymetry results from Monte Carlo simulations with sampling the uncertainties of the **a)** gravity data, **b)** constraint points depths, **c)** ice, water, and sediment density values, **d)** starting bed interpolation tension factor, and **e)** tension factor for interpolating the regional gravity component. **f)** The total uncertainty from the full simulation. 100 m contours in white. Constraints within the ice shelf are shown as dots in **c)**. Grounding line and coastline shown in black (Morlighem, 2022). Background imagery is from Scambos et al. (2007).

original constraint point depths is 44 m. Subtracting the bathymetry from the ice base elevations of BedMachine v3 (Morlighem, 2022; Morlighem et al., 2020) gives the water column thickness, as shown in Figure 4.18b. Without ice base uncertainty estimates from BedMachine v3, we use the bathymetry uncertainty as our uncertainty for the water column thickness, acknowledging that this is a minimum uncertainty. Within the ice shelf boundary, this water column thickness has a mean value of 260 m and a maximum of 1000 m, located near the Nimrod Glacier outlet. Here, the bathymetry has an uncertainty of ± 800 m. Outside of this region, the thickest ocean cavity is $\sim 940 \pm 180$ m, located at the Byrd Glacier outlet. The similarity between the bathymetry depth and the water column thickness shows that the ocean cavity is predominantly controlled by bathymetry and that the ice base topography is smooth compared to the bed. The uncertainty in the bed elevation ranges from $\sim 10 - 850$ m, with a mean of 95 m (Figure 4.13b). It has an approximately normal distribution, with a slight skew to the higher values. In general, the uncertainty is lowest at the constraint points and highest far from constraints. There are elevated uncertainties in several spots, with the largest being along the Transantarctic mountain front.

4.4.5.1 Partitioning uncertainty

The uncertainty in the inverted bathymetry which arises from the uncertainty in gravity data (Figure 4.16a) is relatively spatially uniform, with a mean of 85 m. It is lowest immediately at the constraint points, and generally highest far from constraint points. The uncertainty from the constraint point depths (Figure 4.16b) is also generally spatially uniform, with a mean of 10 m. Conversely, it is highest at the constraint points, and lowest far from constraint points. The uncertainty resulting from the choice of density values (Figure 4.16c) displays a more heterogeneous spatial distribution than the previous two uncertainties. It is lowest at the constraint points and has a mean of 24 m. The largest values are located at the gaps between constraint points. The uncertainty resulting from the interpolation of the starting bed (Figure 4.16d) has a distinct spatial distribution. It is highest along the Transantarctic Mountain front, with values up to 40 m, but it has an overall mean of 7 m. Lastly, the uncertainty resulting from the estimation and removal of the regional component of gravity, prior to the inversion, (Figure 4.16e), also shows highest values along the mountain front, with values over 200 m (up to 700 m at the Nimrod Glacier outlet). The mean value is 24 m. The reported uncertainties and their components from a wide range of past studies are shown in Table 4.1.

4.5 Discussion

Here we discuss the results of our Ross Ice Shelf bathymetry model from the inversion of airborne gravity data. First, we describe the results of the uncertainty and parameter sensitivity analysis. Then we compare our results with two past bathymetry models beneath the Ross Ice Shelf and discuss the differences. Lastly, we discuss various implications of this updated bathymetry model, including how the findings relate to geology, tectonics, and ice sheet dynamics.

4.5.1 Uncertainties and parameter importance

The results of our Monte Carlo simulations provide answers to several important questions. 1) How confident are we in the inverted bathymetry depths? 2) Where are we most and least confident about the bathymetry depth? 3) What are the specific sources of this uncertainty? and finally, 4) What can be done to limit the uncertainty? Figures 4.15b and 4.16f show the resulting spatial uncertainty of the inverted bathymetry, providing an answer to the first two questions. To determine the sources of this uncertainty, the individual inputs to the inversion were isolated and their effects on the estimated uncertainty were found (Figure 4.16).

4.5.1.1 Gravity component

The largest contributor to the overall uncertainty of the inversion is the uncertainty of the gravity data (Figure 4.16a). This uncertainty resulting from the gravity data results in a base-level bathymetry uncertainty of ~ 85 m and is relatively spatially

Study	Inverted bathymetry uncertainty (m)			
	total	from gravity	from geology	from constraints
This study ($\bar{x} \pm 1\sigma$)	95±51	85±32	48±30	10±6
Eisermann et al. (2021)	220	84	116	20
Tinto et al. (2015)	160	26	124	10
Constantino et al. (2020)	133	34	90	5-10
Boghosian et al. (2015)	110	10-28	50-70	10
Tinto and Bell (2011)	70	34	10-15	20
Constantino and Tinto (2023)	69-123	32-39	27-74	10
Tinto et al. (2019)	68	48	10	10
Eisermann et al. (2020)	175-225	-	-	10
Jordan et al. (2020b)	100	23	-	-
An et al. (2019a)	60	60	-	-
Studinger et al. (2004b)	250	-	-	-
Wei et al. (2020)	246	-	-	-
Greenbaum et al. (2015)	190	-	-	-
Brisbourne et al. (2014)	160	-	-	-
Hodgson et al. (2019)	100	-	-	-
Yang et al. (2021)	68	-	-	-
An et al. (2017)	60	-	-	-
Millan et al. (2017)	50-65	-	-	-
Millan et al. (2018)	30-50	-	-	-
Millan et al. (2020)	45	-	-	-
Filina et al. (2008)	-	19	-	-
Mean	117 (N=25)	40 (N=13)	57 (N=11)	12 (N=10)

Table 4.1: Reported inverted bathymetry uncertainties and the various components. Our reported geologic uncertainty is the combination of uncertainties resulting from the density values and the tension factor used in grinding the regional field.

uniform. This is because each gridded gravity data point is contaminated with independent noise of varying levels during the Monte Carlo sampling. It is this point-by-point random noise that creates the noisy component in the final inverted bathymetry. In reality, the uncertainty of nearby gravity data is likely correlated, where entire lines, or sections of lines have similar uncertainty values, due to changing data collection conditions, like turbulence, or mis-levelling, causing values of entire lines to be offset, or tilted. Here our estimate of gravity uncertainty is entirely dependent on cross-over mistakes; likely an oversimplified estimation of uncertainty for an entire survey. This suggests that the true uncertainty resulting from the gravity data likely has a different spatial distribution and may be larger than we report; a finding which is not surprising, since the entire method depends on these data.

4.5.1.2 Constraints component

The uncertainty in the other data input to the inversion, the constraint point depths, has only a small effect on the results (Figure 4.16b). It is worth noting that while the uncertainty resulting from the constraint point measurement uncertainty is low, the constraints themselves are fundamental to the inversion. These constraints feed into all the components of the inversion and thus affect the uncertainty of each component, including the uncertainty from the gravity data. This is shown by the correlation between uncertainty and the distance to the nearest constraint (Figure 4.10) of all the components of Figure 4.16. Our Monte Carlo sensitivity analysis only tests the effects of estimated noise in the inputs, and not their overall importance for the inversion. Since the uncertainty in the constraints only impacts the inversion in the immediate vicinity of the constraint, for constraint data collection, efforts should be focused on quantity over quality, assuming the uncertainty can be limited to a reasonable amount. In practice, for over-ice seismic surveying, this may lead to the choice of fast and efficient systems as opposed to high-resolution systems, if the main goal of the survey is to collect bathymetry constraints. For example, towable snow streamers and sources such as surface detonations or vibroseis (e.g., Hofstede et al., 2021; Smith et al., 2020b) can collect data very efficiently (~ 20 km/day), compared to higher-resolution surveys with buried geophone arrays and drill-emplaced explosives (e.g., Horgan et al., 2013). The remaining sources of uncertainty are related to user-defined inversion parameters.

4.5.1.3 Density component

The choice of density values for the ice, water, and sediment results in a mean uncertainty in the bathymetry model of 24 m (Figure 4.16c). The ranges of densities tested in the Monte Carlo simulation were $\sim 905 - 925 \text{ kg m}^{-3}$ for ice⁵, $\sim 1015 - 1035 \text{ kg m}^{-3}$ for seawater, and $\sim 1600 - 3000 \text{ kg m}^{-3}$ for the seafloor. We only test homogeneous changes in the density values.

The uncertainty arising from the choice in density values has a strong spatial correlation with the absolute value of the inversion's input gravity, the residual gravity

⁵We note that the maximum density of meteoric ice is 917 kg m^{-3} , however; the inclusion of marine ice may raise this value (Fricker et al., 2001)

(Figure 4.12d). This correlation can be explained by the inverse relation between the amplitude of the corrections applied to the bathymetry during the inversion, and the density contrasts used in the inversion. For the same gravity anomaly, a smaller density contrast results in a larger amplitude correction while a larger density contrast results in a smaller correction. This means that changes in the density values just affect the amplitude of the correction applied to the bathymetry. Often, spatially variable density is used as a means to account for the regional component of gravity (e.g., Constantino et al., 2020; Tinto et al., 2019). We note that there is an additional benefit to incorporating spatially variable densities. If adequate *a priori* information is known to justify a density distribution, this can be used to allow differing amplitudes of corrections across the inversion domain. In other words, if the seafloor truly is denser in one region of the inversion compared to the seafloor elsewhere, for a similar gravity anomaly, the inversion correction should be of smaller amplitude in the high-density region. However, due to a lack of geologic knowledge beneath the ice shelf, we use constant density values. We propose Monte Carlo sampling of a wide range of possible density values as a robust and feasible method to avoid biasing the resulting bathymetry model to either too high or too low correction amplitudes, to achieve both the most realistic results and an estimation of the uncertainty.

4.5.1.4 Interpolation component

The final components of the overall uncertainty are related to interpolation conducted during two stages of the inversion; 1) the interpolation of the starting model from the sparse constraint point depths, and 2) the estimation of the regional field from the interpolation of gravity values at the constraint points. Here, we have used a minimum curvature gridding algorithm (Smith & Wessel, 1990), which accepts a tension factor for the interpolation which can range from 0 to 1. Figure 4.9 shows the results of six different values of this tension factor for creating the starting bed model. These figures show that low values of tension are able to accurately reproduce the data with a smooth interpolation, but can result in unconstrained local maxima or minima. Conversely, high tension values produce smooth surfaces without false oscillations but don't adhere to the data as well. For these issues associated with the two end members, intermediate values of 0.25 and 0.35 are often suggested for potential field data and topographic data, respectively. We suggest a more robust alternative to using these suggested values is the Monte Carlo sampling approach we have used. This runs the inversion with a variety of tension factors and uses the standard deviation of the resulting bathymetry models as a means to estimate the uncertainty associated with the choice of the tension factor. While tensioned minimum curvature gridding has been used in several past inversions (e.g., An et al., 2019a; Millan et al., 2020; Yang et al., 2021), the choice of the tension values has not been discussed for these applications.

The uncertainties arising from the choice of tension factors are shown in Figure 4.16d and e. The tension factor for gridding the starting bed model results in a relatively low uncertainty with a mean of 7 m. The resulting uncertainty for the regional separation is comparatively high, with a mean of 24 m. Both of these results show large spatial heterogeneity, with significantly larger uncertainties along the Transantarctic Mountain front. This is likely related to the poor performance

of this gridding algorithm for high-gradient data. This region along the mountain front has both steep topography and high amplitude gravity anomalies.

4.5.1.5 Reducing uncertainties

Of the various components of the uncertainty analysis, only some can feasibly be reduced. Reducing the uncertainty resulting from the interpolation parameters may be possible with future method development, but this is beyond the discussion of this research. To our knowledge, there is no robust method of determining a spatially variable density distribution to be used in the inversion, without the collection of in-situ data. This leaves the data inputs, gravity and constraints, as viable components of a bathymetry inversion where further reductions of uncertainties can occur. We propose a favourability of quantity over quality for constraint data since typical bed elevation uncertainty is already relatively low, and therefore more data of mediocre quality should be prioritized over high-quality but spatially limited data. In order to reduce the uncertainty component resulting from the gravity data, first we must be able to estimate the realistic spatial uncertainty of the gravity data itself. A simple cross-over analysis is too simple to cover the effects of turbulence, changing flight speed and altitude, and errors in processing steps, such as base station ties and levelling. The areas of largest uncertainty are generally a function of 1) distance to the nearest constraint point (Figure 4.10) and 2) proximity to steep gradients of topography and/or gravity (Figure 4.16d and e). This highlights the entire Transantarctic Mountain front of the Ross Ice Shelf and the two major constraint gaps in the central-east portion of the ice shelf (Figure 4.10) as locations that would greatly benefit from additional seismic surveying.

4.5.1.6 Past estimations of uncertainty

Our comprehensive uncertainty and sensitivity analysis is shown to be similar to the approximated uncertainties reported for other ice shelves (Table 4.1). Some differences include; our reported uncertainty resulting from the gravity data uncertainty is the highest reported, while our values resulting from other sources, and the total uncertainty, were similar to those of other studies. Our larger reported uncertainty resulting from the gravity data likely shows that the simple Bouguer slab approximation used by the other studies underestimates the component of uncertainty resulting from the gravity data uncertainty. We take the uncertainties resulting from geologic variations to be the combination of our reported uncertainties from the chosen density values (Figure 4.16c) and from the regional separation gridding (Figure 4.16e) since these both affect the estimation of the regional component. The uncertainty resulting from the constraint point measurement uncertainty was very similar across all studies.

From this, we propose future bathymetry inversions undertake similar uncertainty analysis through the Monte Carlo sampling of the input parameters. This technique not only provides similar uncertainty estimates to past studies, but it accomplishes it in a systematic and reproducible method. Additionally, this technique provides a spatial distribution of the uncertainties, instead of a single value. Once the inversion workflow is set up, the sampling and re-running of the inversion is a simple procedure, and with the use of Latin hypercube sampling, we have shown

that with only 10 runs, the parameter space of all the inputs is adequately sampled (Figure 4.8).

4.5.2 Past bathymetry models

Our gravity-inverted bathymetry model for the sub-Ross Ice Shelf reveals significant differences with previous bathymetry models. However, a portion of these differences are not related to the inversion, but to the creation of the starting model. First, we will discuss the differences between our starting bathymetry model and another interpolation-based bathymetry model, then we will compare our inversion results with two past models. These past models include Bedmap2 (Fretwell et al., 2013) and BedMachine v3 (Morlighem, 2022; Morlighem et al., 2020). The Bedmap2 model for the Ross Ice Shelf region is created from the interpolation of the same constraint points within the ice shelf as used in this study, as well as grounded ice thickness measurements and limited rock outcrop elevation data (Fretwell et al., 2013; Le Brocq et al., 2010; Timmermann et al., 2010). BedMachine v3 used these point measurements and applied additional methods to increase the resolution of the bed. For outside of the ice shelf, this included mass conservation for areas of fast-moving ice (outlet glaciers and ice streams), streamline diffusion for regions of slow-moving ice, as well as minimum curvature gridding to interpolate the remaining gaps (Morlighem et al., 2020). Within the ice shelf, BedMachine used the gravity inversion results of Tinto et al. (2019).

4.5.2.1 Starting model comparison

Figure 4.9 shows the series of six starting bed models we created from the interpolation of the sparse constraints. These were created with six levels of tension applied to a minimum curvature interpolation. The cell-specific standard deviation of these six models shows the uncertainty associated with this interpolation (Figure 4.9g), and the mean of the six grids is our chosen starting model (Figure 4.9h). This is compared with the Bedmap2 model in (Figure 4.9i). The RMS difference between the two grids, within the ice shelf, is 95 m. Our starting bed is deeper proximal to the entire grounding zone, while it is shallower along the ice front and throughout the centre of the ice shelf. However, these differences of up to 200 m do not suggest our starting model is inaccurate. Sampling the grid values at the constraint points and comparing them with the constraint depths shows that our model was significantly better at adhering to these constraints, compared to Bedmap2. The RMS of the difference with our model was 14 m, while the RMS of Bedmap2 was 138 m (Figure 4.1).

These large differences for Bedmap2 are concentrated along the Transantarctic Mountain front, where the interpolation algorithm used in Bedmap2 resulted in excessively shallow bathymetry. This interpolation appears to have favoured smoothness over accuracy for this location of steep terrain. This has resulted in a "leakage" of the high elevations within the mountains into the bathymetry interpolation, as pointed out in this region (Le Brocq et al., 2010), as well as for other ice shelves (Brisbourne et al., 2020). This over-smoothing and "leakage", while strongest along the mountain front, can be seen along the entire grounding zone. This is the reason

why Bedmap2 was shallower than our starting model along the grounding line. This shows that care needs to be taken when picking or creating a starting model for an inversion, especially in regions of steep topography. The re-creation of the starting model from the point data allows the choice of interpolation techniques better suited for the region of interest, compared to techniques determined most suitable for a continent-wide study.

4.5.2.2 Inversion result comparisons

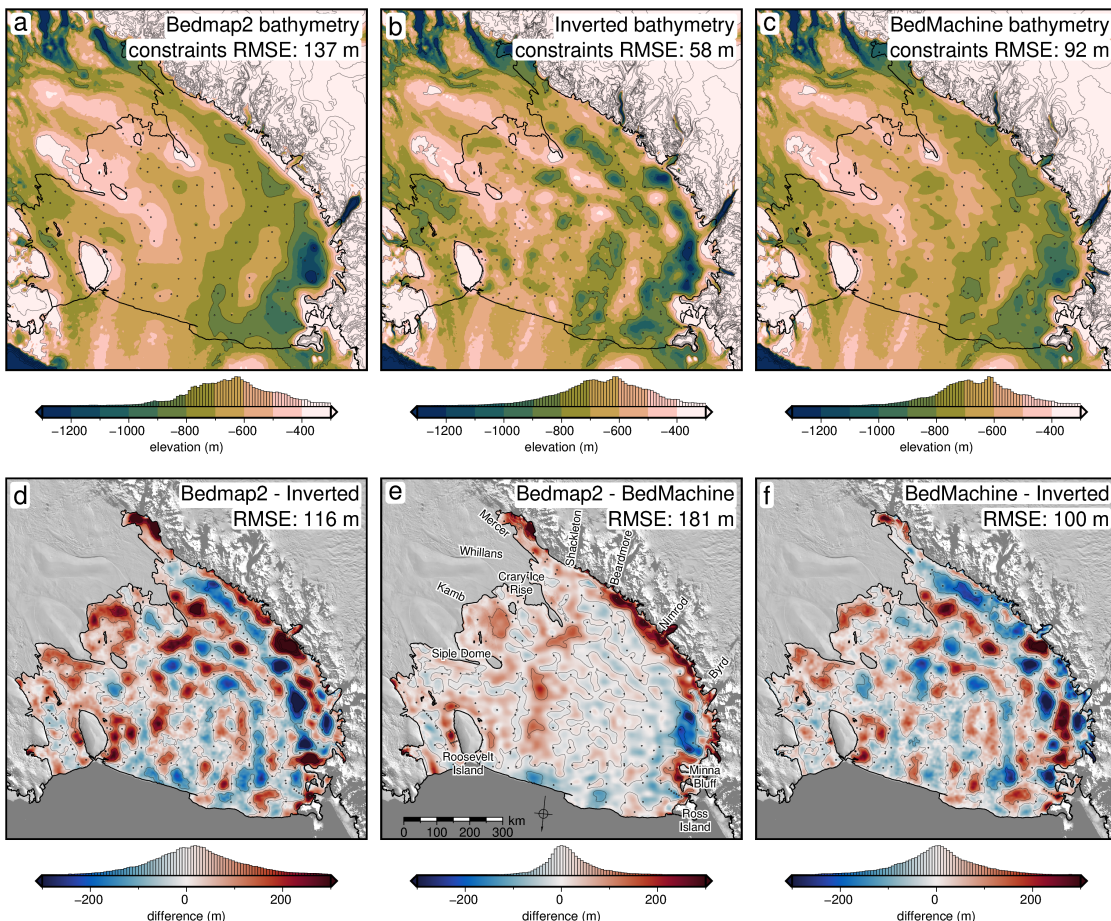


Figure 4.17: Comparison of our inverted bathymetry with past models. **a)** Bedmap2 bathymetry, **b)** our inversion results, from the weighted mean of the full Monte Carlo simulation, and **c)** BedMachine bathymetry. All three share the same colour scale and are contoured at 400 m intervals. RMS difference with the constraint points for each model is stated on the maps. **d)** Difference between our model and Bedmap2, **e)** difference between Bedmap2 and BedMachine v3, and **f)** difference between our model and BedMachine v3. Grids share a colour scale and are contoured at 100 m intervals. Blue regions in **d** and **f** indicate where our results are shallower, while red regions indicate where our results are deeper than the past models. Blue regions in **e** indicate where BedMachine is shallow, while red regions indicate where BedMachine is deeper than Bedmap2. RMS differences are stated on the maps. Grounding line and coastline are shown in black (Morlighem, 2022). Background imagery is from Scambos et al. (2007). Elevations are referenced to the WGS-84 ellipsoid.

Bedmap2 comparison

Figure 4.17 compares our final bathymetry results with the models of Bedmap2 and BedMachine v3. Additionally, several profiles across different regions are shown in

Figure 4.18, comparing the various models. Interestingly, the inversion has raised the RMS difference with Bedmap2, compared to the starting model. But due to the issues with the Bedmap2 grid along the mountain front, this increased difference is expected. The differences between our inverted bed and Bedmap2 have a normal distribution (Figure 4.17d). Our results introduce many small-scale features, as expected since Bedmap2 is an inherently smooth product. However, there are several noticeable large-scale differences with Bedmap2. Proximal to the grounding line, our results are generally deeper, as seen with the starting model comparison (Figure 4.18g). Many of the regions where our results are deeper are related to the issue of over-shallow interpolation of Bedmap2. Portions of the grounding zone along the Siple Coast are over 200 m deeper, including the Kamb (Figure 4.18c) and Mercer ice stream grounding zones.

Another notable difference is an NW-SE oriented trough which appears in our results but is essentially absent in Bedmap2. This feature begins at the southern end of the Crary Ice Rise grounding zone and continues ~ 300 km, paralleling the mountain front (Figure 4.18c). This feature is the southwestern-most of a series of 2 or 3 parallel troughs and ridges, as shown in Figure 4.18d. These features are oriented at a high angle to both E-W and N-S flight lines, increasing their likelihood as true features of the bathymetry and not flight line levelling artifacts. While they are subtle, their presence alters the general *texture* in the region from a primary N-S / NNE-SSW to an NW-SW orientation. This switches the general trend of bathymetry features in the region to be aligned with Siple Coast ice flow, rather than the Transantarctic outlet glacier ice flow. Whether these bedforms are tectonic in nature, revealing the tectonic fabric, or are erosion/depositional, and thus revealing the past flow directions of the previously grounded ice sheet is unknown. The last major difference with Bedmap2 is a significantly deeper bathymetry along the western edge of Roosevelt Island (Figure 4.18a).

Bedmachine comparison

Comparing our results to Bedmachine v3 provides a unique opportunity to evaluate the differences resulting from different gravity inversion algorithms. The gravity inversion results of Tinto et al. (2019), which comprise the Bedmachine v3 data beneath the ice shelf, used similar input datasets (gravity data and constraint points), suggesting that differing inversion algorithms and workflows are likely responsible for the majority of the differences shown in Figure 4.17f. However, some of the differences may arise from re-processing the gravity data, and a different method of gravity reduction applied here, as compared in Section 4.3.

To remove the regional component of gravity, Tinto et al. (2019) used a smoothly varying density model in their inversion. To create this density model, they created an initial prism layer with prisms extending from their starting bathymetry to a depth of 60 km. With the gravity disturbance, they performed a density inversion to recover the density of each prism. This spatially variable density was then low-pass filtered, with a 50 km cutoff. Incorporating this remaining long-wavelength gravity signal within the density model removed the regional component from the gravity input to the inversion. This technique is conceptually similar to high-pass filtering the gravity data to remove the long-wavelength component. For the in-

version, Tinto et al. (2019) used the commercial software Geosoft Oasis Montaj. Limited information is available from Geosoft as to the specifics of this inversion procedure.

Comparing our bathymetry (Figure 4.17f), there is a normal distribution of differences, centred on zero. The RMS difference between the two grids is ~ 100 m. Comparing each grid to the constraint point depths, the BedMachine grid has an RMS difference of 92 m, compared to our RMS of 44 m. Generally, our results are approximately 50-100 m deeper proximal to most of the Siple Coast grounding line. Conversely, our results are approximately 50-100 m shallower along the Transantarctic Mountain front. This could be due to our inability to fully fix the issue of overly-shallow interpolation of data along the mountain front in the creation of our starting model, as discussed.

Alternatively, the differences could be a result of the different gravity reduction steps. Figure 4.12b and e show that correcting the gravity disturbance for the terrain mass effect results in a large negative topo-free disturbance along the Transantarctic Mountain front (dark blues in b). During the regional field estimation, fitting a spline to these large negative values would bring down the nearby regional field, resulting in an underestimation of the regional (more negative), and thus an overestimation of the residual (positive values). This is shown by the profile of Figure 4.12e. On the right side, along the mountain front, in an attempt to fit the negative values of the topo-free disturbance (red dashed line), the regional field (blue) has been underestimated, leaving a large positive residual anomaly (pink dashed). This positive residual results in a shallowing of the inverted bathymetry.

These shallower depths along the mountain front, instead, could be revealing a flaw in the constraint point minimization assumption of the residual being 0 at constraint points. While the constraint point itself doesn't contribute to the residual signal, since the actual bed is equal to the starting bed at those points, deviations between the actual bed and the starting bed in the vicinity of the constraints may lead to a non-zero residual at the constraint. In this case, the interpolation of the regional field attempts to smoothly connect extremely negative values at the mountain front, and high values at the nearby constraint points. This high gradient leads to poor interpolation. This can be seen in 4.12e where the regional (blue line) is forced exactly equal to the topo-free disturbance (red dashed line) at the constraint point at 700 km along the profile. In reality, the residual gravity at that constraint is likely non-zero. A non-zero value may allow the regional field to more closely match the large positive topo-free disturbance located at 720 km.

The remaining major differences between our results and BedMachine v3 include the same series of alternating NW-SE troughs and ridges as discussed above, an ~ 100 m deeper region on the west side of Roosevelt Island, and a significantly deeper (~ 250 m) trough spanning from the south side of Minna Bluff to the outlet of the Byrd Glacier. The greatest depths we model in this trough are $\sim 1350 \pm 100$ m, located offshore of the Byrd Glacier Outlet. Preliminary results of a seismic survey at Discovery Deep, just south of Minna Bluff (cyan line Figure 4.15), in the 2021/2022 field season report depths up to 1450 m (pers. comm. Prof. A. Gorman). These findings confirm the presence of depths of this magnitude. However, our deepest

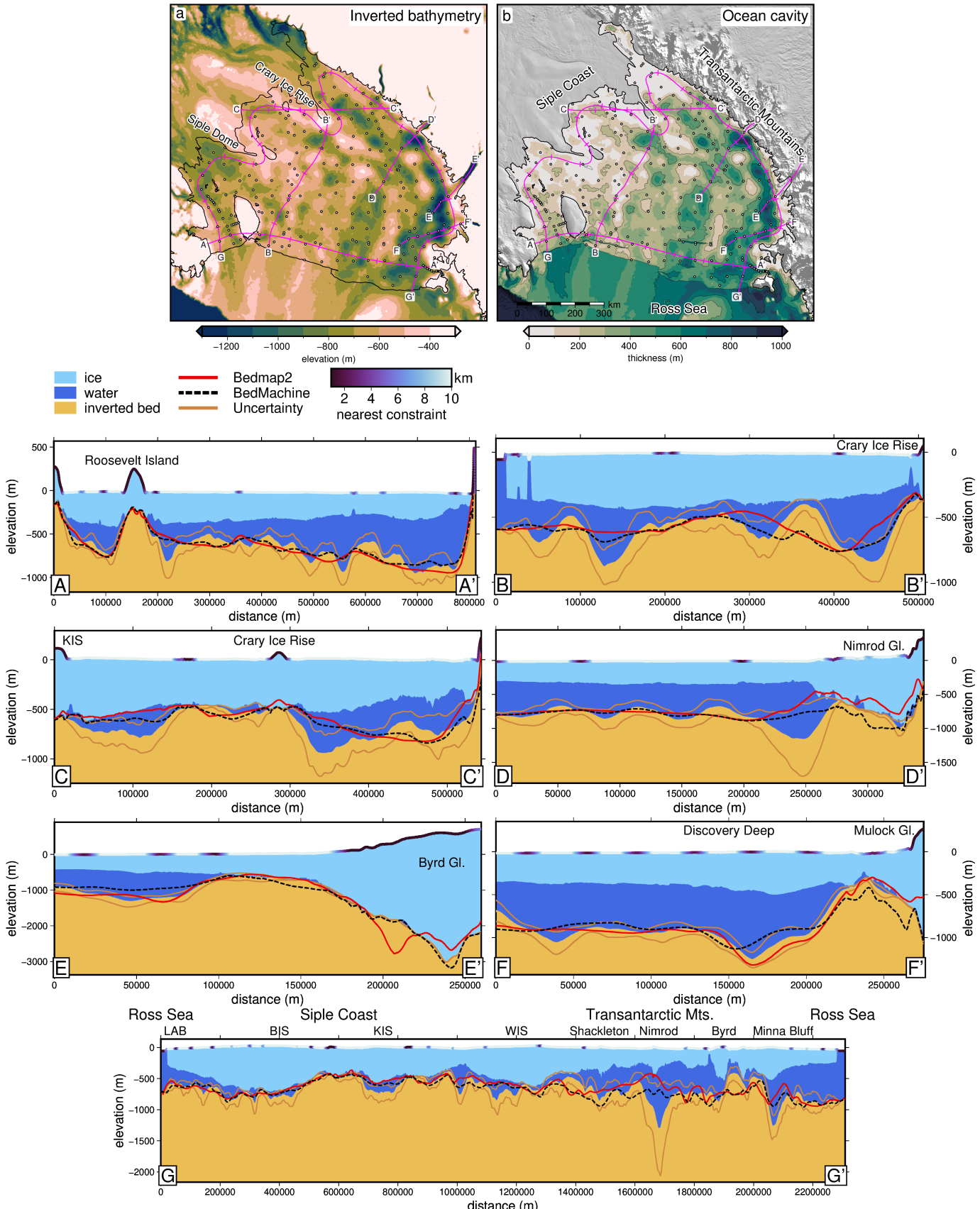


Figure 4.18: Upper panel Ross Ice Shelf inverted bathymetry (left) and water column thickness (bed to ice base) relative to BedMachine v3 ice base (Morlighem, 2022). Pink lines show profile locations with ticks every ~100 km. Grounding line and coastline in black (Mouginot et al., 2017). Constraint points shown as dots. **Profiles A-G** Various cross-sections showing the ice layer (light blue), water layer (darker blue), and bathymetry (yellow), with uncertainties (brown). Red and black lines show Bedmap2 and BedMachine v3 bathymetry, respectively. The colour of the ice surface indicates the distance to the nearest constraint. Legend and colourmap shown above profile A.

location is approximately 100 km south of the Discovery Deep survey. These seismic data were not included in this inversion. An additional comparison to a seismic survey can be made proximal to the Kamb Ice Stream grounding zone (cyan line Figure 4.15). Horgan et al. (2017) image bathymetry depths along a ~ 20 km seismic survey with a mean depth of ~ 605 m. Sampling our bathymetry and uncertainty along this profile yields a mean depth of $\sim 608 \pm 45$ m, while sampling BedMachine v3 bathymetry and uncertainty yields a mean depth of $\sim 572 \pm 79$ m.

Comparing the various difference maps of Figure 4.17 shows that our inversion has resulted in more varied topography across the ice shelf compared to Tinto et al. (2019). This increased amplitude is likely due to the differences in densities used between the inversions. Tinto et al. (2019) used a spatially variable density model, which ranged from $\sim 2600 - 2800$ kg m $^{-3}$, with a mean of ~ 2700 kg m $^{-3}$. While we used a spatially-constant density value, in the Monte Carlo analysis the density was varied between $\sim 1800 - 3000$ kg m $^{-3}$, with a mean of ~ 2400 kg m $^{-3}$. This ~ 300 kg m $^{-3}$ difference between the mean density values would result in a more subdued inverted bathymetry from the (Tinto et al., 2019) model. While the Tinto et al. (2019) density model does a good job of removing the regional field prior to the inversion, whether or not the density values used are representative of the seafloor is questionable. The lowest values in their model of approximately 2600 kg m $^{-3}$ represent the upper end of sedimentary rock densities (Schön, 2015), and are significantly greater than expected densities of unconsolidated sediments. For a region with an expected continuous drape of seafloor sediments (Chapter 2, Tankersley et al., 2022), we expect the densities used in (Tinto et al., 2019) were too high. This explanation for the differences between the inversion results is supported by the strong correlation between our bathymetry uncertainty resulting from the choice in density (Figure 4.16c) and the difference between the inversion results (Figure 4.17f). This shows the importance of picking a plausible density value, and the added benefit of testing many values to estimate the uncertainty related to the chosen density value.

4.5.2.3 Ocean cavity comparison

Due to the smoothness of the base of an ice shelf, relative to bathymetry, the water column thickness beneath many ice shelves is predominately determined by the bathymetry. We use BedMachine v3 ice base elevations and our updated bathymetry to calculate the water column thickness beneath the Ross Ice Shelf and compare the results to the water column thicknesses of Bedmap2 and BedMachine (Figure 4.19). These differences are very similar to those described above, due to the smooth nature of the ice base. Notable areas where our results show a thicker ocean cavity (within uncertainty ranges) compared to past models include;

1. Nearby the Kamb grounding zone ($\sim 100 \pm 50$ m thicker, Figure 4.18c near km 100).
2. The west side of Crary Ice Rise ($\sim 300 \pm 150$ m thicker, Figure 4.18c near km 350).
3. The south side of Minna Bluff ($\sim 300 \pm 200$ m thicker, Figure 4.18g near km 2100).

4. The west side of Roosevelt Island ($\sim 200 \pm 100$ m thicker, Figure 4.18a near km 220)).

Notable areas where our results show a thinner cavity include;

1. The mountain front north of Byrd Glacier ($\sim 300 \pm 50$ m thinner, Figure 4.18g near km 2000)).
2. Three 50 km wide regions in the central ice shelf, which are up to 200 ± 50 m thinner.
3. Several points approximately 50 km off of the Transantarctic Mountain front which are up to 400 ± 50 m thinner (Figure 4.18c near km 450).

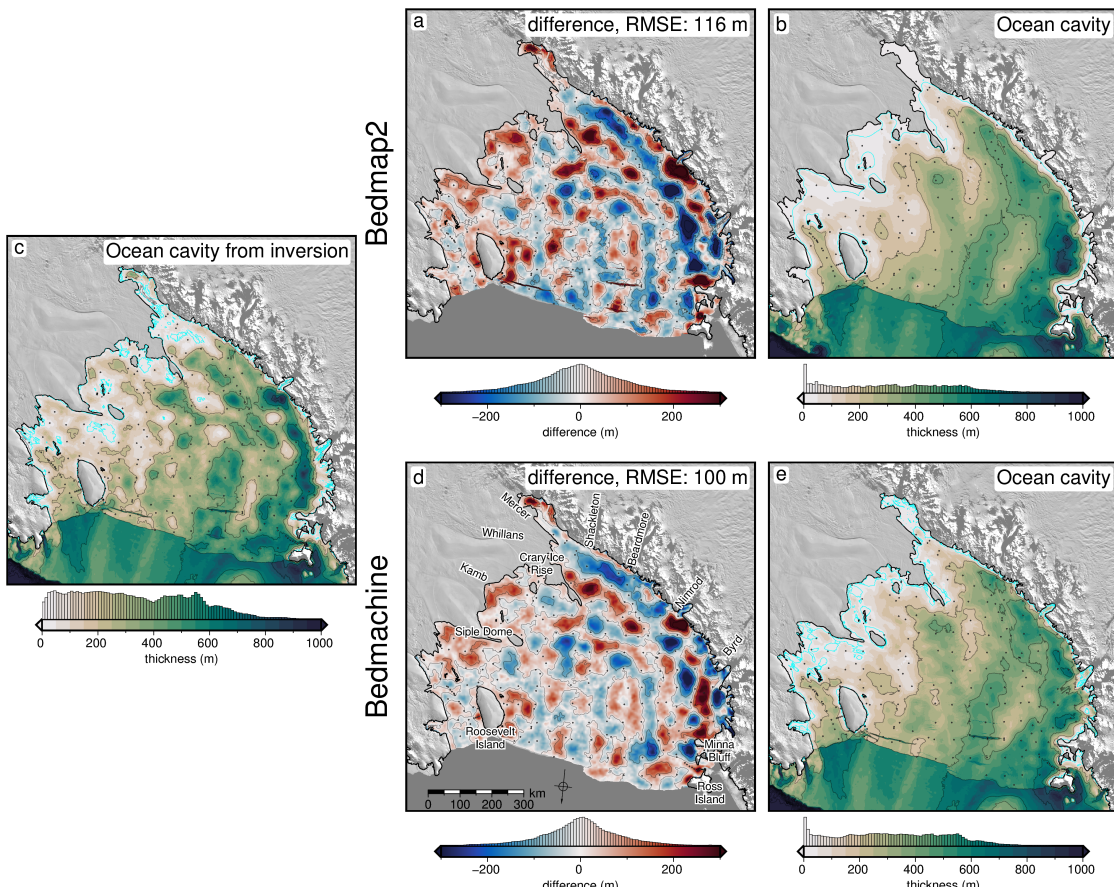


Figure 4.19: Comparison of our updated water column thickness with past models. **a)** Difference between our model and the water column thickness from Bedmap2, and **b)** the Bedmap2 water column thickness. **c)** Water column thickness calculated as the difference between BedMachine v3 icebase and our inverted bathymetry. **d)** Difference between our model and the water column thickness from BedMachine v3, and **e)** the BedMachine v3 water column thickness. Blue regions in the difference maps indicate where our results' water column is thinner, while red regions indicate where our results are thicker than the past models. Grounding line and coastline are shown in black (Morlighem, 2022). Background imagery is from Scambos et al. (2007). Water column thickness grids are contoured at 200 m intervals, and the 20 m contour is shown in bright blue. The difference grids are contoured at 100 m intervals. Water column thickness grids and difference grids share common colour scales.

4.5.3 Implications

Here, we discuss several of the important implications of our updated sub-RIS bathymetry. These implications relate to the stability of the Ross Ice Shelf, geology, and tectonics.

4.5.3.1 New potential pinning points

We have identified several areas of thin water column thickness (< 20 m) with our updated results beneath the Ross Ice Shelf. These areas are shown by the 20 m water column thickness contour, in bright blue in Figure 4.19a. These include a $\sim 100 \times 100$ km region SW of Roosevelt Island, several $\sim 50 \times 50$ km regions on the north flank of Crary Ice Rise (Figure 4.18g at km ~ 900), and a widespread region south of Crary Ice Rise (Figure 4.18g at km ~ 1350). Thin water depths south of Crary Ice Rise have also been modelled by a local gravity survey along the Whillans Ice Stream grounding zone (Muto et al., 2013b). Additionally, two smaller regions of sub-20 m water column thickness are found nearer the centre of the ice shelf. One is approximately 100 km off the point of Crary Ice Rise and is ~ 400 km 2 (Figure 4.18c at km ~ 200). The second is ~ 200 km north of Crary Ice Rise and is slightly smaller (Figure 4.18b at km ~ 350). None of these shallow water column regions are present in either of the past models. Interestingly, these regions coincide with some of the lowest uncertainties we report ~ 20 m. A portion of this low uncertainty may be related to the inversion constraining the bathymetry to the ice base, which in regions of thin water column will reduce the variability of the suite of inversions in the Monte Carlo simulation which were used to define the uncertainty.

These newly-identified shallow regions highlight where the Ross Ice Shelf was likely grounded in the recent past, or could likely become re-grounded in the future. While some of these regions are small, analysis of pinning points on the Ross Ice Shelf has shown some of the smallest pinning points can create the largest effective resistance on the ice shelf (Still et al., 2019). Additionally, some of these locations (north side of Crary Ice Rise) are predicted to have on the order of 1 m/yr of basal accretion (Adusumilli et al., 2020). An already thickening shelf within ~ 20 m of the bed will likely affect the ice sheet dynamics as part of future projections of the ice shelf. Incorporation of these localities of likely past pinning points may aid in resolving the ongoing debate of the style of grounding line retreat and readvance of the Ross Ice Shelf throughout the Holocene (Kingslake et al., 2018; Lowry et al., 2019; Venturelli et al., 2020).

4.5.3.2 Basal melting

Our updated bathymetry, water column thickness, and uncertainty maps provide additional information vital to understanding the distribution of basal melt beneath the ice shelf. Melt beneath the Ross Ice Shelf is thought to predominantly occur 1) along the ice front, where Antarctic Surface Water causes rapid melting in the summer (Figure 4.20 Horgan et al., 2011; Moholdt et al., 2014), and along the deep grounding zones of the Transantarctic Mountain front, where contact with High Salinity Shelf Water induces melting (Figure 4.20b Adusumilli et al., 2020; Tinto et al., 2019). Throughout the centre of the ice shelf are zones of refreezing (Figure

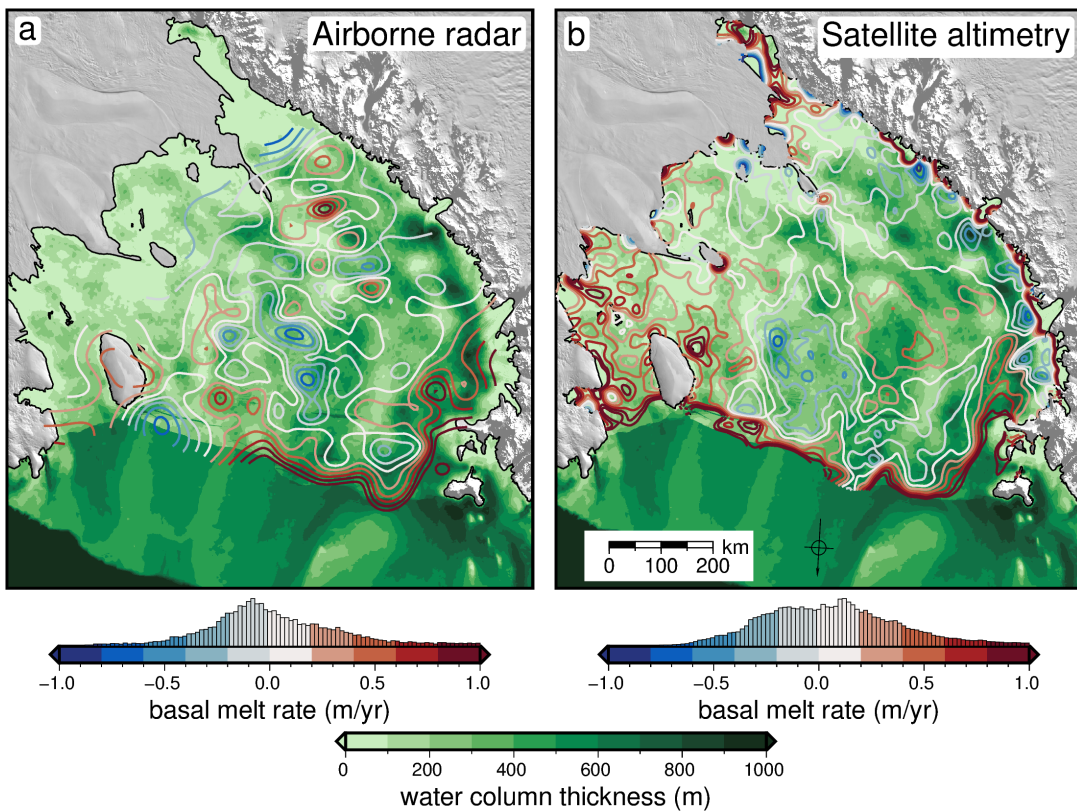


Figure 4.20: Basal melt rate and water column thickness compared for the Ross Ice Shelf. **a)** Blue to red contours show interpolated basal melt rate from Das et al. (2020) derived from ROSETTA-ice airborne ice-penetrating radar. Background shows water column thickness from this study. **b)** Same as **a** but with basal melt rate from Adusumilli et al. (2020) derived from satellite altimetry. Black line is the grounding line from Mouginot et al. (2017). Background imagery is from MODIS-MOA (Scambos et al., 2007).

4.20 Adusumilli et al., 2020; Das et al., 2020). Overall basal melting of the Ross Ice Shelf is thought to be low compared to other shelves due to the blocking of warm Circumpolar Deep Water from entering the cavity. This blocking is from a layer of dense High Salinity Shelf Water (Dinniman et al., 2011; Tinto et al., 2019). The Hayes Bank (Figure 4.1b) has been identified as one location where the Circumpolar Deep Water is able to penetrate the ice shelf cavity and induce melting, but this penetration is thought to be limited to the region near Roosevelt Island (Das et al., 2020; Tinto et al., 2019). Our ocean cavity is ~ 100 m thicker than Tinto et al. (2019) immediately to the west of Roosevelt Island (Figures 4.18a and 4.19d). This region should be investigated with sub-shelf circulation models using our updated bathymetry. Our larger cavity allowing the inflow of warm Circumpolar Deep Water beyond Roosevelt Island could help explain the relatively large basal melt rate found in the region as shown by satellite altimetry (Figure 4.20b).

The high melt rates measured along the Transantarctic Mountain front (Adusumilli et al., 2020) are caused by the inflow of High Salinity Shelf Water (Tinto et al., 2019). This water is thought to be guided by bathymetric troughs and is able to induce melting only at large depths, due to the pressure suppression of the melting temperature of ice. Figures 4.20 show a comparison of both airborne radar and satellite altimetry-derived basal melt rates to the updated water column thickness resulting from our bathymetry inversion. The deeper bathymetry proximal to the

Transantarctic Mountain front found in both our inversion and Tinto et al. (2019), compared to the depths of Bedmap2, help explain the high melt rates measured there. The other locations we report with deeper bathymetry near grounding zones, such as the south side of Minna Bluff, and the far southern end of the ice shelf, at the Mercer Ice Stream grounding zone, may be potential locations where High Salinity Shelf Water is able to induce basal melt. Additionally, some of the very shallow water column thicknesses (< 20 m) we find (Figure 4.19c), for instance to the south of Crary Ice Rise, correspond with low basal melt rates (Figure 4.20). This may be due to the lack of stratification in the water column, which occurs due to tidal mixing possible only in thin water columns (Holland, 2008; Muto et al., 2013b).

4.5.3.3 Geologic and tectonic significance

While there are many interesting implications to explore in this new dataset, we limit our discussion to several sub-Ross Ice Shelf bathymetric features of possible importance to solid-Earth investigations. These features include the bathymetry along the Transantarctic Mountain front, a deep feature on the southwest flank of Crary Ice Rise, and a newly identified orientation of bathymetry features, aligned with the Siple Coast ice streams.

Transantarctic Mountain front

The Transantarctic Mountains (Figure 4.1a) make up the world's largest rift shoulder. Despite their prominence, the uplift mechanisms are still debated (Goodge, 2020). It is likely that these mechanisms vary along-strike, and consist of some combination of thermal, flexural, or isostatic support (Goodge, 2020). For the central TAM, a mechanism of cantilevered flexure is proposed for the uplift of the mountains (Wannamaker et al., 2017; Yamasaki et al., 2008). This theoretically should be accompanied by a deep trough parallel just offshore the range front, and an outer bathymetric high, approximately 200 km from the range front (Stern & ten Brink, 1989). These features have not yet been observed (ten Brink et al., 1993; Wannamaker et al., 2017). Our results show a deep trough along the range front between the Nimrod Glacier and Minna Bluff, with bathymetry highs further offshore. These features may support the theory of flexural uplift along this portion of the TAM (Wannamaker et al., 2017). Further south, where the trough disappears, the mechanism of flexural uplift is not required, since the mountains have a crustal root, which likely provides the uplift mechanism, via Airy isostasy (Block et al., 2009; Wannamaker et al., 2017).

Fault bound Crary Ice Rise

Figure 4.18c shows a profile of the updated bathymetry model across the Crary Ice Rise. Our results show a steep drop off the south flank of the ice rise (at km ~ 320), to depths up to $\sim 1000 \pm 200$ m. This steep drop-off is aligned with an NW-SE fault proposed by Muto et al. (2013b) from a local gravity survey along the Whillan Ice Stream grounding zone. Depth to basement analysis from magnetic data (Chapter 2, Tankersley et al., 2022) also highlights this north flank of Crary Ice Rise as a likely location for faults. We believe this steep bathymetry feature adds evidence to the proposition of the Crary Ice Rise as a fault-bound horst (Muto et al., 2013b). This would imply the current grounding of the Ross Ice Shelf along the Crary Ice Rise is in part controlled by regional tectonics.

New bathymetric trend

From the gridding of point data, the bathymetry of the central Ross Ice Shelf is dominated by an N-S - NNE-SSW trend, aligned with the flow directions of the outlet glaciers of the Transantarctic Mountains (Figure 4.1). Our updated bathymetry model (Figure 4.15a) adds an overprinted NW-SE trend to the bathymetry features of the central portion of the ice shelf. This trend is prevalent, but subtle, in the inversion of Tinto et al. (2019). The features comprising this trend are a series of 2-3 ridges and troughs of ~ 100 m amplitudes and ~ 50 km wavelengths, as shown in Figure 4.18d. These features are oblique to flight lines, adding to their validity, and are well-aligned with the Crary Ice Rise and the general ice flow direction of the Siple Coast ice streams. This trend could signify several things; 1) the most recently grounded ice in this region had a flow direction aligned with the Siple Coast ice streams, leaving behind erosional or depositional features with these orientations, 2) these features are tectonic in origin, and are the surface expressions of rift structures. These structures overprint the large bathymetric depression which runs from the Nimrod glacier to the calving front. If these are features left behind from the most recent grounding line retreat, they might inform the style of retreat. As seen in the Ross Sea, physiography of the sea floor exerts the primary control on ice stream flow and the patterns of retreat (Halberstadt et al., 2016).

4.6 Conclusion

Here we present an updated model of bathymetry depths beneath Antarctica's Ross Ice Shelf, as modelled from airborne gravity data. Our inversion algorithm provides a comprehensive spatial uncertainty analysis and parameter sensitivity estimation. This uncertainty highlights regions of high uncertainty that would benefit from additional seismic constraints. These regions include the entire Transantarctic Mountain front and two points near the centre of the shelf which are up to 40 km from the nearest constraints. We summarize some key findings from the research below;

1. Monte Carlo sampling is a robust method of uncertainty quantification and parameter sensitivity analysis for bathymetric gravity inversions.
2. Sensitivity analysis shows that gravity data are the largest contributor to bathymetry uncertainty, followed by assumptions of the geology of the region.
3. Our updated bathymetry model better matches *a priori* sub-ice shelf measurements compared to past models.
4. Compared to Bedmap2, our results are deeper proximal to the grounding line and shallower along the ice front.
5. Differences with the inversion of Tinto et al. (2019) (BedMachine v3) are mostly due to different chosen density contrasts.
6. Newly identified potential past pinning points are found along the Siple Coast and in the central Ross Ice Shelf.
7. Thick ocean cavity is found along the west flank of Roosevelt Island, where Circumpolar Deep Water flows under the shelf and may highlight a region of importance for ocean circulation modelling.

8. Possible tectonic implications including a fault-bound Crary Ice Rise and a flexural trough associated with Transantarctic Mountain uplift.

Our results provide the datasets necessary to begin answering key questions regarding the role of the Ross Ice Shelf in various components of the Earth system. These questions include: 1) where are melt-inducing bodies of water guided beneath the ice shelf? 2) where was the ice shelf grounded in the recent past, and what was the geometry of Holocene grounding line retreat and re-advance? Are the modern bathymetry features remnants of the last grounding line retreat, or are they tectonic in origin? While we don't provide direct answers to these questions, without adequate knowledge of the sea floor morphology and the associated uncertainties, investigators won't have the relevant boundary conditions to answer these questions. All of the research conducted here is published as open-source Python code (see Chapter 1 Section 1.6), with hopes that the methods presented here can be used by researchers to better model the bathymetry and uncertainty of other Antarctic ice shelves.

Chapter 5

Synthesis

Improving decadal to centennial projections of global sea level rise is of utmost importance for mitigating future environment and socio-economic impacts (Durand et al., 2022). Antarctica's projected contributions to global sea level rise by the end of the century under a high-emission scenario is between 0.03 and 0.28 m (RCP 8.5, Intergovernmental Panel on Climate Change (IPCC), 2022). This wide range of possible values expresses the uncertainty of the Antarctic Ice Sheet's response to a warming world. Over 80% of ice loss from Antarctica occurs through ice shelves (Rignot et al., 2013), highlighting their importance in reducing the uncertainty in sea level rise projections. Antarctica's largest ice shelf, the Ross Ice Shelf, is fed from both the East and West Antarctic Ice Sheets. Its catchment contains a total volume of ice equivalent to 11.6 m of global sea level rise (Fretwell et al., 2013; Rignot et al., 2011; Tinto et al., 2019). While the Ross Ice Shelf is relatively stable currently (Moholdt et al., 2014; Rignot et al., 2013), geologic evidence shows the rapid destabilization of the ice shelf within the past \sim 7,000 years (e.g., Naish et al., 2009; Venturelli et al., 2020).

The destabilization of the ice shelf is thought to have been primarily caused by ocean forcings (Lowry et al., 2019), as bathymetric troughs guide the inflow of melt-inducing ocean circulations (Tinto et al., 2019). The subsequent grounding line retreat however is predominantly controlled by the physiography, geology, and glaciological feedbacks (Halberstadt et al., 2016). This highlights the solid earth, through its bathymetric control on basal melt and its effects on grounding line retreat dynamics, as an important component of the dynamics of the Ross Ice Shelf. To reliably understand the contribution of the Ross Ice Shelf to future sea level rise, we must provide ocean and ice modellers with the necessary geologic boundary conditions. This thesis aimed to provide both these boundary conditions and estimates of their uncertainties to the modelling community. A series of research questions were proposed, as restated below.

1. What is the geologic structure of the upper crust beneath the Ross Ice Shelf? If there are sediments, what is their thickness and distribution? Where are the major faults likely located?
2. How can bathymetry beneath an ice shelf best be modelled? Are there further improvements that can be made to the gravity-inversion process? What are the predominant sources of uncertainty, and how can these be limited?

3. How deep is the bathymetry beneath the Ross Ice Shelf and where are we most and least certain about it?
4. What are the geologic controls on the Ross Ice Shelf's stability?

Here we draw from the various research chapters to provide answers to these questions.

5.1 Investigating geologic structures

Research question 1

To address research question 1 we sought to model the depth of the crystalline basement rock beneath the ice shelf. We accomplished this with a depth-to-magnetic source technique, which used airborne magnetic data and was calibrated to seismically imaged basement depths of the Ross Sea. Our resulting basement topography revealed large-scale, fault-controlled extensional basins throughout the sub-Ross Ice Shelf crust (Figure 5.1f). Above this basement sits various sediments, likely ranging from coherent sedimentary rock to unconsolidated recent glacial and marine deposits. While there is a continuous drape of sediments across the entire ice shelf, we also image several distinct depocenters; the Western Ross Basin, covering the East Antarctic half of the ice shelf, and several basins on the West Antarctic side, including the Siple Dome Basin and the Crary Trough (Figure 5.1f). These results were incorporated into an Antarctic-wide review of sedimentary basins (Figure 5.1a Aitken et al., 2023b), showing the widespread distribution of similar basins across much of Antarctica. From our findings, we were able to draw a wide range of implications, ranging from tectonic influence on ice dynamics along the Siple Coast to the buried and subsided remnants of an above-sea-level Oligocene mountain range, which likely accommodated alpine glaciers. These results provided the first view of the upper crust beneath the entirety of the Ross Ice Shelf.

5.2 Developing a gravity inversion

Research question 2

To provide modellers with accurate bathymetry depths beneath the Ross Ice Shelf, we utilized a gravity inversion technique. While there is an existing gravity-inverted bathymetry model for the Ross Ice Shelf (Tinto et al., 2019), the reported uncertainties were spatially uniform. To provide spatial uncertainties, we chose to develop a new gravity inversion algorithm. In addition, since the majority of gravity inversions use proprietary and expensive software, in an effort towards open-source and reproducible science, we chose to develop our gravity inversion using Python and release the code in an online repository.

Chapter 3 described this algorithm in detail. Extensive testing of various synthetic and semi-realistic datasets revealed several intricacies of performing a gravity inversion to attain a bathymetry model. The estimation and removal of the regional component of gravity, which occurs in the data reduction steps before the inversion, accounts for the majority of the error in the model. There are various techniques to

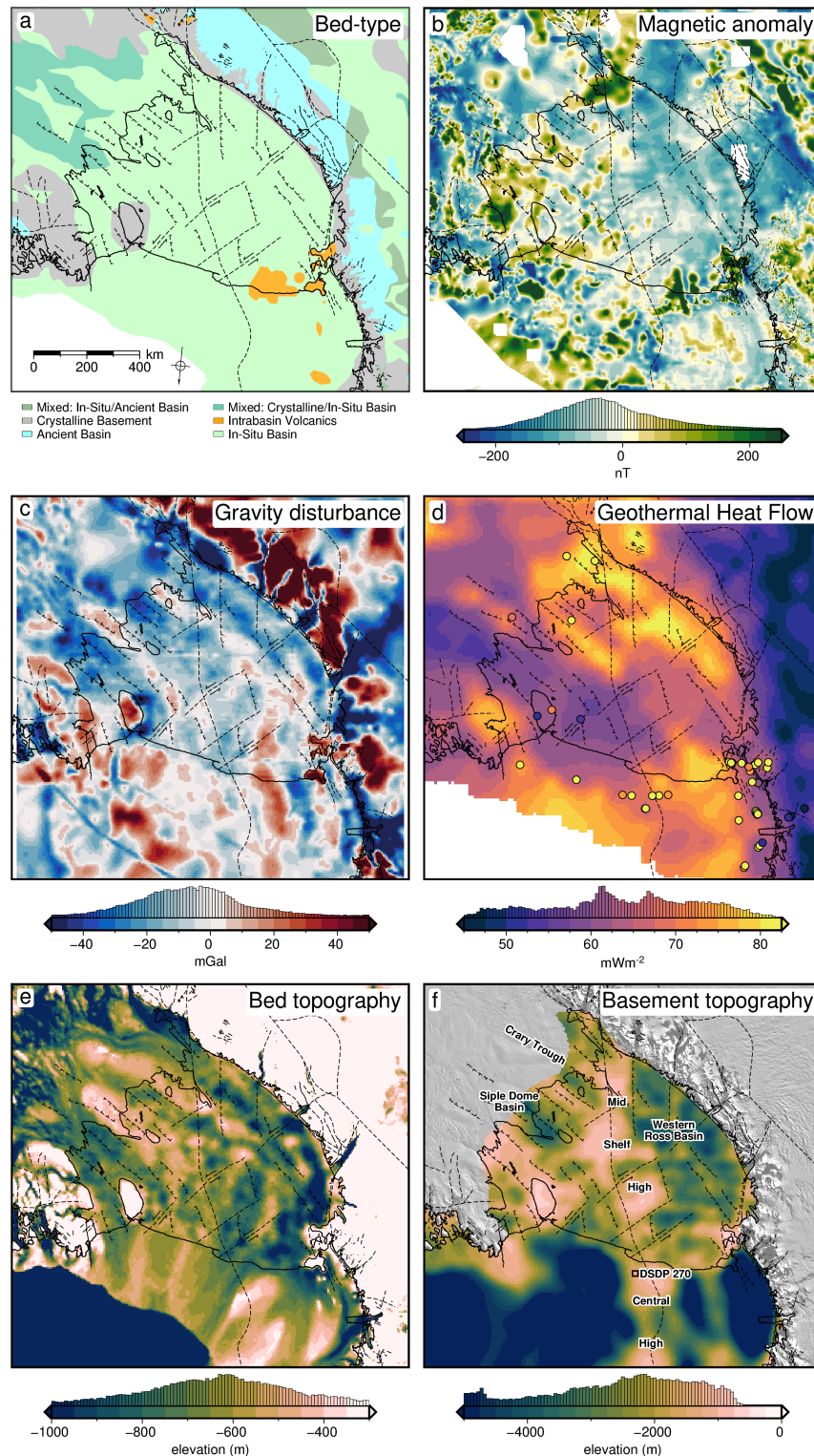


Figure 5.1: Summary of southern Ross Embayment geophysical and geologic information. **a)** Generalized geologic classification of the bed from Aitken et al. (2023a), **b)** ROSETTA-Ice airborne magnetic anomalies (Tinto et al., 2019) merged with ADMAP2 magnetic anomaly compilation (Golynsky et al., 2018), **c)** Gravity disturbance compilation from Forsberg (2020), include ROSETTA-Ice data. **d)** Geothermal heat flux from a seismically-derived model (Shen et al., 2020), and point measurements compiled from Burton-Johnson et al. (2020). **e)** Inverted bathymetry from Chapter 4, **f)** Basement topography from Chapter 2. Solid black line shows the grounding line and ice front from Mouginot et al. (2017). Fainter black lines show inferred (dashed) and exposed (solid) faults from a combination of Chapter 2 and Cox et al. (2023). Background imagery in **f** from MODIS-MOA (Scambos et al., 2007).

remove the regional field. We explore several of these methods and provide recommendations to best reduce the errors. Our uncertainty analysis highlighted regions of either steep topography or high gradient gravity anomalies as key regions where additional bathymetry measurements will make a significant contribution to reducing uncertainties. These suggestions of where to collect additional data should be considered alongside key regions of investigation identified through ocean modelling. Our findings suggest the quantity of bathymetry measurements is more important for reducing inversion uncertainty than the quality of these measurements. Conversely, we show larger sensitivity of the inversion results to the noise in the gravity data, relative to the density of gravity data collected. This suggests optimizing quantity over quality for bathymetry constraints while optimizing quality over quantity for gravity observation data. We hope these suggestions are able to better inform future Antarctic data collection for the goal of improving sub-ice shelf bathymetry models.

As part of Chapter 4, we compared our methods, of both the gravity reduction process and the inversion procedure, to all past bathymetry models conducted in Antarctica, as well as several from Greenland. Several other inversions have used a regional separation method similar to ours; however, none of these have provided an assessment of the associated uncertainties related to this method, which we found to be significant. We also found that all other inversions utilized a non-rigorous method of correcting the gravity data for the effects of ice, water, and topography. While the error introduced is likely small, with modern computing, applying this correction correctly is trivial.

From the other studies, excluding those with undocumented inversion algorithms, we found only one study which used a conventional regularized least-squares approach, similar to ours. Comparing our uncertainty analysis to past inversions revealed only two studies that report spatially variable uncertainties of their bathymetry model. It is our hope that the improvements made for the gravity inversion process are incorporated in future inversions in order to attain better estimates of uncertainties.

5.3 Modelling Ross Ice Shelf Bathymetry

Research question 3

With the gravity inversion methodology laid out in Chapter 3, we created a new model of sub-Ross Ice Shelf bathymetry (Figure 5.1e). This model highlighted some important differences from past bathymetry models. In general, our model has more varied topography, compared to the smooth Bedmap2 model, and the intermediate BedMachine model. Compared to Bedmap2, we report significantly deeper bathymetry proximal to the entire grounding zone, including notably deeper areas near the Kamb Ice Stream, along the west side of Roosevelt Island, and south of Minna Bluff. Compared to the past inverted bathymetry (Tinto et al., 2019), our results are deeper along the Siple Coast but vary between deeper and shallower along the Transantarctic Mountain front. Our uncertainty analysis identified gravity data quality as the largest component of the overall uncertainty, while the distance from the nearest constraint and interpolation parameter values contributed significantly

to the spatial variability of the uncertainty. From this, the largest uncertainties were found either far from constraints, or along the steep topography of the Transantarctic Mountains. This highlighted several locations where future seismic surveys would be able to effectively reduce uncertainties.

5.4 Geologic controls on Ross Ice Shelf Stability

Research question 4

Next, we synthesize our findings which relate to the geologic influence on the Ross Ice Shelf, in an attempt to answer research question 4. We start with the controls on the ice shelf as it is today, before speculating on what these geologic controls were in the past or will be in the future.

5.4.1 Present controls

5.4.1.1 Basal melt

Basal mass loss of the Ross Ice Shelf is dominated at the deep grounding zones, where relatively cool High Salinity Shelf Water is able to induce melting due to the high pressure at depth (Adusumilli et al., 2020; Tinto et al., 2019). These inflows of cold and dense water occur along the seafloor and are guided south beneath the ice shelf by bathymetric features (Holland, 2008). Tinto et al. (2019) model the dominant inflow of High Salinity Shelf Water starting near Ross Island, flowing south along the mountain front, where at the southern flank of Crary Ice Rise the flow turns north and flows back to the ice front through the centre of the ice shelf. This inflow is responsible for much of the basal melting of the Ross Ice Shelf (Adusumilli et al., 2020; Tinto et al., 2019). Our bathymetry model (Figure 5.1e) confirms the presence of a deep trough ranging from the western ice front along the Transantarctic Mountain front which accommodates this High Salinity Shelf Water inflow. Our mountain front trough, however, is both narrower and deeper than past models. At the Nimrod Glacier outlet our trough steps to the east by ~ 100 km, and eventually ends along the south flank of Crary Ice Rise.

This eastward step is likely important for two reasons. 1) South of Nimrod Glacier, we model a shallow bathymetric shelf proximal to the grounding line. This likely blocks grounding line access to southward flowing High Salinity Shelf Water, limiting basal melt for the southernmost outlet glaciers. 2) The eastward step likely re-directs southward flowing High Salinity Shelf Water closer to the Siple Coast grounding zone, particularly the south flank of Crary Ice Rise. In this region, past bathymetry models show a continuous bathymetric ridge for ~ 300 km off the edge of Crary Ice Rise which blocks the inflow of High Salinity Shelf Water to the Siple Coast north of Crary Ice Rise (Tinto et al., 2019). Our results however show this ridge being dissected by two low saddles. If included in ocean circulation models, the lack of a continuous ridge and the presence of these low saddles may allow the inflow of circulations to the Siple Coast; a scenario which should be further explored.

The Hayes Bank, to the west of Roosevelt Island, has been identified as the primary location of inflow of warm Circumpolar Deep Water (Das et al., 2020;

Tinto et al., 2019). We model a region of deeper-than-previously seen bathymetry along the west edge of Roosevelt Island and propose this as a location that may allow the incursion of this ocean water with a high potential for melt. Additionally, along the Shirase Coast, south of Roosevelt Island, we model a thicker ocean cavity than past estimates. This may allow further penetration of water which enters the shelf near Hayes Bank. To address these highlighted regions of importance for basal melt, future ocean circulation models should incorporate our bathymetry model. Further, to test the sensitivity of sub-shelf circulations to bathymetry, the upper and lower bounds of uncertainty should be used in separate circulation models to test the range of possible sub-shelf circulations.

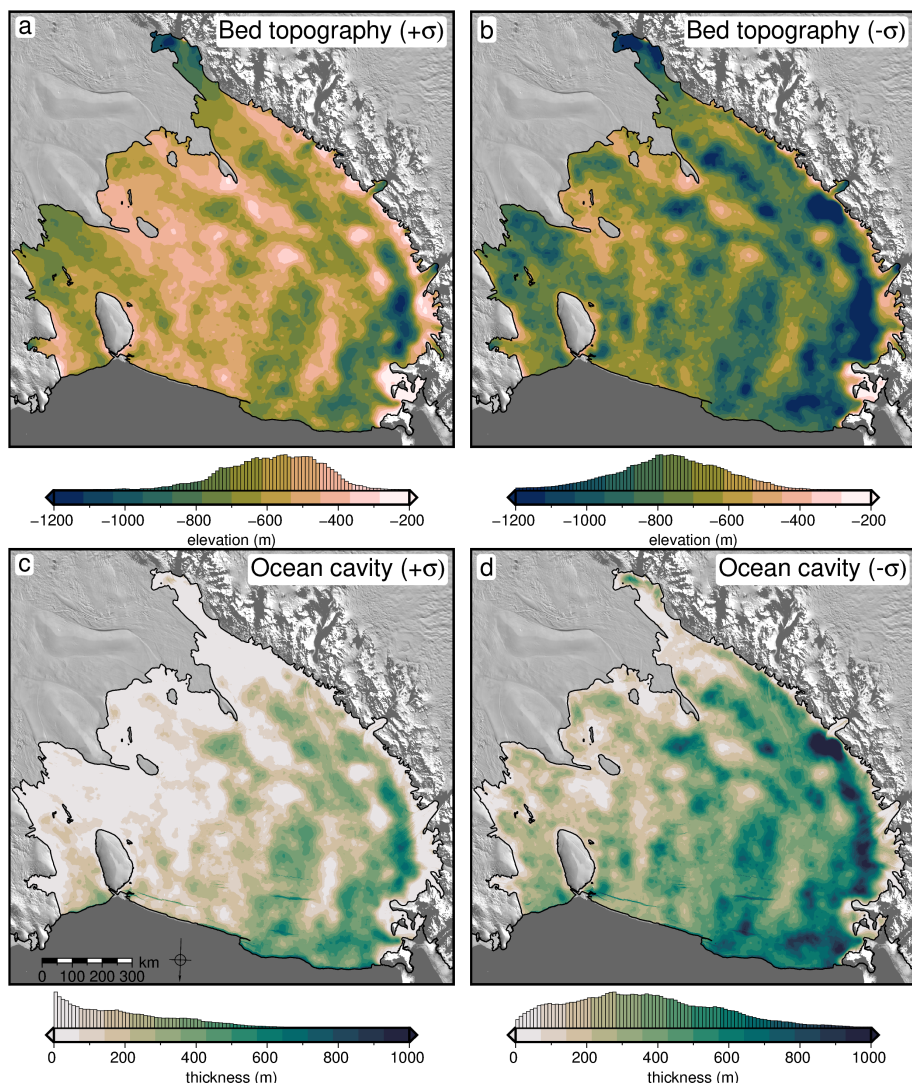


Figure 5.2: Lower and upper uncertainty bounds of Ross Ice Shelf bathymetry and ocean cavity thickness. **a)** Upper bathymetry uncertainty bound, **b)** lower bathymetry uncertainty bound, **c)** upper ocean cavity uncertainty bound, **d)** lower ocean cavity uncertainty bound.

5.4.1.2 Modern pinning points

Analysis of Ross Ice Shelf's pinning points has shown that the effective resistance as well as the temporal persistence of pinning points are not tied solely to their size, but are strongly influenced by the competency of the bedrock (Still et al., 2019; Still & Hulbe, 2021). A really small pinning points which exert large effective resistance are

assumed to be grounded on bed with a high friction coefficient, while large pinning points which exert only minor resistance are assumed to be grounded on an easily deformable substrate. Based on the ratio of area to effective resistance, Still et al. (2019) suggested the bed beneath the Shirase Coast Ice Ripples, to the south-east of Roosevelt Island (Figure 5.3), is likely composed of competent bedrock with a high friction coefficient. Conversely, they suggest pinning point #14, just north of Crary Ice Rise, to be grounded on easily deformable till. The downstream extent of streaklines from pinning points provides an estimate of the temporal persistence of these features. Based on these streaklines, the Shirase Coast Ice Ripples and the Crary Ice Rise have likely been grounded for hundreds of years, while the large Steershead Ice Rise, just west of Siple Dome, only became grounded within the last 400 years (Fahnstock et al., 2000; Still et al., 2019).

Persistent pinning points

Our basement and sediment thickness results provide support for many of these observations of ice dynamics. The Shirase Coast Ice Ripples, predicted to have been long-lasting and grounded on competent bedrock, are shown in our basement results to sit upon a large basement high, with thin sedimentary cover. This implies both that the bedrock beneath the pinning point is either crystalline basement, or very coarse sediment from minimally re-worked basement material, and that the elevation of the bed is stable. This stability is likely due to both the tectonic nature of the bed as a fault-bounded horst, and the higher strength of the bedrock, able to resist erosion by the overriding ice. Similarly, the persistence of Crary Ice Rise in the glaciologic record may be owed to its location above a basement ridge. Of the areas of possible recent grounding we identified, the region to the south of Crary Ice Rise, and the smaller area ~ 200 km north of Crary Ice Rise, both are located on similar large basement highs with thin sedimentary cover. When grounded, these past pinning points likely imparted a large effective resistance on the overriding ice.

Recent pinning points

The predicted deformable substrate of both Steershead Ice Rise and pinning point #14 (Still et al., 2019), as well as the recent grounding of Steershead Ice Rise (Fahnstock et al., 2000), are supported by our findings of these features being located over thick fault-bound sedimentary basins. These thick sediments provide material that is easily weathered into glacial till by the overriding ice, which lowers the effective resistance of the pinning point. If the basin bounding faults we predicted in Chapter 2 are truly active, they could accommodate local vertical bed movements associated with glacial isostatic adjustment following changing ice loads (Peltier et al., 2022; Steffen et al., 2021). For the very low-viscosity upper mantle and thin lithosphere beneath West Antarctica (Chen et al., 2018; Pappa et al., 2019), these solid earth responses to changing ice thickness may occur on decadal timescales (Barletta et al., 2018). This may help explain the short-lived history of these pinning points. One of the possible recent pinning points we identified is within the same sedimentary basin as Steershead Ice Rise (between Steershead Ice Rise and Roosevelt Island), and when grounded, likely shared these qualities. With these observations, we support the notion of a strong geologic control on the buttressing ability and persistence of pinning points throughout the Ross Ice Shelf. As the West Antarctic

Ice Sheet thins, swift glacial isostatic rebound may lead to re-grounding; a response which may promote stability of the ice sheet (Barletta et al., 2018; Coulon et al., 2021; Kachuck et al., 2020). Accurate bathymetry beneath the Ross Ice Shelf is vital for knowing where this re-grounding may occur, and thus where new pinning points will develop.

5.4.1.3 Sediment distribution

The dynamics of Siple Coast ice streams are intrinsically tied to the bed which they flow over. The presence of sediments and sedimentary basins allows for several mechanisms to achieve the fast flow seen in these ice streams. 1) The sediments are able to deform in response to the shear stress of the overriding ice, allowing faster flow (Alley et al., 1986), 2) groundwater stored within the sedimentary basins both lubricates the ice base, reducing basal friction and increases till deformation, through increased pore-fluid pressure (Tulaczyk et al., 2000). Our results of Chapter 2 show a continuous drape of sediments across the ice shelf including along the Siple Coast grounding zone. The presence of these sediments helps explain the fast-flowing ice along this region. Additionally, we image several large sediment basins beneath the Siple Coast (Figure 5.1f). The groundwater storage capabilities of such basins could provide up to half of the groundwater in the subglacial system of West Antarctica (Christoffersen et al., 2014). The southernmost of these sedimentary basins has been confirmed by a recent magnetotelluric survey, which identified > 1 km of sediments with extensive groundwater storage (Gustafson et al., 2022). The other two basins we imaged, the Siple Dome Basin, and the Crary Trough (Figure 5.3), could be key drivers on subglacial hydrology beneath the Siple Coast.

5.4.1.4 Geothermal heat flux at Siple Coast

Spatial control on geothermal heat

The last main geologic control on Ross Ice Shelf stability we propose is the distribution of geothermal heat along the Siple Coast (Figure 5.1d). Geothermal heat flux is one of the least constrained boundary conditions for Antarctica (Larour et al., 2012; Pollard et al., 2005; Seroussi et al., 2017). High geothermal heat supplied to the ice base can accelerate flow by 1) increasing englacial temperatures, reducing ice viscosity, 2) increasing basal lubrication through meltwater production and 3) increasing the ability of subglacial tills to deform, through water-saturation (Golledge et al., 2014; Pollard et al., 2005). While we don't provide any direct measurements of geothermal heat flux, our fault-bound sedimentary basins along the Siple Coast provide important insights into the temporal and spatial variability expected for geothermal heat flux along the Siple Coast.

Measurements and predictions of geothermal heat flux along the Siple Coast are shown to vary significantly, even between nearby (within ~ 100 km) measurements (Figure 5.1d, Begeman et al., 2017; Fox Maule et al., 2005). This high spatial variability is attributed to the localization of heat due to upper crustal structures (Begeman et al., 2017). Faults and basement margins act as efficient fluid conduits, which can localize the already regionally elevated heat (e.g., Burton-Johnson et al., 2020; Fox Maule et al., 2005), resulting in vastly enhanced heat flow to the ice base (Gooch et al., 2016), which is likely the cause of the anomalously high heat

flow measured at Subglacial Lake Whillans (285 mWm^{-2} , Fisher et al., 2015). We hypothesized in Chapter 2 that these faults not only provide a spatial control on geothermal heat flux, but a temporal control as well.

Temporal control on geothermal heat

As ice thickness has varied throughout the Holocene, the changing ice overburden pressure on the subglacial sediments drives the discharge and recharge of these sedimentary aquifers (Gooch et al., 2016; Li et al., 2022). This fluid movement is accommodated along fault-damage zones and impermeable basement margins (Figure 5.1 Jolie et al., 2021). This may present a positive feedback, where thickening ice drives groundwater into the aquifers, advecting heat away from the ice base, which slows the flow of ice, leading to increased thickness. Similarly, as ice thins, the reduced overburden on the aquifers results in water discharge to the ice base and an associated localization of heat. The resulting increased flow speed and thinning of the ice further reduces the overburden pressure. These mechanisms express how crustal structures often thought of as static on a millennial timescale from the viewpoint of ice dynamics may enable rapid changes in ice dynamics. The co-location of highly dynamic ice streams (Bougamont et al., 2015; Catania et al., 2012), extensive groundwater reservoirs (Christoffersen et al., 2014; Gustafson et al., 2022), elevated geothermal heat flux (Burton-Johnson et al., 2020; Shen et al., 2020), and fluid pathways (Chapter 2), highlight the Siple Coast as an ideal study site to investigate these possible relations between changes in ice thickness, groundwater discharge, and the advection of geothermal heat. We now discuss various implications of our geologic findings for understanding past and future ice dynamics of the Ross Ice Shelf region.

5.4.2 Constraining past and future ice sheet behaviour

While the above geologic controls on the ice sheet likely existed in the past and will continue into the future, our study has implications that are exclusive to past or future ice sheet configurations. The pinning points we discussed, and the regions of thin draft, were all likely pinning points during periods of thicker ice. Since the Last Glacial Maximum ($\sim 22 \text{ ka}$) retreat of the grounding line from the outer shelf edge has been primarily controlled by the physiography of the bed, as well as its geologic composition (Anderson et al., 2019; Halberstadt et al., 2016). While the retreat dynamics have been well studied in the Ross Sea, where the open ocean conditions allow seismic and high-resolution multi-beam sonar surveying (Anderson et al., 2019; Halberstadt et al., 2016), and drill cores provide sedimentary records (McKay et al., 2016), under the Ross Ice Shelf there has been very little investigation on retreat dynamics, apart from modelling studies (Kingslake et al., 2018; Lowry et al., 2020). Here we have provided the physiography of the region, through the sub-Ross Ice Shelf bathymetry model, enabling insight into the retreat dynamics throughout the Holocene.

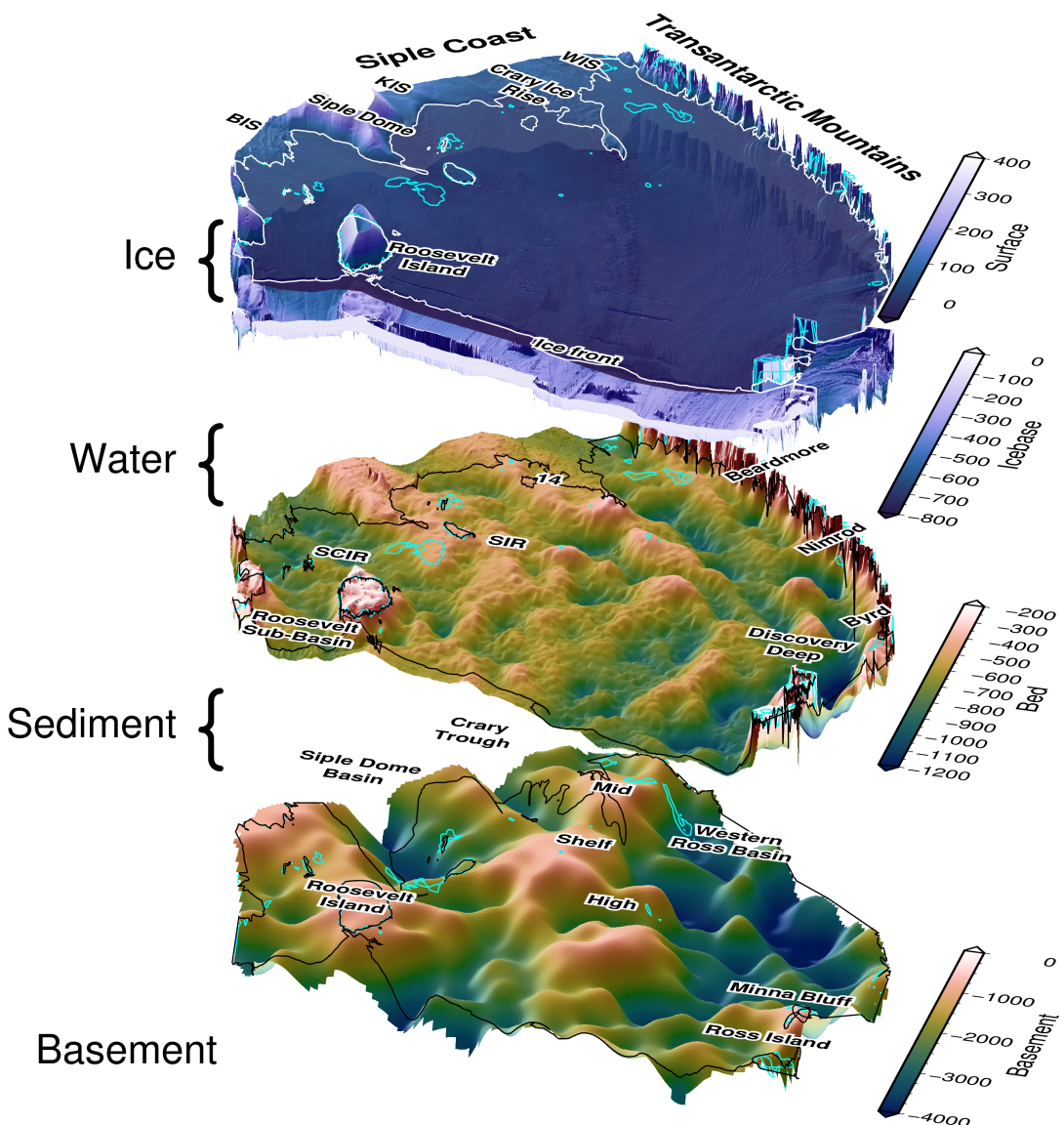


Figure 5.3: A 3D perspective view of the structure of the Ross Ice Shelf. Starting at the top, ice surface, and ice base from BedMachine v3 (Morlighem, 2022; Morlighem et al., 2020), inverted bathymetry results from Chapter 4, and basement topography from Chapter 2. Grounding line shown in all layers if from Morlighem (2022). Bright blue contour shows 20 m water column thickness. Note each layer has an independent vertical exaggeration to aid in visualization. Acronyms: BIS: Bindschadler Ice Stream, KIS: Kamb Ice Stream, WIS: Whillans Ice Stream, SCIR: Shirase Coast Ice Rumples, SIR: Steershead Ice Rise.

5.4.2.1 Retreat dynamics

While we don't constrain the age of the sea floor sediments, the general physiography of the sea floor can provide some insights. The eastern side of the ice shelf, apart from Roosevelt Island, shows similar physiography to the eastern Ross Sea, with relatively flat bathymetry without major banks or troughs (Figure 5.1e). There, the subdued bathymetry likely resulted in a stepwise style of grounding line retreat throughout the Miocene, with the stabilizing build-up of grounding zone wedges, followed by decoupling and rapid retreat of 10's of kilometres (Anderson et al., 2019; Bart et al., 2017). The bathymetry of the western Ross Ice Shelf, characterized by

depth troughs and shallow banks, is similar to that of the western Ross Sea (Figure 5.1e). There, the retreat style, also controlled by the bathymetry, was continuous and complex, as ice streams followed the bathymetry in a continuous retreat back to the outlet valleys in the Transantarctic Mountains (Anderson et al., 2019; Halberstadt et al., 2016). In the western Ross Sea, repeated cycles of advance and retreat within these confined bathymetry troughs led to the scouring of sediments from the inner shelf, and an over-deepened, landward sloping inner shelf (Anderson et al., 2019). These contrasting styles of retreat proposed for the eastern and western Ross Ice Shelf may be in part responsible for the varied bathymetry found on either side of the ice shelf. The above section discussed our bathymetry results in relation to past and future ice dynamics. Next, we discuss the implication of our basement topography on the glacial history of the region.

5.4.2.2 Glacial initialization

During the Oligocene, the Ross Embayment contained a long and broad mountain range emergent above sea level, trending N-S from the Ross Sea through the ice shelf. This feature was first recognized from the drill cores of DSDP (Deep Sea Drilling Project) site 270 in the Ross Sea (Figure 5.1f, Leckie, 1983), where a 400 m sedimentary sequence with depositional environments ranging from above sea level to ~ 500 m below sea level was found, dating from late Oligocene to early Miocene (Kulhanek et al., 2019). Beneath this sequence was crystalline basement. The broad dome-like shape of this basement high was revealed by shipborne seismic surveys (Brancolini et al., 1995), which imaged a similar basement high further north. These basement features were termed the Northern and Southern Central High. Seismic data also revealed small U-shaped channels within the acoustic basement, which were attributed to alpine glaciation (De Santis et al., 1995). Off the flanks of these fault-bound basement highs, wider troughs in the basement were imaged and attributed to the erosion of ice streams flowing off these basement highs. During the late Oligocene, ice caps nucleated on these subaerial basement features (De Santis et al., 1995; Olivetti et al., 2023). Thermal subsidence following the onset of mid-Cretaceous West Antarctic Rift System extension (Karner et al., 2005; Wilson & Luyendyk, 2009) gradually submerged these basement highs (De Santis, 1999; Olivetti et al., 2023). In addition to the North and South Central High features in the Ross Sea, paleotopographic reconstructions of the Oligocene (Paxman et al., 2019; Wilson et al., 2012) have predicted the continuation of this broad subaerial mountain range under the Ross Ice Shelf. Our depth to magnetic basement (Chapter 2) provided the first observations of the feature, which we termed the Mid Shelf High, beneath the Ross Ice Shelf (Figure 5.1f).

The strong continuity of the Mid Shelf High with the Ross Sea's Central High suggests that these features have similar histories. We propose the three blocks of the Mid Shelf High were emergent and hosted ice caps in the Oligocene. Following their submersion, likely in the latest Oligocene (Olivetti et al., 2023) these features would have acted as major bathymetry pinning points, similar to the modern Roosevelt Island. We suggest this chain of shallow basement blocks formed a long-lasting catchment divide of both sediment transport and ice flow between East and West Antarctica. This divide has been predicted as far back as the Paleogene, from distinct microfossil assemblages on either side of the Ross Embayment (Coenen et

al., 2019). Since the Last Glacial Maximum, the Central High has been thought to be an ice flow divide, separating ice originating from the East and West Antarctic Ice Sheets (Li et al., 2020; Licht et al., 2014; Licht et al., 2005). The prominent Mid Shelf High / Central High appears to have played a central role in the history of the Ross Embayment since the Oligocene.

5.5 Future work

Here we provide several suggestions for future research and fieldwork related to this thesis. A primary piece of future work resulting from this thesis should be the incorporation of the updated bathymetry into a sub-ice shelf circulation model. To access the sensitivity of sub-shelf circulations to bathymetry, models should be run for our mean bathymetry model, as well as the upper and lower ranges of our uncertainties, as defined by the mean model plus and minus the spatial uncertainty we present (Figure 5.2). To better improve the bathymetry model and reduce uncertainties, we suggest three alternatives for field seasons on the Ross Ice Shelf.

1. Collect additional seismic depth measurements along the Transantarctic Mountain front. This would serve to lower uncertainties in the bathymetry associated with the nearby steep topography. A traverse-style field season would be best for this to accommodate the linear nature of the grounding zone. Collecting occasional cross lines, running perpendicular to the grounding line, would likely image the range front faults, commonly inferred by only rarely imaged.
2. A seismic survey of the central block of the Mid Shelf High (Figure 5.1f). This survey would accomplish several goals. First, it would fill one of the two major gaps in bathymetry measurements in the central ice shelf, reducing the bathymetry uncertainty. Secondly, it would inform on the nature of the Mid Shelf High as a past pinning point and nucleation site of Oligocene ice caps. Lastly, it would act as a site survey for potential sea-floor drilling. The thin sedimentary cover of the Mid Shelf High may provide a good target for future drilling since a temporally wide-ranging sequence may be concentrated into a thin sedimentary package. Additionally, sampling of the crystalline basement, trace element and provenance analysis will give further insights into 1) the proposed East-West Antarctic geologic boundary along the middle of the Ross Embayment (Tinto et al., 2019), 2) the region's Cretaceous extensional history (Olivetti et al., 2023), and 3) the region's Oligocene to Miocene climatic evolution (Olivetti et al., 2023).
3. Conduct a regional seismic survey across portions of the Siple Coast to better image the sedimentary basins and basin bounding faults, especially where the faults proposed in Chapter 2 may interact with the ice streams.

We make several suggestions for future inversions based on our comprehensive review of past Antarctic bathymetry gravity inversions. To test the inversion method developed here, it would be useful to perform another inversion for an ice shelf that has been previously inverted. The three best options would be the Getz Ice Shelf, the Thwaites Glacier, and the Pine Island Glacier. The bathymetry beneath each of these ice shelves has been inverted three separate times, allowing the comparison of several different methods. The Getz Ice shelf bathymetry has been inverted in 2D

(Cochran et al., 2020; Wei et al., 2020), and with a 3D frequency-based inversion (Millan et al., 2020). The Thwaites cavity has also been inverted in both 2D (Tinto & Bell, 2011) and 3D, with both the "topo-shift method" (Jordan et al., 2020a), and a frequency-based method (Millan et al., 2017). Lastly, the Pine Island Glacier bathymetry has been inversion twice with Simulated Annealing (Muto et al., 2013a; Muto et al., 2016), and once with a frequency-based inversion (Millan et al., 2017). To compare to a wider range of methods, the Thwaites glacier would be optimal. To gain insights into the effectiveness of our uncertainty analysis, Pine Island Glacier should be chosen since spatially variable uncertainty estimates exist from the studies which used Simulated Annealing.

Of the major Antarctic ice shelves, there are four that stand out as prime candidates for a future inversion if the goal is to increase our sub-ice shelf bathymetric knowledge. These include the Larsen C Ice Shelf, the Ronne Filchner Ice Shelf, the Riiser-Larsen Ice Shelf, and the Shackleton Ice Shelf.

1. Larsen C is the largest ice shelf on the Antarctic Peninsula, yet bathymetry knowledge beneath it is still limited. A bathymetry inversion has been conducted (Cochran & Bell, 2012), but comparison with seismic constraints revealed large uncertainties in the model. A recent constraint compilation and new seismic data (Brisbourne et al., 2020) make this an ideal candidate without needing any field work. Additional gravity data has also been collected over the ice shelf during 2016, 2017, and 2018 Operation Ice Bridge flights ("IceBridge Sander AIRGrav L1B Geolocated Free Air Gravity Anomalies, Version 1", 2020).
2. The Ronne Filchner is the second-largest ice shelf, yet has not been included in a gravity inversion. An extensive array of seismic constraints, similar to the RIGGS survey of the Ross Ice Shelf exists (Fretwell et al., 2013; Rosier et al., 2018), and gravity data from compiled from Russian airborne and ground-based surveys (Aleshkova et al., 2000; Studinger & Miller, 1999) is accessible as part of the continent-wide AntGG gravity compilation (Scheinert et al., 2016).
3. and 4. The Riiser-Larsen and the Shackleton Ice Shelves are the 5th and 7th largest ice shelves, respectively. To our knowledge, there is no bathymetry knowledge beneath the entirety of either shelf. Gravity data exists for both shelves from the AntGG compilation (Scheinert et al., 2016). Performing inversions for these shelves would require extensive seismic data acquisition to be adequately constrained.

Lastly, we highlight a few alternative use cases and limitations for our gravity inversion algorithm. While this has been developed for a regional-scale sub-ice shelf application, at its core the inversion is a standard geometric (sometimes referred to as structural) inversion. Therefore, this code can be used to invert any topographic surface of a user-defined density contrast based on input gravity anomaly data. It is compatible with domains ranging from small-scale, local areas, to large domains such as ours (1000×1000 km). However, domains significantly larger than ours (continental scale) will introduce inaccuracies due to our use of vertical right-rectangular prisms, which makes assumptions of a planar Earth. For these

continental to global scale inversions, vertical prisms should be replaced with spherical prisms (tesseroids), as implemented by (Uieda & Barbosa, 2017). With this, our inversion will work for other applications, such as predicting regional Moho depths, the sediment-basement contact, or determining bed depths beneath grounded ice, under subglacial lakes, or in the open ocean. We hope this code is used by others for these various applications.

5.6 Concluding remark

The primary aim of this thesis was to use existing airborne geophysical data to better characterize the geology and physiography beneath Antarctica’s Ross Ice Shelf. We used and developed several geophysical techniques to accomplish this. We first used variations in Earth’s magnetic field measured over the ice shelf to model the spatial distribution and thickness of sediments beneath the ice shelf. We then developed and extensively tested a geophysical inversion, which uses measurements of Earth’s gravity field to model the depth to the seafloor. With this, we created an updated model of the bathymetry beneath the ice shelf.

From this geophysically informed knowledge of the upper crust of the sub-Ross Ice Shelf, we were able to draw inferences on the complex interactions between the solid Earth, ocean, and ice for the Ross Embayment. We highlighted the Siple Coast as a location with strong geologic control on ice dynamics, through 1) the distribution of sediments, which control the competency of bedrock material beneath grounded ice, and 2) the location of deep sedimentary basins, which likely supply the ice base with lubricating water and localize the geothermal heat delivered to the ice. Our bathymetry model confirms the findings of past models which show a deep trough spanning from the ice front near Ross Island south along the Transantarctic Mountain Front. This trough likely guides High Salinity Shelf Water from the ice front to the deep grounding zone of the Transantarctic Mountain outlet glaciers, where it induces significant basal melting. Our spatial uncertainty results highlight the Transantarctic Mountain Front as the least-certain portion of the sub-ice shelf bathymetry model. Combined with this region’s importance for basal melt, we suggest future seismic surveys target the mountain front. This thesis provides the necessary boundary conditions and estimates of their uncertainties for ice and ocean modellers to better characterize the Ross Ice Shelf’s response to past, present, and future changes in the climate.

Appendix A

This appendix section provides supplementary information to Chapter 2, and is taken directly from the published supplementary materials of Tankersley et al. (2022).

A.1 Introduction

This supplement provides additional information on the assumptions behind the process of determining basement depth from magnetic anomalies (Section A.2), the collection and processing of aeromagnetic line data (Section A.3), the methodology of tying ROSETTA-Ice magnetic basement to ANTOSTRAT acoustic basement (Brancolini et al., 1995), through the use of Operation IceBridge (OIB) magnetic data (Cochran et al., 2014a) (Section A.4 & A.5), the gridding, merging, and filtering of the resulting basement grid (Section A.6), the calculation of sediment thickness and β -factors for the region (Section A.7), and our quantification of uncertainties and comparison with points of previously measured sediment thickness (Section A.8). Sediment thickness comparisons with past seismic surveys are included in Table S1. Also included are supplementary figures showing various additional Ross Ice Shelf grids (Figure A.1), the Werner deconvolution solutions of OIB flight 403.3 (A.2), several selected ROSETTA-Ice flight lines with Werner deconvolution solutions (A.3), unfiltered basement solutions with flight line locations and individual Werner deconvolution solutions (A.4), uncertainties applied to basement and sediment thickness results (A.5), and misfit distributions between OIB, ANTOSTRAT, and ROSETTA basement models (A.6). Python code, within a Jupyter notebook, documents our workflow and figure creation and is accessible here: <https://zenodo.org/badge/latestdoi/470814953> or at the GitHub repository: https://github.com/mdtanker/RIS_basement_sediment. Results in the form of netCDF's and csv's are available at <https://doi.pangaea.de/10.1594/PANGAEA.941238>, including figures of all ROSETTA-ice flight line basement solutions.

A.2 Depth to basement assumptions

Our resulting basement grid is the depth to the shallowest magnetic signal. It is assumed that the crystalline basement in this region produces significantly larger magnetic anomalies compared to the overlying sediment fill. Note that in some instances, such as igneous bodies intruded into sedimentary basin fill, Werner determined solutions fall upon the crest of the intrusion, and the actual top of the crystalline basement could be at a deeper level. Intrusions of small lateral extent

will have small widths, resulting in small values of parameter S (susceptibility \times width) and therefore will be removed by our filter (Section A.4). For larger intrusions into existing basins, (i.e. Ross Island and Minna Bluff Cox et al., 2023), the modelled magnetic basement surface will be shallower than the bottom of the sedimentary basin. While this underestimates sediment volume, it better characterizes the competency of the substrate from an ice dynamics perspective. This is similar to how extensive intrusions into basins would be imaged by seismic surveys as shallow basement. However, these extensive regions of late-Cretaceous-Cenozoic magmatism are not expected to be prevalent under the RIS (Andrews & LeMasurier, 2021).

A.3 Magnetic data collection, processing, and Werner deconvolution

Both ROSETTA-Ice and OIB data sets were collected with a Scintrex CS3 Cesium magnetometer. Average flight speeds were 123 m/s and 93 m/s for OIB and ROSETTA-Ice respectively. Altitudes for the sections of OIB flight 403 used here average around 400 m above sea level, while ROSETTA-Ice altitude averaged at 750 m above the ice sheet surface. OIB data were resampled from 20 Hz to 1 Hz to match the frequency of the ROSETTA-Ice data. Both datasets have been despiked, diurnally corrected, and had the International Geomagnetic Reference Field model removed. See Tinto et al. (2019) for more details of the ROSETTA-Ice survey and flight line locations. Due to variable flight elevations, both between and within the datasets, all magnetic data were upward continued to 1000 m above sea level. To avoid artifacts of downwards continuing, any data with flight elevations above 1000 m were removed ($\sim 10\%$ of the data).

Here we use 2D Werner deconvolution Werner (1953), applied to aeromagnetic line data, to image the shallowest magnetic signals in the crust. Assuming that the overlying sediments produce smaller magnetic anomalies than the crystalline basement, we treat the resulting solutions as a depth to the magnetic basement. During Werner deconvolution, moving and expanding windows are passed over the magnetic anomaly line data. Within each window, after linearly detrending the data, the source parameters of the anomalies are estimated with a least-squares approach, assuming the source bodies are infinite-depth dikes or contacts. The source parameters include position (distance along profile and depth), magnetic susceptibility, and source geometry (contact or dike). Solutions are considered valid between 1200 m and 20 km of upward continued flight elevation (approx. 200 m - 19 km bsl). Windows ranged from 500 m - 50 km, with a window shift increment of 1 km and an expansion of 1 km.

Due to passing over the data many times with varying window widths, Werner deconvolution produces a depth-scatter of solutions, which tend to cluster vertically beneath the true magnetic sources. Each of these solutions consists of location, depth, susceptibility (S), window width (W), and a simplified source geometry (dike or contact). For contact-type solutions, parameter S is the estimated magnetic susceptibility of the body, while for dike-type solutions, S is the product of susceptibility and dike width. During filtering (Sections A.4 & A.5), a cut-off based on parameter S is used to remove shallow solutions. Since the value of parameter S for

contact solutions are typically much smaller than for dike solutions (since they are not multiplied by dike width), only dike solutions have been considered here. To achieve a basement surface from this resulting depth-scatter of solutions, we have utilized parameter-based filtering and clustering, described in Sections A.4 & A.5. This Werner deconvolution process was the same for both OIB and ROSETTA-Ice magnetics data. Werner deconvolution was performed in Geosoft's Oasis Montaj and subsequent processing of these results was performed in Python, and is included in a Jupyter notebook; <https://zenodo.org/badge/latestdoi/470814953>.

This magnetic basement approach has been used to map sedimentary basins throughout Antarctica, including the Ross Sea (Karner et al., 2005), western Marie Byrd Land (Bell et al., 2006), and Wilkes Subglacial Basin (Frederick et al., 2016; Studinger et al., 2004a). Our approach is similar to past studies, but our proximity to well-constrained offshore seismic basement depths (Brancolini et al., 1995) allows us to develop the method further. Most studies display their results as 2D profiles with the depth-scatter of solutions mentioned above, and simply use the tops of the clusters as the basement depth. By comparison with seismic basement, we have developed a reliable, automated method of 'draping' a surface over these depth-scattered solutions to produce a 3D surface. This process is described below.

A.4 Tying magnetic basement to seismic basement

To validate the method described in Section A.3 and address uncertainty we perform Werner deconvolution for OIB magnetics data (Figure 2.1b, Cochran et al., 2014a) over the Ross Sea. Here, ice-free conditions have permitted shipborne seismic surveys to image basement depths in the region. These have been compiled by the Antarctic Offshore Acoustic Stratigraphy project (ANTOSTRAT) (Brancolini et al., 1995) (Figure 2.1b). The basement was not imaged for the deepest portions of the basins and data coverage of actual basement reflectors, versus interpolation between basement reflectors, is not reported. Werner deconvolution (Section A.3) produces a series of many solutions (black dots in Figures 2.2 & A.2) at each window along the line.

To achieve a basement surface, instead of a depth-scatter of solutions, solutions were filtered based on Werner window width (W) and the product of magnetic susceptibility and body width (parameter S). Filtered solutions (black circles, scaled to parameter S in Figures 2.2 & A.2) were then horizontally binned with variable bin sizes (parameter B) (vertical grey lines in Figures 2.2 & A.2). Bins with a minimum count of solutions (parameter C) were retained, and the depth of the bin centre was set to the 95th-percentile depth of the solutions in the bin. This removed spurious shallow solutions, while effectively retaining the 'top' of the magnetic signal. These bin centres (orange crosses in Figures 2.2 & A.2) were then interpolated, producing our model of magnetic basement depths (orange line in Figures 2.2 & A.2). The above filtering techniques removed the solutions above the basement, and the clustering technique fitted a surface over the remaining points, which represents the top of the basement. This interpolated line allowed a direct comparison between ANTOSTRAT seismic basement and OIB magnetic basement.

We varied each of the four parameters (W , S , B , and C) with 21 different values

and conducted the above procedures for all unique combinations of them on OIB line 403, segments 1 and 3, in the Ross Sea (location in Figure 2.1b). This resulted in 194,481 iterations, for each of which we calculated a mean absolute difference at points every 5 km between ANTOSTRAT seismic basement and the resulting OIB magnetic basement. We found the parameter values which produced the closest match between OIB magnetic basement and ANTOSTRAT seismic basement, as shown in Figures 2.2 & A.2. These resulting values were a maximum Werner deconvolution window width (parameter W) of 10 km, a minimum product of magnetic susceptibility and body width (parameter S) of 1.0, a horizontal bin width (parameter B) of 36 km, and a minimum number of solutions per bin (parameter C) of 6. The median absolute misfit between OIB and ANTOSTRAT basement for the two line-segments was 480 m (260 m for Line 403.1 (Figure 2.2), and 1040 m for Line 403.3 (Figure A.2)). This equates to 11% of average ANTOSTRAT depths for the two lines. The close fit between the OIB magnetic basement and the ANTOSTRAT seismic basement both supports the validity of this method and gives us the parameters necessary to repeat this method for data over the RIS.

A.5 Tying Ross Sea magnetic basement to Ross Ice Shelf magnetic basement

Having optimized our method to match OIB magnetic basement to ANTOSTRAT seismic basement in the Ross Sea (Section A.4, Figures 2.2 & A.2), we now optimize the method to match ROSETTA-Ice magnetic basement to OIB magnetic basement. This additional optimization is necessary due to differences in processing and survey design, including flight elevations, speed, aircraft, mounting equipment used, and frequency of recording. With the optimized parameters for OIB data (Section A.4), we calculate magnetic basement for OIB flight 404 over the ice shelf. We treat this as the 'true' basement and update the filtering and clustering parameters (Section A.3) to minimize the misfit between OIB basement and the resulting ROSETTA-Ice basement. This tuning was performed on ROSETTA-Ice lines 590 and 650, which were coincident with segments from OIB line 404 (location in Figures 2.1b & A.4). Optimal parameters to match ROSETTA-Ice solutions to OIB basement are found to be $W < 26$ km, $S > 1.2$, $B = 36$ km, and $C > 40$, resulting in a median absolute misfit between OIB basement and ROSETTA-Ice solutions of 400 m (630 m for line 404.590 (Figure A.3e) and 310 m for line 404.590 (Figure A.3f)). This equates to 18% of OIB depths for the two lines. With these parameters which best match ROSETTA magnetic basement to OIB magnetic basement, we performed the same procedure on all the ROSETTA-ice flight lines. A selection of these lines, and the two ties to OIB 404, are shown in Figure A.3. All ROSETTA-ice flight line solutions are available as images at the PANGAEA link.

A.6 Gridding, merging, and filtering

The above processes were performed on all ROSETTA-ice flight lines (white lines in Figure A.4), including the N-S tie lines at ~ 55 km spacing. Where the tie lines crossed over the E-W flight lines, some resulting basement solutions (black dots in Figure A.4) are nearby those from the crossing line. Since we are interested in the

shallowest magnetic signals, we have retained only the shallowest solution with 8 km cells across our region. Since bin widths (parameter B) were set to 36 km, the nearest solutions along individual lines were further apart than the 8 km cell. The closest spacing of E-W flight lines was 10 km, so this process only affected solutions at the crossover between N-S and E-W lines. These points were then gridded with a 5 km cell size and a minimum curvature spline with a tension factor of 0.35 Smith and Wessel, 1990 (Figure A.4). This grid was then merged with a Ross Sea seismic basement grid. The Ross Sea grid, while mostly ANTOSTRAT data, was sourced from a regional compilation of sediment thicknesses (Lindeque et al., 2016; Wilson & Luyendyk, 2009) we have subtracted from bathymetry depths (Morlighem et al., 2020) to achieve basement depths. Where the grids overlap near the ice shelf edge, we retain our RIS values. To aid in the merging at the overlaps, and to match RIS basement wavelengths to the characteristic basement wavelengths of ANTOSTRAT, we filtered the merged grid with an 80 km Gaussian filter (Figure 2.3a). This filtering was performed with a variety of wavelengths (20-120 km), where we found filters <80 km didn't significantly alter the regional basement, while filters >80 km excessively smoothed the basement topography. A few locations with anomalously shallow basement were set equal to BedMachine bathymetry.

A.7 Sediment thickness and β -factor calculations

With the regional basement model (Figure 2.3a) including RIS magnetic basement and offshore seismic basement, we calculated sediment thickness (Figure 2.3b) by subtracting the grid from Bedmachine bathymetry depths (Figure 2.1a & A.1e, Morlighem et al., 2020). Previous estimates of sediment thickness for the sub-RIS come from the extrapolation of gravity anomalies with bathymetry trends (Wilson & Luyendyk, 2009). These were included in the Lindeque et al. (2016) compilation (Figure A.1d). Eocene Oligocene boundary paleotopographic reconstructions (Paxman et al., 2019; Wilson et al., 2012) assumed this sediment estimate was post-Eocene and used it as their maximum sub-RIS sediment thickness, incorporated into their minimum surface reconstruction. The thickness of sediment affects onshore erosion estimates, surface raising due to deposition, and isostatic surface subsidence due to loading. For their maximum paleotopographic reconstructions, they used a thinner sediment model, with the same general trends (Wilson & Luyendyk, 2009). Figure A.1 (c, d, & f) shows the comparison between the sediment thickness models. Figure A.1f colorbar histogram shows the distribution, with our values having a mean thickness ~ 115 m greater than the past model. Yet, along the Siple Coast, we show much greater discrepancies, up to 2 km thicker. β -factor, the ratio of initial crustal thickness to final crustal thickness, is useful for quantifying the thinning of crust in extensional settings. We calculate a distribution of β -factors beneath the RIS by assuming a uniform initial crustal thickness and dividing it by current crustal thickness. We pick an initial crustal thickness of 38 km, which represents a global average for un-thinned plateau-type crust (Mooney et al., 1998), and has been used for the West Antarctic Rift System β -factor calculations (Müller et al., 2007). For the final (current) crustal thickness, we use a continent-wide Moho model from surface wave observations to define the bottom of the crust (An et al., 2015). For the top of the crust, we use our resulting RIS basement grid.

Name	Reference	Seismic sediment thickness (m)	Magnetic sediment thickness (m)	Absolute difference (m)
CIR	(Rooney et al., 1987)	400	514	114
I10S	(Robertson & Bentley, 1989)	750 ± 100	1281	818
J9DC	(Greischar et al., 1992)	1350	770	580
BC	(Robertson & Bentley, 1989)	1900 ± 400	1082	818
RI	(Greischar et al., 1992)	850	822	28
C49	(Crary, 1961)	754	1162	408
LAS	(Crary, 1961)	1325	1799	474
Q13	(Greischar et al., 1992)	255 ± 145	721	466

Table A.1: Previous seismic sediment thickness results for the Ross Ice Shelf. Stations names are labelled in Figure 2.3b. Magnetic sediment thickness column shows our sampled results at the location of each station. Comparing the seismic estimates with our sediment thickness at the eight stations gives a median absolute misfit of 470 m.

A.8 Uncertainties

We estimated a representative uncertainty for our basement model by examining the misfit of our modelled basement compared to offshore seismic basement depths (Brancolini et al., 1995). We did this by sampling our OIB magnetic basement estimate and the coincident ANTOSTRAT basement at 1 km intervals along lines 403.1 and 403.3 (Figures 2.2 and A.2) and compared the values. The resulting absolute values of the differences don't exhibit a normal distribution (Figure A.6a); therefore, we use the median of the absolute misfit (± 480 m) as the basement model uncertainty. This equates to 22% of average basement depths for the sub-RIS. We performed a similar analysis between OIB magnetic basement and ROSETTA-Ice magnetic basement for coincident lines 590 and 650 (Figure A.3 e & f). This resulted in a median absolute misfit of 400 m (Figure A.6b). Tinto et al. (2019) report an uncertainty of 68 m for their bathymetry model. Incorporating this with our basement model gives an uncertainty of 550 m (37% of average thickness) for our sediment thickness results. Comparison with sub-RIS sediment thickness and distribution results from a variety of methods, including active source seismic surveys (Table A.1 and references within), seismic radial anisotropy (Zhou et al., 2022), geophysical machine learning (Li et al., 2022), and magnetotelluric surveying (Gustafson et al., 2022), all show general agreement with our results.

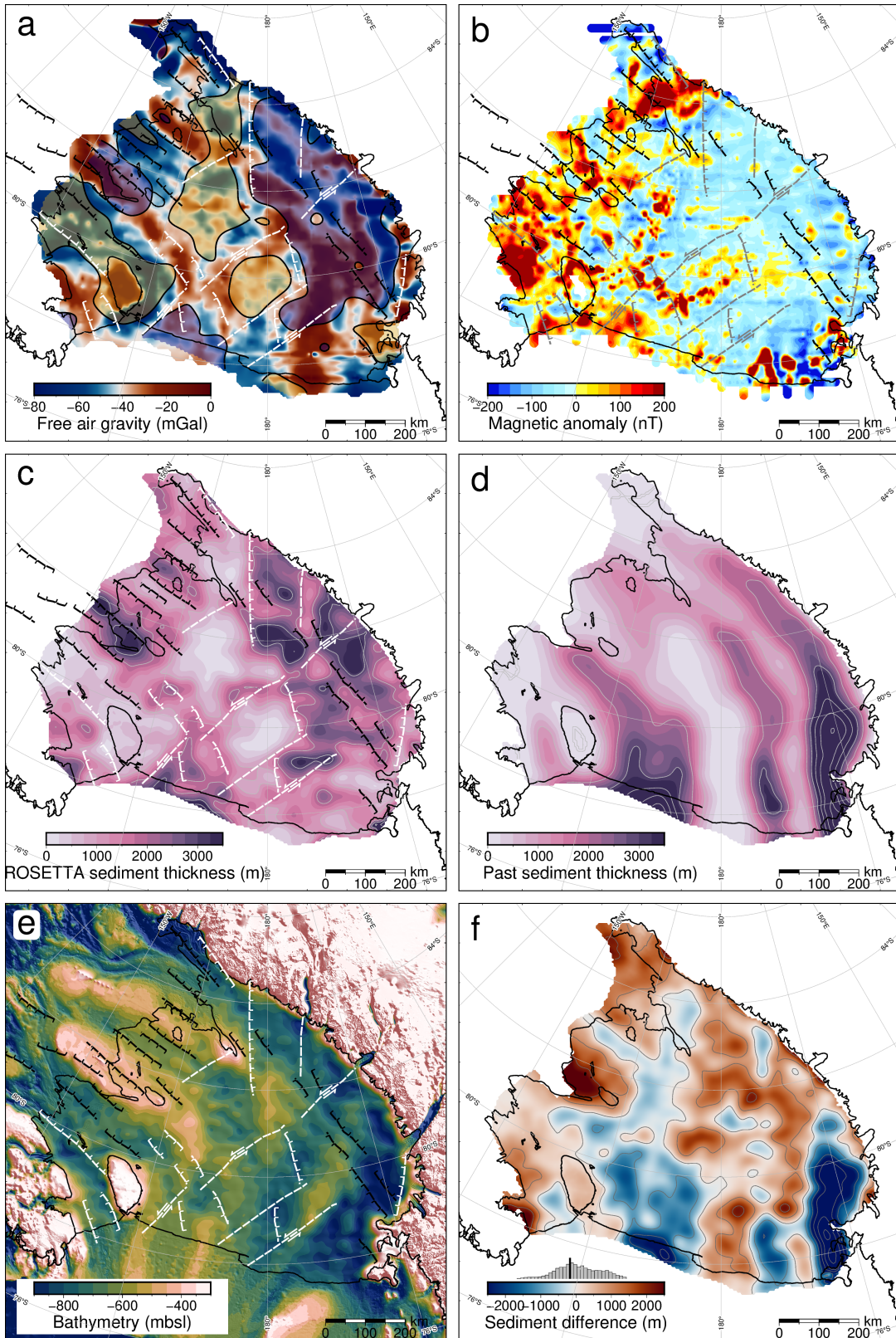


Figure A.1: **a)** ROSETTA-Ice free air gravity (Tinto et al., 2019). Shaded yellow regions are shallow basement ($<\sim 1600$ mbsl), shaded blue regions are deep basement ($>\sim 2600$ mbsl). **b)** ROSETTA-Ice airborne magnetic anomaly data (Tinto et al., 2019). **c)** Sediment thickness from this study (same as Figure 2.3b), with 1 km contours. **d)** Sediment thickness from a regional compilation (Section A.7, Lindeque et al., 2016; Wilson & Luyendyk, 2009), with 1 km contours. **e)** BedMachine2 bathymetry (Morlighem et al., 2020), from which sediment thickness in c) was calculated. **f)** Difference between c) and d). Red signifies our results have more sediment, while blue signifies our results have less sediment. Histogram shows data distribution, with mean value (black) at 115 m. Inferred faults in a), b), c), and e) same as Figure 2.4a. Grounding line and coastlines in black (Rignot et al., 2013). Projection is Antarctic Polar Stereographic: EPSG 3031.

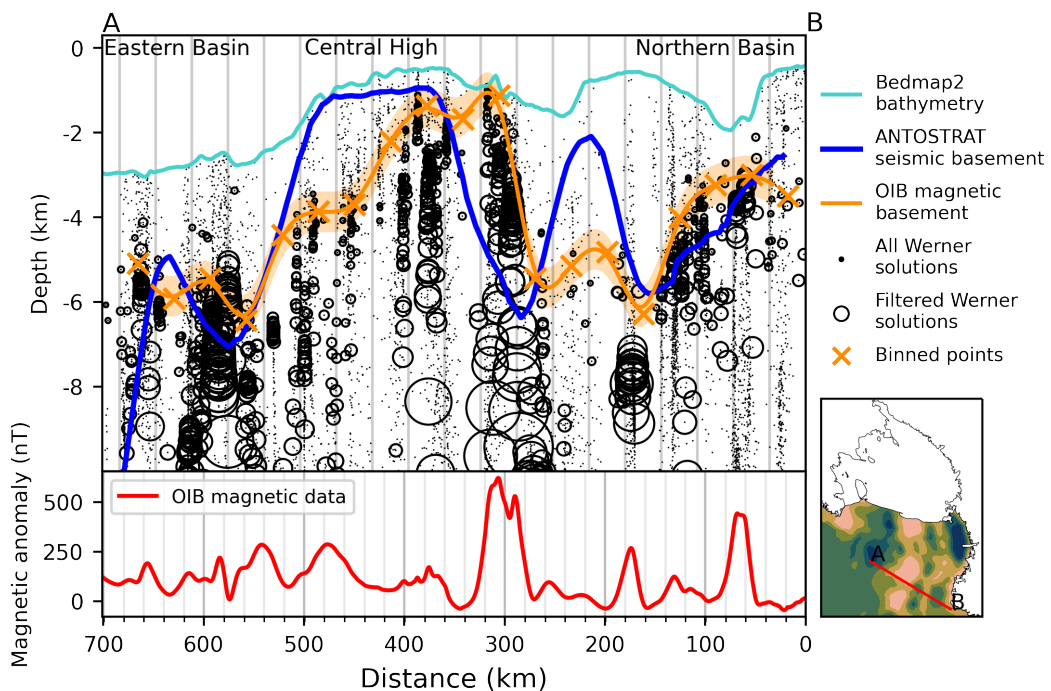


Figure A.2: Ross Sea magnetic and seismic basement comparison. Operation IceBridge airborne magnetic data (lower panel) from segment 403.3 (Figure 2.1b). Small dots show Werner deconvolution solutions, which were filtered based on parameters S and W (Section A.3) to produce black circles, which are scaled to parameter S. These circles were binned at a width equal to parameter B, shown by the vertical grey lines in the upper panel. Orange crosses show bin centres, which were fitted to a line to facilitate the comparison between the magnetic basement (orange line) and seismic basement (blue line). Orange band shows ± 480 m uncertainty for the basement model. Ross Sea basement features are labelled on top.

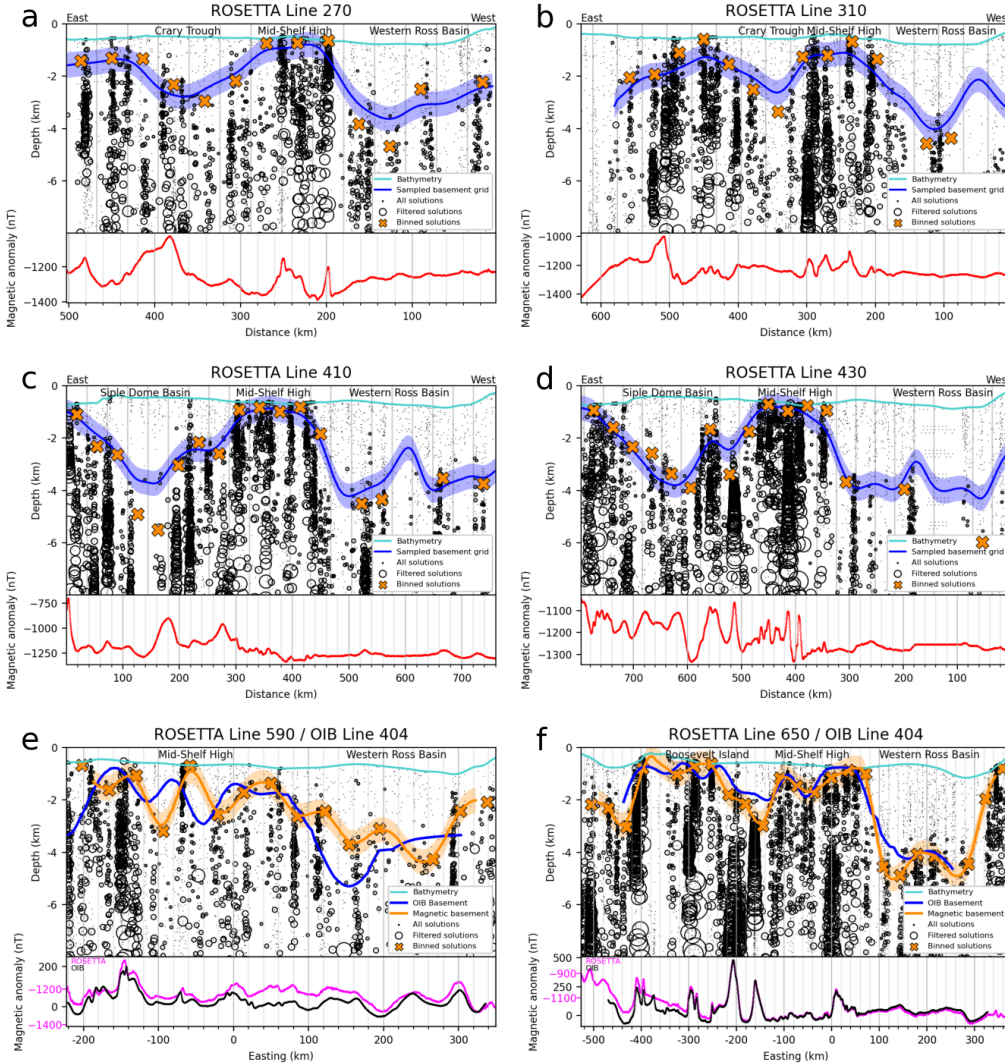


Figure A.3: Werner deconvolution solutions for a selection of ROSETTA-Ice lines, locations highlighted in Figure A.4. Bathymetry from Bedmap2 (Fretwell et al., 2013). Dots, circles, and vertical grey lines same as Figure A.2. **a-d)** Comparison between magnetic basement before and after filtering and gridding. Orange crosses are magnetic basement solutions, shown as black dots in Figure A.4, and highlighted for these lines. Blue lines are magnetic basement sampled from the grid of Figure 1a, after gridding and filtering. Red lines show 258 ROSETTA-Ice magnetics data. **e-f)** Comparison between magnetic basement resulting from Werner deconvolution of coincident OIB and ROSETTA-Ice flight lines. Location is shown in Figures 2.1b and A.4. These two lines were used to tie the ROSETTA-Ice survey to the OIB survey (Section A.5). Blue lines are OIB magnetic basement results, orange crosses and fitted orange lines with uncertainty bands are ROSETTA-Ice magnetic basement. ROSETTA-Ice (pink) and OIB (black) magnetics data are shown in lower panels.

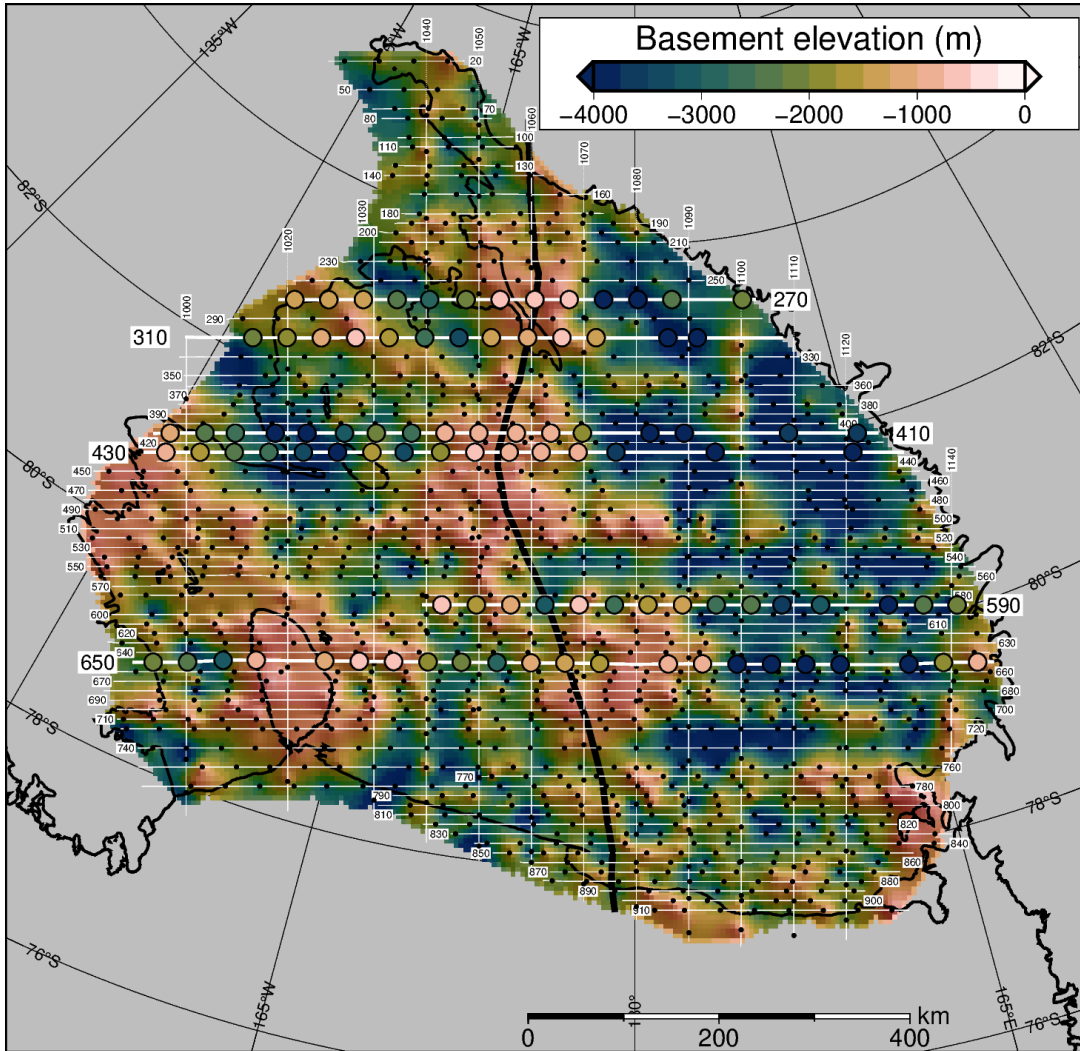


Figure A.4: Unfiltered magnetic basement. Point solutions (black dots here, orange crosses in Figure A.3) along ROSETTA-Ice flight lines (labelled) were gridded with a 5 km cell size and a minimum curvature spline with a tension factor of 0.35. Figure A.3 flight lines (bold white) and point solutions (coloured circles) are shown. Black line through the Mid-Shelf High shows the East-West Antarctic divide used in colorbar histograms of Figures 2.3 and 2.4a. Grounding line and coastlines in black (Rignot et al., 2013).

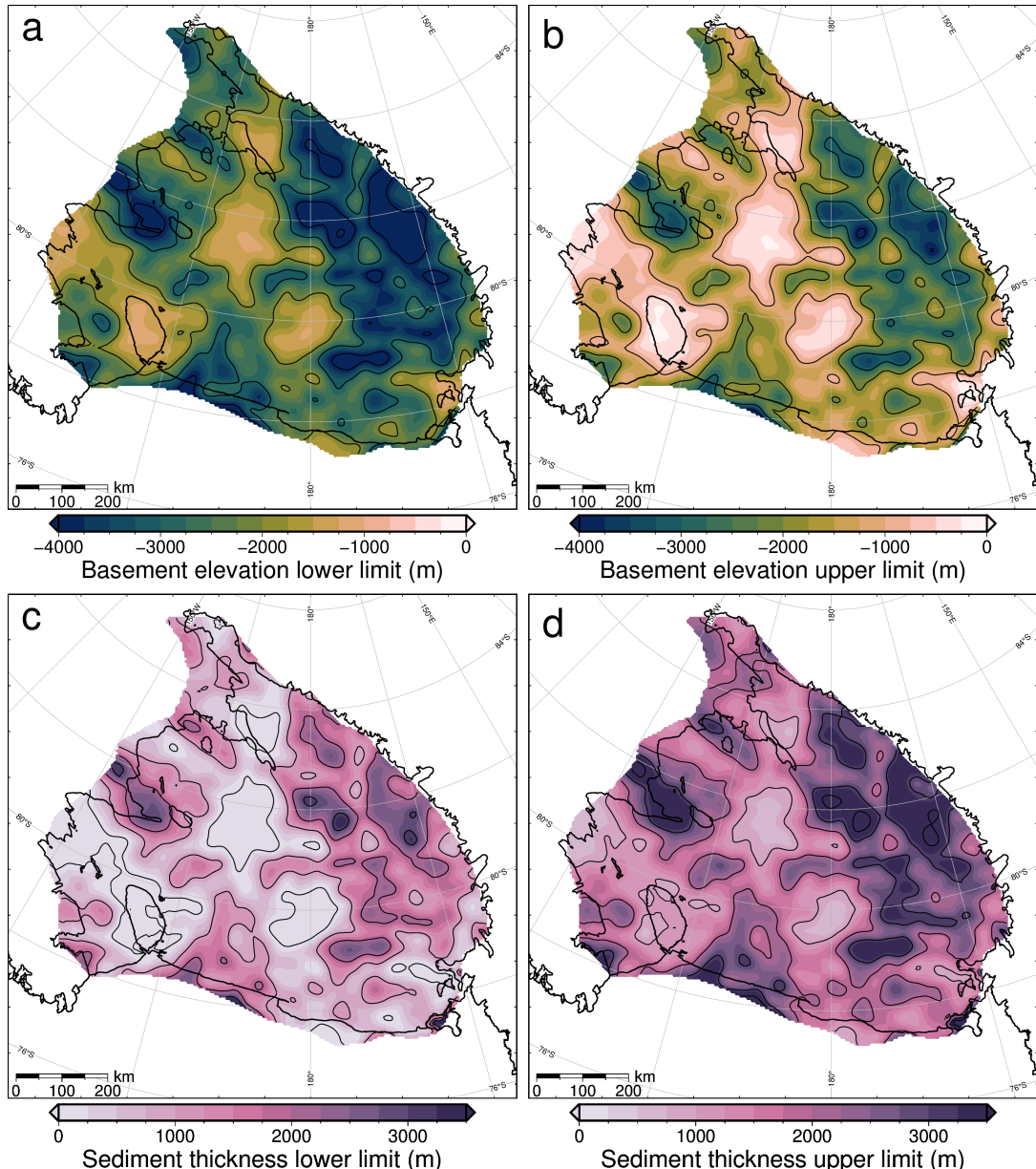


Figure A.5: Upper and lower limits of uncertainty applied to a-b) magnetic basement and c-d) sediment thickness. See Section A.8 for how these uncertainties were determined.

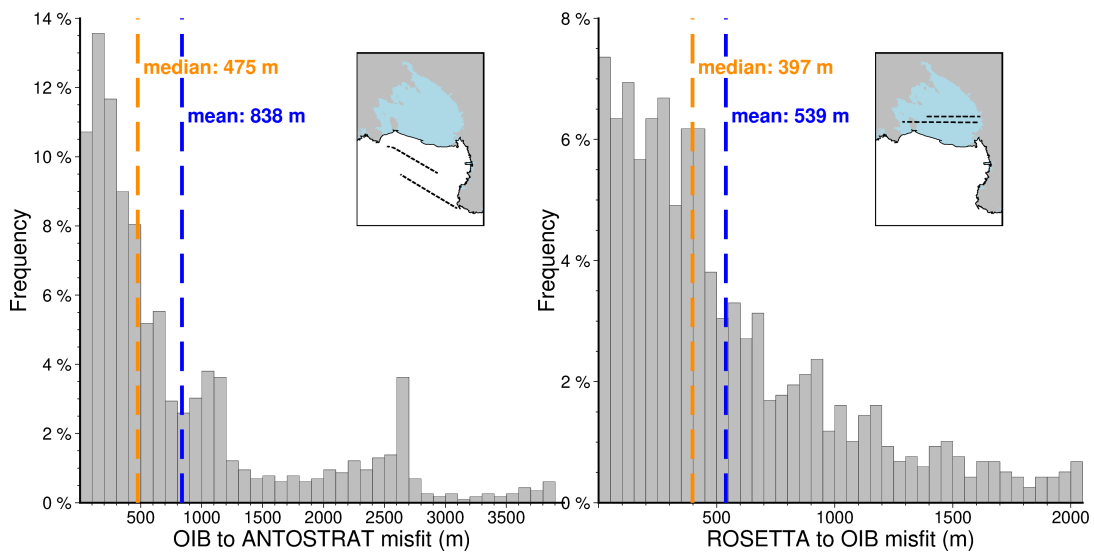


Figure A.6: Misfit distributions for comparisons between **a)** OIB magnetic basement and ANTOSTRAT seismic basement and between **b)** ROSETTA magnetic basement and OIB magnetic basement. Inset maps show the locations of flight lines. Basement models were sampled at 1 km intervals for the comparison.

Appendix B

This appendix section provides supplementary information to Chapter 3.

B.1 Synthetic inversion with a regional field

Regional separation techniques

Figure B.1 shows profiles comparing the various regional separation techniques shown in Figure 3.19 of Chapter 3.

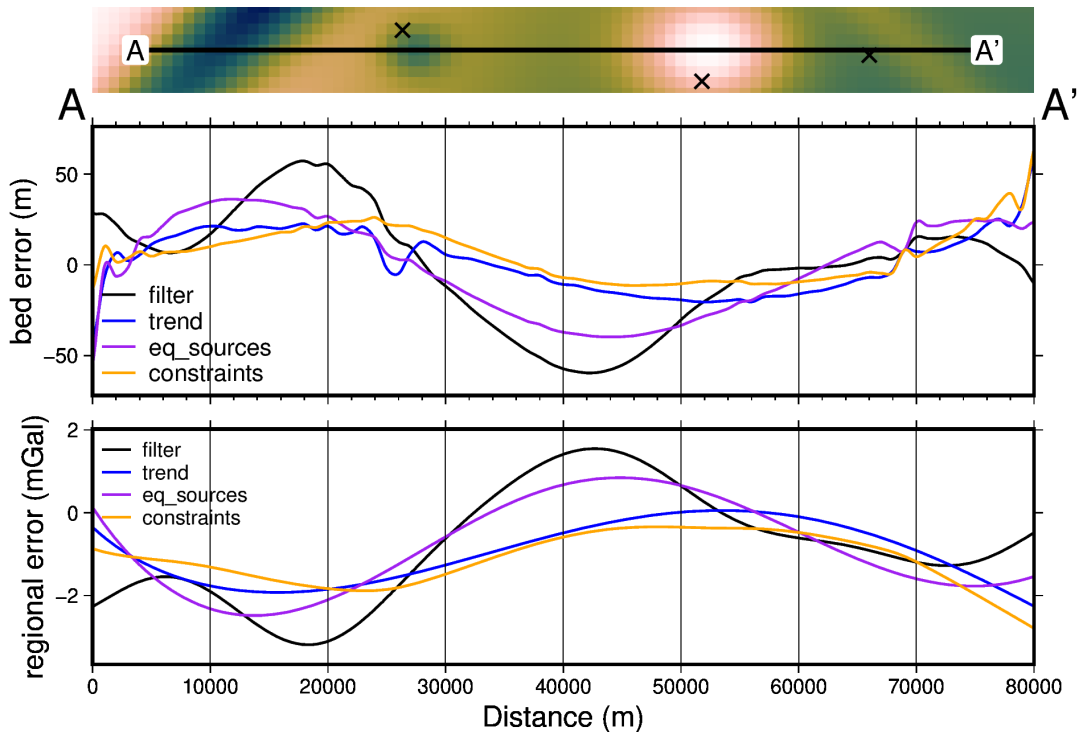


Figure B.1: Comparison of four methods of regional separation. **Upper panel** shows the error in the inverted bathymetry models for each method. **Lower panel** shows the errors in the regional field estimation of each method. Profile location shown at the top.

Constraint point minimization gridding techniques

Figure B.1 shows profiles comparing the various gridding techniques for the constraint point minimization regional separation method. These various gridding techniques are shown in map view in Figure 3.20 of Chapter 3.

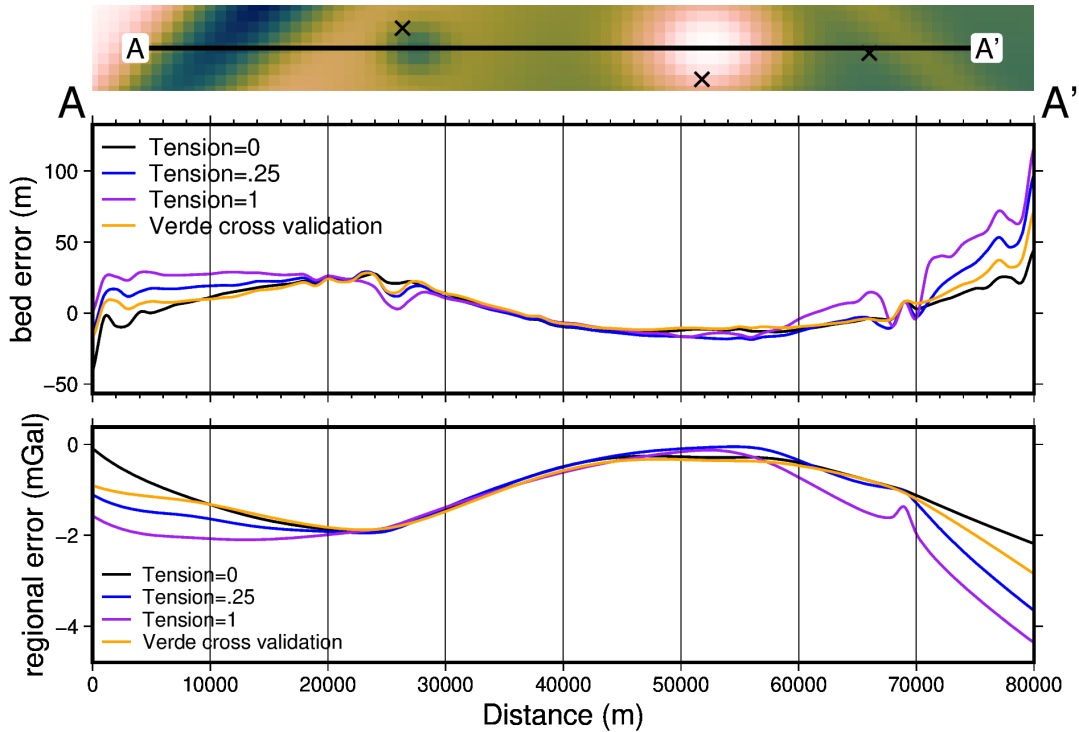


Figure B.2: Comparison of gridding techniques for the constraint point minimization method of regional separation. **Upper panel** shows the error in the inverted bathymetry models for each method. **Lower panel** shows the errors in the regional field estimation of each method. Profile location shown at the top.

Added noise

Here, we repeat the inversion from Section 3.4 with noise added to the observed gravity data. Noise was from a Gaussian distribution with a mean of 0 and a standard deviation of 2% of the max absolute values of the data, equating to 0.24 mGal. The cross-validation curve and a profile across the inverted bathymetry as shown in Figure B.3. The inverted bathymetry and difference with the true bathymetry as shown in Figure B.4. The error in the inverted bathymetry is compared to the error in the regional field estimation in Figure B.5.

Lower-resolution gravity survey

This same inversion is now repeated with a lower-resolution gravity survey. Instead of the original 1 km survey grid, a 4 km grid is used.

B.2 Ross Sea synthetic model

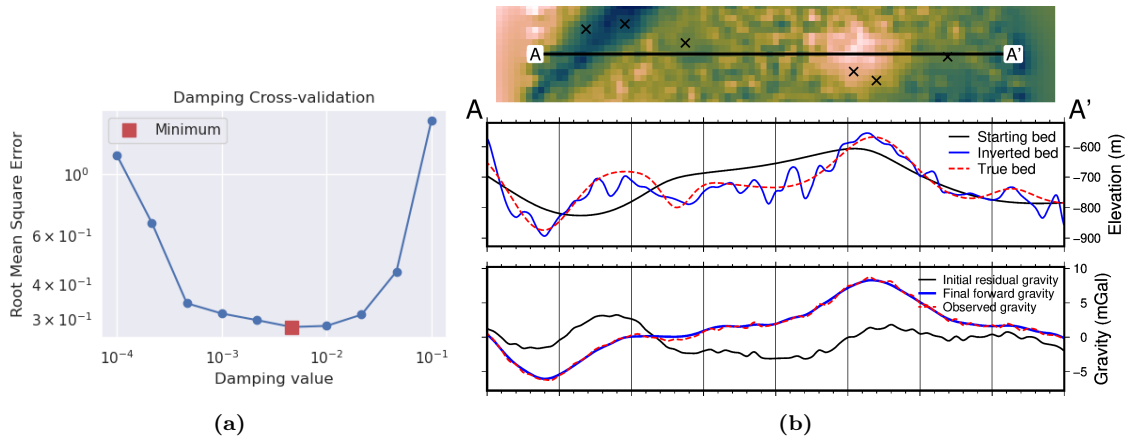


Figure B.3: Cross-validation and profiles for the simple synthetic inversion with a regional component removed and 2% noise added to the observed gravity data. a) Cross-validation curve showing the optimal damping parameter (red square). b) 2D profile of the inversion results. The top panel shows profile location and constraint points (black crosses). The middle panel contains topographic profiles of the starting, inverted, and true bathymetries. The bottom panel contains gravity anomaly profiles.

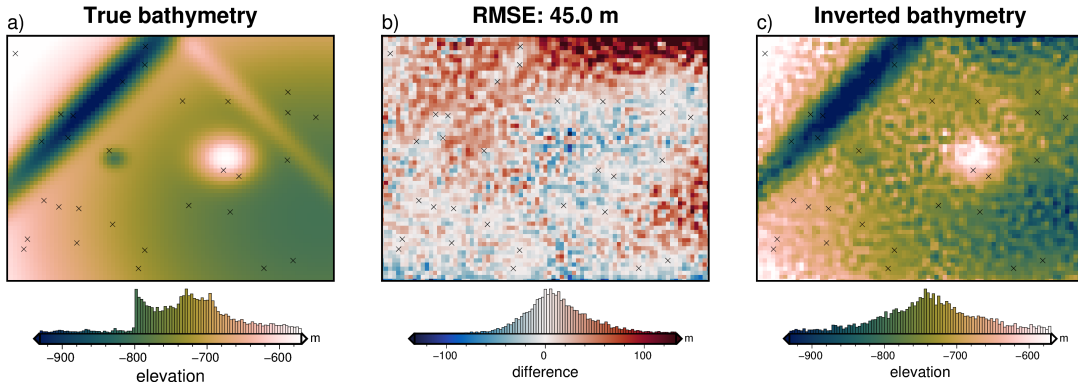


Figure B.4: Simple synthetic model inversion with a removed regional component and noise contamination. a) True bathymetry, b) difference between a) and c), c) final inverted bathymetry. Black crosses are constraint points. The RMS difference with the true bathymetry at these constraints is 2 m.

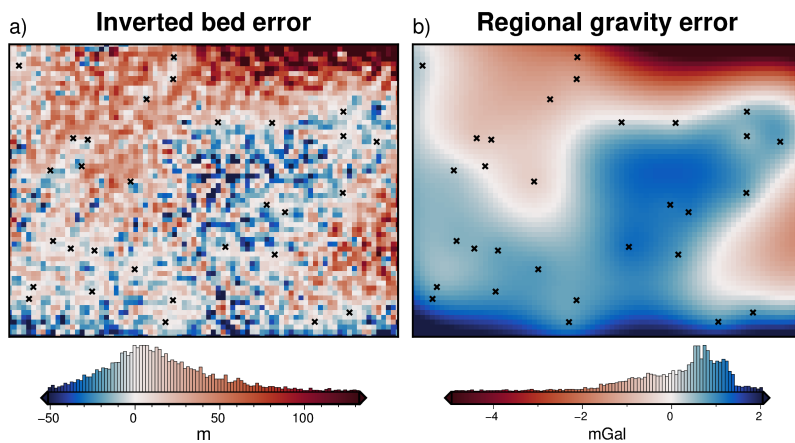


Figure B.5: Source of inverted bathymetry error for model with regional field and noise. a) Inverted bathymetry error from Figure 3.22b. b) Error in the estimation of the regional component of gravity from comparison with the true regional component (Figure 3.18b). Black cross show constraint points. Colourmaps are opposed to highlight the similarities and the mean has been removed from the regional error.

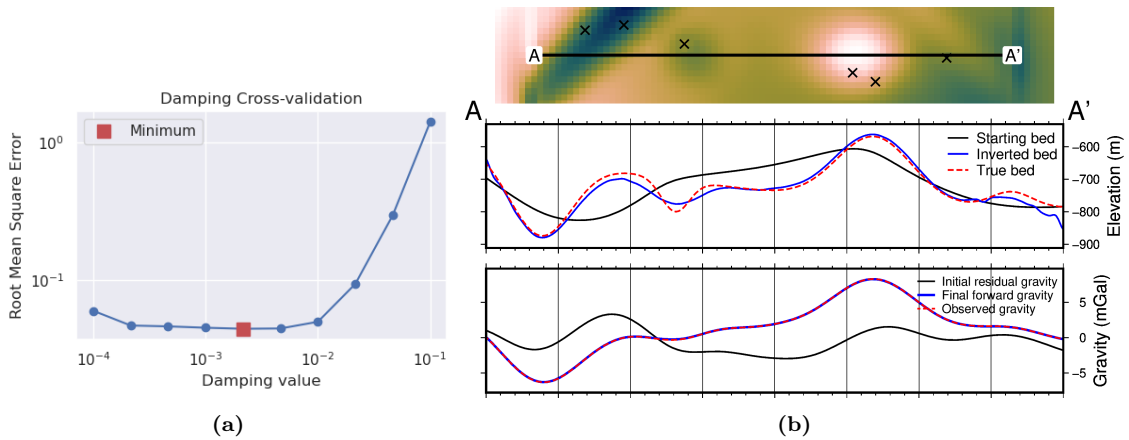


Figure B.6: Cross-validation and profiles for the simple synthetic inversion with a regional component removed and low-resolution gravity data. a) Cross-validation curve showing the optimal damping parameter (red square). b) 2D profile of the inversion results. The top panel shows profile location and constraint points (black crosses). The middle panel contains topographic profiles of the starting, inverted, and true bathymetries. The bottom panel contains gravity anomaly profiles.

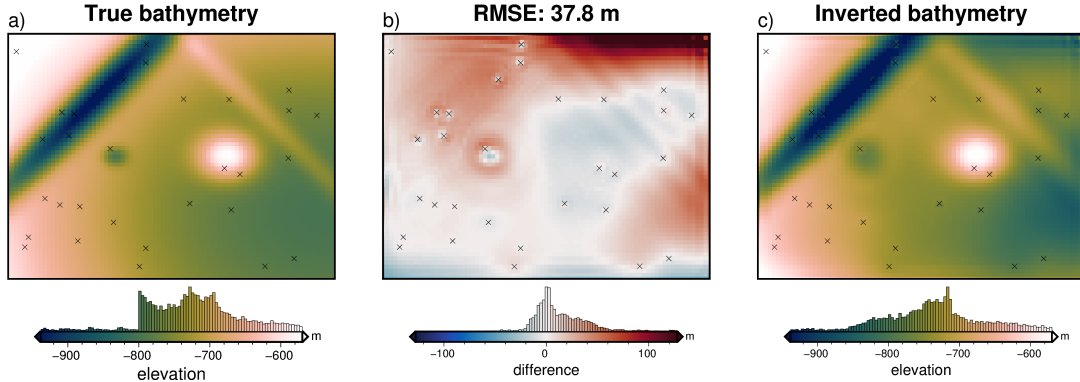


Figure B.7: Simple synthetic model inversion with a removed regional component and gravity resampling. a) True bathymetry, b) difference between a) and c), c) final inverted bathymetry. Black crosses are constraint points. The RMS difference with the true bathymetry at these constraints is 2 m.

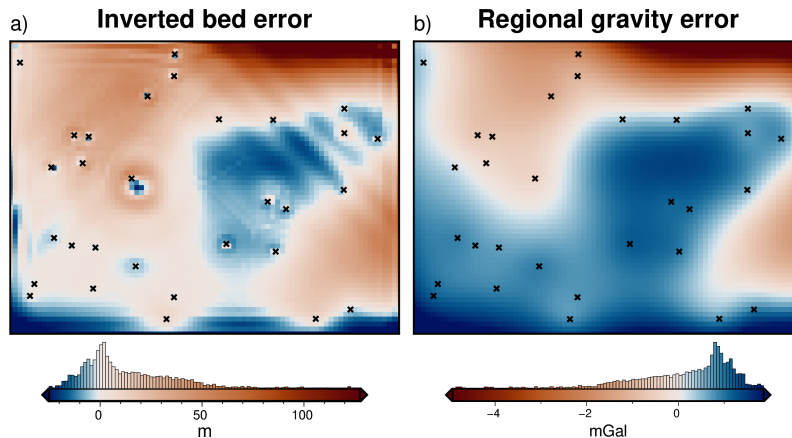


Figure B.8: Source of inverted bathymetry error for model with regional field and re-sampled gravity data. a) Inverted bathymetry error from Figure 3.22b. b) Error in the estimation of the regional component of gravity from comparison with the true regional component (Figure 3.18b). Black crosses show constraint points. Colourmaps are opposed to highlight the similarities and the mean has been removed from the regional error.

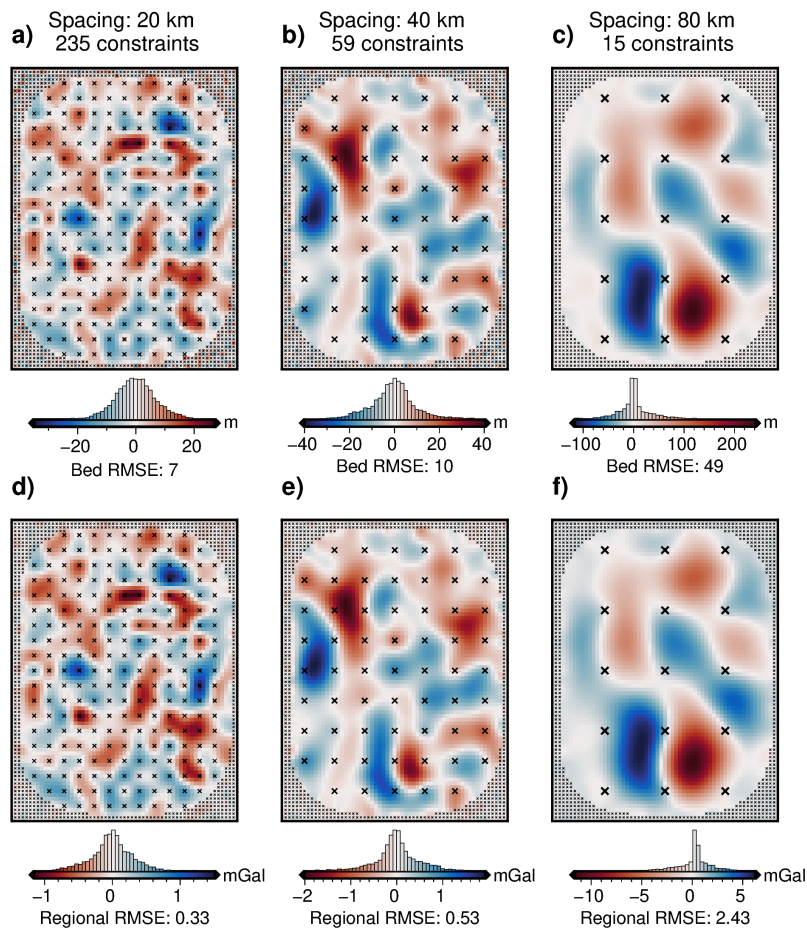


Figure B.9: Source of inverted bathymetry error for three inversion with varying constraint spacings. a) Inverted bathymetry error from three of the models in the constraint ensemble of Figure 3.31. b) Error in the estimation of the regional component of gravity from comparison with the true regional component for each model. Black crosses show constraint points. Colormaps are opposed to highlight the similarities and the mean has been removed from the regional error.

Appendix C

This appendix provides supplemental information to Chapter 4.

C.1 Gravity disturbance vs anomaly

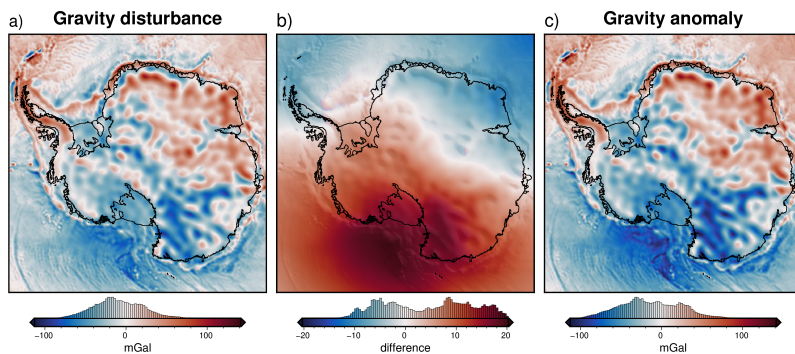


Figure C.1: Difference between the gravity disturbance and anomaly for Antarctica. Observed gravity is from Förste et al. (2014) and the normal gravity for each was calculated with the python package Boule (Fatiando a Terra Project et al., 2022). See Section 4.2.1 for further details.

Appendix D

Antarctic-Plots

This appendix briefly describes the Python package Antarctic-Plots (Tankersley, 2023) which I developed during this thesis and is used in all of the chapters. The documentation of the package is hosted at the following link; <https://antarctic-plots.readthedocs.io/en/latest/index.html> and the code is stored and developed in the following GitHub repository; https://github.com/mdtanker/antarctic_plots.

The Antarctic-Plots Python package aims to help automate common tasks associated with researching Antarctica. There are four main modules of the package; **Fetch**, **Map**, **Profile**, and **Regions**.

D.1 Fetch

The Fetch module contains functions to download data related to Antarctica. These downloads are accomplished with the Python package Pooch Uieda et al. (2020). Calls to these functions will download the respective data and store it in a common folder in your system. Subsequent calls to the same function will retrieve the already downloaded file. There is no need for remembering file paths or having multiple copies of the same data throughout your projects. Additionally, some of this data is pre-processed. This pre-processing includes re-projecting all data (gridded or tabular) to a common projection, South Polar Stereographic (EPSG:3031), and converting pre-gridded tabular data into more useful formats, such as Xarray dataarrays. (Hoyer & Hamman, 2017).

This module currently contains over 40 datasets, which include; topography products, imagery, grounding line, coastline, and basin shapefiles, gravity, magnetics, geothermal heat flow, ice velocity, sediment thickness, moho depths, basal melt, ice mass change, and geologic units and faults. Below is an example that downloads, or retrieves if already download, BedMachine v3 surface elevation data, converted to be referenced to the WGS-84 ellipsoid (as opposed to the original data which is referenced to the geoid), and resampled at a 5 km spacing.

```
from antarctic_plots import fetch

surface_data = fetch.bedmachine(
    layer="surface",
    reference="ellipsoid",
    spacing=5000,
)
```

D.2 Map

The Map module provides convenient methods for plotting geospatial data. Most of these plotting functions use the Python package PyGMT (Uieda et al., 2021). All of the maps in Chapters 3, 4, & 5 were created with the help of these functions. In addition to static figures, there are several functions for creating interactive figures, which help with data visualization.

D.3 Profile

The Profile module is used to sample gridded data along specified profiles, and plot cross-sections and profiles of the data. The cross-section plots of Chapters 3 & 4 were created using these functions. Profiles can be defined by clicking on an interactive map to help with quickly exploring and visualizing datasets.

D.4 Regions

The Regions module provides pre-defined variables of region boundaries in EPSG:3031 for commonly studied Antarctic areas. These region variables are used by the other modules to subset the desired region. For example, if you only want to fetch BedMap2 surface topography only for the Ross Ice Shelf, instead of the whole continent, you can pass the parameter "region = regions.ross_ice_shelf".

Additionally, there are geospatial tools provided for re-projecting, masking, and gridding data. This package is still early in its development and many more datasets and functions will still be added.

Bibliography

- Adusumilli, S., Fricker, H. A., Medley, B., Padman, L., & Siegfried, M. R. (2020). Interannual variations in meltwater input to the Southern Ocean from Antarctic ice shelves. *Nature Geoscience*, 13(9), 616–620. <https://doi.org/10.1038/s41561-020-0616-z> (cit. on pp. 16, 39, 90, 131, 132, 141)
- Aitken, A., Li, L., Kulessa, B., Schroeder, D., Jordan, T., Whittaker, J., Anandakrishnan, S., Dawson, E., Wiens, D., Eisen, O., & Siegert, M. (2023a). *Antarctic sedimentary basin distribution and classification* (Version v1.04). Zenodo. <https://doi.org/10.5281/zenodo.7984586>. (Cit. on p. 139)
- Aitken, A. R., Li, L., Kulessa, B., Schroeder, D. M., Jordan, T. A., Whittaker, J. M., Anandakrishnan, S., Dawson, E. J., Wiens, D. A., Eisen, O., & Siegert, M. J. (2023b). *Antarctica's sedimentary basins and their influence on ice sheet dynamics* (Preprint). Preprints. <https://doi.org/10.1002/essoar.10510905.2>. (Cit. on pp. 17, 20, 138)
- Akiba, T., Sano, S., Yanase, T., Ohta, T., & Koyama, M. (2019). Optuna: A Next-generation Hyperparameter Optimization Framework. *Proceedings of the 25th ACM SIGKDD International Conference on Knowledge Discovery & Data Mining*, 2623–2631. <https://doi.org/10.1145/3292500.3330701> (cit. on p. 51)
- Aleshkova, N. D., Golynsky, A. V., Kurinini, R. G., & Mandrikov, V. S. (2000). Gravity Mapping in the Southern Weddell Sea Region. (Explanatory note for free-air and Bouguer anomalies maps). *Polarforschung*, 15 pages. <https://doi.org/10.2312/POLARFORSCHUNG.67.3.163> (cit. on p. 149)
- Alley, R. B., Blankenship, D. D., Bentley, C. R., & Rooney, S. T. (1986). Deformation of till beneath ice stream B, West Antarctica. *Nature*, 322(6074), 57–59. <https://doi.org/10.1038/322057a0> (cit. on pp. 20, 144)
- An, L., Rignot, E., Elieff, S., Morlighem, M., Millan, R., Mouginot, J., Holland, D. M., Holland, D., & Paden, J. (2017). Bed elevation of Jakobshavn Isbrae, West Greenland, from high-resolution airborne gravity and other data. *Geophysical Research Letters*, 44(8), 3728–3736. <https://doi.org/10.1002/2017GL073245> (cit. on pp. 105, 106, 120)
- An, L., Rignot, E., Chauche, N., Holland, D. M., Holland, D., Jakobsson, M., Kane, E., Wood, M., Klaucke, I., Morlighem, M., Velicogna, I., Weinrebe, W., & Willis, J. K. (2019a). Bathymetry of Southeast Greenland From Oceans Melting Greenland (OMG) Data. *Geophysical Research Letters*, 46(20), 11197–11205. <https://doi.org/10.1029/2019GL083953> (cit. on pp. 46, 63, 105–107, 120, 122)
- An, L., Rignot, E., Millan, R., Tinto, K., & Willis, J. (2019b). Bathymetry of Northwest Greenland Using “Ocean Melting Greenland” (OMG) High-Resolution Airborne Gravity and Other Data. *Remote Sensing*, 11(2), 131. <https://doi.org/10.3390/rs11020131> (cit. on pp. 105–107)
- An, M., Wiens, D. A., Zhao, Y., Feng, M., Nyblade, A. A., Kanao, M., Li, Y., Maggi, A., & Lévéque, J.-J. (2015). S-velocity model and inferred Moho topography beneath the Antarctic Plate from Rayleigh waves: Antarctic S-velocities and Moho. *Journal of Geophysical Research: Solid Earth*, 120(1), 359–383. <https://doi.org/10.1002/2014JB011332> (cit. on pp. 29, 155)
- Anandakrishnan, S., Blankenship, D. D., Alley, R. B., & Stoffa, P. L. (1998). Influence of subglacial geology on the position of a West Antarctic ice stream from seismic observations. *Nature*, 394(6688), 62–65. <https://doi.org/10.1038/27889> (cit. on p. 20)
- Anderson, J. B., Conway, H., Bart, P. J., Witus, A. E., Greenwood, S. L., McKay, R., Hall, B. H., Ackert, R. P., Licht, K., Jakobsson, M., & Stone, J. O. (2014). Ross Sea paleo-ice drainage and deglacial history during and since the LGM. *Quaternary Science Reviews*, 100, 31–54. <https://doi.org/10.1016/j.quascirev.2013.08.020> (cit. on p. 16)

- Anderson, J. B., Simkins, L. M., Bart, P. J., De Santis, L., Halberstadt, A. R. W., Olivo, E., & Greenwood, S. L. (2019). Seismic and geomorphic records of Antarctic Ice Sheet evolution in the Ross Sea and controlling factors in its behaviour. *Geological Society, London, Special Publications*, 475(1), 223–240. <https://doi.org/10.1144/SP475.5> (cit. on pp. 16, 20, 145–147)
- Andrews, J. T., & LeMasurier, W. (2021). Resolving the argument about volcanic bedrock under the West Antarctic Ice Sheet and implications for ice sheet stability and sea level change. *Earth and Planetary Science Letters*, 568, 117035. <https://doi.org/10.1016/j.epsl.2021.117035> (cit. on p. 152)
- Aster, R. C., Borchers, B., & Thurber, C. H. (2018). *Parameter estimation and inverse problems*. Elsevier. (Cit. on pp. 42, 48, 103, 106).
- Austermann, J., Pollard, D., Mitrovica, J. X., Moucha, R., Forte, A. M., DeConto, R. M., Rowley, D. B., & Raymo, M. E. (2015). The impact of dynamic topography change on Antarctic ice sheet stability during the mid-Pliocene warm period. *Geology*, 43(10), 927–930. <https://doi.org/10.1130/G36988.1> (cit. on p. 26)
- Bamber, J. L., Oppenheimer, M., Kopp, R. E., Aspinall, W. P., & Cooke, R. M. (2022). Ice Sheet and Climate Processes Driving the Uncertainty in Projections of Future Sea Level Rise: Findings From a Structured Expert Judgement Approach. *Earth's Future*, 10(10). <https://doi.org/10.1029/2022EF002772> (cit. on pp. 15, 16)
- Bamber, J., & Bentley, C. R. (1994). A comparison of satellite-altimetry and ice-thickness measurements of the Ross Ice Shelf, Antarctica. *Annals of Glaciology*, 20, 357–364. <https://doi.org/10.3189/1994AoG20-1-357-364> (cit. on p. 38)
- Barbosa, V. C., Menezes, P. T., & Silva, J. B. (2007). Gravity data as a tool for detecting faults: In-depth enhancement of subtle Almada's basement faults, Brazil. *GEOPHYSICS*, 72(3), B59–B68. <https://doi.org/10.1190/1.2713226> (cit. on p. 42)
- Barletta, V. R., Bevis, M., Smith, B. E., Wilson, T., Brown, A., Bordoni, A., Willis, M., Khan, S. A., Rovira-Navarro, M., Dalziel, I., Smalley, R., Kendrick, E., Konfal, S., Caccamise, D. J., Aster, R. C., Nyblade, A., & Wiens, D. A. (2018). Observed rapid bedrock uplift in Amundsen Sea Embayment promotes ice-sheet stability. *Science*, 360(6395), 1335–1339. <https://doi.org/10.1126/science.aa01447> (cit. on pp. 18, 143, 144)
- Bart, P., & De Santis, L. (2012). Glacial intensification during the Neogene: A review of seismic stratigraphic evidence from the Ross Sea, Antarctica, continental shelf. *Oceanography*, 25(3), 166–183. <https://doi.org/10.5670/oceanog.2012.92> (cit. on p. 34)
- Bart, P. J., Krogmeier, B. J., Bart, M. P., & Tulaczyk, S. (2017). The paradox of a long grounding during West Antarctic Ice Sheet retreat in Ross Sea. *Scientific Reports*, 7(1), 1262. <https://doi.org/10.1038/s41598-017-01329-8> (cit. on p. 146)
- Beaudoin, B. C., ten Brink, U. S., & Stern, T. A. (1992). Characteristics and processing of seismic data collected on thick, floating ice: Results from the Ross Ice Shelf, Antarctica. *Geophysics*, 57(10), 1359–1372. <https://doi.org/10.1190/1.1443205> (cit. on p. 31)
- Begeman, C. B., Tulaczyk, S. M., & Fisher, A. T. (2017). Spatially Variable Geothermal Heat Flux in West Antarctica: Evidence and Implications. *Geophysical Research Letters*, 44(19), 9823–9832. <https://doi.org/10.1002/2017GL075579> (cit. on pp. 28, 144)
- Bell, R. E., Blankenship, D. D., Finn, C. A., Morse, D. L., Scambos, T. A., Brozena, J. M., & Hodge, S. M. (1998). Influence of subglacial geology on the onset of a West Antarctic ice stream from aerogeophysical observations. *Nature*, 394(6688), 58–62. <https://doi.org/10.1038/27883> (cit. on p. 20)
- Bell, R. E., Studinger, M., Karner, G., Finn, C. A., & Blankenship, D. D. (2006). Identifying major sedimentary basins beneath the West Antarctic Ice Sheet from aeromagnetic data analysis. In D. K. Fütterer, D. Damaske, G. Kleinschmidt, H. Miller, & F. Tessensohn (Eds.), *Antarctica* (pp. 117–121). Springer-Verlag. https://doi.org/10.1007/3-540-32934-X_13. (Cit. on pp. 28, 30–32, 153)
- Bell, R. E., Ferraccioli, F., Creyts, T. T., Braaten, D., Corr, H., Das, I., Damaske, D., Frearson, N., Jordan, T., Rose, K., Studinger, M., & Wolovick, M. (2011). Widespread Persistent Thickening of the East Antarctic Ice Sheet by Freezing from the Base. *Science*, 331(6024), 1592–1595. <https://doi.org/10.1126/science.1200109> (cit. on p. 26)
- Bennett, H. F. (1964). *A gravity and magnetic survey of the Ross Ice Shelf area, Antarctica* (tech. rep. No. 64-3). The University of Wisconsin. Madison. (Cit. on p. 108).
- Bentley, C. R., Crary, A. P., Ostenso, N. A., & Thiel, E. C. (1960). Structure of West Antarctica. *Science*, 131(3394), 131–136. <https://doi.org/10.1126/science.131.3394.131> (cit. on p. 21)

- Bentley, C. R. (1984). The Ross Ice Shelf: Glaciology and Geophysics Paper 1: Introduction and summary of measurements performed. In C. R. Bentley & D. E. Hayes (Eds.), *Antarctic Research Series* (pp. 1–20). American Geophysical Union. <https://doi.org/10.1029/AR042p0001>. (Cit. on pp. 18, 21, 91, 108, 111)
- Block, A. E., Bell, R. E., & Studinger, M. (2009). Antarctic crustal thickness from satellite gravity: Implications for the Transantarctic and Gamburtsev Subglacial Mountains. *Earth and Planetary Science Letters*, 288(1-2), 194–203. <https://doi.org/10.1016/j.epsl.2009.09.022> (cit. on p. 133)
- Boghosian, A., Tinto, K., Cochran, J. R., Porter, D., Elieff, S., Burton, B. L., & Bell, R. E. (2015). Resolving bathymetry from airborne gravity along Greenland fjords. *Journal of Geophysical Research: Solid Earth*, 120(12), 8516–8533. <https://doi.org/10.1002/2015JB012129> (cit. on pp. 78, 104–107, 120)
- Borg, S. G., Depaolo, D. J., & Smith, B. M. (1990). Isotopic structure and tectonics of the central Transantarctic mountains. *Journal of Geophysical Research*, 95(B5), 6647. <https://doi.org/10.1029/JB095iB05p06647> (cit. on pp. 32, 34)
- Borghi, A. (2022). Moho depths for Antarctica Region by the inversion of ground-based gravity data. *Geophysical Journal International*, 231(2), 1404–1420. <https://doi.org/10.1093/gji/ggac249> (cit. on p. 42)
- Bougamont, M., Christoffersen, P., Price, S. F., Fricker, H. A., Tulaczyk, S., & Carter, S. P. (2015). Reactivation of Kamb Ice Stream tributaries triggers century-scale reorganization of Siple Coast ice flow in West Antarctica: Restructuring of Siple Coast Ice Flow. *Geophysical Research Letters*, 42(20), 8471–8480. <https://doi.org/10.1002/2015GL065782> (cit. on p. 145)
- Bourgeois, B. S., Elmore, P. A., Avera, W. E., & Zambo, S. J. (2016). Achieving comparable uncertainty estimates with Kalman filters or linear smoothers for bathymetry data. *Geochemistry, Geophysics, Geosystems*, 17(7), 2576–2590. <https://doi.org/10.1002/2015GC006239> (cit. on pp. 84, 85)
- Brancolini, G., Busetti, M., Marchetti, A., Santis, L. D., Zanolla, C., Cooper, A. K., Cochrane, G. R., Zayatz, I., Belyaev, V., Knyazev, M., Vinnikovskaya, O., Davey, F. J., & Hinze, K. (1995). Descriptive text for the seismic stratigraphic atlas of the Ross Sea, Antarctica. In A. K. Cooper, P. F. Barker, & G. Brancolini (Eds.), *Geology and Seismic Stratigraphy of the Antarctic Margin* (A271–A286). American Geophysical Union. <https://doi.org/10.1002/9781118669013.app1>. (Cit. on pp. 26–28, 67, 68, 147, 151, 153, 156)
- Brisbourne, A. M., Kulessa, B., Hudson, T., Harrison, L., Holland, P., Luckman, A., Bevan, S., Ashmore, D., Hubbard, B., Pearce, E., White, J., Booth, A., Nicholls, K., & Smith, A. (2020). An updated seabed bathymetry beneath Larsen C Ice Shelf, Antarctic Peninsula. *Earth System Science Data*, 12(2), 887–896. <https://doi.org/10.5194/essd-12-887-2020> (cit. on pp. 70, 124, 149)
- Brisbourne, A. M., Smith, A. M., King, E. C., Nicholls, K. W., Holland, P. R., & Makinson, K. (2014). Seabed topography beneath Larsen C Ice Shelf from seismic soundings. *The Cryosphere*, 8(1), 1–13. <https://doi.org/10.5194/tc-8-1-2014> (cit. on pp. 45, 80, 99, 120)
- Burton-Johnson, A., Dziadek, R., & Martin, C. (2020). Geothermal heat flow in Antarctica: Current and future directions. *The Cryosphere Discussions*, 1–45. <https://doi.org/10.5194/tc-2020-59> (cit. on pp. 32, 139, 144, 145)
- Calder, B., & Elmore, P. (2017). Development of an Uncertainty Propagation Equation for Scalar Fields. *Marine Geodesy*, 40(5), 341–360. <https://doi.org/10.1080/01490419.2017.1345811> (cit. on p. 85)
- Catania, G., Hulbe, C., Conway, H., Scambos, T., & Raymond, C. (2012). Variability in the mass flux of the Ross ice streams, West Antarctica, over the last millennium. *Journal of Glaciology*, 58(210), 741–752. <https://doi.org/10.3189/2012JoG11J219> (cit. on p. 145)
- Chen, B., Haeger, C., Kaban, M. K., & Petrunin, A. G. (2018). Variations of the effective elastic thickness reveal tectonic fragmentation of the Antarctic lithosphere. *Tectonophysics*, 746, 412–424. <https://doi.org/10.1016/j.tecto.2017.06.012> (cit. on p. 143)
- Cheng, W., Hu, X. G., & Liu, L. T. (2021). Anisotropy Gradients in the Middle of the Ross Sea Embayment, West Antarctica: Evidence From QL Scattered Surface Waves. *Geophysical Research Letters*, 48(6). <https://doi.org/10.1029/2020GL091232> (cit. on p. 34)
- Chiappini, M., Ferraccioli, F., Bozzo, E., & Damaske, D. (2002). Regional compilation and analysis of aeromagnetic anomalies for the Transantarctic Mountains–Ross Sea sector of the Antarc-

- tic. *Tectonophysics*, 347(1-3), 121–137. [https://doi.org/10.1016/S0040-1951\(01\)00241-4](https://doi.org/10.1016/S0040-1951(01)00241-4) (cit. on p. 30)
- Christoffersen, P., Bougamont, M., Carter, S. P., Fricker, H. A., & Tulaczyk, S. (2014). Significant groundwater contribution to Antarctic ice streams hydrologic budget. *Geophysical Research Letters*, 41(6), 2003–2010. <https://doi.org/10.1002/2014GL059250> (cit. on pp. 19, 26, 144, 145)
- Clough, J. W., & Hansen, B. L. (1979). The Ross Ice Shelf Project. *Science*, 203(4379), 433–434. <https://doi.org/10.1126/science.203.4379.433> (cit. on pp. 18, 91)
- Cochran, J. R., Burton, B., Frearson, N., & Tinto, K. (2014a). IceBridge Scintrex CS-3 Cesium magnetometer L1B geolocated magnetic anomalies, version 2. [Line 403, 404]. *Boulder, Colorado USA. NASA National Snow and Ice Data Center Distributed Active Archive Center*. <https://doi.org/10.5067/OY7C2Y61YSYW> (cit. on pp. 28, 151, 153)
- Cochran, J. R., Jacobs, S. S., Tinto, K. J., & Bell, R. E. (2014b). Bathymetric and oceanic controls on Abbot Ice Shelf thickness and stability. *The Cryosphere*, 8(3), 877–889. <https://doi.org/10.5194/tc-8-877-2014> (cit. on pp. 105, 106)
- Cochran, J. R., & Bell, R. E. (2012). Inversion of IceBridge gravity data for continental shelf bathymetry beneath the Larsen Ice Shelf, Antarctica. *Journal of Glaciology*, 58(209), 540–552. <https://doi.org/10.3189/2012JoG11J033> (cit. on pp. 104–106, 149)
- Cochran, J. R., Tinto, K. J., & Bell, R. E. (2020). Detailed Bathymetry of the Continental Shelf Beneath the Getz Ice Shelf, West Antarctica. *Journal of Geophysical Research: Earth Surface*, 125(10). <https://doi.org/10.1029/2019JF005493> (cit. on pp. 46, 104–106, 149)
- Coenen, J. J., Scherer, R. P., Baudoin, P., Warny, S., Castañeda, I. S., & Askin, R. (2019). Paleogene marine and terrestrial development of the West Antarctic Rift System. *Geophysical Research Letters*, 47(3). <https://doi.org/10.1029/2019GL085281> (cit. on pp. 26, 33, 147)
- Colleoni, F., De Santis, L., Montoli, E., Olivo, E., Sorlien, C. C., Bart, P. J., Gasson, E. G. W., Bergamasco, A., Sauli, C., Wardell, N., & Prato, S. (2018). Past continental shelf evolution increased Antarctic ice sheet sensitivity to climatic conditions. *Scientific Reports*, 8(1), 11323. <https://doi.org/10.1038/s41598-018-29718-7> (cit. on p. 26)
- Constantino, R. R., & Tinto, K. J. (2023). Cook Ice Shelf and Ninnis Glacier Tongue Bathymetry From Inversion of Operation Ice Bridge Airborne Gravity Data. *Geophysical Research Letters*, 50(11), e2023GL103815. <https://doi.org/10.1029/2023GL103815> (cit. on pp. 106, 120)
- Constantino, R. R., Tinto, K. J., Bell, R. E., Porter, D. F., & Jordan, T. A. (2020). Seafloor Depth of George VI Sound, Antarctic Peninsula, From Inversion of Aerogravity Data. *Geophysical Research Letters*, 47(21). <https://doi.org/10.1029/2020GL088654> (cit. on pp. 104, 105, 107, 120, 122)
- Cooper, A. K., Barker, P. F., & Brancolini, G. (Eds.). (1995). *Geology and seismic stratigraphy of the Antarctic margin*. AGU. <https://doi.org/10.1029/AR068>. (Cit. on p. 31)
- Coulon, V., Bulthuis, K., Whitehouse, P. L., Sun, S., Haubner, K., Zipf, L., & Pattyn, F. (2021). Contrasting response of West and East Antarctic Ice Sheets to glacial isostatic adjustment. *Journal of Geophysical Research: Earth Surface*, 126(7). <https://doi.org/10.1029/2020JF006003> (cit. on pp. 18, 33, 144)
- Cox, S. C., Smith Lyttle, B., Elkind, S., Smith Siddoway, C., Morin, P., Capponi, G., Abu-Alam, T., Ballinger, M., Bamber, L., Kitchener, B., Lelli, L., Mawson, J., Millikin, A., Dal Seno, N., Whitburn, L., White, T., Burton-Johnson, A., Crispini, L., Elliot, D., ... Wilson, G. (2023). A continent-wide detailed geological map dataset of Antarctica. *Scientific Data*, 10(1), 250. <https://doi.org/10.1038/s41597-023-02152-9> (cit. on pp. 139, 152)
- Crary, A. P. (1961). Marine-sediment thickness in the eastern Ross Sea area, Antarctica. *Geological Society of America Bulletin*, 72(5), 787. [https://doi.org/10.1130/0016-7606\(1961\)72\[787:MTITER\]2.0.CO;2](https://doi.org/10.1130/0016-7606(1961)72[787:MTITER]2.0.CO;2) (cit. on p. 156)
- Crary, A. P., Robinson, E. S., Bennett, H. F., & Boyd, W. (1962). *Glaciological studies on the Ross Ice Shelf, Antarctica; 1957-1960* (tech. rep. No. 6). American Geographical Society. New York, NY, USA. (Cit. on pp. 91, 108).
- Crary, A. (1959). Oversnow Traverses from IGY Little American Station. *Transactions, American Geophysical Union*, 40(3), 311–315. <https://doi.org/10.1029/TR040i003p00269> (cit. on pp. 21, 91, 108)
- Crary, A., & Robinson, E. (1962). Oversnow Traverse from McMurdo to the South Pole. *Science*, 135(3500), 291–295. <https://doi.org/10.1126/science.135.3500.291> (cit. on pp. 91, 108)

- Dampney, C. N. G. (1969). The equivalent source technique, 15. <https://doi.org/10.1190/1.1439996> (cit. on pp. 57, 112)
- Das, I., Padman, L., Bell, R. E., Fricker, H. A., Tinto, K. J., Hulbe, C. L., Siddoway, C. S., Dhakal, T., Frearson, N. P., Mosbeux, C., Cordero, S. I., & Siegfried, M. R. (2020). Multi-decadal basal melt rates and structure of the Ross Ice Shelf, Antarctica using airborne ice penetrating radar. *Journal of Geophysical Research: Earth Surface*, 1–20. <https://doi.org/10.1029/2019JF005241> (cit. on pp. 21, 38, 132, 141)
- De Rydt, J., Holland, P. R., Dutrieux, P., & Jenkins, A. (2014). Geometric and oceanographic controls on melting beneath Pine Island Glacier. *Journal of Geophysical Research: Oceans*, 119(4), 2420–2438. <https://doi.org/10.1002/2013JC009513> (cit. on pp. 16, 90, 91)
- De Santis, L. (1999). The Eastern Ross Sea continental shelf during the Cenozoic: Implications for the West Antarctic ice sheet development. *Global and Planetary Change*, 23(1-4), 173–196. [https://doi.org/10.1016/S0921-8181\(99\)00056-9](https://doi.org/10.1016/S0921-8181(99)00056-9) (cit. on p. 147)
- De Santis, L., Anderson, J. B., Brancolini, G., & Zayatz, I. (1995). Seismic record of late Oligocene through Miocene glaciation on the central and eastern continental shelf of the Ross Sea. In A. K. Cooper, P. F. Barker, & G. Brancolini (Eds.), *Antarctic Research Series* (pp. 235–260). American Geophysical Union. <https://doi.org/10.1029/AR068p0235>. (Cit. on pp. 34, 147)
- DeConto, R. M., & Pollard, D. (2003). A coupled climate–ice sheet modeling approach to the Early Cenozoic history of the Antarctic ice sheet. *Palaeogeography, Palaeoclimatology, Palaeoecology*, 198(1-2), 39–52. [https://doi.org/10.1016/S0031-0182\(03\)00393-6](https://doi.org/10.1016/S0031-0182(03)00393-6) (cit. on p. 26)
- Deng, X., & Tang, Z.-a. (2011). Moving Surface Spline Interpolation Based on Green's Function. *Mathematical Geosciences*, 43(6), 663–680. <https://doi.org/10.1007/s11004-011-9346-5> (cit. on p. 63)
- Dinniman, M. S., Klinck, J. M., & Smith, W. O. (2011). A model study of Circumpolar Deep Water on the West Antarctic Peninsula and Ross Sea continental shelves. *Deep Sea Research Part II: Topical Studies in Oceanography*, 58(13-16), 1508–1523. <https://doi.org/10.1016/j.dsr2.2010.11.013> (cit. on pp. 90, 132)
- Dorschel, B., Hehemann, L., Viquerat, S., Warnke, F., Dreutter, S., Tenberge, Y. S., Accettella, D., An, L., Barrios, F., Bazhenova, E., Black, J., Bohoyo, F., Davey, C., De Santis, L., Dotti, C. E., Fremand, A. C., Fretwell, P. T., Gales, J. A., Gao, J., ... Arndt, J. E. (2022). The International Bathymetric Chart of the Southern Ocean Version 2. *Scientific Data*, 9(1), 275. <https://doi.org/10.1038/s41597-022-01366-7> (cit. on pp. 67, 68, 70)
IBCSO
- Dowdeswell, J., Evans, J., Mugford, R., Griffiths, G., McPhail, S., Millard, N., Stevenson, P., Brandon, M., Banks, C., Heywood, K., Price, M., Dodd, P., Jenkins, A., Nicholls, K., Hayes, D., Abrahamsen, E., Tyler, P., Bett, B., Jones, D., ... Ackley, S. (2008). Autonomous underwater vehicles (AUVs) and investigations of the ice–ocean interface in Antarctic and Arctic waters. *Journal of Glaciology*, 54(187), 661–672. <https://doi.org/10.3189/002214308786570773> (cit. on p. 18)
- Drenth, B. J., Grauch, V., Turner, K. J., Rodriguez, B. D., Thompson, R. A., & Bauer, P. W. (2019). A shallow rift basin segmented in space and time: The southern San Luis Basin, Rio Grande rift, northern New Mexico, U.S.A. *Rocky Mountain Geology*, 54(2), 97–131. <https://doi.org/10.24872/rmgjournal.54.2.97> (cit. on p. 29)
- Dupont, T. K., & Alley, R. B. (2005). Assessment of the importance of ice-shelf buttressing to ice-sheet flow. *Geophysical Research Letters*, 32, 1–4. <https://doi.org/10.1029/2004GL022024> (cit. on pp. 17, 38, 90)
- Durand, G., van den Broeke, M. R., Le Cozannet, G., Edwards, T. L., Holland, P. R., Jourdain, N. C., Marzeion, B., Mottram, R., Nicholls, R. J., Pattyn, F., Paul, F., Slangen, A. B. A., Winkelmann, R., Burgard, C., van Calcar, C. J., Barré, J.-B., Bataille, A., & Chapuis, A. (2022). Sea-Level Rise: From Global Perspectives to Local Services. *Frontiers in Marine Science*, 8, 709595. <https://doi.org/10.3389/fmars.2021.709595> (cit. on pp. 15, 137)
- Dutrieux, P., De Rydt, J., Jenkins, A., Holland, P. R., Ha, H. K., Lee, S. H., Steig, E. J., Ding, Q., Abrahamsen, E. P., & Schröder, M. (2014). Strong Sensitivity of Pine Island Ice-Shelf Melting to Climatic Variability. *Science*, 343(6167), 174–178. <https://doi.org/10.1126/science.1244341> (cit. on p. 90)
- Edwards, T. L., Nowicki, S., Marzeion, B., Hock, R., Goelzer, H., Seroussi, H., Jourdain, N. C., Slater, D. A., Turner, F. E., Smith, C. J., McKenna, C. M., Simon, E., Abe-Ouchi, A.,

- Gregory, J. M., Larour, E., Lipscomb, W. H., Payne, A. J., Shepherd, A., Agosta, C., ... Zwinger, T. (2021). Projected land ice contributions to twenty-first-century sea level rise. *Nature*, 593(7857), 74–82. <https://doi.org/10.1038/s41586-021-03302-y> (cit. on p. 15)
- Eisermann, H., Eagles, G., Ruppel, A., Smith, E. C., & Jokat, W. (2020). Bathymetry Beneath Ice Shelves of Western Dronning Maud Land, East Antarctica, and Implications on Ice Shelf Stability. *Geophysical Research Letters*, 47(12). <https://doi.org/10.1029/2019GL086724> (cit. on pp. 45, 104–106, 120)
- Eisermann, H., Eagles, G., Ruppel, A. S., Läufer, A., & Jokat, W. (2021). Bathymetric Control on Borchgrevink and Roi Baudouin Ice Shelves in East Antarctica. *Journal of Geophysical Research: Earth Surface*, 126(10). <https://doi.org/10.1029/2021JF006342> (cit. on pp. 105, 106, 120)
- Fahnestock, M. A., Scambos, T. A., Bindschadler, R. A., & Kvaran, G. (2000). A millennium of variable ice flow recorded by the Ross Ice Shelf, Antarctica. *Journal of Glaciology*, 13. <https://doi.org/10.3189/172756500781832693> (cit. on p. 143)
- Fatiando a Terra Project, Dinneen, C., Gomez, M., Li, L., Pesce, A., Soler, S. R., & Uieda, L. (2022). Boule v0.4.1: Reference ellipsoids for geodesy and geophysics. <https://doi.org/10.5281/zenodo.7258175>. (Cit. on p. 169)
- Fatiando a Terra Project, Esteban, F. D., Li, L., Oliveira, V. C., Pesce, A., Shea, N., Soler, S. R., Tankersley, M., & Uieda, L. (2023). Harmonica v0.6.0: Forward modeling, inversion, and processing gravity and magnetic data. <https://doi.org/10.5281/zenodo.7690145>. (Cit. on pp. 43, 48, 51, 95)
- Ferraccioli, F., Bozzo, E., & Damaske, D. (2002). Aeromagnetic signatures over western Marie Byrd Land provide insight into magmatic arc basement, mafic magmatism and structure of the Eastern Ross Sea Rift flank. *Tectonophysics*, 347, 139–165. [https://doi.org/10.1016/S0040-1951\(01\)00242-6](https://doi.org/10.1016/S0040-1951(01)00242-6) (cit. on p. 30)
- Filina, I. Y., Blankenship, D. D., Thoma, M., Lukin, V. V., Masolov, V. N., & Sen, M. K. (2008). New 3D bathymetry and sediment distribution in Lake Vostok: Implication for pre-glacial origin and numerical modeling of the internal processes within the lake. *Earth and Planetary Science Letters*, 276(1-2), 106–114. <https://doi.org/10.1016/j.epsl.2008.09.012> (cit. on pp. 106, 120)
- Finn, C. (2002). *Examples of the utility of magnetic anomaly data for geologic mapping* (Open-File Report No. 02-400). USGS. Denver, Colorado. (Cit. on p. 29).
- Fisher, A. T., Mankoff, K. D., Tulaczyk, S. M., Tyler, S. W., Foley, N., & and the WISSARD Science Team. (2015). High geothermal heat flux measured below the West Antarctic Ice Sheet. *Science Advances*, 1, 1–9. <https://doi.org/10.1126/sciadv.1500093> (cit. on pp. 33, 145)
- Ford, A., & Barrett, P. J. (1975). *Basement rocks of the south-central Ross Sea, site 270, DSDP leg 28* (tech. rep.). Texas A & M University, Ocean Drilling Program. College Station, TX, United States. <https://doi.org/10.2973/dsdp.proc.28.130.1975>. (Cit. on p. 26)
- Forsberg, R. (2020). Preliminary compilation of Antarctica gravity and gravity gradient data (cit. on p. 139).
- Förste, C., Bruinsma, S., Abrikosov, O., Lemoine, J.-M., Marty, J. C., Flechtner, F., Balmino, G., Barthelmes, F., & Biancale, R. (2014). EIGEN-6C4 The latest combined global gravity field model including GOCE data up to degree and order 2190 of GFZ Potsdam and GRGS Toulouse. <https://doi.org/10.5880/ICGEM.2015.1>. (Cit. on pp. 95, 169)
- Fox Maule, C., Purucker, M. E., Olsen, N., & Mosegaard, K. (2005). Heat Flux Anomalies in Antarctica Revealed by Satellite Magnetic Data. *Science*, 309(5733), 464–467. <https://doi.org/10.1126/science.1106888> (cit. on p. 144)
- Frederick, B. C., Young, D. A., Blankenship, D. D., Richter, T. G., Kempf, S. D., Ferraccioli, F., & Siegert, M. J. (2016). Distribution of subglacial sediments across the Wilkes Subglacial Basin, East Antarctica. *Journal of Geophysical Research: Earth Surface*, 121(4), 790–813. <https://doi.org/10.1002/2015JF003760> (cit. on pp. 28, 153)
- Frémard, A. C., Fretwell, P., Bodart, J., Pritchard, H. D., Aitken, A., Bamber, J. L., Bell, R., Bianchi, C., Bingham, R. G., Blankenship, D. D., Casassa, G., Catania, G., Christianson, K., Conway, H., Corr, H. F. J., Cui, X., Damaske, D., Damm, V., Drews, R., ... Zirizzotti, A. (2022). Antarctic Bedmap data: FAIR sharing of 60 years of ice bed, surface and thickness data. *Earth System Science Data Discussions*, 1–25. <https://doi.org/10.5194/essd-2022-355> (cit. on p. 17)

- Fretwell, P., Pritchard, H. D., Vaughan, D. G., Bamber, J. L., Barrand, N. E., Bell, R. E., Bianchi, C., Bingham, R. G., Blankenship, D. D., Casassa, G., Catania, G., Callens, D., Conway, H., Cook, A. J., Corr, H. F. J., Damaske, D., Damm, V., Ferraccioli, F., Forsberg, R., ... Zirizzotti, A. (2013). Bedmap2: Improved ice bed, surface and thickness datasets for Antarctica. *The Cryosphere*, 7(1), 375–393. <https://doi.org/10.5194/tc-7-375-2013> (cit. on pp. 15, 18, 20, 77, 90, 91, 97, 98, 108, 124, 137, 149, 159)
- Fricker, H. A., Popov, S., Allison, I., & Young, N. (2001). Distribution of marine ice beneath the Amery Ice Shelf. *Geophysical Research Letters*, 28(11), 2241–2244. <https://doi.org/10.1029/2000GL012461> (cit. on p. 121)
- Fürst, J. J., Durand, G., Gillet-Chaulet, F., Tavard, L., Rankl, M., Braun, M., & Gagliardini, O. (2016). The safety band of Antarctic ice shelves. *Nature Climate Change*, 6(5), 479–482. <https://doi.org/10.1038/nclimate2912> (cit. on p. 90)
- Gladish, C. V., Holland, D. M., Rosing-Asvid, A., Behrens, J. W., & Boje, J. (2015). Oceanic Boundary Conditions for Jakobshavn Glacier. Part I: Variability and Renewal of Ilulissat Icefjord Waters, 2001–14. *Journal of Physical Oceanography*, 45(1), 3–32. <https://doi.org/10.1175/JPO-D-14-0044.1> (cit. on p. 90)
- Goldberg, D. N., Gourmelen, N., Kimura, S., Millan, R., & Snow, K. (2019). How Accurately Should We Model Ice Shelf Melt Rates? *Geophysical Research Letters*, 46(1), 189–199. <https://doi.org/10.1029/2018GL080383> (cit. on p. 91)
- Goldberg, D. N., Smith, T. A., Narayanan, S. H. K., Heimbach, P., & Morlighem, M. (2020). Bathymetric Influences on Antarctic Ice-Shelf Melt Rates. *Journal of Geophysical Research: Oceans*, 125(11). <https://doi.org/10.1029/2020JC016370> (cit. on pp. 16, 91, 92)
- Golledge, N. R., Marsh, O. J., Rack, W., Braaten, D., & Jones, R. S. (2014). Basal conditions of two Transantarctic Mountains outlet glaciers from observation-constrained diagnostic modelling. *Journal of Glaciology*, 60(223), 855–866. <https://doi.org/10.3189/2014JoG13J131> (cit. on p. 144)
- Golynsky, A. V., Ferraccioli, F., Hong, J. K., Golynsky, D. A., von Frese, R. R. B., Young, D. A., Blankenship, D. D., Holt, J. W., Ivanov, S. V., Kiselev, A. V., Masolov, V. N., Eagles, G., Gohl, K., Jokat, W., Damaske, D., Finn, C., Aitken, A., Bell, R. E., Armadillo, E., ... Roberts, J. L. (2018). New Magnetic Anomaly Map of the Antarctic: ADMAP2. *Geophysical Research Letters*, 45(13), 6437–6449. <https://doi.org/10.1029/2018GL078153> (cit. on p. 139)
- Gooch, B. T., Young, D. A., & Blankenship, D. D. (2016). Potential groundwater and heterogeneous heat source contributions to ice sheet dynamics in critical submarine basins of East Antarctica. *Geochemistry, Geophysics, Geosystems*, 17(2), 395–409. <https://doi.org/10.1002/2015GC006117> (cit. on pp. 19, 28, 33, 144, 145)
- Goodge, J. W. (2020). Geological and tectonic evolution of the Transantarctic Mountains, from ancient craton to recent enigma. *Gondwana Research*, 80, 50–122. <https://doi.org/10.1016/j.gr.2019.11.001> (cit. on pp. 26, 30, 133)
- Granot, R., & Dyment, J. (2018). Late Cenozoic unification of East and West Antarctica. *Nature Communications*, 9(1), 3189. <https://doi.org/10.1038/s41467-018-05270-w> (cit. on pp. 26, 32)
- Greenbaum, J. S., Blankenship, D. D., Young, D. A., Richter, T. G., Roberts, J. L., Aitken, A. R. A., Legresy, B., Schroeder, D. M., Warner, R. C., van Ommen, T. D., & Siegert, M. J. (2015). Ocean access to a cavity beneath Totten Glacier in East Antarctica. *Nature Geoscience*, 8(4), 294–298. <https://doi.org/10.1038/ngeo2388> (cit. on pp. 104–106, 120)
- Greene, C. A., Gardner, A. S., Schlegel, N.-J., & Fraser, A. D. (2022). Antarctic calving loss rivals ice-shelf thinning. *Nature*, 609(7929), 948–953. <https://doi.org/10.1038/s41586-022-05037-w> (cit. on p. 16)
- Grieschar, L. L., Bentley, C. R., & Whiting, L. R. (1992). An analysis of gravity measurements on the Ross Ice Shelf, Antarctica. In *Contributions to Antarctic Research III* (pp. 105–155). American Geophysical Union (AGU). <https://doi.org/10.1029/AR057p0105>. (Cit. on pp. 21, 32, 156)
- Griggs, J. A., & Bamber, J. L. (2011). Antarctic ice-shelf thickness from satellite radar altimetry. *Journal of Glaciology*, 57(203), 485–498. <https://doi.org/10.3189/002214311796905659> (cit. on pp. 38, 112)
- Gustafson, C. D., Key, K., Siegfried, M. R., Winberry, J. P., Fricker, H. A., Venturelli, R. A., & Michaud, A. B. (2022). A dynamic saline groundwater system mapped beneath an

- Antarctic ice stream. *Science*, 376(6593), 640–644. <https://doi.org/10.1126/science.abm3301> (cit. on pp. 19, 26, 32, 33, 144, 145, 156)
- Halberstadt, A. R. W., Simkins, L. M., Greenwood, S. L., & Anderson, J. B. (2016). Past ice-sheet behaviour: Retreat scenarios and changing controls in the Ross Sea, Antarctica. *The Cryosphere*, 10(3), 1003–1020. <https://doi.org/10.5194/tc-10-1003-2016> (cit. on pp. 16, 20, 34, 134, 137, 145, 147)
- Hammer, S. (1939). Terrain corrections for gravimeter stations. *GEOPHYSICS*, 4(3), 184–194. <https://doi.org/10.1190/1.1440495> (cit. on p. 47)
- Harlan, R. B. (1968). Eotvos corrections for airborne gravimetry. *Journal of Geophysical Research*, 73(14), 4675–4679. <https://doi.org/10.1029/JB073i014p04675> (cit. on p. 111)
- Helton, J., Johnson, J., Sallaberry, C., & Storlie, C. (2006). Survey of sampling-based methods for uncertainty and sensitivity analysis. *Reliability Engineering & System Safety*, 91(10-11), 1175–1209. <https://doi.org/10.1016/j.ress.2005.11.017> (cit. on pp. 73, 100–102, 116)
- Hinze, W. J., Aiken, C., Brozena, J., Coakley, B., Dater, D., Flanagan, G., Forsberg, R., Hildenbrand, T., Keller, G. R., Kellogg, J., Kucks, R., Li, X., Mainville, A., Morin, R., Pilkington, M., Plouff, D., Ravat, D., Roman, D., Urrutia-Fucugauchi, J., ... Winchester, D. (2005). New standards for reducing gravity data: The North American gravity database. *GEOPHYSICS*, 70(4), J25–J32. <https://doi.org/10.1190/1.1988183> (cit. on pp. 92, 93)
- Hinze, W. J., Von Frese, R., & Saad, A. H. (2013). *Gravity and magnetic exploration: Principles, practices, and applications*. Cambridge University Press. (Cit. on p. 92).
- Hodgson, D. A., Jordan, T. A., De Rydt, J., Fretwell, P. T., Seddon, S. A., Becker, D., Hogan, K. A., Smith, A. M., & Vaughan, D. G. (2019). Past and future dynamics of the Brunt Ice Shelf from seabed bathymetry and ice shelf geometry. *The Cryosphere*, 13(2), 545–556. <https://doi.org/10.5194/tc-13-545-2019> (cit. on pp. 46, 105, 106, 120)
- Hofmann-Wellenhof, B., & Moritz, H. (2006). *Physical geodesy* (2nd, corrected ed). SpringerWienNewYork. (Cit. on pp. 92, 94).
- Hofstede, C., Beyer, S., Corr, H., Eisen, O., Hattermann, T., Helm, V., Neckel, N., Smith, E. C., Steinhage, D., Zeising, O., & Humbert, A. (2021). Evidence for a grounding line fan at the onset of a basal channel under the ice shelf of Support Force Glacier, Antarctica, revealed by reflection seismics. *The Cryosphere*, 15(3), 1517–1535. <https://doi.org/10.5194/tc-15-1517-2021> (cit. on p. 121)
- Holland, P. R. (2008). A model of tidally dominated ocean processes near ice shelf grounding lines. *Journal of Geophysical Research*, 113(C11), C11002. <https://doi.org/10.1029/2007JC004576> (cit. on pp. 16, 133, 141)
- Horgan, H. J., Hulbe, C., Alley, R. B., Anandakrishnan, S., Goodsell, B., Taylor-Offord, S., & Vaughan, M. J. (2017). Poststagnation Retreat of Kamb Ice Stream's Grounding Zone. *Geophysical Research Letters*, 44(19), 9815–9822. <https://doi.org/10.1002/2017GL074986> (cit. on pp. 21, 129)
- Horgan, H. J., Walker, R. T., Anandakrishnan, S., & Alley, R. B. (2011). Surface elevation changes at the front of the Ross Ice Shelf: Implications for basal melting. *Journal of Geophysical Research*, 116(C2), C02005. <https://doi.org/10.1029/2010JC006192> (cit. on p. 131)
- Horgan, H. J., Christianson, K., Jacobel, R. W., Anandakrishnan, S., & Alley, R. B. (2013). Sediment deposition at the modern grounding zone of Whillans Ice Stream, West Antarctica. *Geophysical Research Letters*, 40(15), 3934–3939. <https://doi.org/10.1002/grl.50712> (cit. on p. 121)
- Hoyer, S., & Hamman, J. (2017). Xarray: N-D labeled Arrays and Datasets in Python. *Journal of Open Research Software*, 5(1), 10. <https://doi.org/10.5334/jors.148> (cit. on p. 171)
- IceBridge Sander AIRGrav L1B Geolocated Free Air Gravity Anomalies, Version 1. (2020). (Cit. on p. 149).
- Intergovernmental Panel on Climate Change (IPCC). (2022). *The Ocean and Cryosphere in a Changing Climate: Special Report of the Intergovernmental Panel on Climate Change* (First). Cambridge University Press. <https://doi.org/10.1017/9781009157964>. (Cit. on pp. 15, 137)
- Jacobs, S., Helmer, H., Doake, C. S. M., Jenkins, A., & Frolich, R. M. (1992). Melting of ice shelves and the mass balance of Antarctica. *Journal of Glaciology*, 38(130), 375–387. <https://doi.org/10.3189/S0022143000002252> (cit. on p. 90)
- Jacoby, W., & Smilde, P. L. (2009). *Gravity interpretation: Fundamentals and application of gravity inversion and geological interpretation ; with CD-ROM*. Springer. (Cit. on pp. 42, 93) OCLC: 845389531.

- Jansen, M. J. W., Rossing, W. A. H., & Daamen, R. A. (1994). Monte Carlo Estimation of Uncertainty Contributions from Several Independent Multivariate Sources. In J. Grasman & G. van Straten (Eds.), *Predictability and Nonlinear Modelling in Natural Sciences and Economics* (pp. 334–343). Springer Netherlands. https://doi.org/10.1007/978-94-011-0962-8_28. (Cit. on pp. 73, 100, 101)
- Jenkins, A., Dutrieux, P., Jacobs, S. S., McPhail, S. D., Perrett, J. R., Webb, A. T., & White, D. (2010). Observations beneath Pine Island Glacier in West Antarctica and implications for its retreat. *Nature Geoscience*, 3(7), 468–472. <https://doi.org/10.1038/ngeo890> (cit. on p. 38)
- Jolie, E., Scott, S., Faulds, J., Chambefort, I., Axelsson, G., Gutiérrez-Negrín, L. C., Regenspurg, S., Ziegler, M., Ayling, B., Richter, A., & Zemedkun, M. T. (2021). Geological controls on geothermal resources for power generation. *Nature Reviews Earth & Environment*, 2(5), 324–339. <https://doi.org/10.1038/s43017-021-00154-y> (cit. on pp. 19, 26, 145)
- Jordan, T. A., Ferraccioli, F., Vaughan, D. G., Holt, J. W., Corr, H., Blankenship, D. D., & Diehl, T. M. (2010). Aerogravity evidence for major crustal thinning under the Pine Island Glacier region (West Antarctica). *Geological Society of America Bulletin*, 122(5-6), 714–726. <https://doi.org/10.1130/B26417.1> (cit. on pp. 78, 85)
- Jordan, T. A., Riley, T. R., & Siddoway, C. S. (2020a). The geological history and evolution of West Antarctica. *Nature Reviews Earth & Environment*, 1, 117–133. <https://doi.org/10.1038/s43017-019-0013-6> (cit. on pp. 31, 149)
- Jordan, T. A., Porter, D., Tinto, K., Millan, R., Muto, A., Hogan, K., Larter, R. D., Graham, A. G. C., & Paden, J. D. (2020b). New gravity-derived bathymetry for the Thwaites, Crosson, and Dotson ice shelves revealing two ice shelf populations. *The Cryosphere*, 14(9), 2869–2882. <https://doi.org/10.5194/tc-14-2869-2020> (cit. on pp. 104–106, 120)
- Kachuck, S. B., Martin, D. F., Bassis, J. N., & Price, S. F. (2020). Rapid Viscoelastic Deformation Slows Marine Ice Sheet Instability at Pine Island Glacier. *Geophysical Research Letters*, 47(10). <https://doi.org/10.1029/2019GL086446> (cit. on pp. 18, 144)
- Karner, G. D., Studinger, M., & Bell, R. E. (2005). Gravity anomalies of sedimentary basins and their mechanical implications: Application to the Ross Sea basins, West Antarctica. *Earth and Planetary Science Letters*, 235, 577–596. <https://doi.org/10.1016/j.epsl.2005.04.016> (cit. on pp. 26, 28, 147, 153)
- Kingslake, J., Scherer, R. P., Albrecht, T., Coenen, J., Powell, R. D., Reese, R., Stansell, N. D., Tulaczyk, S., Wearing, M. G., & Whitehouse, P. L. (2018). Extensive retreat and re-advance of the West Antarctic Ice Sheet during the Holocene. *Nature*, 558(7710), 430–434. <https://doi.org/10.1038/s41586-018-0208-x> (cit. on pp. 33, 131, 145)
- Kirkpatrick, S., Gelatt, C. D., & Vecchi, M. P. (1983). Optimization by Simulated Annealing. *Science*, 220(4598), 671–680. <https://doi.org/10.1126/science.220.4598.671> (cit. on p. 106)
- Koch, P., Wujek, B., Golovinov, O., & Gardner, S. (2017). Automated Hyperparameter Tuning for Effective Machine Learning. *SAS Institute Inc.* (cit. on p. 103).
- Kulhanek, D. K., Levy, R. H., Clowes, C. D., Prebble, J. G., Rodelli, D., Jovane, L., Morgans, H. E., Kraus, C., Zwingmann, H., Griffith, E. M., Scher, H. D., McKay, R. M., & Naish, T. R. (2019). Revised chronostratigraphy of DSDP Site 270 and late Oligocene to early Miocene paleoecology of the Ross Sea sector of Antarctica. *Global and Planetary Change*, 178, 46–64. <https://doi.org/10.1016/j.gloplacha.2019.04.002> (cit. on pp. 34, 147)
- Larour, E., Morlighem, M., Seroussi, H., Schiermeier, J., & Rignot, E. (2012). Ice flow sensitivity to geothermal heat flux of Pine Island Glacier, Antarctica. *Journal of Geophysical Research: Earth Surface*, 117(F04023), 1–12. <https://doi.org/10.1029/2012JF002371> (cit. on p. 144)
- Le Brocq, A. M., Payne, A. J., & Vieli, A. (2010). An improved Antarctic dataset for high resolution numerical ice sheet models (ALBMAP v1). *Earth System Science Data*, 2(2), 247–260. <https://doi.org/10.5194/essd-2-247-2010> (cit. on pp. 91, 124)
- Leckie, F. M. (1983). Late Oligocene-early Miocene glacial record of the Ross Sea, Antarctica: Evidence from DSDP Site 270. *Geology*, 11, 578–582. [https://doi.org/10.1130/0091-7613\(1983\)11<578:LOMGRO>2.0.CO;2](https://doi.org/10.1130/0091-7613(1983)11<578:LOMGRO>2.0.CO;2) (cit. on pp. 34, 147)
- Li, L., Aitken, A. R. A., Lindsay, M. D., & Kulessa, B. (2022). Sedimentary basins reduce stability of Antarctic ice streams through groundwater feedbacks. *Nature Geoscience*. <https://doi.org/10.1038/s41561-022-00992-5> (cit. on pp. 19, 31, 145, 156)

- Li, X., Zattin, M., & Olivetti, V. (2020). Apatite fission track signatures of the Ross Sea ice flows during the Last Glacial Maximum. *Geochemistry, Geophysics, Geosystems*, 21(10), 1–21. <https://doi.org/10.1029/2019GC008749> (cit. on pp. 33, 148)
- Li, X., & Götze, H.-J. (2001). Ellipsoid, geoid, gravity, geodesy, and geophysics. *Geophysics*, 66(6), 1660–1668. <https://doi.org/10.1190/1.1487109> (cit. on pp. 93, 95)
- Licht, K. J., Hennessy, A. J., & Welke, B. M. (2014). The U-Pb detrital zircon signature of West Antarctic ice stream tills in the Ross embayment, with implications for Last Glacial Maximum ice flow reconstructions. *Antarctic Science*, 26(6), 687–697. <https://doi.org/10.1017/S0954102014000315> (cit. on pp. 33, 148)
- Licht, K. J., Lederer, J. R., & Jeffrey Swope, R. (2005). Provenance of LGM glacial till (sand fraction) across the Ross embayment, Antarctica. *Quaternary Science Reviews*, 24(12-13), 1499–1520. <https://doi.org/10.1016/j.quascirev.2004.10.017> (cit. on p. 148)
- Lindeque, A., Gohl, K., Wobbe, F., & Uenzelmann-Neben, G. (2016). Preglacial to glacial sediment thickness grids for the Southern Pacific Margin of West Antarctica: Preglacial, transitional and full glacial isopach maps, West Antarctica. *Geochemistry, Geophysics, Geosystems*, 17(10), 4276–4285. <https://doi.org/10.1002/2016GC006401> (cit. on pp. 155, 157)
- Lloyd, A. J., Wiens, D. A., Nyblade, A. A., Anandakrishnan, S., Aster, R. C., Huerta, A. D., Wilson, T. J., Dalziel, I. W. D., Shore, P. J., & Zhao, D. (2015). A seismic transect across West Antarctica: Evidence for mantle thermal anomalies beneath the Bentley Subglacial Trench and the Marie Byrd Land Dome. *Journal of Geophysical Research: Solid Earth*, 120(12), 8439–8460. <https://doi.org/10.1002/2015JB012455> (cit. on p. 33)
- Llubes, M., Lanseau, C., & Rémy, F. (2006). Relations between basal condition, subglacial hydrological networks and geothermal flux in Antarctica. *Earth and Planetary Science Letters*, 241(3-4), 655–662. <https://doi.org/10.1016/j.epsl.2005.10.040> (cit. on p. 18)
- Lowry, D. P., Golledge, N. R., Bertler, N. A. N., Jones, R. S., & McKay, R. (2019). Deglacial grounding-line retreat in the Ross Embayment, Antarctica, controlled by ocean and atmosphere forcing. *Science Advances*, 5, 1–12. <https://doi.org/10.1126/sciadv.aav8754> (cit. on pp. 20, 33, 90, 131, 137)
- Lowry, D. P., Golledge, N. R., Bertler, N. A., Jones, R. S., McKay, R., & Stutz, J. (2020). Geologic controls on ice sheet sensitivity to deglacial climate forcing in the Ross Embayment, Antarctica. *Quaternary Science Advances*, 1, 1–17. <https://doi.org/10.1016/j.qsa.2020.100002> (cit. on pp. 33, 145)
- Luyendyk, B., Sorlien, C. C., Wilson, D. S., Bartek, L. R., & Siddoway, C. S. (2001). Structural and tectonic evolution of the Ross Sea rift in the Cape Colbeck region, Eastern Ross Sea, Antarctica. *Tectonics*, 20(6), 933–958. <https://doi.org/10.1029/2000TC001260> (cit. on p. 30)
- Luyendyk, B., Wilson, D. S., & Siddoway, C. S. (2003). Eastern margin of the Ross Sea Rift in western Marie Byrd Land, Antarctica: Crustal structure and tectonic development. *Geochemistry, Geophysics, Geosystems*, 4(10), 1–25. <https://doi.org/10.1029/2002GC000462> (cit. on p. 26)
- Martins, C. M., Barbosa, V. C., & Silva, J. B. (2010). Simultaneous 3D depth-to-basement and density-contrast estimates using gravity data and depth control at few points. *GEO PHYSICS*, 75(3), I21–I28. <https://doi.org/10.1190/1.3380225> (cit. on p. 106)
- Matsuoka, K., Hindmarsh, R. C., Moholdt, G., Bentley, M. J., Pritchard, H. D., Brown, J., Conway, H., Drews, R., Durand, G., Goldberg, D., Hattermann, T., Kingslake, J., Lenaerts, J. T., Martín, C., Mulvaney, R., Nicholls, K. W., Pattyn, F., Ross, N., Scambos, T., & Whitehouse, P. L. (2015). Antarctic ice rises and ripples: Their properties and significance for ice-sheet dynamics and evolution. *Earth-Science Reviews*, 150, 724–745. <https://doi.org/10.1016/j.earscirev.2015.09.004> (cit. on pp. 16, 90)
- McCubbine, J. (2016). *Airborne Gravity Across New Zealand - For An Improved Vertical Datum* (Doctoral dissertation). Victoria University of Wellington. (Cit. on p. 47).
- McKay, R., Golledge, N., Maas, S., Naish, T., Levy, R., Dunbar, G., & Kuhn, G. (2016). Antarctic marine ice-sheet retreat in the Ross Sea during the early Holocene. *Geology*, 44(1), 7–10. <https://doi.org/10.1130/G37315.1> (cit. on p. 145)
- Menke, W. (2012). *Geophysical data analysis: Discrete inverse theory* (Matlab ed., 3rd ed). Academic Press. (Cit. on p. 39).
- Millan, R., Rignot, E., Mouginot, J., Wood, M., Bjørk, A. A., & Morlighem, M. (2018). Vulnerability of Southeast Greenland Glaciers to Warm Atlantic Water From Operation Ice-

- Bridge and Ocean Melting Greenland Data. *Geophysical Research Letters*, 45(6), 2688–2696. <https://doi.org/10.1002/2017GL076561> (cit. on pp. 105, 106, 120)
- Millan, R., Rignot, E., Bernier, V., Morlighem, M., & Dutrieux, P. (2017). Bathymetry of the Amundsen Sea Embayment sector of West Antarctica from Operation IceBridge gravity and other data. *Geophysical Research Letters*, 44(3), 1360–1368. <https://doi.org/10.1002/2016GL072071> (cit. on pp. 104–106, 120, 149)
- Millan, R., St-Laurent, P., Rignot, E., Morlighem, M., Mouginot, J., & Scheuchl, B. (2020). Constraining an Ocean Model Under Getz Ice Shelf, Antarctica, Using A Gravity-Derived Bathymetry. *Geophysical Research Letters*, 47(13). <https://doi.org/10.1029/2019GL086522> (cit. on pp. 46, 63, 104–106, 120, 122, 149)
- Moholdt, G., Padman, L., & Fricker, H. A. (2014). Basal mass budget of Ross and Filchner-Ronne ice shelves, Antarctica, derived from Lagrangian analysis of ICESat altimetry: Ice shelf basal melting from altimetry. *Journal of Geophysical Research: Earth Surface*, 119(11), 2361–2380. <https://doi.org/10.1002/2014JF003171> (cit. on pp. 20, 90, 131, 137)
- Mooney, W. D., Laske, G., & Masters, T. G. (1998). CRUST 5.1: A global crustal model at 5° × 5°. *Journal of Geophysical Research: Solid Earth*, 103(B1), 727–747. <https://doi.org/10.1029/97JB02122> (cit. on p. 155)
- Morlighem, M. (2022). MEaSUREs BedMachine Antarctica, Version 3. (Cit. on pp. 39, 92, 108, 109, 112, 113, 115, 117, 118, 124, 125, 128, 130, 146) <https://doi.org/10.5067/FPSU0V1MWUB6>.
- Morlighem, M., Rignot, E., Binder, T., Blankenship, D., Drews, R., Eagles, G., Eisen, O., Ferraccioli, F., Forsberg, R., Fretwell, P., Goel, V., Greenbaum, J. S., Gudmundsson, H., Guo, J., Helm, V., Hofstede, C., Howat, I., Humbert, A., Jokat, W., ... Young, D. A. (2020). Deep glacial troughs and stabilizing ridges unveiled beneath the margins of the Antarctic ice sheet. *Nature Geoscience*, 13(2), 132–137. <https://doi.org/10.1038/s41561-019-0510-8> (cit. on pp. 18, 27, 28, 32, 39, 69, 92, 108, 109, 112, 113, 115, 117, 118, 124, 146, 155, 157) BedMachine
- Mouginot, J., Rignot, E., & Scheuchl, B. (2019). Continent-wide, interferometric SAR phase, mapping of Antarctic ice velocity. *Geophysical Research Letters*, 46(16), 9710–9718. <https://doi.org/10.1029/2019GL083826> (cit. on p. 32)
- Mouginot, J., Scheuchl, B., & Rignot, E. (2017). MEaSUREs Antarctic Boundaries for IPY 2007–2009 from Satellite Radar, Version 2. (Cit. on pp. 91, 108–110, 128, 132, 139) <https://doi.org/10.5067/AXE4121732AD>.
- Müller, R. D., Gohl, K., Cande, S. C., Goncharov, A., & Golynsky, A. V. (2007). Eocene to Miocene geometry of the West Antarctic Rift System. *Australian Journal of Earth Sciences*, 54(8), 1033–1045. <https://doi.org/10.1080/08120090701615691> (cit. on pp. 29, 155)
- Muto, A., Anandakrishnan, S., & Alley, R. B. (2013a). Subglacial bathymetry and sediment layer distribution beneath the Pine Island Glacier ice shelf, West Antarctica, modeled using aerogravity and autonomous underwater vehicle data. *Annals of Glaciology*, 54(64), 27–32. <https://doi.org/10.3189/2013AoG64A110> (cit. on pp. 104, 106, 149)
- Muto, A., Christianson, K., Horgan, H. J., Anandakrishnan, S., & Alley, R. B. (2013b). Bathymetry and geological structures beneath the Ross Ice Shelf at the mouth of Whillans Ice Stream, West Antarctica, modeled from ground-based gravity measurements. *Journal of Geophysical Research: Solid Earth*, 118(8), 4535–4546. <https://doi.org/10.1002/jgrb.50315> (cit. on pp. 21, 32, 105, 131, 133)
- Muto, A., Peters, L. E., Gohl, K., Sasgen, I., Alley, R. B., Anandakrishnan, S., & Riverman, K. L. (2016). Subglacial bathymetry and sediment distribution beneath Pine Island Glacier ice shelf modeled using aerogravity and in situ geophysical data: New results. *Earth and Planetary Science Letters*, 433, 63–75. <https://doi.org/10.1016/j.epsl.2015.10.037> (cit. on pp. 46, 105–107, 149)
- Nagy, D., Papp, G., & Benedek, J. (2000). The gravitational potential and its derivatives for the prism. *Journal of Geodesy*, 74(7–8), 552–560. <https://doi.org/10.1007/s001900000116> (cit. on pp. 43, 46, 48, 97)
- Naish, T., Powell, R., Levy, R., Wilson, G., Scherer, R., Talarico, F., Krissek, L., Niessen, F., Pompilio, M., Wilson, T., Carter, L., DeConto, R., Huybers, P., McKay, R., Pollard, D., Ross, J., Winter, D., Barrett, P., Browne, G., ... Williams, T. (2009). Obliquity-paced Pliocene West Antarctic ice sheet oscillations. *Nature*, 458(7236), 322–328. <https://doi.org/10.1038/nature07867> (cit. on pp. 20, 90, 137)

- Nerem, R. S., Beckley, B. D., Fasullo, J. T., Hamilton, B. D., Masters, D., & Mitchum, G. T. (2018). Climate-change-driven accelerated sea-level rise detected in the altimeter era. *Proceedings of the National Academy of Sciences*, 115(9), 2022–2025. <https://doi.org/10.1073/pnas.1717312115> (cit. on p. 15)
- Neuhaus, S. U., Tulaczyk, S. M., Stansell, N. D., Coenen, J. J., Scherer, R. P., Mikucki, J. A., & Powell, R. D. (2021). Did Holocene climate changes drive West Antarctic grounding line retreat and readvance? *The Cryosphere*, 15(10), 4655–4673. <https://doi.org/10.5194/tc-15-4655-2021> (cit. on p. 33)
- Nicholls, K. W., Abrahamsen, E. P., Buck, J. J. H., Dodd, P. A., Goldblatt, C., Griffiths, G., Heywood, K. J., Hughes, N. E., Kaletzky, A., Lane-Serff, G. F., McPhail, S. D., Millard, N. W., Oliver, K. I. C., Perrett, J., Price, M. R., Pudsey, C. J., Saw, K., Stansfield, K., Stott, M. J., ... Wilkinson, J. P. (2006). Measurements beneath an Antarctic ice shelf using an autonomous underwater vehicle. *Geophysical Research Letters*, 33(8), L08612. <https://doi.org/10.1029/2006GL025998> (cit. on p. 18)
- Oldenburg, D. W. (1974). The inversion and interpretation of gravity anomalies. *Geophysics*, 39(4), 526–536 (cit. on p. 106).
- Oldenburg, D. W., & Li, Y. (2005). Inversion for applied geophysics: A tutorial. In D. K. Butler (Ed.), *Near-Surface Geophysics*. Society of Exploration Geophysicists. <https://doi.org/10.1190/1.9781560801719>. (Cit. on pp. 39, 40, 103)
- Oldenburg, D. W., & Pratt, D. (2007). Geophysical inversion for mineral exploration: A decade of progress in theory and practice. In B. Milkereit (Ed.), *Proceedings of Exploration 07* (pp. 61–95). (Cit. on p. 42).
- Oliveira, V. C., & Uieda, L. (2014). Tópicos de inversão em geofísica. *figshare*. <https://doi.org/http://dx.doi.org/10.6084/m9.figshare.1192984> (cit. on p. 40)
- Oliveira, V. C., Uieda, L., & Hallam, K. A. T. (2018). Should geophysicists use the gravity disturbance or the anomaly?, 11. <https://doi.org/10.5281/zenodo.1255305> (cit. on p. 94)
- Olivetti, V., Balestrieri, M. L., Chew, D., Zurli, L., Zattin, M., Pace, D., Drakou, F., Cornamusini, G., & Perotti, M. (2023). Ice volume variations and provenance trends in the Oligocene-early Miocene glaciomarine sediments of the Central Ross Sea, Antarctica (DSDP Site 270). *Global and Planetary Change*, 104042. <https://doi.org/10.1016/j.gloplacha.2023.104042> (cit. on pp. 147, 148)
- Otosaka, I. N., Shepherd, A., Ivins, E. R., Schlegel, N.-J., Amory, C., van den Broeke, M. R., Horwath, M., Joughin, I., King, M. D., Krinner, G., Nowicki, S., Payne, A. J., Rignot, E., Scambos, T., Simon, K. M., Smith, B. E., Sørensen, L. S., Velicogna, I., Whitehouse, P. L., ... Wouters, B. (2023). Mass balance of the Greenland and Antarctic ice sheets from 1992 to 2020. *Earth System Science Data*, 15(4), 1597–1616. <https://doi.org/10.5194/essd-15-1597-2023> (cit. on pp. 15, 16)
- Paige, C. C., & Saunders, M. A. (1982). LSQR: An Algorithm for Sparse Linear Equations and Sparse Least Squares. *ACM Transactions on Mathematical Software*, 8(1), 43–71. <https://doi.org/10.1145/355984.355989> (cit. on p. 48)
- Pappa, F., Ebbing, J., & Ferraccioli, F. (2019). Moho Depths of Antarctica: Comparison of Seismic, Gravity, and Isostatic Results. *Geochemistry, Geophysics, Geosystems*, 20(3), 1629–1645. <https://doi.org/10.1029/2018GC008111> (cit. on pp. 106, 143)
- Parker, R. L. (1972). The Rapid Calculation of Potential Anomalies. *Geophysical Journal International*, 31(4), 447–455. <https://doi.org/10.1111/j.1365-246X.1973.tb06513.x> (cit. on p. 106)
- Pašteka, R., Mikuška, J., & Meurers, B. (2017). *Understanding the Bouguer Anomaly*. Elsevier. <https://doi.org/10.1016/B978-0-12-812913-5.00008-7>. (Cit. on p. 94)
- Patterson, M. O., Levy, R. H., Kulhanek, D. K., van de Flierdt, T., Horgan, H., Dunbar, G. B., Naish, T. R., Ash, J., Pyne, A., Mandeno, D., Winberry, P., Harwood, D. M., Florindo, F., Jimenez-Espejo, F. J., Läufer, A., Yoo, K.-C., Seki, O., Stocchi, P., Klages, J. P., ... the SWAIS 2C Science Team. (2022). Sensitivity of the West Antarctic Ice Sheet to +2 °C (SWAIS 2C). *Scientific Drilling*, 30, 101–112. <https://doi.org/10.5194/sd-30-101-2022> (cit. on pp. 18, 21)
- Paulsen, T., Encarnación, J., & Grunow, A. (2004). Structure and timing of transpressional deformation in the Shackleton Glacier area, Ross orogen, Antarctica. *Journal of the Geological Society*, 161(6), 1027–1038. <https://doi.org/10.1144/0016-764903-040> (cit. on p. 34)
- Paxman, G. J. G., Jamieson, S. S., Hochmuth, K., Gohl, K., Bentley, M. J., Leitchenkov, G., & Ferraccioli, F. (2019). Reconstructions of Antarctic topography since the Eocene–Oligocene

- boundary. *Palaeogeography, Palaeoclimatology, Palaeoecology*, 535, 109346. <https://doi.org/10.1016/j.palaeo.2019.109346> (cit. on pp. 26, 34, 147, 155)
- Pekar, S. F., DeConto, R. M., & Harwood, D. M. (2006). Resolving a late Oligocene conundrum: Deep-sea warming and Antarctic glaciation. *Palaeogeography, Palaeoclimatology, Palaeoecology*, 231, 29–40. <https://doi.org/10.1016/j.palaeo.2005.07.024> (cit. on p. 34)
- Peltier, W. R., Wu, P. P.-C., Argus, D. F., Li, T., & Velay-Vitow, J. (2022). Glacial isostatic adjustment: Physical models and observational constraints. *Reports on Progress in Physics*, 85(9), 096801. <https://doi.org/10.1088/1361-6633/ac805b> (cit. on pp. 19, 143)
- Pérez, F., & Granger, B. E. (2007). IPython: A system for interactive scientific computing. *Computing in Science and Engineering*, 9(3), 21–29. <https://doi.org/10.1109/MCSE.2007.53> (cit. on p. 51)
- Pérez, L. F., De Santis, L., McKay, R. M., Larter, R. D., Ash, J., Bart, P. J., Böhm, G., Brancatelli, G., Browne, I., Colleoni, F., Dodd, J. P., Geletti, R., Harwood, D. M., Kuhn, G., Sverre Laberg, J., Leckie, R. M., Levy, R. H., Marschalek, J., Mateo, Z., ... 374 Scientists, I. O. D. P. E. (2021). Early and middle Miocene ice sheet dynamics in the Ross Sea: Results from integrated core-log-seismic interpretation. *GSA Bulletin*. <https://doi.org/10.1130/B35814.1> (cit. on p. 26)
- Perozzi, L., Guglielmetti, L., & Moscariello, A. (2021). Quantitative uncertainty analysis of gravity disturbance. The case of the Geneva Basin (Switzerland). *Journal of Applied Geophysics*, 193, 104431. <https://doi.org/10.1016/j.jappgeo.2021.104431> (cit. on p. 85)
- Phillips, G., & Läufer, A. (2009). Brittle deformation relating to the Carboniferous–Cretaceous evolution of the Lambert Graben, East Antarctica: A precursor for Cenozoic relief development in an intraplate and glaciated region. *Tectonophysics*, 471(3-4), 216–224. <https://doi.org/10.1016/j.tecto.2009.02.012> (cit. on p. 33)
- Pollard, D., DeConto, R. M., & Nyblade, A. A. (2005). Sensitivity of Cenozoic Antarctic ice sheet variations to geothermal heat flux. *Global and Planetary Change*, 49(1-2), 63–74. <https://doi.org/10.1016/j.gloplacha.2005.05.003> (cit. on pp. 18, 144)
- Pritchard, H. D., Ligtenberg, S. R. M., Fricker, H. A., Vaughan, D. G., van den Broeke, M. R., & Padman, L. (2012). Antarctic ice-sheet loss driven by basal melting of ice shelves. *Nature*, 484(7395), 502–505. <https://doi.org/10.1038/nature10968> (cit. on pp. 38, 90)
- Rashidifard, M., Giraud, J., Lindsay, M., Jessell, M., & Ogarko, V. (2021). Constraining 3D geometric gravity inversion with a 2D reflection seismic profile using a generalized level set approach: Application to the eastern Yilgarn Craton. *Solid Earth*, 12(10), 2387–2406. <https://doi.org/10.5194/se-12-2387-2021> (cit. on p. 55)
- Ravier, E., & Buonchristiani, J.-F. (2018). Glaciohydrogeology. In *Past Glacial Environments* (pp. 431–466). Elsevier. <https://doi.org/10.1016/B978-0-08-100524-8.00013-0>. (Cit. on pp. 19, 33)
- Rignot, E., Jacobs, S., Mouginot, J., & Scheuchl, B. (2013). Ice-Shelf Melting Around Antarctica. *Science*, 341(6143), 266–270. <https://doi.org/10.1126/science.1235798> (cit. on pp. 16, 20, 27, 90, 108, 137, 157, 160)
- Rignot, E., Mouginot, J., & Scheuchl, B. (2011). Antarctic grounding line mapping from differential satellite radar interferometry. *Geophysical Research Letters*, 38, 1–6. <https://doi.org/10.1029/2011GL047109> (cit. on pp. 20, 137)
- Rignot, E., Mouginot, J., Scheuchl, B., van den Broeke, M., van Wessem, M. J., & Morlighem, M. (2019). Four decades of Antarctic Ice Sheet mass balance from 1979–2017. *Proceedings of the National Academy of Sciences*, 116(4), 1095–1103. <https://doi.org/10.1073/pnas.1812883116> (cit. on p. 38)
- Robertson, J. D., & Bentley, C. R. (1989). The Ross Ice Shelf: Glaciology and geophysics paper 3: Seismic studies on the grid western half of the Ross Ice Shelf: RIGGS I and RIGGS II. In C. R. Bentley & D. E. Hayes (Eds.), *Antarctic Research Series* (pp. 55–86). American Geophysical Union. <https://doi.org/10.1029/AR042p0055>. (Cit. on p. 156)
- Rooney, S. T., Blankenship, D. D., & Bentley, C. R. (1987). Seismic refraction measurements of crustal structure in West Antarctica. In G. D. McKenzie (Ed.), *Geophysical Monograph Series* (pp. 1–7). American Geophysical Union. <https://doi.org/10.1029/GM040p0001>. (Cit. on p. 156)
- Rosier, S. H. R., Hofstede, C., Brisbourne, A. M., Hattermann, T., Nicholls, K. W., Davis, P. E. D., Anker, P. G. D., Hillenbrand, C.-D., Smith, A. M., & Corr, H. F. J. (2018). A New Bathymetry for the Southeastern Filchner-Ronne Ice Shelf: Implications for Modern Oceanographic Processes and Glacial History. *Journal of Geophysical Research: Oceans*, 123(7), 4610–4623. <https://doi.org/10.1029/2018JC013982> (cit. on p. 149)

- Roy, L., Sen, M. K., Blankenship, D. D., Stoffa, P. L., & Richter, T. G. (2005). Inversion and uncertainty estimation of gravity data using simulated annealing: An application over Lake Vostok, East Antarctica. *Geophysics*, 70(1), J1–J12. <https://doi.org/10.1190/1.1852777> (cit. on p. 106)
- Salvini, F., Brancolini, G., Busetti, M., Storti, F., Mazzarini, F., & Coren, F. (1997). Cenozoic geodynamics of the Ross Sea region, Antarctica: Crustal extension, intraplate strike-slip faulting, and tectonic inheritance. *Journal of Geophysical Research: Solid Earth*, 102(B11), 24669–24696. <https://doi.org/10.1029/97JB01643> (cit. on pp. 30, 31)
- Sandwell, D. T. (1987). Biharmonic spline interpolation of GEOS-3 and SEASAT altimeter data. *Geophysical Research Letters*, 14(2), 139–142. <https://doi.org/10.1029/GL014i002p00139> (cit. on pp. 62, 63, 100, 108)
- Santos, D. F., Silva, J. B. C., Martins, C. M., dos Santos, R. D. C. S., Ramos, L. C., & de Araújo, A. C. M. (2015). Efficient gravity inversion of discontinuous basement relief. *GEO-PHYSICS*, 80(4), G95–G106. <https://doi.org/10.1190/geo2014-0513.1> (cit. on pp. 42, 106)
- Sauli, C., Sorlien, C., Busetti, M., De Santis, L., Geletti, R., Wardell, N., & Luyendyk, B. P. (2021). Neogene development of the Terror Rift, western Ross Sea, Antarctica. *Geochemistry, Geophysics, Geosystems*, 22(3). <https://doi.org/10.1029/2020GC009076> (cit. on pp. 30, 32)
- Scambos, T. A., Bohlander, J., Shuman, C., & Skvarca, P. (2004). Glacier acceleration and thinning after ice shelf collapse in the Larsen B embayment, Antarctica. *Geophysical Research Letters*, 31(18), L18402. <https://doi.org/10.1029/2004GL020670> (cit. on p. 90)
- Scambos, T., Haran, T., Fahnestock, M., Painter, T., & Bohlander, J. (2007). MODIS-based Mosaic of Antarctica (MOA) data sets: Continent-wide surface morphology and snow grain size. *Remote Sensing of Environment*, 111(2-3), 242–257. <https://doi.org/10.1016/j.rse.2006.12.020> (cit. on pp. 27, 91, 113, 117, 118, 125, 130, 132, 139)
- Scheinert, M., Ferraccioli, F., Schwabe, J., Bell, R., Studinger, M., Damaske, D., Jokat, W., Aleshkova, N., Jordan, T., Leitchenkov, G., Blankenship, D. D., Damiani, T. M., Young, D., Cochran, J. R., & Richter, T. D. (2016). New Antarctic gravity anomaly grid for enhanced geodetic and geophysical studies in Antarctica. *Geophysical Research Letters*, 43(2), 600–610. <https://doi.org/10.1002/2015GL067439> (cit. on p. 149)
- Schlegel, N.-J., Seroussi, H., Schodlok, M. P., Larour, E. Y., Boening, C., Limonadi, D., Watkins, M. M., Morlighem, M., & van den Broeke, M. R. (2018). Exploration of Antarctic Ice Sheet 100-year contribution to sea level rise and associated model uncertainties using the ISSM framework. *The Cryosphere*, 12(11), 3511–3534. <https://doi.org/10.5194/tc-12-3511-2018> (cit. on p. 15)
- Schnaidt, S., & Heinson, G. (2015). Bootstrap resampling as a tool for uncertainty analysis in 2-D magnetotelluric inversion modelling. *Geophysical Journal International*, 203(1), 92–106. <https://doi.org/10.1093/gji/ggv264> (cit. on pp. 73, 101)
- Schön, J. H. (2015). Density. In *Developments in Petroleum Science* (pp. 109–118). Elsevier. <https://doi.org/10.1016/B978-0-08-100404-3.00004-4>. (Cit. on pp. 112, 116, 129)
- Seroussi, H., Ivins, E. R., Wiens, D. A., & Bondzio, J. (2017). Influence of a West Antarctic mantle plume on ice sheet basal conditions. *Journal of Geophysical Research: Solid Earth*, 122(9), 7127–7155. <https://doi.org/10.1002/2017JB014423> (cit. on p. 144)
- Shen, W., Wiens, D. A., Anandakrishnan, S., Aster, R. C., Gerstoft, P., Bromirski, P. D., Hansen, S. E., Dalziel, I. W. D., Heeszel, D. S., Huerta, A. D., Nyblade, A. A., Stephen, R., Wilson, T. J., & Winberry, J. P. (2018a). The crust and upper mantle structure of Central and West Antarctica from bayesian inversion of Rayleigh wave and receiver functions. *Journal of Geophysical Research: Solid Earth*, 123(9), 7824–7849. <https://doi.org/10.1029/2017JB015346> (cit. on pp. 32, 35)
- Shen, W., Wiens, D. A., Lloyd, A. J., & Nyblade, A. A. (2020). A geothermal heat flux map of Antarctica empirically constrained by seismic structure. *Geophysical Research Letters*, 47(14). <https://doi.org/10.1029/2020GL086955> (cit. on pp. 139, 145)
- Shen, W., Wiens, D. A., Stern, T., Anandakrishnan, S., Aster, R. C., Dalziel, I., Hansen, S., Heeszel, D. S., Huerta, A., Nyblade, A., Wilson, T. J., & Winberry, J. P. (2018b). Seismic evidence for lithospheric foundering beneath the southern Transantarctic Mountains, Antarctica. *Geology*, 46(1), 71–74. <https://doi.org/10.1130/G39555.1> (cit. on p. 33)
- Shipp, S., Anderson, J., & Domack, E. (1999). Late Pleistocene-Holocene retreat of the West Antarctic Ice-Sheet system in the Ross Sea: Part 1 - Geophysical results. *Geological Society*

- of America Bulletin*, 111(10), 32. <https://doi.org/10.1130/0016-7606%281999%29111%3C1486%3ALPHROT%3E2.3.CO%3B2> (cit. on p. 16)
- Siddoway, C. S. (2008). Tectonics of the West Antarctic Rift System: New light on the history and dynamics of distributed intracontinental extension. In A. K. Cooper, P. J. Barrett, H. Stagg, B. C. Storey, W. Stump, W. Wise, & 10th ISAES editorial team (Eds.), *Antarctica: A Keystone in a Changing World*. The National Academies Press. <https://doi.org/10.3133/ofr20071047KP09>. (Cit. on p. 30)
- Siegert, M. J., Kulessa, B., Bougamont, M., Christoffersen, P., Key, K., Andersen, K. R., Booth, A. D., & Smith, A. M. (2018). Antarctic subglacial groundwater: A concept paper on its measurement and potential influence on ice flow. *Geological Society, London, Special Publications*, 461(1), 197–213. <https://doi.org/10.1144/SP461.8> (cit. on p. 26)
- Siegert, M. J., Taylor, J., Payne, A. J., & Hubbard, B. (2004). Macro-scale bed roughness of the simple coast ice streams in West Antarctica. *Earth Surface Processes and Landforms*, 29(13), 1591–1596. <https://doi.org/10.1002/esp.1100> (cit. on p. 20)
- Slater, T., & Shepherd, A. (2018). Antarctic ice losses tracking high. *Nature Climate Change*, 8(12), 1025–1026. <https://doi.org/10.1038/s41558-018-0284-9> (cit. on p. 15)
- Smith, B., Fricker, H. A., Gardner, A. S., Medley, B., Nilsson, J., Paolo, F. S., Holschuh, N., Adusumilli, S., Brunt, K., Csatho, B., Harbeck, K., Markus, T., Neumann, T., Siegfried, M. R., & Zwally, H. J. (2020a). Pervasive ice sheet mass loss reflects competing ocean and atmosphere processes. *Science*, eaaz5845. <https://doi.org/10.1126/science.aaz5845> (cit. on p. 38)
- Smith, E. C., Hattermann, T., Kuhn, G., Gaedicke, C., Berger, S., Drews, R., Ehlers, T. A., Franke, D., Gromig, R., Hofstede, C., Lambrecht, A., Läufer, A., Mayer, C., Tiedemann, R., Wilhelms, F., & Eisen, O. (2020b). Detailed Seismic Bathymetry Beneath Ekström Ice Shelf, Antarctica: Implications for Glacial History and Ice-Ocean Interaction. *Geophysical Research Letters*, 47(10). <https://doi.org/10.1029/2019GL086187> (cit. on p. 121)
- Smith, W. H. F., & Wessel, P. (1990). Gridding with continuous curvature splines in tension. *GEOPHYSICS*, 55(3), 293–305. <https://doi.org/10.1190/1.1442837> (cit. on pp. 60, 62, 63, 99, 100, 108, 122, 155)
- Soler, S. R., & Uieda, L. (2021). Gradient-boosted equivalent sources. *Geophysical Journal International*, 227(3), 1768–1783. <https://doi.org/10.1093/gji/ggab297> (cit. on pp. 51, 57, 60, 112)
- Sorlien, C. C., Luyendyk, B., Wilson, D. S., Decesari, R. C., Bartek, L. R., & Diebold, J. B. (2007). Oligocene development of the West Antarctic Ice Sheet recorded in eastern Ross Sea strata. *Geology*, 35(5), 467. <https://doi.org/10.1130/G23387A.1> (cit. on p. 26)
- Spector, P., Stone, J., Cowdery, S. G., Hall, B., Conway, H., & Bromley, G. (2017). Rapid early-Holocene deglaciation in the Ross Sea, Antarctica. *Geophysical Research Letters*, 44(15), 7817–7825. <https://doi.org/10.1002/2017GL074216> (cit. on p. 90)
- Steffen, H., Olesen, O., & Sutinen, R. (2021). Glacially Triggered Faulting: A Historical Overview and Recent Developments. In H. Steffen, O. Olesen, & R. Sutinen (Eds.), *Glacially-Triggered Faulting* (First, pp. 3–19). Cambridge University Press. <https://doi.org/10.1017/9781108779906.003>. (Cit. on pp. 19, 143)
- Stern, T. A., Davey, F. J., & Delisle, G. (1991). Lithospheric flexure induced by the load of the Ross Archipelago, southern Victoria land, Antarctica. In M. Thomson, A. Crame, & J. Thomson (Eds.), *Geological Evolution of Antarctica* (pp. 323–328). Cambridge University Press. (Cit. on p. 31).
- Stern, T. A., Ten Brink, U. S., Beaudoin, B. C., & Bannister, S. (1994). Seismic Reflection Experiments on the Ross Ice Shelf: 1985-1991. *Terra Antarctica*, 1(3), 513–516 (cit. on p. 21).
- Stern, T. A., & ten Brink, U. S. (1989). Flexural uplift of the Transantarctic Mountains. *Journal of Geophysical Research: Solid Earth*, 94(B8), 10315–10330. <https://doi.org/10.1029/JB094iB08p10315> (cit. on p. 133)
- Stevens, C., Hulbe, C., Brewer, M., Stewart, C., Robinson, N., Ohneiser, C., & Jendersie, S. (2020). Ocean mixing and heat transport processes observed under the Ross Ice Shelf control its basal melting. *Proceedings of the National Academy of Sciences*, 117(29), 16799–16804. <https://doi.org/10.1073/pnas.1910760117> (cit. on p. 91)
- Still, H., Campbell, A., & Hulbe, C. (2019). Mechanical analysis of pinning points in the Ross Ice Shelf, Antarctica. *Annals of Glaciology*, 60(78), 32–41. <https://doi.org/10.1017/aog.2018.31> (cit. on pp. 20, 26, 33, 91, 131, 142, 143)

- Still, H., & Hulbe, C. (2021). Mechanics and dynamics of pinning points on the Shirase Coast, West Antarctica. *The Cryosphere*, 15(6), 19. <https://doi.org/10.5194/tc-15-2647-2021> (cit. on p. 142)
- St-Laurent, P., Klinck, J. M., & Dinniman, M. S. (2013). On the Role of Coastal Troughs in the Circulation of Warm Circumpolar Deep Water on Antarctic Shelves. *Journal of Physical Oceanography*, 43(1), 51–64. <https://doi.org/10.1175/JPO-D-11-0237.1> (cit. on p. 38)
- Studinger, M., Bell, R., Fitzgerald, P., & Buck, W. (2006). Crustal architecture of the Transantarctic Mountains between the Scott and Reedy Glacier region and South Pole from aerogeophysical data. *Earth and Planetary Science Letters*, 250(1-2), 182–199. <https://doi.org/10.1016/j.epsl.2006.07.035> (cit. on p. 34)
- Studinger, M., Bell, R. E., Buck, W., Karner, G. D., & Blankenship, D. D. (2004a). Sub-ice geology inland of the Transantarctic Mountains in light of new aerogeophysical data. *Earth and Planetary Science Letters*, 220(3-4), 391–408. [https://doi.org/10.1016/S0012-821X\(04\)00066-4](https://doi.org/10.1016/S0012-821X(04)00066-4) (cit. on pp. 28, 153)
- Studinger, M., Bell, R. E., & Tikku, A. A. (2004b). Estimating the depth and shape of subglacial Lake Vostok's water cavity from aerogravity data: ESTIMATING LAKE VOSTOK'S WATER DEPTH. *Geophysical Research Letters*, 31(12), n/a–n/a. <https://doi.org/10.1029/2004GL019801> (cit. on pp. 106, 120)
- Studinger, M., & Miller, H. (1999). Crustal structure of the Filchner-Ronne Shelf and Coats Land, Antarctica, from gravity and magnetic data: Implications for the breakup of Gondwana. *Journal of Geophysical Research: Solid Earth*, 104(B9), 20379–20394. <https://doi.org/10.1029/1999JB900117> (cit. on p. 149)
- Talwani, M., Worzel, J. L., & Landisman, M. (1959). Rapid gravity computations for two-dimensional bodies with application to the Mendocino submarine fracture zone. *Journal of Geophysical Research*, 64(1), 49–59. <https://doi.org/10.1029/JZ064i001p00049> (cit. on p. 106)
- Tankersley, M., Horgan, H. J., Siddoway, C. S., Caratori Tontini, F., & Tinto, K. J. (2022). Basement Topography and Sediment Thickness Beneath Antarctica's Ross Ice Shelf. *Geophysical Research Letters*, 49(10). <https://doi.org/10.1029/2021GL097371> (cit. on pp. 22, 116, 129, 133, 151)
- Tankersley, M. D. (2023). Antarctic_plots: V0.0.6. <https://doi.org/10.5281/zenodo.7750998>. (Cit. on pp. 23, 51, 171)
- Tankersley, M. (2022). Mdtanker/RIS_basement_sediment: V2.0. <https://doi.org/10.5281/zenodo.6499863>. (Cit. on p. 23)
- Tankersley, M., Horgan, H., & Caratori-Tontini, F. (2023). Mdtanker/RIS_gravity_inversion: First release associated with PhD thesis. <https://doi.org/10.5281/zenodo.8084469>. (Cit. on p. 23)
- Tarantola, A. (2005). *Inverse Problem Theory and Methods for Model Parameter Estimation*. Society for Industrial and Applied Mathematics. <https://doi.org/10.1137/1.9780898717921>. (Cit. on p. 39)
- ten Brink, U. S., Bannister, S., Beaudoin, B. C., & Stern, T. A. (1993). Geophysical investigations of the tectonic boundary between East and West Antarctica. *Science*, 261(5117), 45–50. <https://doi.org/10.1126/science.261.5117.45> (cit. on pp. 21, 31, 133)
- Thomas, R. H. (1979). Ice Shelves: A Review. *Journal of Glaciology*, 24(90), 273–286. <https://doi.org/10.3189/S0022143000014799> (cit. on p. 17)
- Timmermann, R., Brocq, A. L., Deen, T., Domack, E., Dutrieux, P., Galton-Fenzi, B., Hellmer, H., Humbert, A., Jansen, D., Jenkins, A., Lambrecht, A., Makinson, K., Niederjasper, F., Nitsche, F., Nøst, O. A., Smedsrød, L. H., & Smith, W. H. F. (2010). A consistent data set of Antarctic ice sheet topography, cavity geometry, and global bathymetry. *Earth System Science Data*, 2(2), 13. <https://doi.org/10.5194/essd-2-261-2010> (cit. on pp. 91, 124)
- Tinto, K. J., & Bell, R. E. (2011). Progressive unpinning of Thwaites Glacier from newly identified offshore ridge: Constraints from aerogravity. *Geophysical Research Letters*, 38, 1–6. <https://doi.org/10.1029/2011GL049026> (cit. on pp. 46, 105, 106, 120, 149)
- Tinto, K. J., Padman, L., Siddoway, C. S., Springer, S. R., Fricker, H. A., Das, I., Caratori Tontini, F., Porter, D. F., Frearson, N. P., Howard, S. L., Siegfried, M. R., Mosbeux, C., Becker, M. K., Bertinato, C., Boghosian, A., Brady, N., Burton, B. L., Chu, W., Cordero, S. I., ... Bell, R. E. (2019). Ross Ice Shelf response to climate driven by the tectonic imprint on seafloor bathymetry. *Nature Geoscience*, 12(6), 441–449. <https://doi.org/10.1038/s41561-019-0370-2> (cit. on pp. 20, 21, 26–28, 30, 32, 34, 38, 46, 68, 90–92, 104–108, 111, 120, 122, 124, 126, 127, 129, 131–134, 137–141, 148, 152, 156, 157)

- Tinto, K. J., Bell, R. E., Cochran, J. R., & Münchow, A. (2015). Bathymetry in Petermann fjord from Operation IceBridge aerogravity. *Earth and Planetary Science Letters*, 422, 58–66. <https://doi.org/10.1016/j.epsl.2015.04.009> (cit. on pp. 16, 45, 46, 105, 106, 120)
- Tulaczyk, S., Kamb, W. B., & Engelhardt, H. F. (2000). Basal mechanics of Ice Stream B, west Antarctica: 2. Undrained plastic bed model. *Journal of Geophysical Research: Solid Earth*, 105(B1), 483–494. <https://doi.org/10.1029/1999JB900328> (cit. on pp. 18, 144)
- Uieda, L. (2018). Verde: Processing and gridding spatial data using Green's functions. *Journal of Open Source Software*, 3(29), 957. <https://doi.org/10.21105/joss.00957> (cit. on pp. 51, 60, 61, 63, 70, 99)
- Uieda, L., & Barbosa, V. C. (2017). Fast nonlinear gravity inversion in spherical coordinates with application to the South American Moho. *Geophysical Journal International*, 208(1), 162–176. <https://doi.org/10.1093/gji/ggw390> (cit. on pp. 42, 48, 49, 53, 55, 85, 100, 106, 150)
- Uieda, L., Soler, S., Rampin, R., van Kemenade, H., Turk, M., Shapero, D., Banihirwe, A., & Leeman, J. (2020). Pooch: A friend to fetch your data files. *Journal of Open Source Software*, 5(45), 1943. <https://doi.org/10.21105/joss.01943> (cit. on p. 171)
- Uieda, L., Tian, D., Leong, W. J., Jones, M., Schlitzer, W., Toney, L., Grund, M., Yao, J., Magen, Y., Materna, K., Newton, T., Anant, A., Ziebarth, M., Wessel, P., & Quinn, J. (2021). PyGMT: A Python interface for the Generic Mapping Tools. <https://doi.org/10.5281/zenodo.5607255>. (Cit. on pp. 36, 51, 172)
- Vajda, P., Ellmann, A., Meurers, B., Vaníček, P., Novák, P., & Tenzer, R. (2008a). Global ellipsoid-referenced topographic, bathymetric and stripping corrections to gravity disturbance. *Studia Geophysica et Geodaetica*, 52(1), 19–34. <https://doi.org/10.1007/s11200-008-0003-5> (cit. on p. 104)
- Vajda, P., Ellmann, A., Meurers, B., Vaníček, P., Novák, P., & Tenzer, R. (2008b). Gravity disturbances in regions of negative heights: A reference quasi-ellipsoid approach. *Studia Geophysica et Geodaetica*, 52(1), 35–52. <https://doi.org/10.1007/s11200-008-0004-4> (cit. on p. 94)
- Vajda, P., Vaníček, P., & Meurers, B. (2006). A new physical foundation for anomalous gravity. *Studia Geophysica et Geodaetica*, 50(2), 189–216. <https://doi.org/10.1007/s11200-006-0012-1> (cit. on p. 96)
- Vajda, P., Vaníček, P., Novák, P., Tenzer, R., & Ellmann, A. (2007). Secondary indirect effects in gravity anomaly data inversion or interpretation. *Journal of Geophysical Research*, 112(B6), B06411. <https://doi.org/10.1029/2006JB004470> (cit. on pp. 95, 103)
- Vajda, P., Vaníček, P., & Meurers, B. (2004). On the removal of the effect of topography on gravity disturbance in gravity data inversion or interpretation. *Contributions to Geophysics and Geodesy*, 34 (cit. on p. 94).
- Vaňková, I., Winberry, J. P., Cook, S., Nicholls, K. W., Greene, C. A., & Galton-Fenzi, B. K. (2023). High Spatial Melt Rate Variability Near the Totten Glacier Grounding Zone Explained by New Bathymetry Inversion. *Geophysical Research Letters*, 50(10), e2023GL102960. <https://doi.org/10.1029/2023GL102960> (cit. on pp. 105, 107)
- Venturelli, R. A., Siegfried, M. R., Roush, K. A., Li, W., Burnett, J., Zook, R., Fricker, H. A., Priscu, J. C., Leventer, A., & Rosenheim, B. E. (2020). Mid-Holocene grounding line retreat and readvance at Whillans Ice Stream, West Antarctica. *Geophysical Research Letters*, 47(15). <https://doi.org/10.1029/2020GL088476> (cit. on pp. 20, 32, 33, 36, 90, 131, 137)
- Virtanen, P., Gommers, R., Oliphant, T. E., Haberland, M., Reddy, T., Cournapeau, D., Burovski, E., Peterson, P., Weckesser, W., Bright, J., van der Walt, S. J., Brett, M., Wilson, J., Millman, K. J., Mayorov, N., Nelson, A. R. J., Jones, E., Kern, R., Larson, E., ... SciPy 1.0 Contributors. (2020). SciPy 1.0: Fundamental algorithms for scientific computing in python. *Nature Methods*, 17, 261–272. <https://doi.org/10.1038/s41592-019-0686-2> (cit. on p. 51)
- Wannamaker, P., Hill, G., Stodt, J., Maris, V., Ogawa, Y., Selway, K., Boren, G., Bertrand, E., Uhlmann, D., Ayling, B., Green, A. M., & Feucht, D. (2017). Uplift of the central transantarctic mountains. *Nature Communications*, 8(1), 1588. <https://doi.org/10.1038/s41467-017-01577-2> (cit. on pp. 21, 133)
- Wei, W., Blankenship, D. D., Greenbaum, J. S., Gourmelen, N., Dow, C. F., Richter, T. G., Greene, C. A., Young, D. A., Lee, S., Kim, T.-W., Lee, W. S., & Assmann, K. M. (2020). Getz Ice Shelf melt enhanced by freshwater discharge from beneath the West Antarctic Ice Sheet. *The Cryosphere*, 14(4), 1399–1408. <https://doi.org/10.5194/tc-14-1399-2020> (cit. on pp. 105, 106, 120, 149)

- Werner, S. (1953). Interpretation of magnetic anomalies at sheet-like bodies. In *Sveriges Geologiska Undersök* (pp. 413–449). Stockholm Norstedt. (Cit. on pp. 28, 152).
- Wessel, P., Luis, J. F., Uieda, L., Scharroo, R., Wobbe, F., Smith, W. H. F., & Tian, D. (2019). The Generic Mapping Tools version 6. *Geochemistry, Geophysics, Geosystems*, 20(11), 5556–5564. <https://doi.org/10.1029/2019GC008515> (cit. on pp. 36, 63)
- Wessel, P., & Bercovici, D. (1998). Interpolation with splines in tension: A Green's function approach. *Mathematical Geology*, 30(1), 77–93. <https://doi.org/10.1023/A:1021713421882> (cit. on p. 63)
- White-Gaynor, A. L., Nyblade, A. A., Aster, R. C., Wiens, D. A., Bromirski, P. D., Gerstoft, P., Stephen, R. A., Hansen, S. E., Wilson, T., Dalziel, I. W., Huerta, A. D., Paul Winberry, J., & Anandakrishnan, S. (2019). Heterogeneous upper mantle structure beneath the Ross Sea Embayment and Marie Byrd Land, West Antarctica, revealed by P-wave tomography. *Earth and Planetary Science Letters*, 513, 40–50. <https://doi.org/10.1016/j.epsl.2019.02.013> (cit. on p. 34)
- Whitehouse, P. L., Gomez, N., King, M. A., & Wiens, D. A. (2019). Solid Earth change and the evolution of the Antarctic Ice Sheet. *Nature Communications*, 10(1), 503. <https://doi.org/10.1038/s41467-018-08068-y> (cit. on pp. 19, 33)
- Wilkinson, M. D., Dumontier, M., Aalbersberg, I. J., Appleton, G., Axton, M., Baak, A., Blomberg, N., Boiten, J.-W., da Silva Santos, L. B., Bourne, P. E., Bouwman, J., Brookes, A. J., Clark, T., Crosas, M., Dillo, I., Dumon, O., Edmunds, S., Evelo, C. T., Finkers, R., ... Mons, B. (2016). The FAIR Guiding Principles for scientific data management and stewardship. *Scientific Data*, 3(1), 160018. <https://doi.org/10.1038/sdata.2016.18> (cit. on p. 23)
- Wilson, D. S., Jamieson, S. S., Barrett, P. J., Leitchenkov, G., Gohl, K., & Larter, R. D. (2012). Antarctic topography at the Eocene–Oligocene boundary. *Palaeogeography, Palaeoclimatology, Palaeoecology*, 335–336, 24–34. <https://doi.org/10.1016/j.palaeo.2011.05.028> (cit. on pp. 34, 147, 155)
- Wilson, D. S., & Luyendyk, B. (2009). West Antarctic paleotopography estimated at the Eocene–Oligocene climate transition. *Geophysical Research Letters*, 36(16), L16302. <https://doi.org/10.1029/2009GL039297> (cit. on pp. 26, 34, 147, 155, 157)
- Wilson, D. S., Pollard, D., DeConto, R. M., Jamieson, S. S., & Luyendyk, B. (2013). Initiation of the West Antarctic Ice Sheet and estimates of total Antarctic ice volume in the earliest Oligocene. *Geophysical Research Letters*, 40(16), 4305–4309. <https://doi.org/10.1002/grl.50797> (cit. on pp. 26, 34)
- Yamasaki, T., Miura, H., & Nogi, Y. (2008). Numerical modelling study on the flexural uplift of the Transantarctic Mountains. *Geophysical Journal International*, 174(1), 377–390. <https://doi.org/10.1111/j.1365-246X.2008.03815.x> (cit. on p. 133)
- Yang, J., Guo, J., Greenbaum, J. S., Cui, X., Tu, L., Li, L., Jong, L. M., Tang, X., Li, B., Blankenship, D. D., Roberts, J. L., Ommen, T., & Sun, B. (2021). Bathymetry Beneath the Amery Ice Shelf, East Antarctica, Revealed by Airborne Gravity. *Geophysical Research Letters*, 48(24). <https://doi.org/10.1029/2021GL096215> (cit. on pp. 38, 46, 63, 104–106, 120, 122)
- Yang, J., Jekeli, C., & Liu, L. (2018). Seafloor Topography Estimation From Gravity Gradients Using Simulated Annealing. *Journal of Geophysical Research: Solid Earth*. <https://doi.org/10.1029/2018JB015883> (cit. on p. 106)
- Yang, J., Luo, Z., & Tu, L. (2020a). Ocean Access to Zachariæ Isstrøm Glacier, Northeast Greenland, Revealed by OMG Airborne Gravity. *Journal of Geophysical Research: Solid Earth*, 125(11). <https://doi.org/10.1029/2020JB020281> (cit. on pp. 78, 105, 106)
- Yang, J., Luo, Z., Tu, L., Li, S., Guo, J., & Fan, D. (2020b). On the Feasibility of Seafloor Topography Estimation from Airborne Gravity Gradients: Performance Analysis Using Real Data. *Remote Sensing*, 12(24), 4092. <https://doi.org/10.3390/rs12244092> (cit. on p. 104)
- Yokoyama, Y., Anderson, J. B., Yamane, M., Simkins, L. M., Miyairi, Y., Yamazaki, T., Koizumi, M., Suga, H., Kusahara, K., Prothro, L., Hasumi, H., Southon, J. R., & Ohkouchi, N. (2016). Widespread collapse of the Ross Ice Shelf during the late Holocene. *Proceedings of the National Academy of Sciences*, 113(9), 2354–2359. <https://doi.org/10.1073/pnas.1516908113> (cit. on p. 90)
- Zhao, C., Gladstone, R. M., Warner, R. C., King, M. A., Zwinger, T., & Morlighem, M. (2018). Basal friction of Fleming Glacier, Antarctica – Part 1: Sensitivity of inversion to temperature and bedrock uncertainty. *The Cryosphere*, 12(8), 2637–2652. <https://doi.org/10.5194/tc-12-2637-2018> (cit. on p. 15)

- Zhao, K. X., Stewart, A. L., & McWilliams, J. C. (2019). Sill-Influenced Exchange Flows in Ice Shelf Cavities. *Journal of Physical Oceanography*, 49(1), 163–191. <https://doi.org/10.1175/JPO-D-18-0076.1> (cit. on pp. 16, 91)
- Zhou, Z., Wiens, D. A., Shen, W., Aster, R. C., Nyblade, A., & Wilson, T. J. (2022). Radial Anisotropy and Sediment Thickness of West and Central Antarctica Estimated From Rayleigh and Love Wave Velocities. *Journal of Geophysical Research: Solid Earth*, 127(3). <https://doi.org/10.1029/2021JB022857> (cit. on pp. 31, 156)